THE UNIVERSITY OF HULL

FOLDED RF-EXCITED CO_2 WAVEGUIDE LASERS

being a Thesis submitted for the Degree of

Doctor of Philosophy

in the University of Hull

by

Paul Edward Jackson, B.Sc. (Hull)

March 1988

SUMMARY OF THESIS SUBMITTED FOR Ph.D. DEGREE

BY PAUL E JACKSON

ON

FOLDED RF EXCITED CO_2 WAVEGUIDE LASERS

This thesis describes theoretical and experimental work on RF excited CO_2 waveguide lasers and amplifiers.

The mode coupling losses at a bend in a folded waveguide have been evaluated as a function of the selectable parameters to determine the low-loss folding geometries. A direct comparison is made between three types of optical arrangement used for folding in a compact, sealed-off, Z-fold CO_2 waveguide laser excited by a transverse RF discharge. In particular, the measured laser output power as a function of discharge conditions and mirror alignment for plane and curved mirror, and partial waveguide folded resonators are compared.

The Z-fold laser output power is predicted by incorporating the known and estimated laser parameters into a Rigrod-type analysis. A simultaneous solution of the Rigrod equations predicting the laser powers for different intra-cavity gain lengths is used with the experimental data to derive the discharge and resonator parameters. Experimental results are in good agreement with the theoretical predictions, and suggest that a ~1% power loss per fold has been achieved with partial waveguide folding. Also, the preliminary theoretical results of a multi-mode resonator model predicting the laser output power as a function of the angular mis-alignment of one of the Z-fold laser folding mirrors are in qualitative agreement with the experimental determinations.

Experiments related to laser efficiency and frequency stability are discussed briefly. These include an investigation into an automatic impedance matching scheme for dynamic optimisation of the power transfer efficiency between RF generator and the laser head; the Opto-Hertzian effect (RF equivalent to the opto-Galvanic effect) for laser frequency stabilisation; a novel parallel-resonant distributed inductance excitation technique using a multi-start solenoid; and finally, identification of hooting laser resonator modes responsible for impeding heterodyne measurements when a clean RF spectrum is required.

In addition, theoretical and experimental studies of laser amplification are presented. The suitability of folded waveguide and non-waveguide structures for power amplification or pre-amplification is assessed to determine their applicability to coherent LIDAR. Optical amplification of wideband transmitter and/or receiver signals is considered a favourable way of improving the discrimination of range and velocity determinations.

Finally, as a result of this work, up to 53.4 Watts output power in a high quality fundamental Gaussian beam has been obtained from a compact, sealed-off, Z-fold CO_2 waveguide laser with a 115 cm discharge length, which implies a specific power performance of 0.46 W/cm. Efficiencies (laser output power/RF input power) of up to 9.2% have also been observed.

TO MY MOTHER AND FATHER

CONTENTS

FOREWORD

I was born in Leicester, England, on April 5, 1963. My interest in the sciences and particularly physics, stems back to my school days. It was during my 'A' level studies at Lutterworth Grammar School, a period that I shall always look back on with much fondness, that I decided to pursue a career in physics. I received the B.Sc. degree in Applied Physics with Laser Technology from the University of Hull, England, in 1984. Involvement with the laser research groups at Hull, as part of my undergraduate training and through vacation work, strongly influenced my decision to apply for doctoral work there. I joined the RF laser group under Denis Hall in the Autumn of 1984 as an SERC (CASE) student with RSRE (Malvern, England).

This thesis describes my research efforts over the last three years. It is not intended that the reader should necessarily work through the text in the order in which the chapters appear. Each chapter begins by summarising its main contents and together with the contents page may help cross-referencing. Literature references are listed numerically at the end. Some more detailed accounts, intended for the serious reader, appear in the Appendix.

There are, of course, many academic and technical staff to whom I shall always be grateful, for their assistance and friendship over the last few years, and for making my stay at Hull an enjoyable and memorable one. In particular I would

like to thank SERC for their financial support and express my sincere thanks and indebtedness to my supervisor, Professor Denis Hall, for his professional guidance and continuing support. I am also extremely grateful to Dr. Christopher Hill for countless informal discussions and encouragement. My appreciation is also extended to my immediate colleagues Dr. Patrick Vidaud de Plaud, Dr. Howard Baker, Guy Pearson, Ayub Durrani and Dr. Krzysztof Abramski; and to my industrial supervisors Mike Jenkins (RSRE) and Dr. Michael Vaughan (RSRE).

I thank the technical staff under Harold Pashby, and particularly Ernie Thompson, for workshop support; Peter Wilson for his continual technical support, and Stephen Haughey for his computer expertise. I am grateful to Janice McClelland for the rapid and professional typing of this manuscript and to Sherron Watt for the art work.

Finally, I am especially thankful to my wife, Sheila, for her understanding and unflagging support.

PUBLISHED WORK

CONFERENCE PRESENTATIONS

[1] P.E. Jackson, D.R. Hall, R.M. Jenkins and J.M. Vaughan "Simultaneous Measurements of Gain and Spontaneous Emission Noise in RF-Excited CO_2 Amplifying Media" Paper 15, pp. 46-53, SPIE Vol. 806, Active Infrared Systems and Technology, The Hague, April 1987.

[2] P.E. Jackson, D.R. Hall and C.A. Hill "RF-Excited Z-Fold CO_2 Laser: Theory and Experiment", Paper 5, presented at the Eighth National Quantum Electronics Conference, St. Andrews, September 1987.

[3] P.E. Jackson, K.M. Abramski and D.R. Hall "Automatic Impedance Matching and Opto-Hertzian Effect in RF-Excited CO_2 Waveguide Lasers" Paper 22, presented at the Eighth National Quantum Electronics Conference, St. Andrews, September 1987.

[4] P.E. Jackson, D.R. Hall and R.M. Jenkins "Mode Coupling Losses at a Fold in a Hollow Dielectric Waveguide Laser" Paper 23, presented at the Eighth National Quantum Electronics Conference, St. Andrews, September 1987.

[5] P.E. Jackson and D.R.Hall "Laser Amplifiers for Coherent LIDAR: An Overview" Paper W8, presented at the Rank Prize Fund Mini-Symposium on Fundamental Limits of Coherent LIDAR, Broadway (U.K.), December 1987.

[6] P.E. Jackson, D.R. Hall and C.A. Hill, "Comparisons of CO_2 Laser Resonator Folding Techniques" Paper ThT5, to be presented at CLEO '88, Anaheim.

JOURNAL PUBLICATIONS

[1] P.E. Jackson, K.M. Abramski and D.R. Hall "Automatic Impedance Matching and Opto-Hertzian Effect in RF-Excited CO_2 Waveguide Lasers" Submitted to J. Appl. Phys. B, October 1987.

[2] C.A. Hill and P.E. Jackson "Hooting Modes in CO_2 Waveguide Lasers" Submitted to IEEE J. Quantum Electron., January 1988.

[3] P.E. Jackson, D.R. Hall and C.A. Hill
"Comparisons of CO_2 Laser Resonator Folding Techniques"
To be published.

[4] C.A. Hill, P.E. Jackson and D.R. Hall, "CO_2 Waveguide Lasers with Folds and Tilted Mirrors", to be published.

[5] J. Banerji, A.R. Davies, P.E. Jackson and R.M. Jenkins
"Transmission and Coupling Losses in a Folded Waveguide"
To be published.

CHAPTER 1

INTRODUCTION

1.1 General Intoduction

The first laser was built in 1960 and within a decade laser wavelengths spanned the range from infrared to ultraviolet. The technology needed to produce these systems was fast evolving and research quickly mushroomed. Many materials were investigated as the active laser medium, including crystals, semiconductors, ionised gases, molecular gases, and dye solutions. Various pumping mechanisms have been used to create the required population inversion for light amplification, including pulsed and continuous optical pumping, gaseous discharges, and chemical reactions. Several cavity arrangements for optical feedback have evolved from the original Fabry-Perot etalon, such as confocal, hemi-spherical, and waveguide resonators. Over twenty five years on laser technology is still a dynamic field. Lasers have ventured out of the laboratory and into factories, offices and homes. Laser applications from communication links, surgery, welding and cutting to nuclear fusion, to name only a few, have demonstrated the applicability of the laser.

This thesis is principally concerned with folded radio-frequency excited carbon dioxide waveguide lasers. In this type of device the active laser medium is the carbon

dioxide molecule, which lases between vibrational modes and emits in the infrared around 10 micrometers. Laser action is sustained by a radio-frequency (RF) excited discharge confined within an optical waveguide. The waveguide resonator may be folded in space for convenience. The objectives of the work described in this thesis have been to further the understanding of the physics of folded waveguides, to design and construct a laser of the type described above, and to assess its performance.

The plan of this thesis is not chronological, but structured in a logical fashion. This chapter develops into a discussional review of RF gas discharge technology pertaining to lasers and amplifiers. Chapter 2 investigates why folded waveguide resonators are desirable and surveys the possible folding configurations. After a brief introduction to the basic waveguide equations a more rigorous analytical treatment of mode coupling losses at a fold is presented to determine the low-loss folding geometries. In Chapter 3 the resonator mode content and round-trip loss is modelled by a numerical, iterative and multimode treatment using the coupling coefficients derived in Chapter 2. The resonator round-trip loss data is incorporated into a laser output power estimation using a Rigrod analysis. This approach requires knowledge of the gain and saturation intensity of the active medium, which is not easily measured in practice. Single pass gain measurements generally involve probe lasers telescopically coupled to a waveguide containing the active

medium. Excitation of a single waveguide mode or a known combination of modes to simulate a predicted resonator mode gain is not practicable. There is however an alternative method involving the simultaneous solution of the Rigrod equations. Folded lasers with multiple parallel or near parallel channels with selective RF excitation (i.e. one, two or three channels excited, etc.) may conceivably operate with different gain-length products with otherwise (nearly) identical conditions. The corresponding measured output powers can then be incorporated into a simultaneous solution of the Rigrod equations to determine the unknowns, namely, gain, saturation intensity and resonator round-trip loss. The latter determination serves as a comparison for that predicted by the theoretical treatment described above.

The second part of this thesis is mostly concerned with experimental work with lasers and amplifiers. Chapter 4 describes the design considerations and construction of a z-fold waveguide laser and its RF excitation scheme. Chapter 5 gives a detailed account of laser experiments performed with three folding geometries chosen in Chapter 2. The laser operating characteristics for both well-aligned and mis-aligned mirrors are used for comparisons with the theoretical work. Chapter 6 describes four short experiments related to laser efficiency and frequency stability. These are; firstly, a novel automatic impedance matching scheme (AIMing) for dynamic optimisation of the power transfer efficiency between RF generator and laser head, in the face

of changes in the RF power input as a means of adjusting the laser output power; secondly, the opto-Hertzian effect (RF equivalent of the opto-galvanic or opto-voltaic effect) produced by circulating laser power fluctuations and detected in the RF reflected power, which may be used for laser frequency stabilisation; thirdly, a novel parallel-resonant distributed inductance excitation technique using a multi-start solenoid; and finally, identification of hooting modes in a CO_2 waveguide laser produced when two or more resonator modes lase simultaneously in a common laser line seriously impeding heterodyne measurements when a clean RF spectrum is required. Although these topics tend to digress a little from the general theme of this thesis they were some of the interesting and novel ideas developed en route, either in the course of the experimental work, or inadvertently observed during an experiment and judged worth pursuing.

Chapters 7 and 8 are concerned with laser amplification studies and the suitability of folded laser structures for single pass power amplification and small-signal amplification. Chapter 7 starts by reviewing optical amplification techniques with a brief look at laser amplifier theory, then addresses the problems associated with mode-matched injection for waveguide amplifiers. Non-waveguide laser amplifiers with noise reduction structures are considered for small-signal amplification. The approach in this chapter is mainly geared towards applications to coherent LIDAR, where both wideband power amplification of the transmitter signal and small-signal

amplification of the receiver signal is considered to be a favourable way of improving range and signal-to-noise ratio respectively. Chapter 8 describes measurements of laser amplification in two separate experiments. The first involved injection and single pass amplification of a probe signal in the z-fold laser structure described in Chapter 4. The second involved the simultaneous measurements of gain and spontaneous emission noise in an RF excited pre-amplifier discharge module.

Finally, in Chapter 9, a summary of the findings of the theoretical and experimental work are presented with proposals for future work.

1.2 A Review of RF Excited CO_2 Waveguide Laser Technology

Radio-frequency excitation has been extensively used in the past to pump various gas lasers, for example, the first carbon dioxide laser was excited by an RF discharge [1]. This technique removes some of the deleterious effects associated with direct-current excitation, such as cataphoresis, some striations and instabilities, and gas contamination by the electrodes. Recently, transverse RF excitation in the region 50-250 MHz has been successfully applied to the hollow dielectric waveguide geometry of the carbon-dioxide laser, taking advantage of the low excitation voltage requirement of the transverse pumping and eliminating the need for internal metallic electrodes [2-6].

The positive impedance characteristic exhibited by the RF discharge [7] and the efficient matching between the

waveguide mode volume and the laser excitation region contribute to an effective pumping system. The reduction in discharge tube diameter and the corresponding increase in gas pressure inherent in CO_2 waveguide devices has resulted in pressure-broadened linewidths in excess of 1500 MHz. The substantial increases observed in gain [8], output power per unit volume and saturation intensity [9,10] were expected from the scaling relations of [11], also modified to include the frequency dependence in RF discharge excited devices [12]. These benefits result from favourable de-excitation by wall collisions [13], operation at increased pressure, and reduction of the gas temperature [14] because of improved thermal conduction to the walls of the discharge tube [15].

The waveguide region consists of a hollow dielectric tube which may have arbitrary geometrical cross-sections including circular [16], elliptical, rectangular [17-19] or planar [20]. For a comprehensive review of the early work in the field of waveguide lasers see [21-23]. In each case the dominant laser mode is usually the EH_{11} yielding a quasi-TEM_{00} output mode [24,25].

The lowest guiding losses are obtained with ceramic materials such as Beryllia, Alumina and Boron Nitride, which have high refractive indices and low absorption coefficients at 10.6 μm [26]. The high thermal conductivity of these materials allows the laser to be cooled easily by either forced air or liquid coolants. The limitations of fabrication techniques generally preclude unbroken waveguides

of sufficient straightness much longer than 40-60 cm. However, multiple capillaries in a folded configuration, a series of collinear capillary tubes, of a metal/ceramic sandwich stucture can be used to obtain the desired length. Suitable dielectric components are costly and difficult to fabricate, and they may also limit laser performance and lifetime.

As the length of the waveguide is increased an undesirable non-uniform gas discharge arises due to the electrical transmission line properties of the electrodes [27]. This longitudinal non-uniformity can be eliminated by inductive termination of the line, multiple feed points, or parallel resonance between coils placed at intervals along the channel and the channel capacitance [28-30]. The transverse gain uniformity may be influenced by the presence of discharge striations observed in small cross-section discharge vessel [12,31].

The transfer of RF power from a generator to a laser head requires an impedance matching network [7,32]. Early RF waveguide laser designs employed RF input power densities of less than 85 W cm^{-3} [28]. These lasers also exhibited efficiencies of less than 10% with output powers of no more than 20 W at a maximum of 0.2 W cm^{-1} [3,4]. In more recent designs the RF input power has been increased to greater than 110 W cm^{-3} yielding a maximum laser output of 0.82 W cm^{-1} for a total of 30 W at 10% efficiency [6,33]. This exceeds the best reported DC discharge waveguide laser specific power performance [34,35].

The choices of RF operating frequency, gas pressure, gas mixture, and RF input power are very interdependent. The laser medium consists of a mixture of helium, carbon dioxide, nitrogen, and a few trace gases. The output power and efficiency of a sealed-off waveguide laser were reported to have been significantly increased by the addition of xenon [36,37]. This enhancement effect is generally attributed to the relatively low ionising potential of xenon.

The problem of coupling between the modes of a hollow dielectric waveguide and the modes in free space has been studied by several authors [38-44]. The treatment has been approached in two main ways: the first is to express the initial field as a linear combination of free space transverse modes [38,39] which are then propagated according to the familiar Gaussian beam equations [45]. The second is described by a Fresnel-Kirchoff diffraction integral [40-44]. (For a review of the coupling loss literature to date and the discrepancies therein see [46]). These techniques provide useful information for the design of low-loss resonators.

The same considerations that lead to the design of waveguide laser oscillators can be applied to the wideband laser power amplifier, and pre-amplifier designs [47,48]. High gain wide-band amplifiers are of interest for use in CO_2 laser radar transmitters and receivers where the bandwidth is required for FM Doppler radar signals.

The commercial exploitation of the RF excited waveguide CO_2 lasers have produced a reliable, low cost, fieldable and versatile device [50,52]. Progress in the development of these lasers has been very rapid, so that they are now commercially available from a number of companies, with improved construction and stability relative to the earlier models. Applications include precision material processing such as fusing optical fibres, micro-drilling holes and welding plastics, etching and marking thermoplastics, and resistor trimming; infrared beacons and scanners; plasma diagnostics; and laser surgery [53].

CHAPTER 2

MODE COUPLING LOSSES AT A FOLD IN A HOLLOW DIELECTRIC WAVEGUIDE

Summary

In this chapter the mode coupling losses at the bend in a folded waveguide are evaluated as a function of the selectable parameters, namely, the bore dimensions, the free-space propagation distance, the fold-angle, and the reflector curvature. In particular, the mode coupling loss matrix evaluations for several low-loss folding geometries are determined by applying existing theoretical treatments, except for those with curved reflectors where the development of a special treatment was necessary to include the effects of astigmatism. The results are used in later chapters to estimate the corresponding z-fold laser resonator mode round-trip losses for a comparison between the predicted and experimentally determined laser powers.

2.1 Introduction

There is an ever increasing demand for high power (25-75 W) compact CO_2 waveguide lasers for a range of military and industrial applications. To date, the best reported CO_2 waveguide laser specific power performance, for a sealed-off device, is 0.83 W/cm, due to He and Hall [6] in 1983 and since equalled by workers at the United Technologies Research Centre [54]. These results represent the highest and near (predicted) optimum output power per unit length achieved with a sealed-off (static gas) waveguide laser. Hence, a significant increase in the output powers of these sealed-off devices can only be provided by longer gain lengths. The extended gain length could be achieved with a longer excited waveguide segment, or alternatively, and especially if there are restrictions on the device size and shape (as is often the case), by folded waveguide paths. With the latter option, the increase in gain length per unit device volume is, not surprisingly, afforded at the cost of a power reduction through the inevitable introduction of an additional intracavity loss by the folding mirrors and mode coupling losses, and hence the near optimum output power per unit length is not maintained.

The equations and scaling laws relating the output power to the parameters of a homogeneously broadened cw laser will be examined in detail in Chapter 3. As an example, consider the linear (as opposed to folded) gain length extension of the laser in [6] above, responsible for the best reported

specific power performance. If the active lenth of this 30 W device was increased from 37 cm to 58 cm, the estimated output power (all other things being equal) would increase to 50 W. In practice, additional intracavity losses would be incurred, namely waveguide mode propagation losses (which are a small, yet significant fraction of the available gain per unit length), and approximately 6 cm additional length would be required for every 1% increase in the total resonator round-trip loss. There are problems with the fabrication of long waveguides with bores of typically 0.5 - 2.5 mm dimensions in machined ceramic [55]. The need to achieve low loss waveguiding imposes stringent requirements on bore finish and straightness. Consequently, the present limitations of ultra-sonic drilling, glass-glaze bonding, thermo-diffusion bonding and slab polishing techniques generally precludes the construction of waveguides longer than 50 cm. One way round this problem is to use shunt coupling between multiple waveguide segments [47]. The problems of pre-alignment and alignment drift, however, make this option unattractive.

The alternative solution is the folding waveguide laser, consisting of two or more coupled parallel or near-parallel waveguide channels. The two basic types of folding geometries are the 'u'-fold and the 'v'-fold, shown schematically in Figure 2.1. Both geometries form a two-dimensional or planar waveguide folding system. The pair of 'u'-folding mirrors can be placed at an arbitrary distance

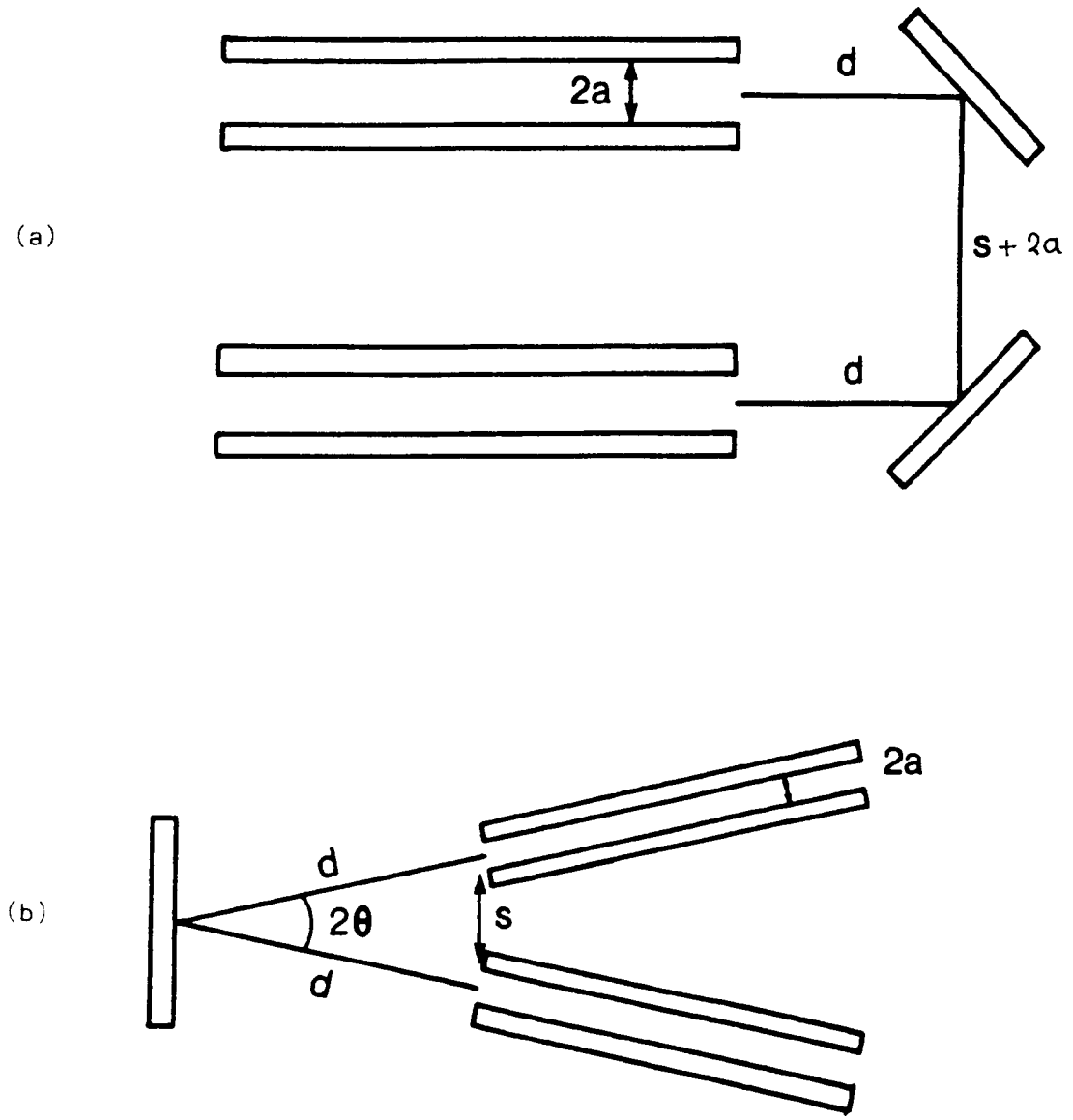

Figure 2.1. The waveguide 'u'-fold (a) and the 'v'-fold (b).

near to the ends of the waveguides. The 'u'-fold can also be used to couple between planar systems in the third dimension to produce layers of waveguide paths. The 'v'-fold requires only one reflecting surface, most sensibly placed at the intercept of the waveguide axes with its normal lying on their bisector. When repeated and/or combined these folding geometries can be used to concatenate several metres of active length into a compact structure to form, for example, a 'z'-fold or 'x'-fold (ring) waveguide laser resonator. The waveguide bores (or channels) can be milled into the same ceramic slab, possibly between common electrodes, forming a rigid alignment bed.

Although the use of folded gain sections has the obvious benefits of large overall gain length in a compact resonator, there are a number of important problems to be solved if the full benefits of multiple gain lengths are to be realised. Firstly, there are waveguide mode coupling losses and mirror losses (on reflection) at each fold. The evaluation of the mode coupling losses for a variety of folding geometries is the main topic of this chapter. These losses are in addition to the waveguide propagation losses (guiding losses) and contribute to the resonator round trip loss, giving an effective distributed loss (or negative gain). Evidently, there must be a trade-off between the device length and the number of folds (width) to meet the desired laser performance. Secondly, and on a more practical note, the tolerances for pre-alignment and the consequences of mis-alignment of the folding mirrors is of great concern.

Alignment techniques are discussed in Chapter 4, and an experimental determination of the effects of mirror mis-alignment on output power and beam quality is presented in Chapter 5. Obviously, the priorities attached to the consequences of mis-alignment depend very much on the intended application of the laser.

A major concern in the work described here is to evaluate the waveguide mode coupling losses at the bend in a folded waveguide and to understand how such losses vary with the selectable parameters, namely, the bore dimensions, the free-space propagation distances, the fold angle ('v'-fold), and the reflector curvature. Clearly, such a calculation requires a basic understanding of waveguide modes and their propagation, coupling into free-space modes, and recoupling into waveguide modes.

2.2 Hollow Dielectric Waveguide Theory

For a comprehensive discussion on hollow dielectric waveguide theory the reader is referred to several excellent review articles on waveguide gas lasers that were published in the last decade, by Degnan [21], Abrams [22], Smith et al. [23] and Hall and Hill [56].

In this thesis the theoretical treatments are restricted to rectangular waveguides, while the experimental investigations are concerned only with square waveguides. These restrictions arise from practical considerations; rectangular waveguides can easily be fabricated from four polished slabs of dielectric fitted together to form hollow

structures that lend themselves to transversely excited discharges. A general rectangular hollow dielectric waveguide is shown schematically in Figure 2.2. This waveguide consists of an infinitely long bore of rectangular cross-section 2a x 2b (free-space dielectric constant) which is embedded in another medium with a complex dielectric constant. The magnetic permeability is assumed to be that of free-space for both media.

An exact analytical solution of the field configurations and propagation constants of the waveguide modes is not possible because of the difficulty in matching boundary conditions. The modes of hollow square and rectangular dielectric waveguides have been studied by Krammer [19] and Laakmann and Steier [18], and of composite metal and dielectric waveguides by Adam and Kneubuhl [17]. Krammer [19] found an approximate solution by using a perturbation technique to solve separate boundary conditions in x and y. It should be noted that this solution corresponds to an approximate analytical solution of Maxwell's equations, obtained under the assumptions that the mode propagation losses are small and the waveguide dimensions are large compared with the free-space wavelength λ. The relevant equations and nomenclature adopted throughout this thesis are given in Table 2.1.

Waveguide modes are leaky modes, that is, some power can always leak to the high dielectric region and thus be lost by the guided modes. Rectangular waveguides only support the

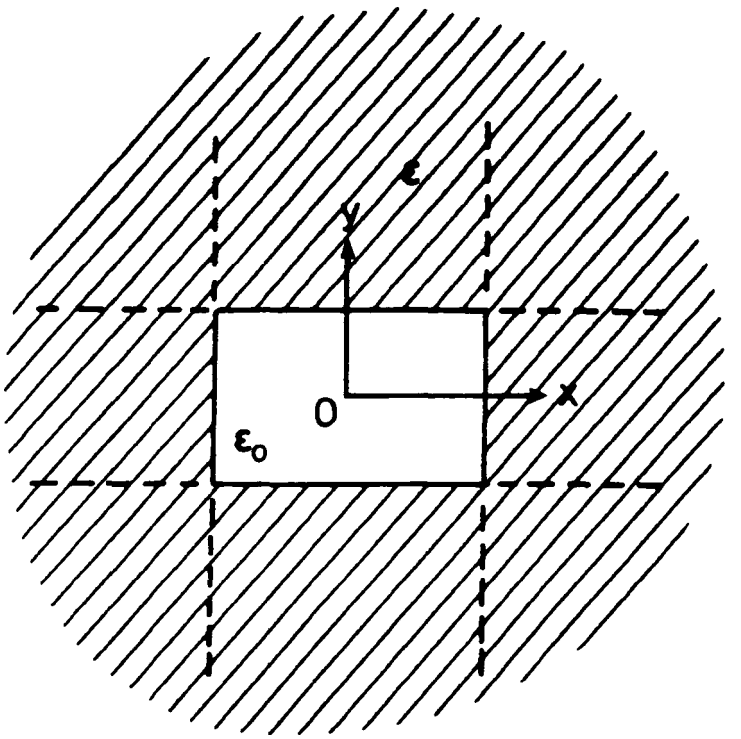

Figure 2.2. A hollow rectangular waveguide is embedded in a medium with the complex dielectric constant ε

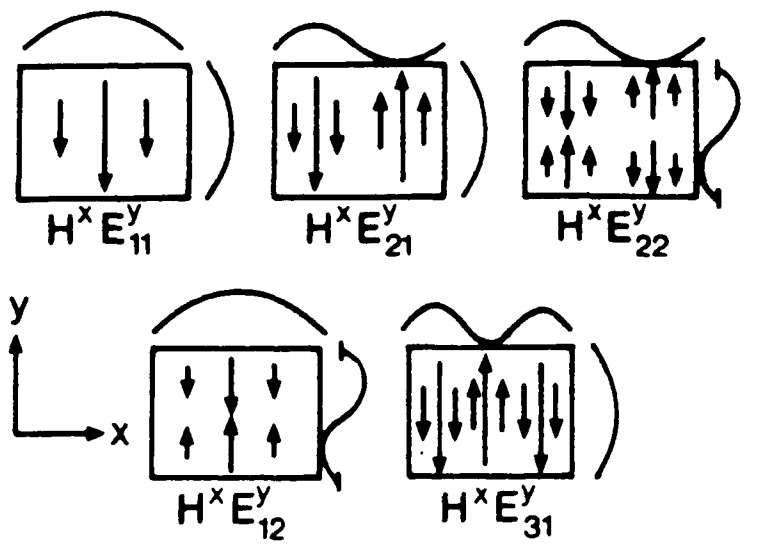

Figure. 2.3(a). Electric field lines of modes $H^x E^y_{pq}$. The amplitude of H_x or E_y is shown as it depends on x and y (after Krammer [19]).

$E^yH^x_{pq}$ modes

$$H_x = -E_y/Z = M\begin{Bmatrix}\cos(p_1\pi x/2a)\\ \sin(p_2\pi x/2a)\end{Bmatrix}\begin{Bmatrix}\cos(q_1\pi y/2b)\\ \sin(q_2\pi y/2b)\end{Bmatrix}$$

$$H_z = -\pi M/2jka\begin{Bmatrix}-p_1\sin(p_1\pi x/2a)\\ p_2\cos(p_2\pi x/2a)\end{Bmatrix}\begin{Bmatrix}\cos(q_1\pi y/2b)\\ \sin(q_2\pi y/2b)\end{Bmatrix}$$

$$E_z = -j\pi MZ/2kb\begin{Bmatrix}\cos(p_1\pi x/2a)\\ \sin(p_2\pi x/2a)\end{Bmatrix}\begin{Bmatrix}-q_1\sin(q_1\pi y/2b)\\ q_2\cos(q_2\pi y/2b)\end{Bmatrix}$$

$$\alpha = \frac{(p\pi)^2}{4k^2a^3}\,\mathrm{Re}(N_1) + \frac{(q\pi)^2}{4k^2b^3}\,\mathrm{Re}(N_2)$$

$$\beta = k\left\{1 - \frac{1}{2}\left[\left[\frac{p\pi}{2ka}\right]^2 \cdot \left[1 - \frac{2}{ka}\,\mathrm{Im}(N_1)\right] + \left[\frac{q\pi}{2kb}\right]^2 \cdot \left[1 - \frac{2}{kb}\,\mathrm{Im}(N^2)\right]\right]\right\}$$

$E^xH^y_{pq}$ modes

$$H_y = -E_x/Z = M\begin{Bmatrix}\cos(p_1\pi x/2a)\\ \sin(p_2\pi x/2a)\end{Bmatrix}\begin{Bmatrix}\cos(q_1\pi y/2b)\\ \sin(q_2\pi y/2b)\end{Bmatrix}$$

$$H_z = -\pi M/2jkb\begin{Bmatrix}\cos(p_1\pi x/2a)\\ \sin(p_2\pi x/2a)\end{Bmatrix}\begin{Bmatrix}-q_1\sin(q_1\pi y/2b)\\ q_2\cos(q_2\pi y/2b)\end{Bmatrix}$$

$$E_z = -\pi MZ/2jka\begin{Bmatrix}-p_1\sin(p_1\pi x/2a)\\ p_2\cos(p_2\pi x/2a)\end{Bmatrix}\begin{Bmatrix}\cos(q_1\pi y/2b)\\ \sin(q_2\pi y/2b)\end{Bmatrix}$$

$$\alpha = \frac{(p\pi)^2}{4k^2a^3}\,\mathrm{Re}(N_2) + \frac{(q\pi)^2}{4k^2b^3}\,\mathrm{Re}(N_1)$$

$$\beta = k\left\{1 - \frac{1}{2}\left[\left[\frac{p\pi}{2ka}\right]^2 \cdot \left[1 - \frac{2}{ka}\,\mathrm{Im}(N_2)\right] + \left[\frac{q\pi}{2kb}\right]^2 \cdot \left[1 - \frac{2}{kb}\,\mathrm{Im}(N^1)\right]\right]\right\}$$

$$Z = \sqrt{\frac{\mu_0}{\epsilon_0}} \qquad N_1 = \frac{1}{\sqrt{(n^2 - 1)}} \qquad N_2 = \frac{n^2}{\sqrt{(n^2 - 1)}}$$

Note: M, arbitrary amplitude factor.

Nomenclature:

a,b	-	waveguide dimensions (2a x 2b)
ϵ_0	-	free space dielectric constant
ϵ	-	complex dielectric constant
n	-	complex refractive index
μ_0	-	free space magnetic permeability
k	-	free space phase constant
α	-	modal attenuation constant
β	-	modal phase constant
M	-	arbitrary amplitude factor (normalised when $M = 1/(ab)^{1/2}$)
p_1, q_1	-	symmetric mode indices (odd)
p_2, q_2	-	antisymmetric mode indices (even)
p,q	-	transverse field component indices
x,y,z	-	Cartesian coordinates (mode propagation in z direction)

Table 2.1. Fields and propagation constants of modes of the hollow rectangular waveguide (after Krammer [19]).

hybrid EH_{pq} modes that are similar to the Hermite-Gaussian modes of conventional resonator theory and denoted by $E^{x}H^{y}{}_{pq}$ and $E^{y}H^{x}{}_{pq}$, where the superscripts indicate the major polarisation of the transverse component of the electric and magnetic fields. The field distributions and intensity profiles for the lowest order modes are shown schematically in Figure 2.3. The lowest order hybrid mode, EH_{11}, is linearly polarised and closely resembles a TEM_{00} free-space Gaussian mode. For square guides, symmetry requires that the modes be degenerate, and therefore different linear combinations of the two modes simply give different polarisation states.

The $E^{x}H^{y}{}_{pq}$ modes suffers the least attenuation if $a > b$, whereas the orthogonally polarised $E^{y}H^{x}{}_{pq}$ modes are the lowest loss modes if $a < b$. The propagation losses of these waveguide modes can be calculated from the equations in Table 2.1 provided a suitable value for the dielectric refractive index at the free-space wavelength can be found. In practice these values are not easily determined, but measurements of the guiding losses of the fundamental modes at 10.6 μm in pyrex, alumina (Al_2O_3) and beryllia (BeO) gave attenuation constants of between 0.01 and 1%/cm for 0.5 - 2.5 mm bores [26]. In general, the modal guiding losses scale with the inverse cube of the bore half-width and the square of the mode indices, and are greatly increased for even small bore curvatures and surface roughness. For these reasons hollow dielectric waveguides are impracticable for

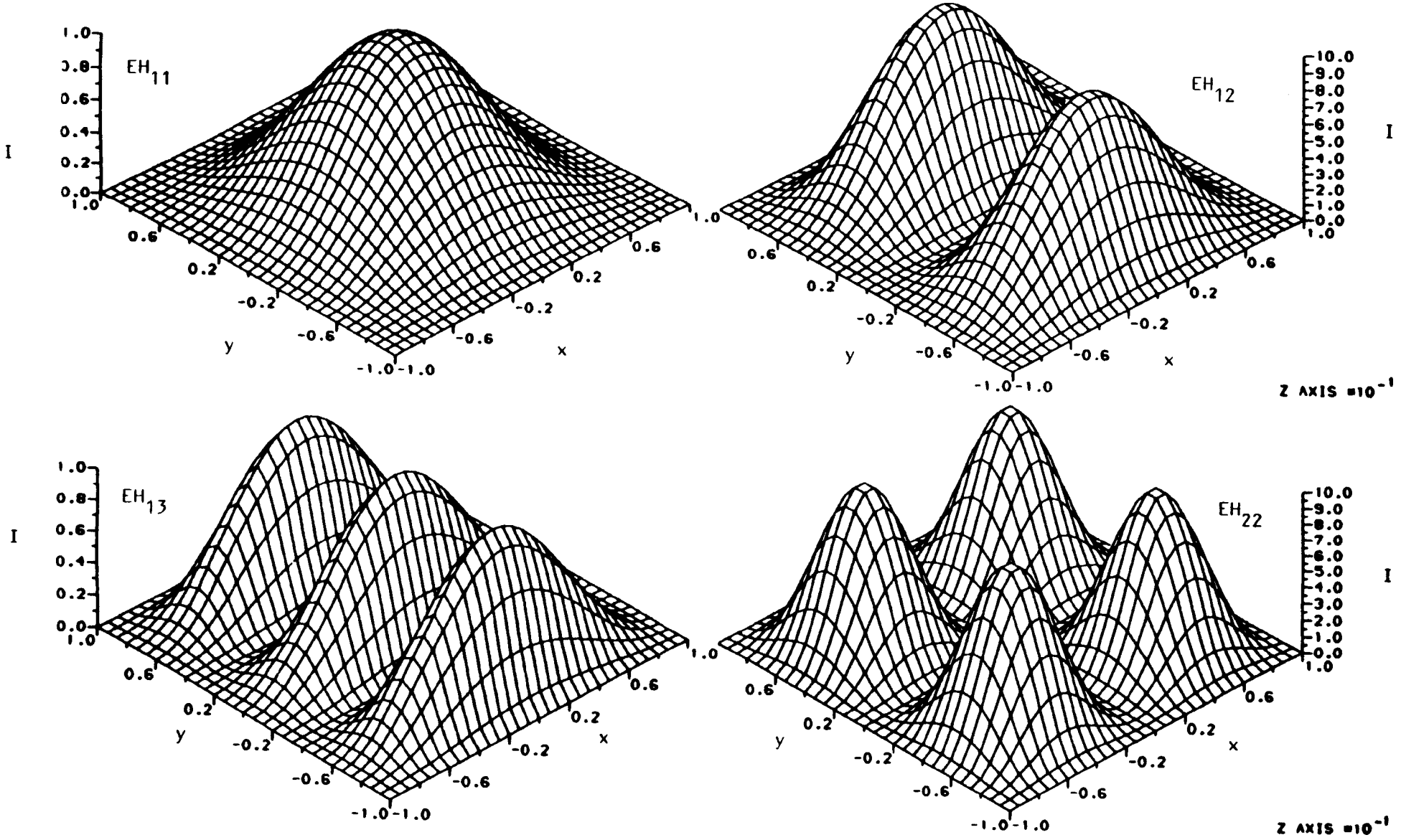

Figure 2.3(b). Normalised intensity profiles of the lowest order waveguide modes.

long distance transmission, they are, however, well suited for the confinement of laser radiation over distances of the order of tens of centimetres.

A waveguide laser can be distinguished from a conventional laser by the characteristic that, over some portion of its propagation path, the circulating radiation is guided and does not obey the laws of free-space propagation. The modes of waveguide resonators are certain field distributions that repeat themselves after one round trip to within an arbitrary multiple of 2π in phase and an arbitrary loss factor in amplitude. Formally, any field can be expressed as a combination of the basic Gaussian modes (in free-space) or the waveguide modes (within the guide).

A subset of waveguide theory termed "coupling loss theory" has evolved to further the understanding of how radiation behaves as it is launched from one end of a guide and recoupled by a laser reflector. The following sections briefly review the published coupling loss treatments of single mode waveguide resonators and their application to folded waveguide laser design. The literature, although extensive, does not describe the mode coupling losses at a waveguide v-fold with a curved reflector, or one with a partial waveguide to a plane reflector; these are folding geometries apparently hitherto unconsidered, and ones that (intuitively) might provide low-loss folding. Consequently, new applications of the existing theory are developed.

2.3 Plane Mirror Coupling Coefficients

There is much published work that describes the mode coupling behaviour for a variety of waveguide reflectors (for a critical review on the subject see for example Hill and Hall [46]). Coupling loss treatments generally fall into two categories; the mode-expansion method and the diffraction integral method. The first approach is to express the field in the output plane of the waveguide as a linear combination of free-space modes, which are then propagated to and from the mirror according to the familiar Gaussian beam equations of Kogelnik and Li [45]. Their recombination gives the field distribution in the input plane of the waveguide. The second approach is to calculate the field at each point on the mirror surface by applying a scalar diffraction calculation using the Huyghens-Fresnel principle. The field distribution returned to the input aperture is determined by considering each point on the mirror surface as a source and re-applying the same calculation. In both cases an amplitude overlap integral of the initial and returned field distributions across the aperture, is performed to determine the mode coupling coefficient matrix.

The mode coupling coefficient matrix is a rectangular array. A general element in the matrix is denoted by $C_{pq,p'q'}$ (or $C^{p'q'}{}_{pq}$), where p and q, p' and q' are the transverse field component indices of the EH_{pq} and $EH_{p'q'}$ waveguide modes respectively. The

individual quantities $C^{p'q'}_{pq}$ are called the modal cross-coupling coefficients unless p = p' and q = q' (the diagonal matrix elements, which are often abbreviated to C_{pq}); in which case they are referred to as the modal self-coupling coefficients.

The general coupling coefficient is defined by $C^{p'q'}_{pq} = |\chi^{p'q'}_{pq}|^2$, where $\chi^{p'q'}_{pq}$ is given by an amplitude overlap integral of the 'launched' and re-entrant field components across the waveguide aperture. Hence $C^{p'q'}_{pq}$ is defined as the fraction of the energy carried by the EH_{pq} mode emerging from the guide which is coupled into the $EH_{p'q'}$ mode of the guide after reflection.

For a square guide and well-aligned reflector, symmetry considerations reveal that

$$C^{p'q'}_{pq} = 0 \text{ if } p + p' \text{ or } q + q' \text{ are odd} \qquad (2.1)$$

$$C^{p'q'}_{pq} = C^{p'q}_{pq'} \qquad (2.2)$$

$$C^{p'q'}_{pq} = C^{pq'}_{p'q} \qquad (2.3)$$

$$C^{p'q'}_{pq} = C^{pq}_{p'q'} \qquad (2.4)$$

$$C_{pq} = (C_{pp}.C_{qq})^{\frac{1}{2}} \qquad (2.5)$$

Evaluation of the mode coupling coefficients generally involves numerical integration, although there are a few

special cases where approximations can be justified to give closed form solutions. The modal composition of the waveguide field excited by the re-entrant field is determined by summing the coupling coefficient matrix row elements for each mode (column element designator). In some applications a 3 x 3 matrix (i.e. one including all mode indices up to $EH_{3,3}$) is quite adequate. For low order modes (say, up to $EH_{3,3}$) the modal composition is often approximately given by the self-coupling coefficients alone.

A general waveguide reflector, that is, a spherical mirror (with radius c) placed at an arbitrary distance (d) from the end of a waveguide with its centre of curvature lying on the optic axis, is shown schematically in Figure 2.4. The coupling behaviour of the 'u'-fold and 'v'-fold waveguide reflectors shown in Figure 2.1, are equivalent to that of the general reflector for the special case when the mirrors are plane and their free-space propagation distances are equal. The latter condition is satisfied when the 'u'-fold and 'v'-fold waveguide to mirror spacings, d_u and d_v, respectively, are given by

$$d_u = \tfrac{1}{2} (2d + S + 2a) \qquad (2.6)$$

$$d_v = \tfrac{1}{2} (2a \cot\theta + S\csc\theta) \qquad (2.7)$$

Boulnois and Agrawal [40] have derived expressions for the mode coupling coefficients for rectangular waveguides (with

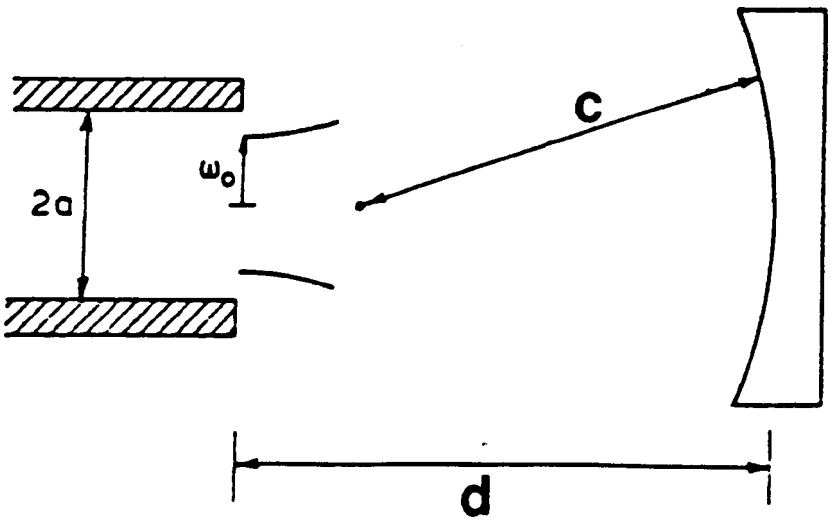

Figure 2.4. General waveguide reflector.

dimensions 2a x 2b). For the limiting case of a well-aligned plane-parallel mirror placed near the waveguide end, they obtained a closed form solution for the self-coupling coefficients given by

$$C_{pp} = \left[1 - \frac{p^2}{6N^{3/2}} - \frac{\pi}{240N^{5/2}} + \frac{p^4}{72N^3} + \ldots.\right]^2 \quad N \gg 1 \qquad (2.8)$$

and

$$C_{pq} = \frac{(p^2 + q^2)}{6N^{3/2}} \quad N > P \qquad (2.9)$$

where N is the Fresnel number, a dimensionless product given by

$$N = \frac{(\alpha\delta)^{1/2}}{2\pi\beta} \qquad (2.10)$$

and α, β and δ are the useful dimensionless products defined by Degnan and Hall [43] given by

$$\alpha = ka^2/c \qquad (2.11)$$

$$\beta = d/c \qquad (2.12)$$

$$\delta = kb^2/c \qquad (2.13)$$

where k is the wave number ($2\pi/\lambda$). For a square bore and plane reflector, N reduces to

$$N = \frac{a^2}{\lambda d} \qquad (2.14)$$

Equations (2.8) to (2.14) allow the evaluation of the self-coupling coefficients for any well-aligned plane-parallel mirror waveguide reflector, or its equivalent, provided that the mirror is placed near the waveguide end (or more formally provided N >> 1). In the derivation of these equations Boulnois and Agrawal assumed a mirror of unit reflectivity and infinite aperture. These conditions are generally adequately satisfied by waveguide resonators, where mirror dimensions of 5 - 10 times the guide dimensions are typical, and mirror reflectivities of > 99.6% are possible with high reflectivity dielectic coatings on, for example, silicon or germanium substrates. Mirror reflectivities other than unity can, of course, be allowed for in resonator mode round-trip loss evaluations, etc.

General three-dimensional plots showing the fundamental self-coupling coefficient, C_{11}, evaluated using equation (2.8), over a wide range of parameters values for both 'u'-and 'v'-fold geometries are presented in Figures 2.5(a and b) respectively. Evidently, small bore waveguides with small fold-angles ('v') or generously spaced corner mirrors ('u'), present large folding losses.

Curves showing the relationships between the 'u'- and 'v'-fold free-space propagation distances and the Fresnel numbers, for several square-bore waveguide sizes are presented in Figure 2.5(c). The corresponding values of C_{11} are shown in Figure 2.5(d). Indicated on these graphs are the 'v'-fold design parameters chosen for the 'z'-fold laser

(a)

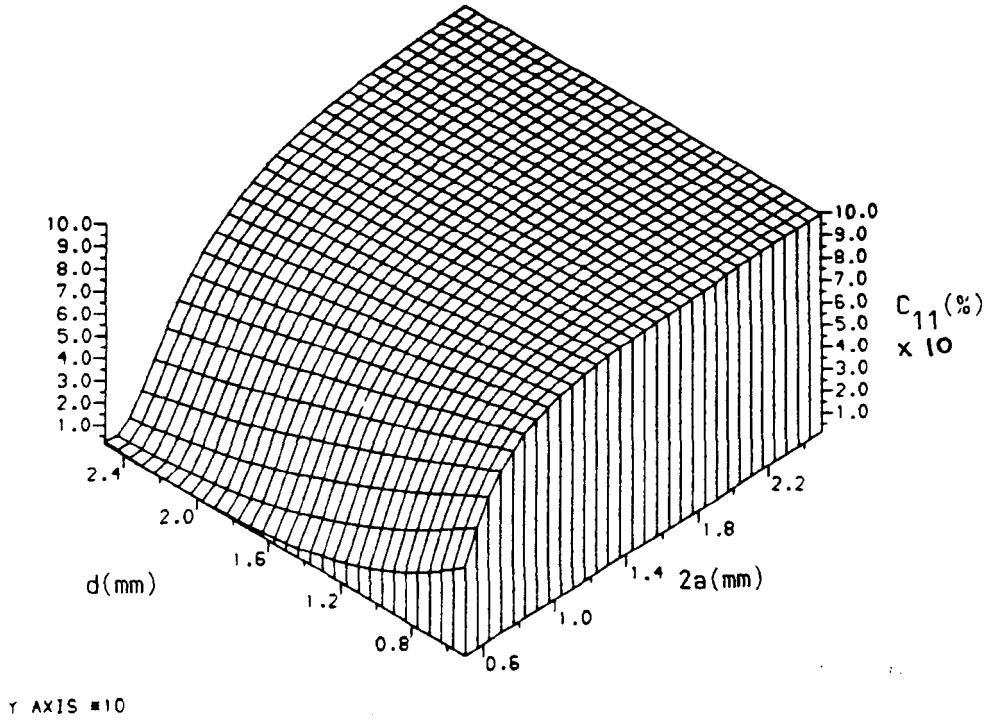

Y AXIS =10

(b)

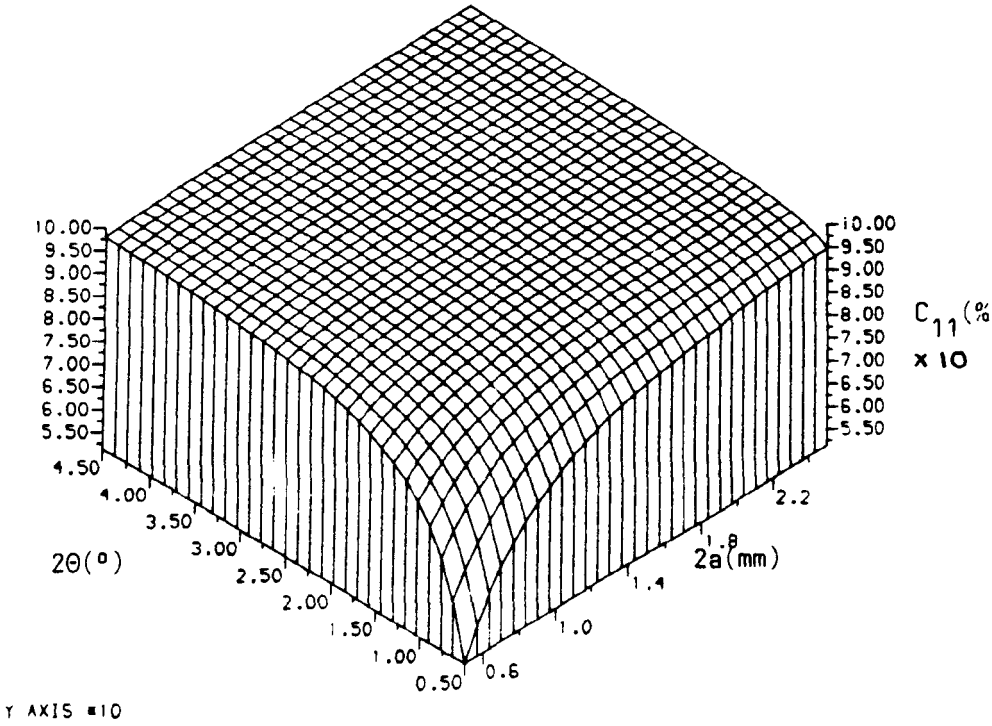

Y AXIS =10

Figure 2.5. The fundamental waveguide mode self-coupling coefficient as functions of the selectable parameters for the plane mirror 'u'-fold (a) and 'v'-fold (b).

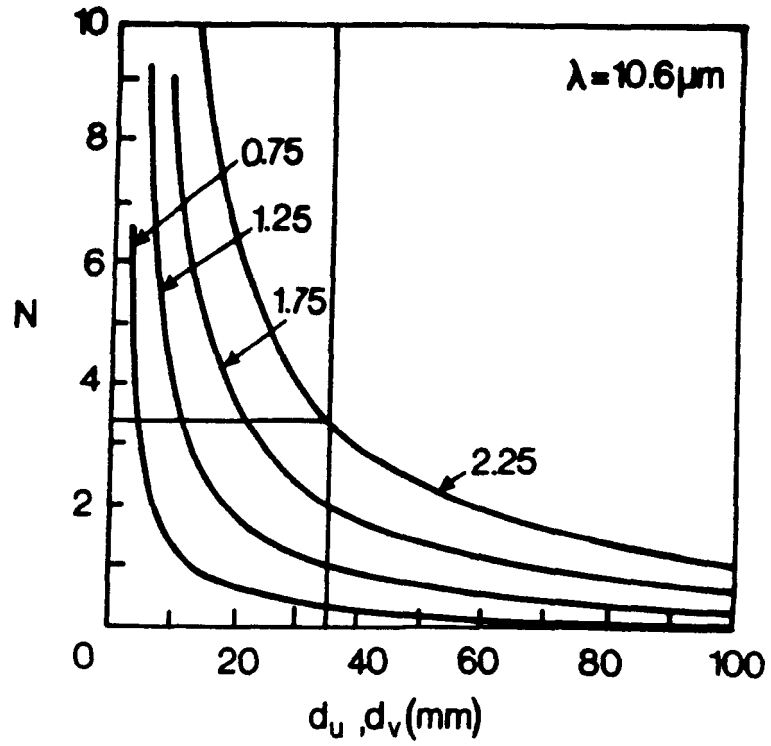

(c)

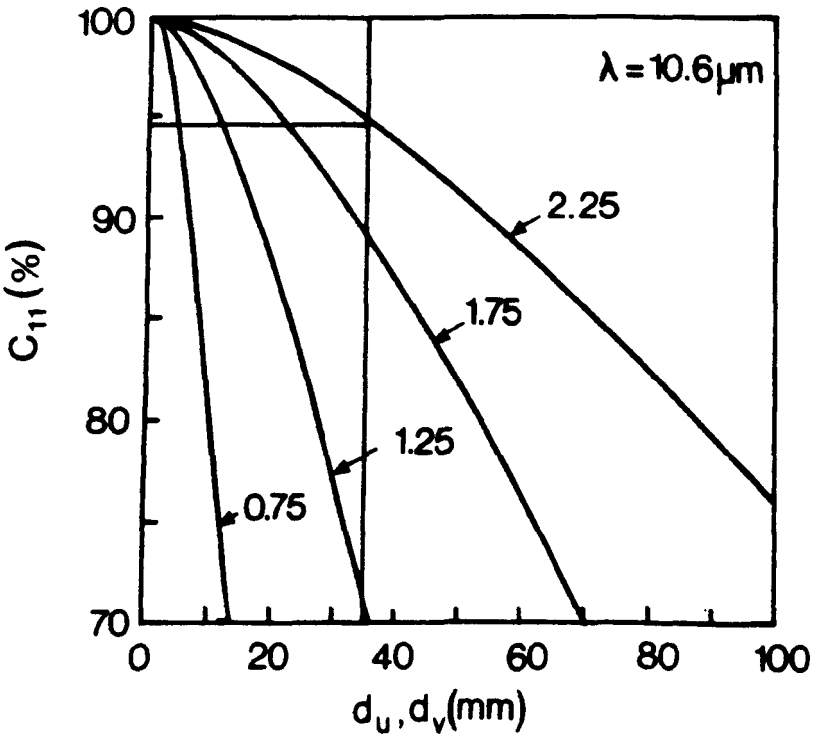

(d)

Figure 2.5. c) The Fresnel number (N) as a function of the 'u'- or 'v'-fold free-space propagation distances for various waveguide square bore dimensions (2a).

d) The EH_{11} mode self-coupling efficiency (C_{11}) corresponding to the curves in Figure 2.5c.

construction, namely 2a = 2.25 mm and d_v = 35.3 mm. The choice of d_v was not arbitrary but governed by the choice of fold-angle (through equation (2.7)), which in turn was influenced by size restrictions on the width of the composite z-fold waveguide. These practical restrictions are discussed in detail in Chapter 4; suffice it to say, that they arose through other considerations, such as the dimensions of the RF electrodes, their mutual capacitance and thermal capacity, etc.

The minimum common electrode areas, A_u and A_v, required for multiple (n) 'u'- and 'v'-fold waveguide excitation, respectively, are given by

$$A_u = L[(n-1)s + 2na] \tag{2.15}$$

$$A_v(n \text{ odd}) = L[(\tan 2\theta)(L+2d_v)(n/2-1/2) + 2a] \tag{2.16}$$

$$A_v(n \text{ even}) = L[(\tan 2\theta)(L+2d_v)(n/2) + a(1+\cos 2\theta)] \tag{2.17}$$

where L is the length of the longest (except for the 'v'-fold where it is the shortest) waveguide segment. Figure 2.6(a) shows the minimum electrode widths, calculated using equation (2.16), needed to cover a 386 mm long 'z'-fold waveguide laser, for a range of fold-angles. The corresponding low-loss mode self-coupling coefficients are presented in Figure 2.6(b), showing the degree of mode discrimination. From these curves and bearing in mind the practical

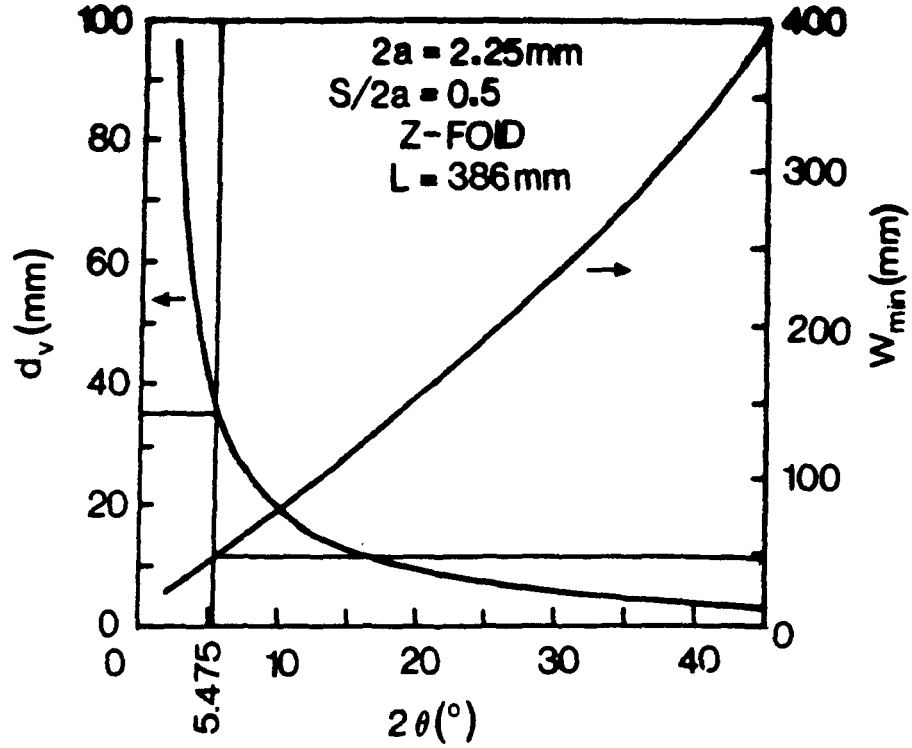

(a)

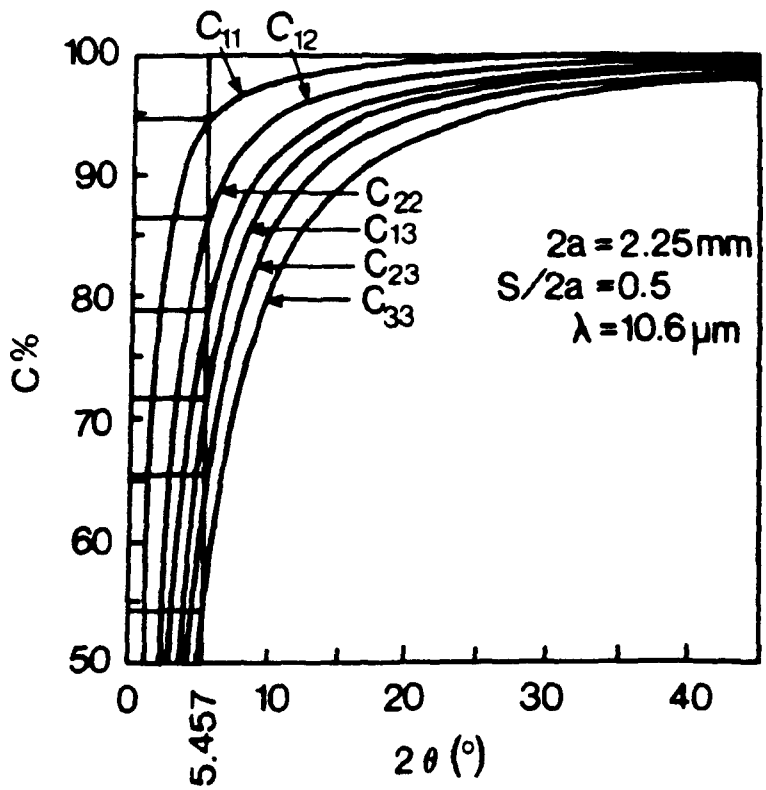

(b)

Figure 2.6. a) Minimum electrode width needed to cover the 'z'-fold waveguide as a function of the 'v' fold angle.

b) The mode self-coupling coefficients for the lowest-order modes corresponding to the 'v'-fold dimension in Figure 2.6a.

restrictions mentioned above, a fold-angle of 5.475° was chosen.

Although the waveguide mode self-coupling coefficients are readily given by the closed-form equations above, the cross-coupling coefficients are less readily evaluated, often requiring numerical integration. One method [38,39] involves the amplitude overlap coupling between the waveguide modes EH_{pq} and the Hermite-Gaussian free-space modes ψ_{mn}. The EH_{pq} fields and their propagation constants $k_{pq} = \alpha_{pq} + j\beta_{pq}$ are given in [19] and Table 2.1. The amplitude coupling, A^{pq}_{mn} at a distance z from the end of the guide, between EH_{pq} and ψ_{mn} for a square bore waveguide is given by

$$A^{pq}_{mn}(z) = (2/\pi)^{1/2} (2m_{m!}2n_{n!})^{-1/2} \alpha r \exp(j\phi_{mn}) I_{mp} I_{nq} \qquad (2.18)$$

where

$$\alpha = [1 + (2z/b_0)]^{-1/2} \qquad (2.19)$$

$$r = a/\omega_0 \qquad (2.20)$$

$$\phi_{mn} = (m+n+1)\tan^{-1}(2z/b_0) \qquad (2.21)$$

$$b_0 = \pi\omega_0^2/\lambda \qquad (2.22)$$

and

$$I_{mp} = \int_{-1}^{1} H_m[\sqrt{2}\alpha ru] \exp[-(\alpha ru)^2(1+j2z/b_0)] \begin{Bmatrix}\cos\\ \sin\end{Bmatrix}\left[\frac{m\pi u}{2}\right] d_u;\ m = \begin{Bmatrix}\text{odd}\\ \text{even}\end{Bmatrix} \qquad (2.23)$$

where $H_m(x)$ is the mth Hermite polynomial. The waist parameter, r, is often chosen to maximise $A^{pq}_{mn}(0)$ (for example r = 1.422 [51] gives $A^{11}_{00} = 0.99$). Note that if z = 0 (coupling to I_{pq} at the guide exit) then $\alpha = 1$ and $\phi_{pq} = 0$ and A^{pq}_{mn} are purely real.

The amplitude coupling for EH_{pq} at the exit of the guide, through free-space (summed over all the I_{mn}), to $EH_{p'q'}$ back at the entrance of the guide, is given by

$$C^{p'q'}_{pq} = \sum_{m,n} A^{pq}_{m'n'}(z)\ A^{pq}_{mn}(0) \qquad (2.24)$$

A BASIC program written by Hill [58] has been used to evaluate equation (2.24) to determine the coupling matrix elements up to $C_{3,3}$ for $z = d_v = 35.3$ mm (the chosen 'v'-fold guide-to-mirror spacing): the results are presented in Table 2.2.

The 'z'-fold resonator end mirrors are the back mirror (total reflector) and the output coupler (partial reflector), placed at the 'loose' ends of the 'z'. The mode coupling in both cases is conveniently provided by a 'simple' Case I reflector [43]. A Case I reflector is a large radius of curvature (or plane) mirror placed very close (typically a few millimetres) to the end of the waveguide, which re-couples the outgoing radiation with negligible diffraction losses. This rather loose definition has been quantified by Hill [59] with the additional criterion that, where Case I reflectors are involved the EH_{pq} self-coupling loss,

		p'q'									
		11	12	13	21	22	23	31	32	33	
	11	0.8631 0.4430 0.9412		8.68×10^{-2} -7.097×10^{-2} 1.2557×10^{-2}				8.68×10^{-2} -7.097×10^{-2} 1.257×10^{-2}		-3.508×10^{-2} -1.247×10^{-2} 1.678×10^{-4}	Re(χ) Im(χ) |χ|²
	12		0.5604 0.7623 0.8951						0.1066 -2.415×10^{-2} 1.195×10^{-2}		
	13	0.1223 -1.237×10^{-2} 1.512×10^{-2}		9.058×10^{-2} 0.8894 0.7992				4.34×10^{-3} -1.353×10^{-2} 2.019×10^{-4}		9.84×10^{-2} 3.148×10^{-2} 1.067×10^{-2}	
	21				0.5604 0.7623 0.8951		0.1066 -2.415×10^{-2} 1.195×10^{-2}				
pq	22					0.1572 0.9091 0.8512					
	23				0.1121 4.245×10^{-2} 1.438×10^{-2}		-0.3080 0.8155 0.7600				
	31	0.1223 -1.237×10^{-2} 1.512×10^{-2}		4.34×10^{-3} -1.353×10^{-2} 2.019×10^{-4}				9.058×10^{-2} 0.8893 0.7992		9.84×10^{-2} 3.148×10^{-2} 1.067×10^{-2}	
	32		0.1121 4.245×10^{-2} 1.438×10^{-2}						-0.3081 0.8155 0.7600		
	33	1.216×10^{-2} -9.748×10^{-1} 2.428×10^{-4}		7.093×10^{-2} 8.835×10^{-2} $1.284\times1-^{2}$				7.093×10^{-2} 8.835×10^{-2} 1.284×10^{-2}		-0.6420 0.5161 0.6786	

Table 2.2. The plane mirror 'v'-fold coupling coefficient matrix (only the non-zero matrix elements up to and including C_{33}^{33} are shown).

c_{pq} should be much less than the waveguiding loss α_{pq}. The Case I self- and cross-coupling coefficients can also be evaluated using the equations (2.8) and (2.24) above. In Chapter 3, the Case I coupling coefficient matrices for the end reflectors are used together with those for the 'v'-fold reflectors (Table 2.2), to estimate the 'z'-fold resonator mode round-trip loss.

When, instead of a plane mirror, a curved mirror is used at a 'v'-fold (to hopefully reduce the coupling losses there), a special mode coupling treatment is necessary to include the effects of astigmatism. This is the topic addressed in the next section.

2.4 Curved Mirror Coupling Coefficients

In this section the investigation of the mode coupling behaviour of a 'v'-fold in a waveguide is continued. In the previous section it was evident that for plane mirror folding the mode coupling (diffraction) losses can be considerable, especially for devices with small fold-angles, which undermines the advantages of creating a fold in this manner. In the following, a 'v'-fold with a spherical reflector is considered.

Previous spherical mirror coupling loss treatments for hollow dielectric waveguide reflectors can not be applied directly to a fold geometry. In general, a curved fold mirror produces an asymmetric phase front upon reflection and a more complex theory is necessary in order to explore its coupling behaviour.

The coordinate system and the waveguide and mirror geometry used for calculation of the coupling efficiency are shown in Figure 2.7. A spherical mirror with a radius of curvature c centred on the z-axis is positioned with its pole at the origin which coincides with the intercepts of the waveguide axes. The unguided radiation is folded through an angle 2θ with an on-axis path length 2d. The waveguide consists of hollow tubes of rectangular cross-section 2a x 2b embedded in a dielectric medium with a complex dielectric constant ϵ. The whole structure is symmetrical about the z-axis.

The considerations in this treatment are restricted to linearly polarised modes and neglect the effects of finite mirror aperture, of mirror mis-alignment, and of the active gain medium within the waveguide.

The field distribution $E_{pq}(x_0,y_0,z_0)$, in the plane of the aperture at the end of the waveguide, is assumed to be the same as for an infinite length waveguide,. In this way, the field component at a point $M_0(x_0,y_0,z_0)$ of the aperture is given by Krammer ([19] and Table 2.1) with a suitable coordinate transformation, viz,

$$E_{pq}(x_0,y_0,z_0) = \frac{1}{(ab)^{1/2}} \begin{Bmatrix} \cos(px_0'\pi/2a) \\ \sin(px_0'\pi/2a) \end{Bmatrix} \begin{Bmatrix} \cos(qy_0\pi/2b) \\ \sin(qy_0\pi/2b) \end{Bmatrix} \tag{2.25}$$

where $x_0' = x_0\sec\theta - d\tan\theta$, and the upper and lower terms are used with odd and even values of the integers p and q respectively.

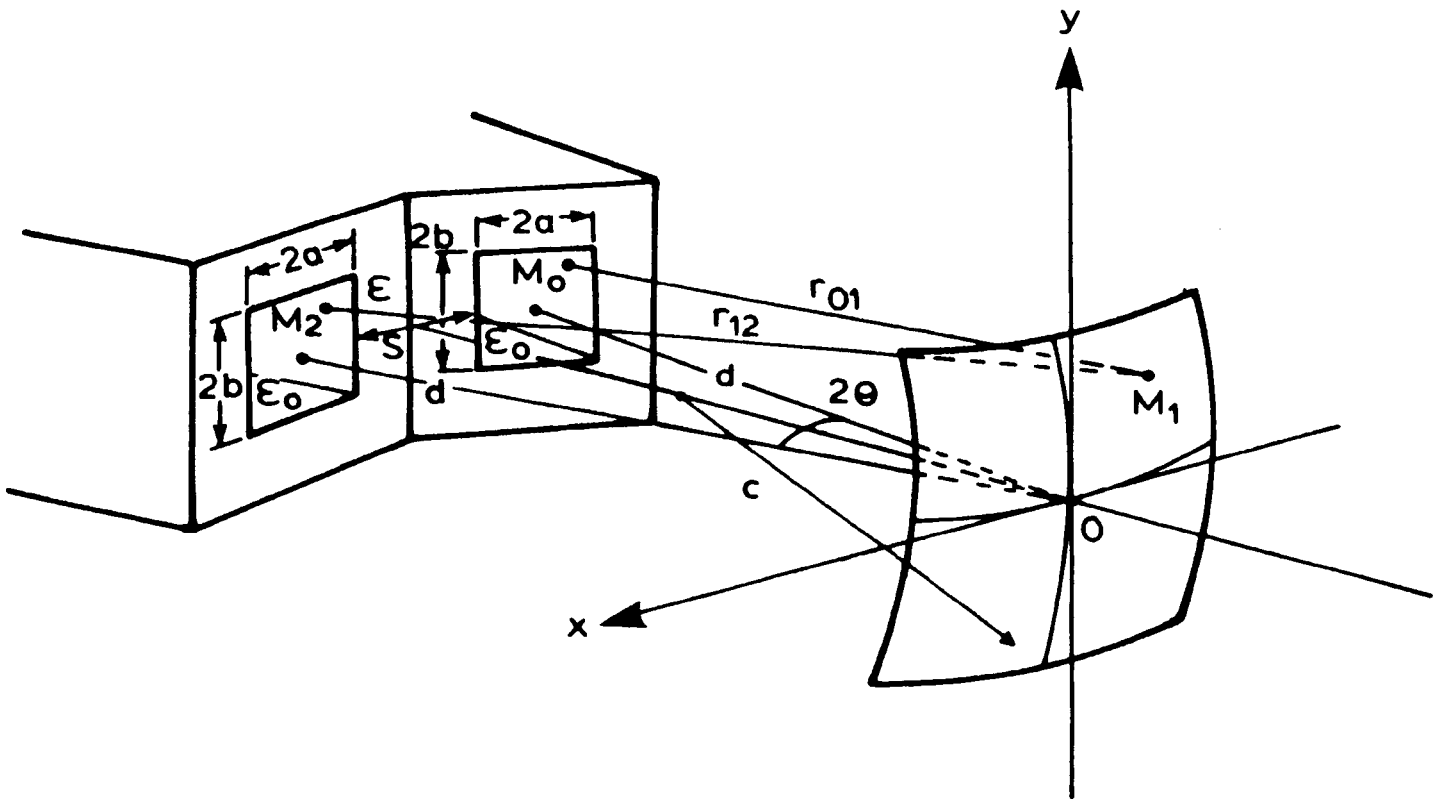

Figure 2.7(a). Schematic of the waveguide and mirror configuration and the coordinate system used for calculation of the curved mirror 'v'-fold coupling efficiency.

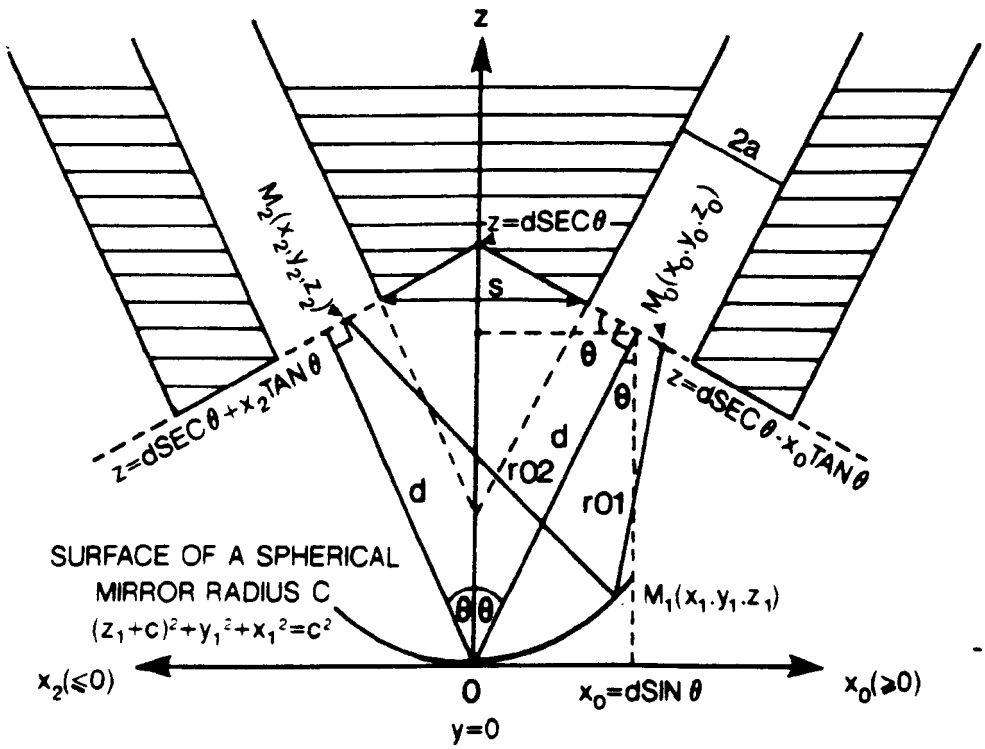

Figure 2.7(b). Plan view of the curved mirror 'v'-fold geometry (Figure 2.7a).

As mentioned previously, there are several approaches to describe the mode propagation in the free-space region. One method is to expand the mode into a set of Laguerre-Gaussian or Hermite-Gaussian modes which propagate according to the laws of Gaussian beam propagation. A second method involves the numerical evaluation of diffraction integrals. Avrillier and Verdonck [42] used the latter technique to determine the losses in coupling radiation from a guide into free-space and back into the same guide for a hollow rectangular dielectric waveguide resonator with external spherical mirrors. Their theory has an intuitive appeal and it is along these lines that the present treatment is developed.

The field component $E(x_1,y_1,z_1)$ at the observation point $M_1(x_1,y_1,z_1)$, which lies on the spherical surface of the mirror, is given by a scalar diffraction calculation using the Huyghens-Fresnel principle with the approximation of the paraxial beam.

$$E(x_1,y_1,z_1) = \int_{d\sin\theta-a\cos\theta}^{d\sin\theta+a\cos\theta} \int_{-b}^{+b} \left(\frac{1}{j\lambda r_{01}}\right) \exp(jkr_{01}) E_{pq}(x_0,y_0,z_0)\, dx_0 dy_0 \qquad (2.26)$$

where r_{01} is the distance between M_0 and M_1. r_{01} is given implicitly by

$$r_{01}^2 = (x_0 - x_1)^2 + (y_0 - y_1)^2 + (z_0 - z_1)^2 \qquad (2.27)$$

where

$$z_0 = d\sec\theta - x_0\tan\theta \qquad (2.28)$$

and

$$z_1 = c - (c^2 - x_1^2 - y_1^2)^{\frac{1}{2}} \qquad (2.29)$$

Equation (2.29) just describes the surface of a sphere centred at (o,o,c).

An exact but clumsy expression for r_{01} is thus obtained by substituting equations (2.28) and (2.29) into equation (2.27). However, expanding terms containing

$[1 - (\frac{x_1^2-y_1^2}{c^2})]^{\frac{1}{2}}$ binomially to the first order, and taking

$r_{01}^2 = 2r_{01}d - d^2$ gives an approximate and more manageable expression for r_{01}, viz,

$$r_{01} = \frac{d}{2} + [1 - \frac{d\sec\theta}{c} + \frac{x_0\tan\theta}{c}] \frac{(x_1^2+y_1^2)}{2d} + \frac{(d\sec\theta-x_0\tan\theta)^2}{2d}$$

$$+ \frac{(x_0^2+y_0^2)}{2d} - \frac{(x_0x_1-y_0y_1)}{d} \qquad (2.30)$$

which requires that $|\frac{x_1^2+y_1^2}{c^2}| < 1.$

In order to calculate the field components $E_2(x_2,y_2,z_2)$ at a point $M_2(x_2,y_2,z_2)$ in the plane of the second aperture, each point on the mirror surface is considered as a source.

Evidently,

$$E(x_2,y_2,z_2) = \int_{-\infty}^{+\infty}\int_{-\infty}^{+\infty} (\frac{1}{j\lambda r_{02}}) \exp(jkr_{02})\, E(x_1,y_1,z_1)\, dx_1\, dy_1$$

(2.32)

where r_{02} is the distance between M_1 and M_2 and is derived in a fashion similar to steps (2.27) - (2.30). Here it is assumed that the aperture radius of the mirror is infinite, although finite mirror apertures can be treated naturally by restricting the range of integration over the mirror surface.

The mode coupling efficiency is defined as the fraction of the energy carried by the EH_{pq} mode emerging from the guide which is coupled into the $EH_{p'q'}$ mode of its neighbouring guide after reflection. It equals $|\chi^{p'q'}_{pq}|^2$ where $\chi^{p'q'}_{pq}$ is the amplitude overlap integral given by

$$\chi^{p'q'}_{pq} = \int_{d\sin\theta-a\cos\theta}^{d\sin\theta+a\cos\theta} \int_{-b}^{+b} E(x_2,y_2,z_2)\; E^*_{pq}(x_2,y_2,z_2)\; dx_2\; dy_2 \qquad (2.32)$$

where the phase conjugate term $E^*_{p'q'}(x_2,y_2,z_2)$ is similar to the form of equation (2.25).

Applying Fubini's rule, which permits a change in the order of integration, and using the variables

$$x_0 = \frac{x_0\sec\theta - d\tan\theta}{a}$$

$$Y_0 = \frac{y_0}{b}$$

$$X_2 = \frac{x_2\sec\theta - d\tan\theta}{a}$$

and

$$Y_2 = \frac{Y_2}{b}$$

we have

$$\chi_{pq}^{p'q'} = -\frac{abcos^2\theta}{\lambda^2} \int_{-1}^{+1}\int_{-1}^{+1}\int_{-1}^{+1}\int_{-1}^{+1}\int_{-\infty}^{+\infty}\int_{-\infty}^{+\infty} \frac{1}{R_{01}\,R_{02}} \exp[jk(R_{01}+R_{02})]$$

$$\begin{Bmatrix}\cos(pX_0\pi/2)\\ \sin(pX_0\pi/2)\end{Bmatrix}\begin{Bmatrix}\cos(qY_0\pi/2)\\ \sin(qY_0\pi/2)\end{Bmatrix}\begin{Bmatrix}\cos(p'X_2\pi/2)\\ \sin(p'X_2\pi/2)\end{Bmatrix}\begin{Bmatrix}\cos(q'Y_2\pi/2)\\ \sin(q'Y_2\pi/2)\end{Bmatrix}$$

$$dX_0dY_0dx_1dy_1dX_2dY_2 \qquad (2.33)$$

where $R_{01} = r_{01}\ (aX_0\cos\theta + d\sin\theta,\ bY_0,\ z_0)$ and $R_{02} = r_{02}\ (aX_2\cos\theta - d\sin\theta,\ bY_2,\ z_2)$. For simplicity, it is assumed that the quantities R_{01} and R_{02} in the denominator will not differ significantly from d. This requires that d is much larger than the maximum linear dimensions of the aperture. This substitution cannot be extended to the exponent as the resulting errors would be multiplied by a very large number k, and consequently could generate phase errors much greater than 2π radians.

Using the Fourier transform pair identity [60],

$$F(y) = \int_{-\infty}^{+\infty} f(x)\ \exp(-jxy) \quad : \quad f(x) = A\ \exp(jB^2x) \qquad (2.34)$$

$$F(y) = \left(\frac{\pi}{2}\right)^{\frac{1}{2}} A\ \frac{(1+j)}{B}\ \exp(-jy/4B^2) \qquad (2.35)$$

and with recourse to a little algebra equations (2.33) may be reduced to a 4-fold integration. At this point it is convenient to introduce the Fresnel number $N = (\alpha\delta)^{\frac{1}{2}}/2\pi\beta$, where $\alpha = ka^2/c$, $\delta = kb^2/c$ and $\beta = d/c$ are useful parameters defined by Degnan and Hall [43]. The final result for the EH_{11} coupling efficiency for a square guide may be written as

$$C_{11} = \left(\frac{N\cos^2\theta}{2}\right) \left| \int_{-1}^{+1}\int_{-1}^{+1}\int_{-1}^{+1}\int_{-1}^{+1} \exp[j\pi N\ (X_0^2+X_2^2+Y_0^2+Y_2^2 \right.$$

$$- \frac{(X_0+X_2)^2\ \cos^2\theta + (Y_0+Y_2)^2}{2(1-\beta[\text{vos}\theta - \frac{\sin_2\theta(X_0-X_2)}{2(\cos\theta + F)}]}$$

$$\left. \frac{\cos(X_0\pi/2)\cos(X_2\pi/2)\cos(Y_0\pi/2)\cos(Y_2\pi/2)}{1-\beta[\cos\theta - \frac{\sin^2\theta(X_0-X_2)}{2(\cos\theta + F)}]}\ dX_0dY_0dX_2dY_2 \right|^2$$

(2.36)

where $C_{11} = |X_{11}^{11}|^2$ and $F = S/2a$. Extensions to rectangular waveguides and/or higher order mode coupling coefficients are

straightforward.

Note that the asymmetric phase front produced upon reflection means that in general, the curved mirror coupling coefficient matrix is not symmetrical, which was not the case for the plane mirror matrix derived in Section 2.3. Some of the symmetry relations given in equations (2.1) - (2.5) are, however, maintained; while the remainder are in some cases approximately true. An investigation into, and proofs of the symmetry relations and their approximations, for the curved mirror coupling coefficient matrix are presented in Appendix A.

Equation (2.36) ceases to be analytic when $X_0 - X_2 = 2\csc^2\theta(\cos\theta+F)(\cos\theta-1/\beta)$. At these points of singularity it is more appropriate to replace the Fourier transforms with delta functions. The resulting integrand is only non-zero when $X_0 + X_2 = 0$ and $Y_0 + Y_2 = 0$. These conditions are rarely satisfied within the range of parameter values determined by practical considerations or limitations imposed by approximations made in the preceeding theory. This aberrant behaviour has no physical significance and is consequently of little concern.

For the special cases when $\theta = 0$ and $\theta = \beta = 0$ equation (2.36) is equivalent to the results previously reported by Avrillier and Verdonck [42]. In general, however, unlike

their configuration, the choice of the guide-to-mirror separation is not arbitrary but given by

$$d = a(\cot\theta - F\csc\theta) \qquad (2.37)$$

A NAG Fortran Library Routine (D01FCF) was used with a Harris H800 mainframe computer to evaluate the real and imaginary components of C_{11} (eqn. (2.36)). The routine operates in an adaptive strategy by repeated subdivision of the hyper-rectangular region of integration into smaller hyper-rectangles. In each subregion, the integral is estimated using a seventh degree rule, and an error estimate is obtained by comparison with a fifth degree rule. CPU time considerations and memory storage limitations generally precluded high accuracy work. The present results were derived from integral evaluations where the estimated relative error was at least one part in 10^3.

Figure 2.8(a) shows polynomial fits to the numerical evaluations of the self-coupling losses for the lowest-order mode of a square guide as a function of $\beta = d/c$ for a fixed 'v'-fold angle (5.475°) and guide-to-mirror distance (the value of which depends on the choice of a), for various values of S/2a. Evidently, coupling efficiencies greater than those obtained with plane mirror folding ($\beta = 0$) are possible with curved mirror folding ($\beta > 0$). Also apparent

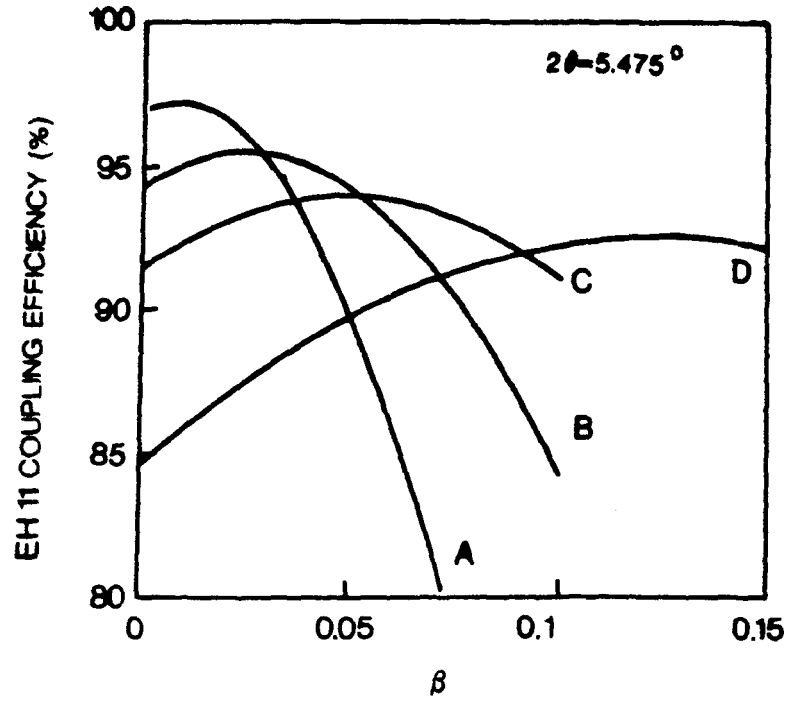

(a)

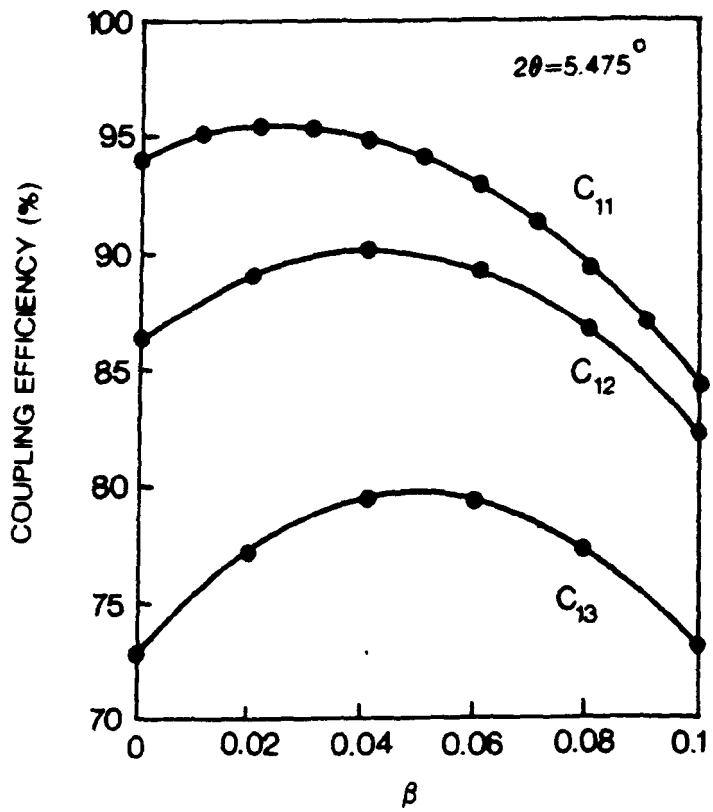

(b)

Figure. 2.8 a) EH_{11} coupling efficiency at a fold in a square guide. Curves A-D show the theoretical EH_{11} coupling efficiency versus $\beta = d / c$ for $S / 2a = 0$, 0.5, 1.0 and 2.0 with Fresnel numbers 5.075, 3.382, 2.536 and 1.690 respectively.

b) Higher order mode self coupling efficiency versus β for the folding geometry with parameters as in Figure 2.8a curve B.

is that the percentage increase in efficiency $\{(C_{11})max/C_{11}(\beta = 0)\}$ is greater for larger values of S/2a. Curve B in Figure 2.8(a) corresponds to S/2a = 0.5 and for 2a = 2.25 mm it predicts the curved mirror coupling behaviour for the 'v'-fold geometry discussed in section 2.3 (the one chosen for the 'z'-fold laser design). Curve B is reproduced in Figure 2.8(b) along with the self-coupling efficiencies for the EH_{12} an EH_{13} modes (for the same fold geometry). These curves predict a maximum EH_{11} self-coupling efficiency enhancement of 1.42% with $\beta = 0.024$ (corresponding to a mirror radius of curvature of 1.5 m), with little change in the degree of mode discrimination. For the 'z'-fold laser this suggests a reduction in the (single mode) EH_{11} round-trip loss of approximately 4.84%; although the resonator (multi-mode) round-trip loss can be more or less than the pure EH_{11} mode round-trip loss because of interference from other modes.

The 3 x 3 curved folding mirror coupling coefficient matrix (i.e. up to EH_{33}) is presented in Table 2.3, and will be used in Chapter 3 to estimate the 'z'-fold (curved mirror) resonator multi-mode round-trip loss for comparison with the 'z'-fold (plane mirror) loss.

A third folding geometry, a candidate that one might intuitively expect to provide low-loss folding, is the partial waveguide fold; its performance is assessed in the next section.

pq	p'q' 11	12	13	21	22	23	31	32	33	
11	0.3193		C_{11}^{31}				3.615×10^{-2}		-6.615×10^{-4}	Re(χ)
	0.9238						1.925×10^{-2}		1.998×10^{-3}	Im(χ)
	0.9554						1.7×10^{-3}		0.0000	|χ'|
	8.882×10^{-4}						8.165×10^{-5}		4.12×10^{-4}	Error
12		0.6223						0.1812		
		0.7125						0.3785		
		0.8949						1.8×10^{-3}		
		1.777×10^{-3}						3.49×10^{-4}		
13	-2.326×10^{-3}		0.8361				-6.628×10^{-4}		C_{31}^{33}	
	4.74×10^{-2}		0.2830				1.998×10^{-3}			
	2.3×10^{-3}		0.7791				0.0000			
	3.287×10^{-4}		1.765×10^{-3}				3.78×10^{-4}			
21				C_{12}^{12}		C_{12}^{32}				
22					?					
23				C_{32}^{12}		C_{32}^{32}				
31	C_{13}^{11}		C_{13}^{31}				0.8322		3.228×10^{-2}	
							0.2882		2.805×10^{-2}	
							0.7756		1.8×10^{-3}	
							1.761×10^{-5}		4.491×10^{-5}	
32		1.814×10^{-2}						0.8512		
		3.785×10^{-2}						-4.405×10^{-2}		
		1.8×10^{-3}						0.7265		
		3.592×10^{-4}						1.734×10^{-3}		
33	-6.624^{-4}		3.228×10^{-2}				C_{33}^{13}		0.6662	
	1.998×10^{-3}		2.204×10^{-2}						-0.4347	
	0.0000		1.5×10^{-3}						0.6328	
	3.711×10^{-4}		4.928×10^{-4}						1.521×10^{-3}	

Table 2.3. The curved mirror 'v'-fold coupling coefficient matrix. To save computer time the symmetry relations in Appendix A were employed (for example, only the non-zero elements are shown, and in the table $C_{13}^{11} = C_{31}^{11}$ etc.).

2.5 Partial Waveguide Folding

Another apparently hitherto unconsidered v-fold geometry, that (intuitively) might provide low-loss folding, is one with a partial waveguide to a plane mirror (or partial waveguide folding), shown schematically in Figure 2.9. As can be seen, light exiting the four-walled waveguide (through plane A) experiences three-walled or partial waveguiding over a path length d_1, followed by free-space propagation over a short path length d_2 to a plane reflector. The normal to the reflector at the origin lies on the v-fold angle bisector (the x-axis), which is also the line of symmetry. Consequently, the reflected light experiences the same path train in reverse before entering the adjacent four-walled waveguide (through plane B). For the case of the well-aligned reflector the paths A to B and B to A are reciprocal.

The partial waveguide folding and plane mirror folding geometries are similar insofar as the path trains (A to B) can be of identical length for the same fold angles (if a and S are the same in each case). The partial waveguide folding is created by the extention of the top, bottom and outer guide walls to (or near to) the reflector surface, thus greatly reducing the free-space path length. A treatment of the coupling behaviour of this type of fold would involve an amplitude overlap integration of the launched and entrant fields over the waveguide aperture (in plane B); i.e. a product of an X-integral and a Y-integral. The Y-integral

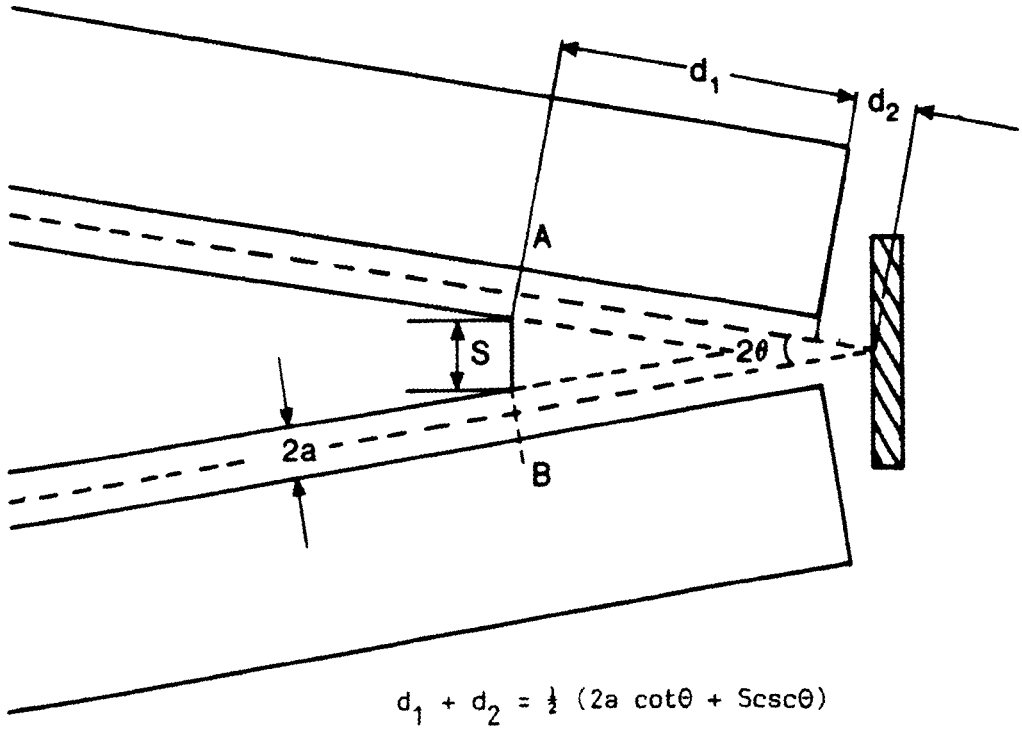

Fig. 2.9. Partial waveguide folding geometry.

(top to bottom of guide) would be nearly identical to that for the Case I reflector provided $N = a^2/\lambda d_2 >> 1$; whereas the X-integral (side to side) would be complicated by the partial waveguiding and the asymmetric fields associated with it. A theoretical treatment of the partial waveguide folding coupling behaviour will not be found here: it would seem reasonable, however, to expect that the resonator mode coupling loss would be less than for the plane mirror folding geometry, although the resulting higher output power of a laser utilising partial waveguide folding might be obtained at the expense of output beam mode quality.

The partial waveguide folding parameters chosen for the experimental investigation of the z-fold laser operating characteristics, and their deviance from the plane or curved folding parameters, were as follows:-

Parameter	Symbol	Value	
		Plane/curved mirror	Partial waveguide
Guide half-width	a	1.125 mm	1.125 mm
Width at apex	S	1.125 mm	1.00 mm
Fold-angle	2θ	5.475°	5.9°
Partial waveguide length	d_1	-	27.80 mm
Free-space propagation length	d_2	35.3 mm	3.75 mm
z-fold laser:			
Passive length	L_p	124.1 cm	117.8 cm
Active length	L_a	115.0 cm	115.0

The change in fold-angle to 5.9° (used in the plane and curved mirror folding geometries), arose through practical considerations of alignment with the existing z-fold laser mirror mounts and output window, and the desire to retain the same active length for comparison purposes. The difference in angle and the change in passive length that accompanied it, were not considered to invalidate any comparison between the laser operating characteristics for the three folding geometries, obtained under otherwise identical conditions (Chaper 5).

CHAPTER 3

LASER RESONATOR MODELS

Summary

It is of immediate interest to determine how the output power of a folded waveguide laser depends upon the physical, resonator, and active medium parameters. In this chapter the output power for the proposed z-fold laser is predicted by incorporating the known and estimated laser parameters into a Rigrod-type analysis, to determine the optimum selectable parameters. Some of the laser parameters are not known with adequate precision a priori, but may be determined retrospectively by measuring the laser output power for different intra-cavity gain lengths, and solving the simultaneous Rigrod equations predicting the outcome. The solution curves and their associated errors derived in this chapter will be used later with the experimental data in Chapter 5 to determine the small-signal gain coefficient, the saturation intensity and the resonator mode round-trip loss. A theoretical prediction of the latter parameter is also described here using a numerical and iterative resonator treatment incorporating the mode coupling matrices derived in Chapter 2.

3.1 Rigrod Analysis

The output power of a homogeneously broadened cw laser, such as the CO_2 waveguide laser, can be estimated using the Rigrod equation [61,62]; one of a generic approach to predict the output power of a laser. There are multiple versions; one type assumes that the resonator losses are concentrated near the mirrors [61], and another assumes a uniform distributed loss between the mirrors [62]. Both types give an approximate solution to an implicit transcendental function of the intracavity irradiance and the macroscopic laser parameters. The analyses considered here treats only the case of homogeneous laser transitions, in which the line shape does not change during gain saturation. The resonator is assumed to support substantially plane electromagnetic waves that experience uniform and isotropic gain. The macroscopic laser parameters are the unsaturated gain coefficient (g), the gain saturation intensity (I_s), the distributed absorption loss (α), the lumped loss (giving the effective reflectivities, r_1 and r_2, of mirrors one and two), the effective cross-sectional area of the beam (A), and the gain length (L). The expressions that permit computation of the available laser output power and the optimum output mirror transmission are as follows:-

$$\text{lumped:} \quad P = \frac{I_s A \sqrt{r_1}(1-r_2)[gL+Ln\sqrt{r_1 r_2}]}{(\sqrt{r_1}+\sqrt{r_2})(1-\sqrt{r_1 r_2})} \qquad (3.1)$$

$$(r_2)_{opt} = 1 - \sqrt{2gL(1-r_1)} \tag{3.2}$$

$$\text{distributed:} \quad P = \frac{I_s A[(g-\alpha)L+Ln\sqrt{r}]}{1 - \frac{\alpha L}{Ln\sqrt{r}}} \tag{3.3}$$

$$(r)_{opt} = [\exp(\sqrt{\alpha L}(\sqrt{\alpha L}-\sqrt{gL}))]^2 \; : \; r_1 = 1 \; : \; r_2 = r \tag{3.4}$$

The effective cross-sectional area of the beam is usually taken to be that circumscribed by the 1/e power points of the laser mode. For a waveguide laser with a predominantly EH_{11} output mode profile, a suitable value is given by [18]

$$A = \pi \left(\frac{0.69a}{\sqrt{2}}\right)^2 \tag{3.5}$$

where a is the guide half-width.

The effective lumped (η^e) and distributed (α^e) round-trip-losses are related by

$$\eta^e = 1 - \exp(-2\alpha^e L) \tag{3.6}$$

The resonator mode round-trip losses associated with a z-fold waveguide laser are not adequately described as lumped or distributed. The major components of the overall resonator loss are the coupling losses at each fold mirror. In addition there are coupling losses at the Case I reflectors and waveguide attenuation between them. Hence, there are four discrete lumped losses (two pairs) distributed at equal

intervals (L/3) along the gain length with a truly distributed, albeit segmented and mode dependent, waveguide attenuation loss. In the face of all these different losses, it is convenient to simplify matters by considering the loss as either an effective lumped (η^e) or distributed (α^e) loss.

The effective lumped round-trip loss for EH_{pq} may be expressed as follows:-

$$\eta^e_{pq} = [1 - C^{bm}_{pq} (C^{f_1}_{pq} C^{f_2}_{pq})^2 C^{om}_{pq}] + 2\alpha'_{pq} L_{wg} \qquad (3.7)$$

where C^{bm}_{pq}, $C^{f_1,2}_{pq}$ and C^{om}_{pq} are the EH_{pq} mode coupling efficiences at the back-mirror, folding mirrors and output mirror, respectively. L_{wg} is the total waveguide length (single pass). The modal power attenuation coefficient α'_{pq} is given by [19] and in Table 2.1,

$$\alpha'_{pq} = 2\alpha_{pq} = \frac{\lambda^2}{8q^3} \left\{ \mathrm{Re}\left[\frac{p^2}{(\epsilon-1)^{1/2}}\right] + \mathrm{Re}\left[\frac{q^2\epsilon}{(\epsilon-1)^{1/2}}\right] \right\} \qquad (3.8)$$

where α_{pq} is the (usual) amplitude attenuation coefficient and $\epsilon = (n-jk)^2$; n and k are, respectively, the refractive index and extinction coefficient of the waveguide wall material at the wavelength, λ. For polycrystalline alumina waveguides, the proposed values are n = 0.65 and k =0.038 at 10.6 μm [63].

For the plane mirror folding geometry considered in Chapter 2, a = 1.125 mm, L_{wg} = 116 cm, $C^{f_1}{}_{11} = C^{f_2}{}_{11}$ = 94.66% (Table 2.2) and $C^{bm}{}_{11} = C^{om}{}_{11}$ = 99.75% (5 mm spaced Case I reflectors). These values and those for n and k above give α_{11} = 0.14%/m and $\eta^{e}{}_{11}$ = 20.4%. The resonator mode will not in general be purely EH_{11}, but a linear combination of all the allowed waveguide modes. The lowest-loss resonator mode can be predicted iteratively by propagating a normalised multi-component mode round the resonator until a solution is found. This is the approach described in section 3 of this chapter.

The effective distributed loss is given by equation (3.6), and for a lumped round-trip loss of 20.4% (from above) it gives $\alpha^{e}{}_{11}$ = 0.10%/cm. Notice that the waveguiding loss component is only 1.4% of the total loss and may be neglected. For curved mirror folding the predicted coupling losses were $C^{f_1}{}_{11} = C^{f_2}{}_{11}$ = 95.54% (Table 2.3) giving $\eta^{e}{}_{11}$ = 17.4% and $\alpha^{e}{}_{11}$ = 0.08%/cm. These loss figures represent a significant fraction of the available gain, which is typically 0.5 - 1.0%/cm in CO_2 lasers.

The choice of Rigrod equation to predict the laser output power is of little consequence for the figures associated with the z-fold laser considered here, as their evaluation gives almost coincident results. The next section, however, described an attempt to find a simultaneous solution to a set of Rigrod equations, where the lumped

Rigrod equation is too intractable analytically, and consequently the distributed loss version is adopted.

The predicted z-fold laser output power for a range of macroscopic laser parameter values incorporated into the Rigrod equation (3.4) is presented in Figures 3.1(a and b). Evidently, attempts must be made to reduce the round-trip loss if the desired 50 W power level is to be realised. There will be an inevitable trade-off between the available gain and the saturation intensity to give an optimum operating gas pressure. Figure 3.2 shows how the laser output power should increase as the round-trip loss is reduced - for instance, the use of curved fold mirrors (Chapter 2, Section 4) should give ≈ 5% reduction in loss and about 6 W extra power. This falls somewhat short of the predicted ∿ 14% reduction in the loss for the additional 20 W required to meet the 50 W power goal. The gain and saturation intensity values used in the figure were derived from experimental determinations (described later). Finally, in Figure 3.3 the optimum output coupling is calculated for various loss figures. The 75% reflectivity output mirror chosen lies close to the optima within the loss figure range likely to be encountered.

3.2 Simultaneous Solution of the Rigrod Equations

As already mentioned, the Rigrod equations can be used to predict the output power of a homogeneously broadened cw laser if a few resonator and laser medium parameters are known. Of these, the resonator mode round-trip loss, the

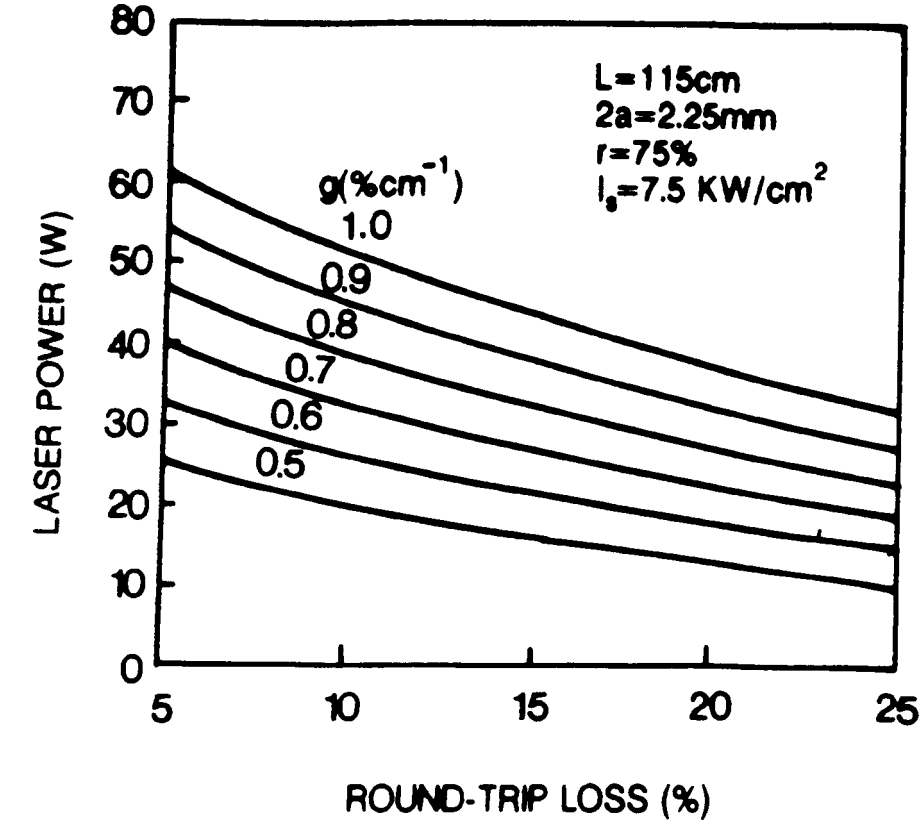

(a)

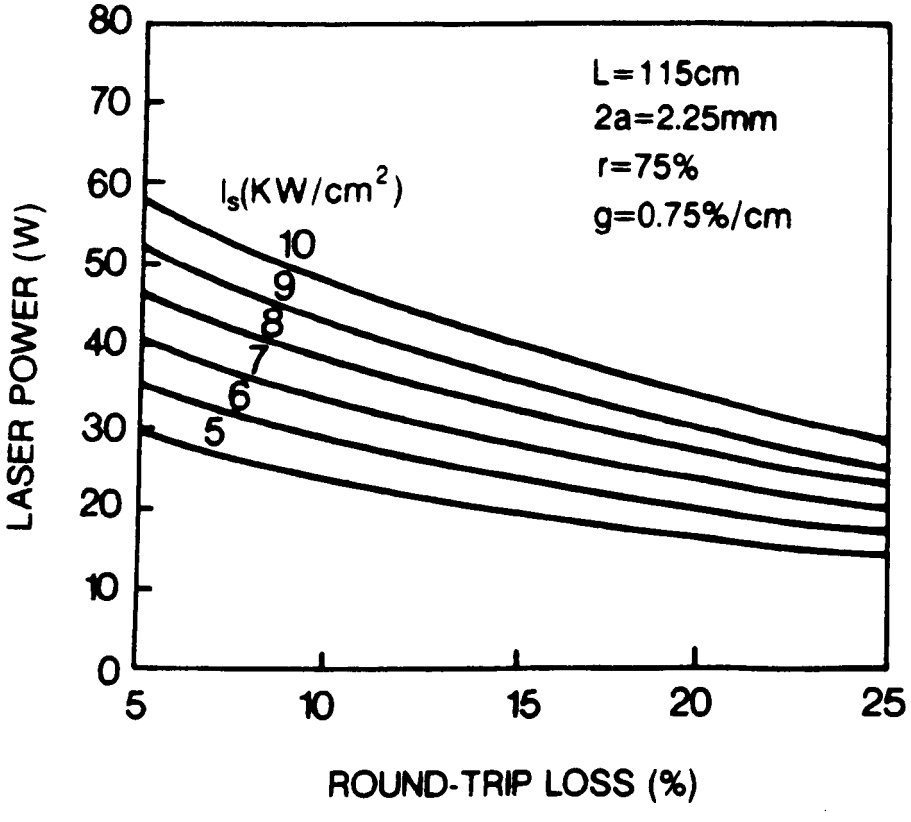

(b)

Figure 3.1. The z-fold laser output power predictions as a function of the resonator mode round trip loss for various values of the active medium small-signal gain coefficient (a) and saturation intensity (b).

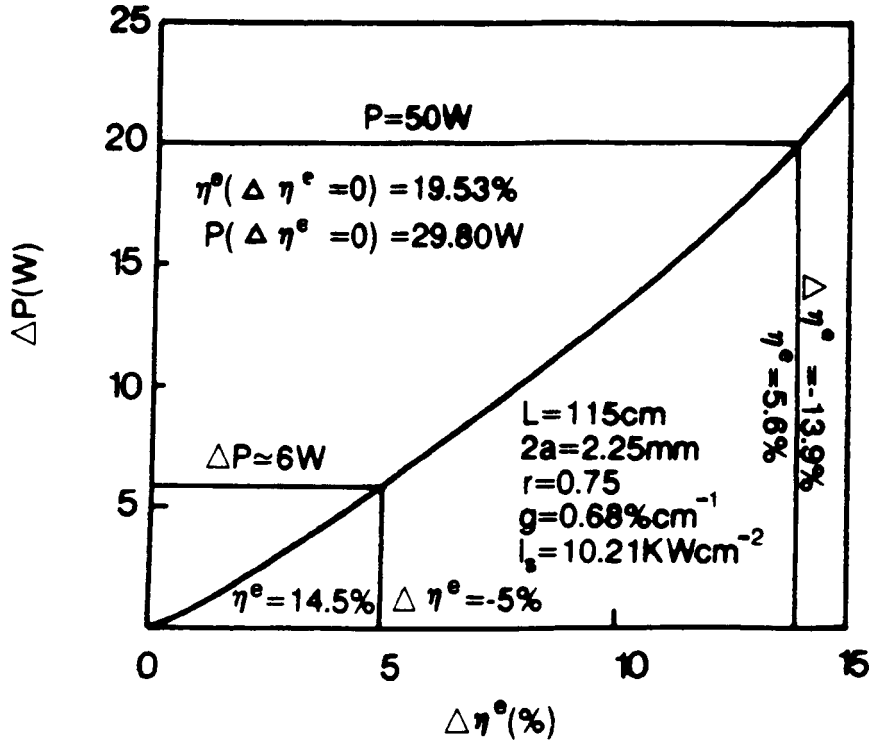

Figure 3.2. The predicted increase in z-fold laser output power resulting from the reduction of the resonator mode round-trip loss.

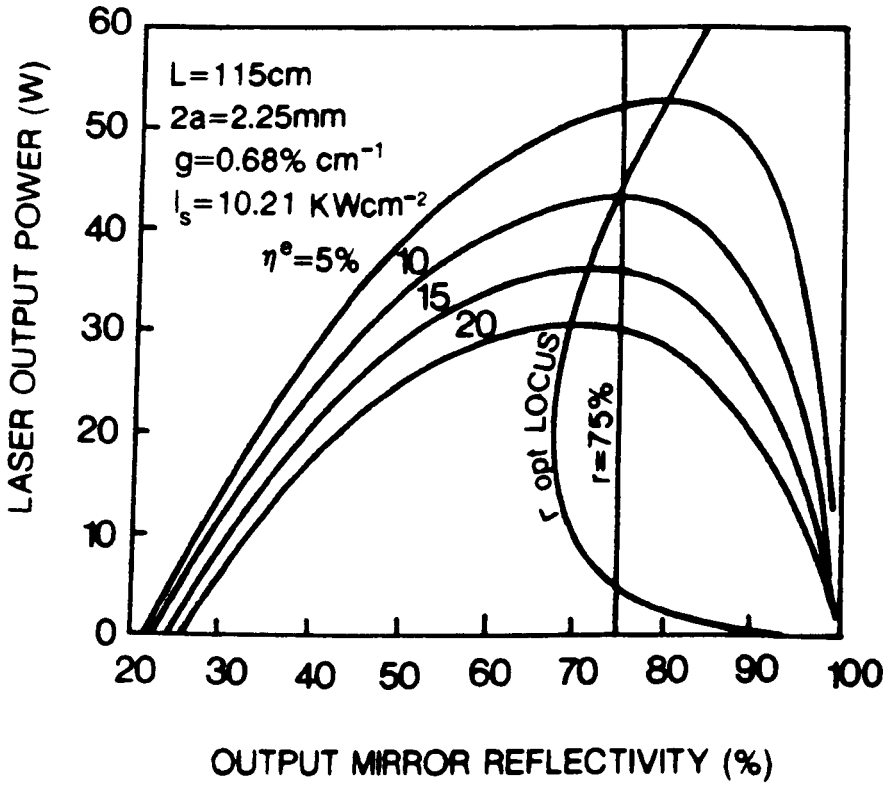

Figure 3.3. z-fold laser output power as a function of the output mirror reflectivity for various round-trip loss figures.

small-signal gain coefficient, and the gain saturation intensity, are often not known with adequate precision a priori. The remaining parameters, the effective beam cross-sectional area, the mirror reflectivities, and the gain length, on the other hand, are more easily determined. An error analysis of the Rigrod equations is complicated by the interdependence (or covariance) of some of its parameters; for example, the small-signal gain and its saturation intensity are inherently coupled by the laser medium sustaining them, and the resonator mode content affects its profile and (hence) beam area. In a waveguide the round-trip loss and the cross-sectional area are functions of the guide half-width. Ignoring these complications and assuming that each parameter value carries an uncorrelated standard deviation error, the error in the evaluation of the laser power (distributed version) may be expressed as a standard error of a compound quantity [64] as follows:-

$$\sigma_p^2 = \left(\frac{\partial p}{\partial Is}\right)^2 \sigma_{I_s}^2 + \left(\frac{\partial p}{\partial A}\right)^2 \sigma_A^2 + \left(\frac{\partial p}{\partial g}\right)^2 \sigma_g^2 + \left(\frac{\partial p}{\partial \alpha}\right)^2 \sigma_\alpha^2 + \left(\frac{\partial p}{\partial L}\right)^2 \sigma_L^2 + \left(\frac{\partial p}{\partial r}\right) \sigma_r^2 \qquad (3.9)$$

For the parameter values given in Figure 3.3 (at the origin) this reduces to:-

$$\left(\frac{\sigma_p}{p}\right)^2 = \left(\frac{\sigma_{I_s}}{I_s}\right)^2 + \left(\frac{\sigma_A}{A}\right)^2 + \frac{q}{4}\left(\frac{\sigma_g}{g}\right)^2 + \frac{4}{q}\left(\frac{\sigma_\alpha}{\alpha}\right)^2 + \frac{16}{25}\left(\frac{\sigma_L}{L}\right)^2 + \frac{1}{4}\left(\frac{\sigma_r}{r}\right)^2 \qquad (3.10)$$

Evidently, the gain coefficient term yields the largest percentage error, closely followed by the gain length term. The saturation intensity and the cross-sectional area errors scale directly as expected from the form of the Rigrod equation. The distributed loss coefficient and the output mirror reflectivity parameters are both associated with loss (the laser output is a useful loss!). Their errors yield the smallest percentage errors, reiterated in Figure 3.3, where the output power is weakly dependent on the output mirror reflectivity about the optimum output coupling. It should be appreciated, however, that although $\partial p/\partial r = 0$ in a power-optimised laser, $\partial p/\partial \alpha < 0$ always; so, in this simple approach, any percentage error in α is bound to be more important than the same error in r. The error coefficients above are specific to the laser described, while the inference is general.

There are few reported measurements of gain coefficients and saturation intensities pertaining to CO_2 waveguide lasers in the literature. The results available are seldom for the gas mixtures and pressures required, or the mode of excitation employed, or the gas temperatures considered, etc., etc. Single pass measurements of gain and saturation are complicated by the need for frequency stable probe lasers, perhaps with high input powers tunable over many lines. The excitation of a nearly pure waveguide mode requires precise alignment of the probe beam and control of its beam waist (it is easy to excite EH_{11}, for example, but

not so easy to excite EH_{11} alone!). The simulation of a resonator mode field interaction with the gain medium is not practicable (even if the mode composition were known).

There are alternative (in situ) ways to determine experimentally the uncertain laser parameters. One method [62,65,66] involves fitting measurements of the laser output power to the Rigrod relation, with a number of different output mirror reflectivities. Graphical solutions are used together with measurements of the beam area to evaluate g, α, and I_s. A second method, not usually practicable, is to measure the laser output power for different gain lengths. This method is particularly suited to folded lasers because of their inherent segmented design, although neither an analytical or graphical solution to the resultant Rigrod equations has been found in the literature (other than those for the latter method, which are not directly applicable). Consequently, the author considered it necessary to derive his own expressions for the evaluation of g, α and I_s, viz:-

The distributed Rigrod equation may be re-written in the form:-

$$P_a = P_s \, [L(ag-\alpha) + R] \, \left[1 - \frac{L}{R}\alpha\right]^{-1} \qquad (3.11)$$

where $R = Ln\sqrt{r}$, $P_s = AI_s$ (the saturation power), and a is the fraction of the available gain length giving the laser output power P_a. The unknown parameters are α, g and P_s. Since there are three unknowns, at least three equations are needed for a solution. If there are three different laser

output power levels corresponding to three different gain lengths, with otherwise identical conditions, then the Rigrod equations describing the laser performance form a set of nonlinear simultaneous equations. Unfortunately any attempt to solve these equations, using for example the Newton-Raphson iteration method [67], will fail because there can only be two unique equations, and hence insufficient information to solve for the three unknowns. Consider the general expressions for P_a, P_b, P_c and the combination $mP_a + nP_b$, viz:-

$$P_a = P_s \left[L(ag-\alpha) + R\right] \left[1 - \frac{L}{R}\alpha\right]^{-1} \qquad (3.12)$$

$$P_b = P_s \left[L(bg-\alpha) + R\right] \left[1 - \frac{L}{R}\alpha\right]^{-1} \qquad (3.13)$$

$$P_c = P_s \left[L(cg-\alpha) + R\right] \left[1 - \frac{L}{R}\alpha\right]^{-1} \qquad (3.14)$$

$$mP_a + nP_b = P_s \left[L(\left[ma+nb\right]g) - \alpha) + R\right] \left[1 - \frac{L}{R}\alpha\right]^{-1} \qquad (3.15)$$

For equations (3.14) and (3.15) to be equivalent, requires that

$$P_c = mP_a + nP_b \qquad (3.16)$$

and

$$c = ma + nb \tag{3.17}$$

giving

$$n = \frac{aP_c - cP_a}{aP_b - bP_a} \tag{3.18}$$

$$m = \frac{bP_c - cP_a}{bP_a - aP_b} \tag{3.19}$$

Hence, three or more equations are superfluous and contain no additional information, since they are linear combinations of any other two equations.

For a = 1/3, b = 2/3 and c = 1, as might be the case for a z-fold laser,

$$P_{2/3}-P_{1/3} = P_s\,[L([2/3-1/3]g-\alpha) + R][1 - \frac{L}{R}\alpha]^{-1} \tag{3.20}$$

$$P_1-P_{2/3} = P_s\,[L([1-2/3]g-\alpha) + R][1 - \frac{L}{R}\alpha]^{-1} \tag{3.21}$$

giving a solution $P_{2,3}-P_{1,3} = P_1-P_{2,3}$. In general, the rate of change of power with respect to length is a constant (all other things being equal). The Rigrod pair of equations can be re-written in the form

$$F_a = P_a + \alpha S_a - P_s[aLg + R] = 0 \tag{3.22}$$

$$F_b = P_b + \alpha S_b - P_s[bLg + R] = 0 \tag{3.23}$$

where

$$S_a = LP_s - \frac{P_a L}{R} \tag{3.24}$$

$$S_b = LP_s - \frac{P_b L}{R} \tag{3.25}$$

Solving the linear simultaneous equations (3.22) and (3.23) for P_s, by taking $F_a-(S_a/S_b)F_b$, gives

$$P_s = \frac{P_a - S_a/S_b\, P_b}{Lg\left(\frac{a}{c} - \frac{bS_a}{cS_b}\right) + R\left(1 - \frac{S_a}{S_b}\right)} \tag{3.26}$$

Substituting equations (3.12) and (3.13) into equations (3.24) and (3.25) respectively, the ratio S_a/S_b simplified to the dimensionless quantity a/b, giving

$$P_s = \frac{bP_a - aP_b}{(b-a)R} \tag{3.27}$$

This simple solution reveals that the saturation power can be determined implicitly from two experimentally determined laser output powers corresponding to two different gain lengths (with otherwise identical conditions), without knowledge of the gain coefficient or the resonator round-trip loss.

The quantity $(bP_a - aP_b)/(b-a)$ in equation (3.27) describes the P-axis intercept (c) of a straight line with gradient $m = P_b/(b-a)$. Hence,

$$P_s = \frac{c}{R} \tag{3.28}$$

Fitting a straight line to two experimental data points is likely to lead to large errors in the determination of the saturation power. A more sensible approach would be to obtain many data points and use the method of least squares to calculate the mean slope and intercept. This approach also caters for a comprehensive error analysis [67], summarised as follows

$$I_s = \frac{c}{AL\ln\sqrt{r}} \tag{3.29}$$

$$\left(\frac{\sigma_{I_s}}{I_s}\right)^2 = \left(\frac{\sigma_c}{c}\right)^2 + \left(\frac{\sigma_A}{A}\right)^2 + \left(\frac{1}{L\ln r}\right)^2 \left(\frac{\sigma_r}{r}\right)^2 \tag{3.30}$$

$$c = \frac{\Sigma L_i^2 \Sigma P_i - \Sigma L_i \Sigma L_i P_i}{n\Sigma L_i^2 - (\Sigma L_i)^2} \qquad (w) \qquad \Sigma \equiv \sum_{i=1}^{n} \tag{3.31}$$

$$m = \frac{\Sigma P_i - nc}{\Sigma L_i} \qquad (w/m) \tag{3.32}$$

$$\text{Regression line variance} \approx s^2 = \frac{\Sigma P_i^2 - c\Sigma P_i - m\Sigma_i LP}{n-2} \qquad (3.33)$$

$$\sigma_c^2 = \frac{s^2 \Sigma L_i^2}{n\Sigma (L_i - \bar{L}_i)^2} \qquad (3.34)$$

$$\sigma_{c,m}^2 = \frac{s^2 \bar{L}_i}{\Sigma (L_i - \bar{L}_i)^2} \qquad (3.35)$$

$$\sigma_m^2 = \frac{s^2}{\Sigma (L_i - \bar{L}_i)^2} \qquad (3.36)$$

$$\text{Determinating coefficient} = \frac{m\Sigma P_i + c\Sigma L_i P_i - (\Sigma P_i)^2/n}{\Sigma P_i^2 - (\Sigma P_i)^2/n} \qquad (3.37)$$

The error analysis above assumes that each power reading is an observation from a normal population with constant variance, and that the corresponding values of gain length are known precisely.

A solution giving the remaining unknown parameter values, g and α, is not possible. One of these parameters must be estimated by some other means, and, together with the saturation intensity determination, incorporated into the Rigrod equation to give the remaining unknown parameter value. The error analysis above can be utilised once more

if the relation between g and α is written in a suitable form.

Consider the re-written Rigrod functions

$$F'_a = P_a \left[1 - \frac{L\alpha}{R}\right] - P_s \left[(ag-\alpha) + R\right] = 0 \qquad (3.38)$$

$$F'_b = P_b \left[1 - \frac{L\alpha}{R}\right] - P_s \left[(bg-\alpha) + R\right] = 0 \qquad (3.39)$$

and their difference

$$F'_b - F'_a = (P_b - P_a) \left[1 - \frac{L\alpha}{R}\right] - P_s(b-a)g = 0 \qquad (3.40)$$

Re-arranging (3.40) and substituting the relations for P_s and m from above gives

$$g = \frac{m}{c} (R - L\alpha) \qquad (3.41)$$

or in terms of an effective lumped round-trip loss

$$g = \frac{m}{c} \left(R + \frac{1}{2} \text{Ln} \left[1-\eta^e\right]\right) \qquad (3.42)$$

Alternatively, if g is known then η^e is given by

$$\eta^e = 1 - \exp\left[2\left(\frac{gc}{m} - R\right)\right] \qquad (3.43)$$

The standard errors of g and η^e, including the covariance

of c and m are given by

$$\sigma_g^2 = e_1\sigma_c^2 + e_2\sigma_m^2 + e_3\sigma_{c,m}^2 + e_4\sigma_r^2 \quad e_5\sigma^2_{\eta^e} \tag{3.44}$$

$$\sigma^2_{\eta^e} = E_1\sigma_c^2 + E_2\sigma_m^2 + E_3\sigma_{c,m}^2 + E_4\sigma_r^2 + E_5\sigma_g^2 \tag{3.45}$$

where

$$e_1 = \left(\frac{\partial g}{\partial c}\right)^2 , \; e_3 = 2\left(\frac{\partial g}{\partial c}\right)\left(\frac{\partial g}{\partial m}\right) \quad \text{etc.} \tag{3.46}$$

$$E_1 = \left(\frac{\partial \eta^e}{\partial c}\right)^2 , \; E_3 = 2\left(\frac{\partial \eta^e}{\partial c}\right)\left(\frac{\partial \eta^e}{\partial m}\right) \quad \text{etc.} \tag{3.47}$$

More specifically

$$\sigma_g^2 = g^2 \left[\left(\frac{\sigma_m}{m}\right)^2 + \left(\frac{-\sigma_c}{c}\right)^2 - \frac{2L_i}{\Sigma(L_i-\bar{L}_i)^2}\left(\frac{S}{\sqrt{|mc|}}\right)^2 + \right.$$

$$\left. + \left(\frac{m}{2c}\right)^2 \left[\left(\frac{\sigma_r}{r}\right)^2 + \left(\frac{\sigma_{\eta^e}}{1-\eta^e}\right)^2\right]\right] \tag{3.48}$$

$$\sigma^2_{\eta^e} = (\eta^e-1)^2 \left[\left(\frac{2cg}{m}\right)^2 \left[\left(\frac{\sigma_c}{c}\right)^2 + \left(\frac{-\sigma_m}{m}\right)^2 - \frac{2\bar{L}_i}{\Sigma(L_i-\bar{L}_i)^2}\left(\frac{S}{\sqrt{|mc|}}\right)^2\right.\right.$$

$$\left.\left. + \left(\frac{\sigma_g}{g}\right)^2\right] + \left(\frac{-\sigma_r}{r}\right)^2\right] \tag{3.49}$$

It can be shown that

$$\frac{e_j \sigma^2}{\Sigma|e_j|} = \frac{E_j \sigma^2}{\Sigma|E_j|} \qquad (3.50)$$

Hence, the relative contributions of the weighted parameter variances to the total variance are the same for the gain coefficient and the round-trip loss error evaluations; although in general their percentage errors are not equal.

The preceeding solution to the simultaneous Rigrod equations will be used in Chapter 5 to interpret the measurements of the output power of the z-fold laser for the conditions when one, two and all three of its discharge segments were lit.

3.3 Iterative Round-Trip Modes

A laser resonator mode is a field distribution that replicates itself after one round-trip. More specifically, any circulating field with a round-trip phase shift equal to an integer number of 2π radians and an arbitrary round-trip amplitude factor greater or equal to that required to satisfy the threshold conditions for laser oscillation, can be described as a laser resonator mode.

A waveguide laser resonator mode can not, in general, be described by a single waveguide mode. In some cases where the waveguide laser round-trip path contains highly discriminating components that greatly attenuate all but one waveguide mode, the resonator mode can be approximately

modelled by a single waveguide mode treatment. An example of a mode discriminating component is the Case III reflector [43]; a curved mirror placed at a distance equal to half its radius of curvature from the end of a waveguide. The mode discrimination is determined by the relative re-entrant self-coupling efficiencies of the various launched waveguide modes. A Case III reflector greatly favours coupling to the fundamental EH_{11} waveguide mode and 'drives' the remaining higher order waveguide mode round-trip propagation losses above the threshold for lasing. Consequently, the laser output mode is almost purely EH_{11} or quasi-TEM_{00}. In practice, however, even the output of a well-aligned waveguide laser with mode discrimination may exhibit mode beating between the fundamental mode and a faint higher order mode (a topic addressed in Chapter 6).

Hence, a multimode treatment of waveguide resonator modes is required to accurately predict its round-trip propagation loss and the laser output power and mode content. The resonator mode content can be derived by iteratively propagating an initial normalised multimode field distribution round and round the resonator path until it becomes self-consistent. The matrix describing the field propagation must include all mode losses and gain, including guiding losses, coupling losses incurred during re-entrance after free-space propagation and reflection, and the homogeneously broadened Lorentzian gain lineshape.

More formally, the resonator is fully described by the waveguide geometry, the waveguide mode propagation constants k_{mn} and coupling coefficients $\chi^{m'n'}_{mn}$. By summing the normalised mode powers over some portion of the mode 'table' after each round-trip it is possible to determine whether significant power has been coupled into higher order modes not included in the treatment, and adjust the iteration algorithm accordingly. For well-aligned and symmetric resonators it is often adequate to consider only modes up to and including $EH_{3,3}$. The steady-state resonator mode round-trip loss is calculated as the sum of the individual round-trip power losses.

The iteration algorithm chain for the z-fold laser resonator is essentially

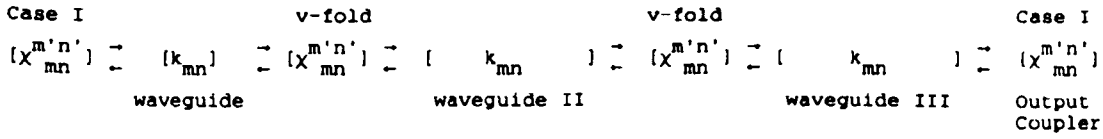

An existing programme written by Hill [58] was used to evaluate the round-trip loss figures for the z-fold laser with a) plane folding mirrors and b) curved folding mirrors using the coupling coefficient matrices derived in Chapter 2 (Tables 2.2 and 2.3 respectively). The parameters common to each resonator configuration were as follows:-

Parameter:	Symbol:	Value:
Waveguide height	2b	2.25 mm
Waveguide width	2a	2.25 mm
Waveguide lengths	L1	386 mm
	L2	388 mm
	L3	386 mm
Parallel loss factor (Al_2O_3)	$Re\{(\epsilon-1)^{-1\ 2}\}$	0.5
Perpendicular loss factor (Al_2O_3)	$Re\{\epsilon(\epsilon-1)^{-1\ 2}\}$	0.8

The round-trip loss values derived in this manner were 18.8 ± 2.0% and 19.8 ± 2.0% for the plane and curved folding mirrors respectively. In each case only the waveguide modes up to and including $EH_{3,3}$ were included in the iteration algorithm. This restriction was a result of the difficulty in obtaining accurate high order curved folding mirror coupling coefficients (Chapter 2). The range of plane folding mirror coupling coefficients was not restricted in this manner, although held the same to allow for a direct comparison of the round-trip losses. The error associated with each loss figure was reasonably assumed by comparing the plane mirror loss figures for different modal ranges. The predicted 1.0 ± 2.0%increase in round-trip loss between the plane and curved folding mirrors was not expected from the single mode treatment in Chapter 2, that predicted a decrease of approximately 5.68%. A change in round-trip loss for otherwise identical conditions (apart from modal

composition), is indicative of a laser output power change. Chapter 5 describes the experimental characterisation of the z-fold laser for both resonator geometries thus providing a third opinion.

CHAPTER 4

Z-FOLD LASER DESIGN AND CONSTRUCTION

Summary

This chapter describes the practical implementation of the folded waveguide resonator geometry chosen through the theoretical considerations in Chapter 2, into hardware. The final laser design was influenced by the limitations of the existing and available construction materials and technologies, and the desire for adequate operational flexibility. Also described are the RF and coolant support systems, and the routine waveguide resonator alignment procedure.

4.1 Laser Box

The final design of a laser is often a compromise because there are many trade-offs and practical limitations; the z-fold laser was no exception.

The z-fold laser package comprised a vacuum tight envelope, a waveguide and electrode assembly, adjustable resonator mirrors, an RF power supply and delivery system, a coolant network, a gas mixing chamber and supply, and a vacuum pump. The z-fold laser external and internal features are presented in Figures 4.1 and 4.2 respectively.

The vacuum envelope was a box machined out of a single block of aluminium alloy, topped by an alloy lid and sealed with a rubber membrane. Vacuum tight infrared window and observation ports, coolant and RF feed-throughs, and gas pipe/vacuum hose connections were maintained using rubber 'o'-ring technology. The vacuum envelope approach was preferred to the alternative 'hard seal' approach [55] because of the versatility it provided, in terms of access to laser components and their modifications (of which there were several). The evolving 'hard seal' technologies (often associated with commercial and military field devices) permits the construction of vacuum tight waveguide resonator assemblies by brazing the mirrors onto the end of the waveguide. Although neat and compact, lasers fabricated using 'hard seal' methods do not offer adequate operational flexibility for research investigations; moreover they are not devoid of problems, and are often expensive.

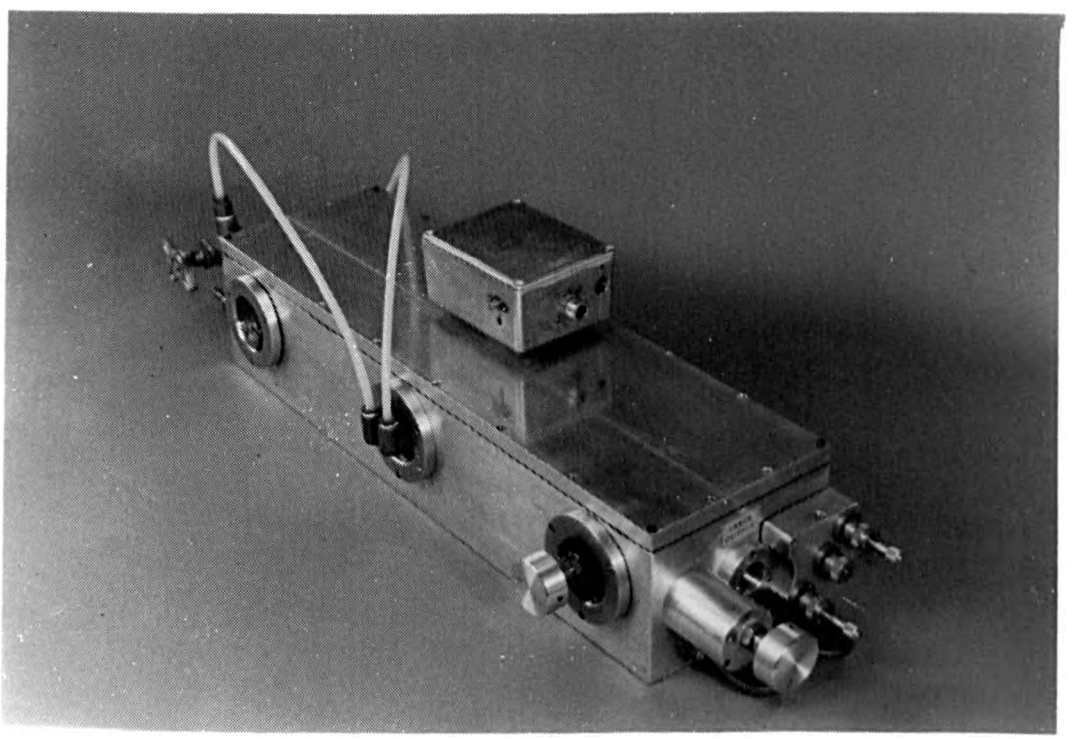

Figure 4.1. The Z-fold laser external features

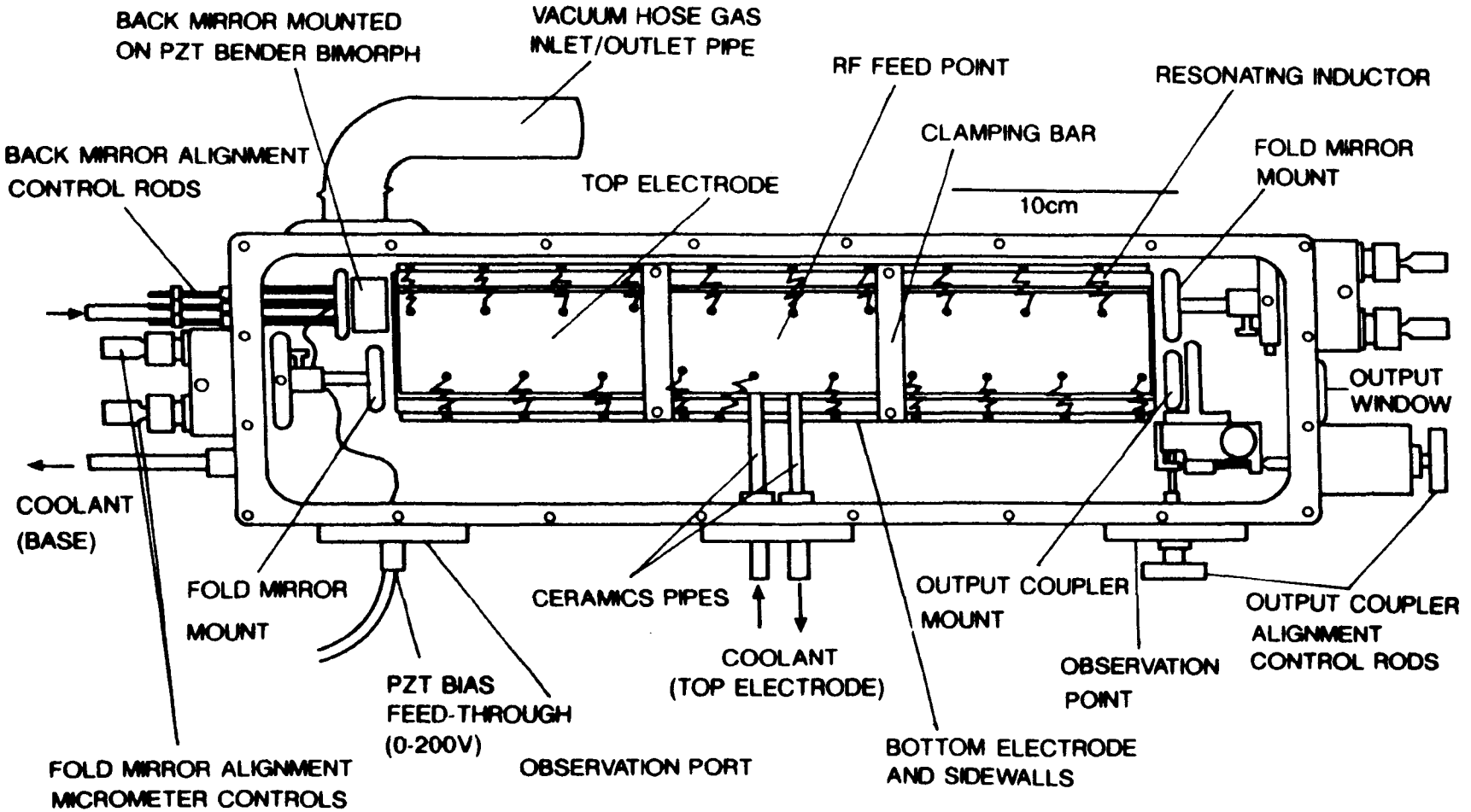

Figure 4.2. The z-fold laser internal features.

4.2 Waveguide Assembly

The z-fold hollow dielectric waveguide was fabricated from eight polished slabs of alumina ceramic (Figure 4.3), precisely located and clamped between two aluminium electrodes (Figure 4.4). All four of the waveguide channel walls were made of ceramic, as opposed to the metal plus ceramic walls of the hybrid variety. The larger electrode spacing associated with the all ceramic type helped to reduce the electrode capacitance to a suitable value (discussed later). The all ceramic walls were not expected to provide any waveguide mode polarisation discrimination (discussed in Chapter 5). The alumina manufacturers [68] specify a 97.5% polycrystalline Al_2O_3 and a 2.5% glassy phase content, with fine grain size. A surface finish of less than 1 μm c.l.a. for the machined ceramic is typical (although not verified), lying within the stringent requirements for low-loss waveguiding [55].

A 2.25 mm square bore waveguide and a 5.475° 'v'-fold angle were chosen. The 2.25 mm bore dimension was considered a suitable choice, considering that the highest reported specific power extraction for an RF-excited CO_2 waveguide laser (namely 0.83 W/cm) is associated with this bore [6]. Further, the waveguiding loss for the fundamental waveguide mode at these dimensions is negligible when compared to the available gains (roughly two orders of magnitude less), yet still providing sufficient mode discrimination. The waveguide mode coupling losses at the 'v'-folds were

Scale: 1:1.4

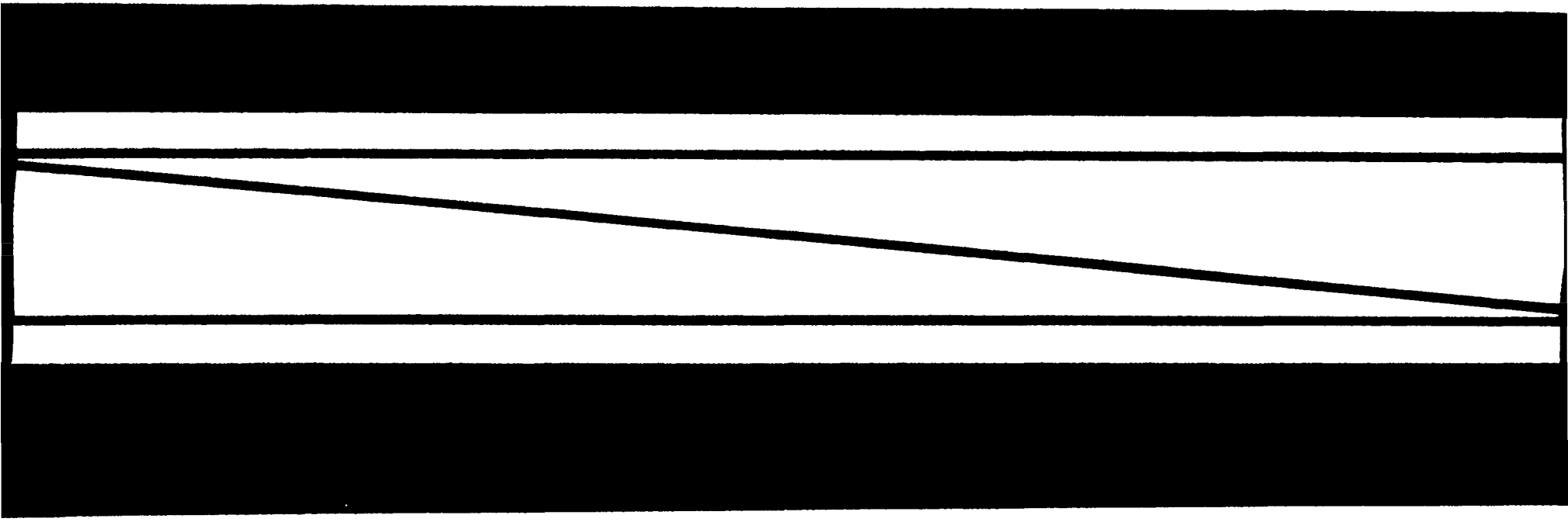

Figure 4.3. The z-fold hollow dielectric waveguide fabricartion was achieved by sandwiching the wedge-shaped ceramic pieces (above) between two slabs of ceramic (not shown).

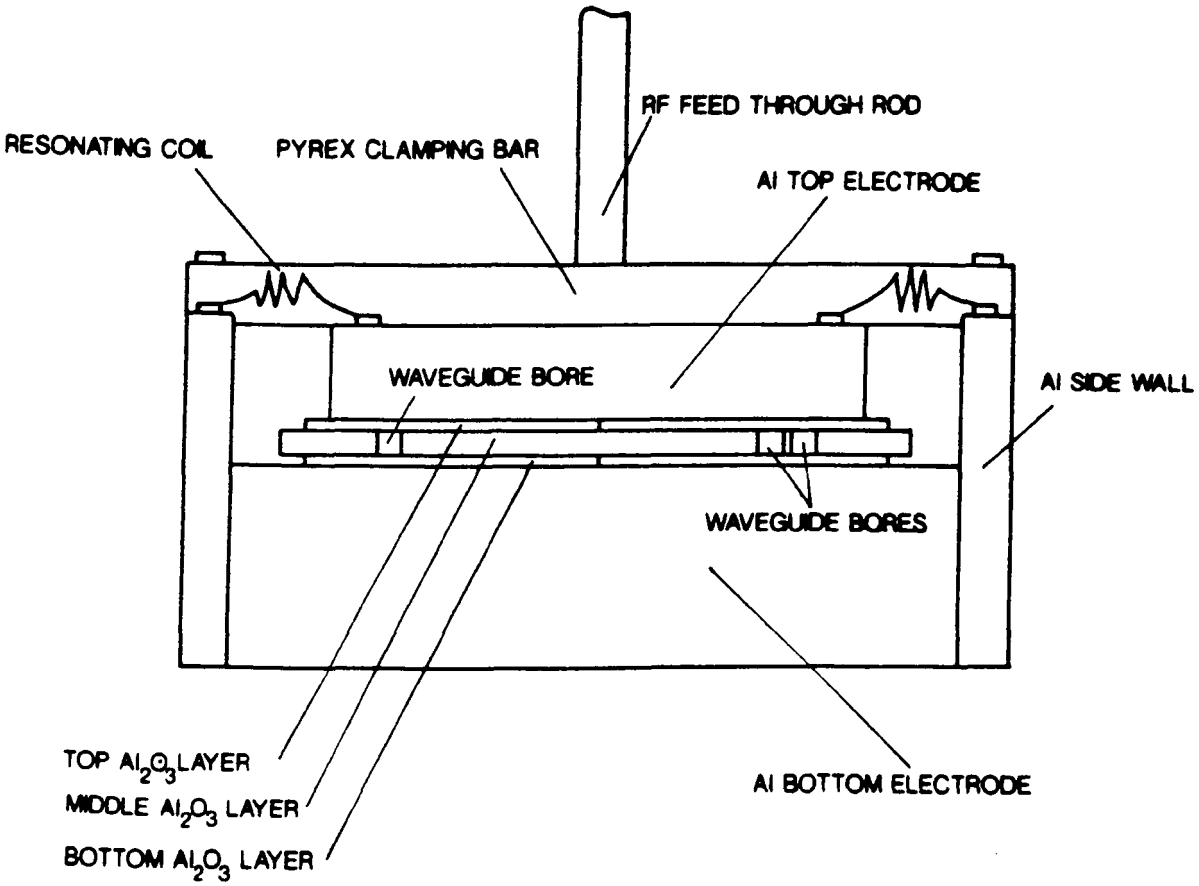

Fig. 4.4. (a) waveguide and electrode assembly (end view).

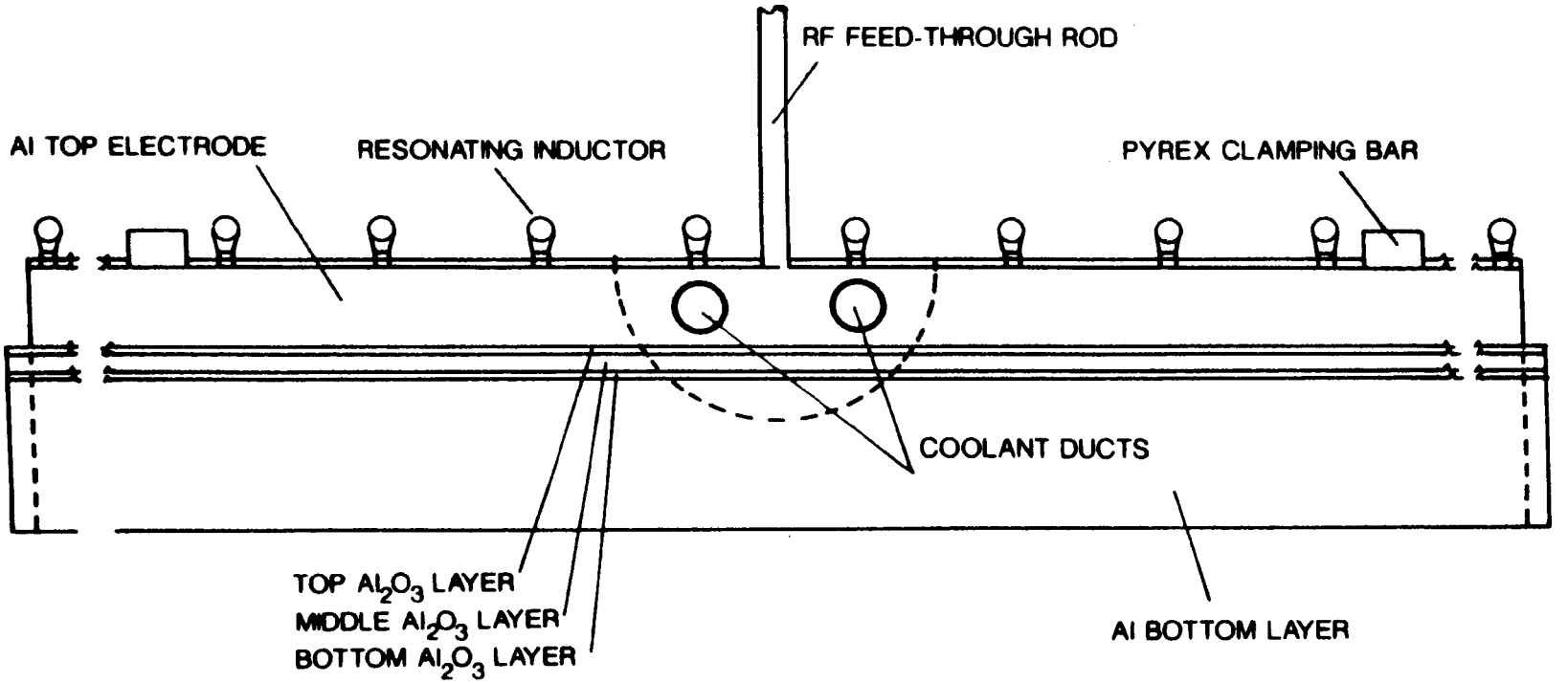

Fig. 4.4. (b) Waveguide and electrode assembly (side view).

predicted in Chapter 2. There was an inevitable trade-off between the fold-angle (width of ceramic) and the folding losses. To ease the dilema somewhat the maximum available polished ceramic length (at the time) of 386 mm was used, hence reducing the effective distributed loss by sharing the folding losses (and end mirror coupling losses) over a considerable guide length. The width of ceramic (approximately 6 cm in this case) was purposely kept to a minimum; firstly, so as not to undermine the advantages of the device size reduction provided by the folding geometry, and secondly, to permit excitation of the three discharge channels using a common electrode and single RF feed.

4.3 Radio Frequency Excitation Scheme

The top electrode dimensions were slightly less than the composite ceramic dimensions to give a tracking distance to the bottom electrode of over 2 1/3 times the electrode separation at its perimeter; thus greatly reducing the chance of a 'leak' discharge formation there. The passive (in the absence of a discharge) electrode capacitance (C) was estimated from the relation [69]),

$$C = \frac{\epsilon_0 \, \epsilon_r \, A}{d} \qquad (4.1)$$

where ϵ_0 is the free-space permittivity, ϵ_r is the relative permittivity of the ceramic, A is the mutual electrode area, and d their separation. For ϵ_r = 9.53 (manufacturers

specification at 70 MHz), A = (380 x 55)mm² and d = 4.25 mm this gives C = 415 pF. Here a homogeneous intra-electrode permittivity was assumed, and the contributions of the waveguide bore volume (which is approximately 1/15 th of the total volume) was neglected. Experimental verification was sought with a Wayne Kerr AC bridge and a Sencore test meter that gave measurements of 346 ± 20 pF (at 1.592 KHz) and 352 ± 50 pF respectively. The predicted and experimental values are in reasonable agreement, although their determinations were not performed at the 125 MHz or 145 MHz radio-frequencies and electrode voltage levels used for gas discharge excitation. Furthermore, the presence of a discharge (with a capacitance in series with the electrodes) will invariably decrease the total electrode capacitance. The expected weak frequency and voltage dependence [70] of the ceramic relative permittivity, and the relatively small discharge capacitance contributions [71,72], suggests that a value of C = 350 pF can be taken for the estimation purposes described below.

The mode of RF excitation employed was the parallel resonant distributed inductance excitation technique [54] mentioned in Chapter 1, and discussed further in Chapter 6. The advantages associated with this technique are essentially two fold; firstly, the longitudinal electrode voltage variations that arise because of the transmission-like (distributed reactance) properties of the electrode structure are greatly reduced, and hence conducive to a

uniform discharge. Secondly, the input impedance to the discharge assembly is often real and can be efficiently transformed using, for example π or LC network, to match the output impedance of the RF source for maximum power transfer. The parallel-resonant distributed inductance implementation was achieved with multiple discrete coils placed across the electrodes at equal intervals along their length (Figure 4.4). The inductance (L_i) required for the individual coil elements was calculated using the relation,

$$L_i = \frac{n}{C} \left(\frac{1}{2\pi f_{res}}\right)^2 \qquad (4.2)$$

where f_{res} is the desired operating frequency and n is the total number of coils. For C = 350 pF from above and f_{res} = 125 MHz, a combined inductance of 4.6 nH was required and provided by twenty coils. The number of coils is not completely arbitrary, but bound by a minimum that gives the acceptable voltage variance (because of the discrete and interval nature of the coils), and a maximum governed by the amount of power (possibly hazardous), dissipated in their ohmic components, that can be tolerated. The 92 nH coils were made from helically wound S.W.G. 20 bare copper wire; the coil diameter and the turn density needed to obtain the desired inductance was empirically determined using AC bridge measurements. The resonant frequency of the assembled structure (passive) was measured with an RF 'dip' meter, and subsequent coil adjustments made until the readings were within 0.5 MHz of 125 MHz.

The input impedance to the passive laser head was monitored by an RF network analyser (which comprised a sweep generator, 50 ohm VSWR auto-tester and oscilloscope) and transformed to near 50 ohms with an LC matching network [69]. Measurements of the voltage across the electrodes were made at low input power levels (a few mW) at the resonant frequency using an RF vector voltmeter. Longitudinal voltage variations of less than 5% were observed, mostly due to a slight potential drop at the coil sites.

An RF generator capable of providing power densities up to, say, 140 W/cm^3 was required for the power versus pressure characterisation of the z-fold laser. The total discharge (waveguide) volume was about 5.9 cm^3 and at these power densities would consume up to 800 W total RF power. Initial experiments were restricted to a maximum of 500 W RF power at 145 MHz. The 25 W output of an FDK (model multi-725x) 145 MHz amateur radio transmitter was split equally to drive two identical Dressler (model D2005) RF power amplifiers: their 250 W maximum outputs were recombined and applied (via an impedance matching network) to the centre of the top electrode. The splitting and combining functions were provided by Wilkinson networks [73] shown schematically in Figure 4.5. These consisted of two 75 ohm quarter wave coaxial cables, joined at one end and straddled by a 100 ohm load resistor at the other. To ensure efficient addition of the 250 W outputs, it was necessary to maintain equal power levels with a zero phase difference. In practice this was

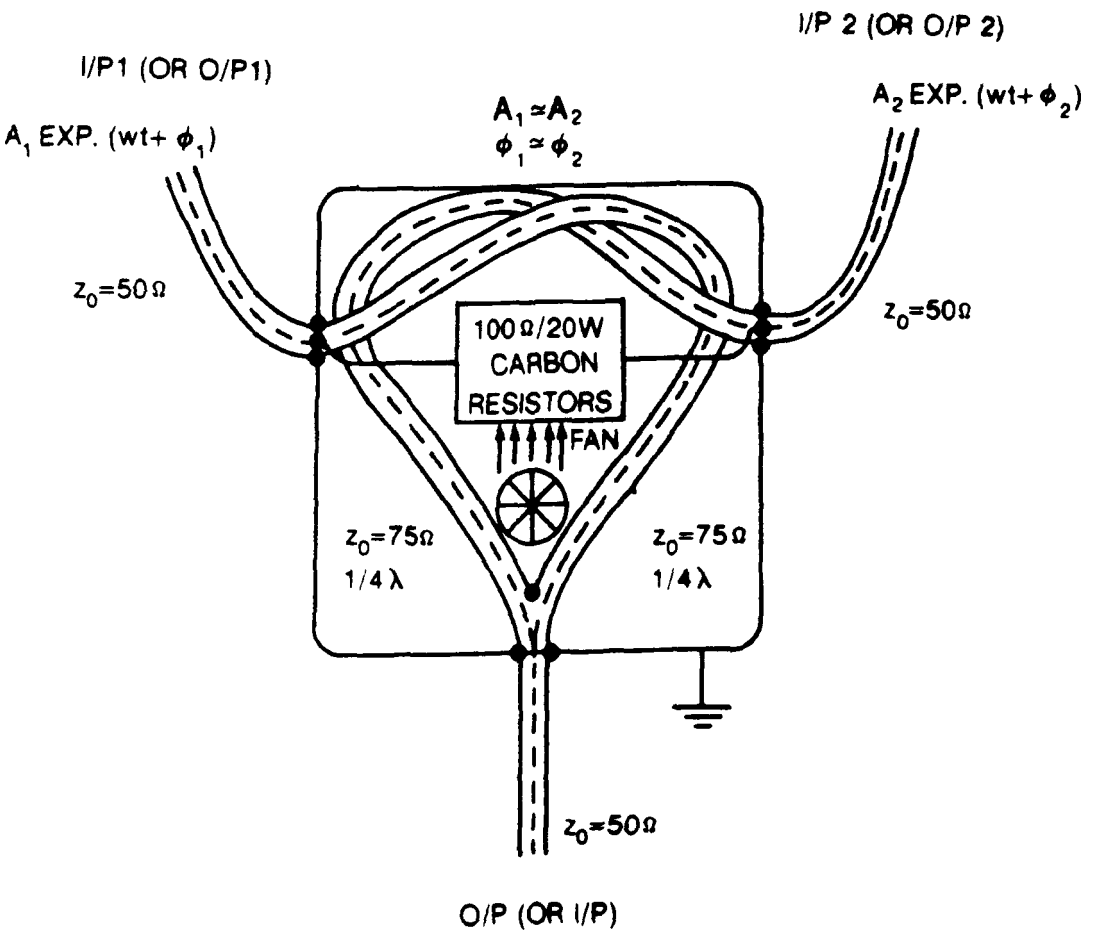

Figure 4.5. The Wilkinson network.

difficult to achieve with the resulting mis-match appearing as heat in the 100 ohm load.

An alternative RF power source was sought that could comfortably provide 800 W. This made-to-order Dressler 2 KW supply operated at 125 MHz and removed the earlier power restrictions. The previous 145 MHz operating frequency is often used for exciting waveguide lasers because of the availability of commercial 2 m band amateur radio supplies. There was a choice of frequency with the tailor-made supply, and this was made with the knowledge that the 125 MHz operation is reported to provide the optimum laser power extraction for a 2.25 mm bore [12]. It was necessary to screen the laser and its supply to minimise radio-frequency interference (RFI), which is capable of impeding diagnostic measurements (a problem addressed in Chapter 8). Leaking radiation could well frustrate radio communicators in the vicinity, an especially sensitive issue at 125 MHz which lies within the UK airborne military band. The safety recommendations [74], which require that a user be subjected to less than 1 mW/cm^2 of RF radiation, were adhered to (monitored by a Narda radiation monitor and probe).

4.4 Coolant Network

The power dissipated as heat in the discharge is equal to the net (forward minus reflected) RF input power minus the sum of the lost powers; these being the heat dissipated in the ohmic components of the impedance matching network

elements and the resonating coils, the radiated RF power, the incoherent light emissions and the laser output power. All but the latter dissipation were small when compared to the available RF power, and although laser efficiencies of up to 10% were observed, there were times when zero watts of laser power were extracted (during resonator mirror alignment measurements for example). Consequently, it was possible to have hundreds of watts of heat dissipated in 5.9 cm^3 of discharge.

The laser efficiency is, among other things, governed by the kinetics of the gas discharge, and in particular the population inversion mechanism. For the CO_2 laser transition, the emptying of the 10^00 lower laser level is via the 10^10 vibrational level. The thermal population of this level worsens the 'bottleneck' in the cascade to the ground state. In general this problem is alleviated by thermal diffusion cooling to the walls containing the discharge. The proximity of the discharge channels to one another in the z-fold laser was likely to overstretch the heat sinking capacity of the ceramic and electrode assemblies (the thermal conductivity of aluminium is $\sim$ 250 W/m/K, while that of alumina is approximately one order of magnitude less [70]). Consequently, a coolant network was introduced to assist the flow of heat away from the discharge volumes. This comprised two parallel water flowing ¼" bore circuits through the laser base and top electrode. Coolant temperatures of between 15 and 20°C were maintained during laser operation

with a tap water flow rate of approximately 1 l/s. The improvements in performance provided by the water cooling network are discussed in Chapter 5.

4.5 Laser Mirror Alignment Procedure

The resonator and folding mirrors were mounted in adjustable mounts. Initially, these were in-house made supports with three pivot points cushioned by disc springs and manually adjusted by tightening fine thread screws. Mirror tilts about either the x or y orthogonal axes could not be made independently or during laser operation. The alignment of the mirrors with respect to the waveguide axes was performed prior to laser operation on an optical alignment bench using two He-Ne lasers (discussed below). Later, the desire to be able to 'tweak' the mirrors during laser operation and observe the effects of finite folding mirror misalignments, led to several modifications. The folding mirror mounts were replaced by Newport (model FP-2) micro-positioning mounts with independent tilt controls and fine resolution, and vacuum tight feed-through stems were introduced to permit adjustment of any one of the four laser mirrors during laser operation.

The laser optics manufacturer specifications (at 10.6 μm) were as follows:-

Back mirror: 3/8" diameter plane germanium total reflector, 99.6% reflectivity

Plane folding mirrors:	1" diameter silicon total reflector, 99.6% reflectivity
Curved folding mirrors:	1" diameter 1.5 m radius of curvature silicon total reflector, 99.6% reflectivity
Input window: (amplifier only)	1" diameter plane zinc selenide window, 99.0% transmission
Output window:	1" diameter plane germanium window, 97.0% transmission

The plane and curved folding mirrors were coated in the same batch to ensure equal reflectivity, and hence permitted an uncluttered comparison of the coupling losses associated with their folding configurations (via laser output power measurements).

Although there were several variations in the laser mirror alignment procedure, the underlying technique can be summarised as follows:- The z-fold laser (without its mirrors or windows) was inserted half way between two opposing and collinear He-Ne lasers. The He-Ne laser pre-alignments were aided by the presence of pinhole cards placed immediately in front of their output windows and the centralisation of the Airy patterns on the pinholes in the opposing cards produced by their truncated Gaussian (TEM_{00}) outputs. Card separations of 3 m and pinhole diameters of 0.5 mm were typical. The passage of these laser beams through one of the waveguide segments of the z-fold laser

(usually the one terminated by the output coupler) produced modified Airy patterns with rectangular symmetry on the cards. Fine adjustments were made to the waveguide attitude while observing the patterns on the cards, until centralisation to and symmetry about the pinholes was achieved, thus ensuring collinearity.

The introduction and alignment of the laser mirrors was a sequential process; each mirror tilt was adjusted until the passage of its reflection through the next waveguide(s) gave the desired symmetrical output image. Evidently, the final mirror alignment (in this case the output mirror) could not be performed in this way. This problem was avoided by recording the incidence of the pre-aligned output mirror back relfection on one of the cards, removing the said mirror during the alignment of the remaining mirrors, and finally re-inserting it with the same tilt verified with a coincident back reflection.

Alignments performed in the way described above were conducted on many different occasions and considered reliable. It should be appreciated that the alignment errors for a z-fold laser mirror are passed on to next mirror in the alignment process (output mirror excluded). For this reason the mirror alignment adjustment controls were extended through the vacuum envelope wall to facilitate mirror 'tweaking' during laser operation to achieve maximum output power.

The back mirror was mounted on a PZT bimorph bender which allowed fine control of the resonator length, thus permitting the extraction of the laser output power fluctuations with length (the laser signature). The z-fold laser output power fluctuations induced by the cavity length variations arising through drifts in the temperature of the laser box (to which the laser resonator mirrors were attached), were large when compared to those typically observed with single segment lasers. This property is attributed to the amplification of the laser box length thermal drifts by a factor of three (in this case) or one plus the number of folds (in general). The large optical length associated with folded laser resonators, give rise to a small axial mode spacing (defined in Chapter 5, Section 2.4), calculated as approximately 120 MHz for the 124 cm z-fold laser cavity length; at pressure broadened waveguide laser linewidths this is conducive to single line operation but not necessarily a high frequency stable output.

CHAPTER 5

Z-FOLD LASER OPERATING CHARACTERISTICS

Summary

In this chapter the performance of the z-fold laser is assessed. In particular, a comparison is made between the operating characteristics of the laser for the plane and curved mirror, and partial waveguide folding geometries. This includes measurements of the laser output power as a function of discharge conditions and mirror alignment. Experimental determinations of the dependence of the laser power on tilt for the laser with plane fold mirrors are qualitatively compared to those predicted by a multi-mode resonator model. Finally, measurement of the laser powers when one, two and all three of its discharge segments are lit are incorporated into the simultaneous Rigrod solutions derived in Chapter 3, to evaluate the gain and resonator parameters.

5.1 Laser Diagnostics

The measurements performed during the experimental determinations described in this chapter can be split into two main categories: those involving measurements of the basic laser output parameters, and those involving measurements of the laser operating parameters. The basic laser parameters are the laser output power, mode profile and frequency (vibration line or beat signal). The (variable) laser operating parameters can themselves be split into two sub-categories, namely, the discharge and resonator related parameters. The discharge parameters are essentially the gas mixture and pressure, RF excitation frequency and power, and electrode voltage and coolant temperature. The resonator parameters are the cavity length and mirror tilt. More specialist measurements are described where necessary.

The z-fold laser output powers were measured with a calibrated thermopile (Coherent Model 201), which was enclosed in a screened box and battery operated to minimise radio-frequency interference (RFI). Full scale power readings of between 1 and 100 W with scale resolutions of 1 or 1·6 % (depending on the range selected) were possible, although in general a reasonably assumed ± 0.5 W error bar was assigned to each power reading. Cross-calibration checks with other thermopile meters were performed from time to time, especially to confirm absolute power readings (such as maximum output powers).

Laser beam profile measurements were conducted in several different ways:- observations of burn patterns on thermal paper or card or perspex, and heat patterns on liquid crystal paper, gave qualitative information for mode identification purposes. Continuous observations were possible by allowing the laser beam to strike the fluorescing surface of a thermal image plate (Optical Engineering Model 22-A). Two-dimensional beam intensity profile determinations were performed with a home-made 'transverse mode profiler' that comprised a spinning mirror, pinhole detector, and micro-computer interface combination (described elsewhere [75]). Once aligned, the transverse mode profiler could be used to take a rapid succession of profile measurements in a matter of seconds for instant viewing or signal averaging. Data collected in this way were recorded on micro-drives for later analysis, and/or sent to a plotter for permanent documentation.

The lasing vibrational line was identified with a CO_2 spectrum analyser (Optical Engineering Model 1ba). On some occasions the intermediate frequency (if) beat signal between two lasing waveguide modes was monitored with a fast photo-voltaic detector (SAT Model PV) and an RF spectrum analyser (Hewlett-Packard Model HP855B). Although the absolute intra-line laser wavelengths were not determined, the laser signature was obtained with cavity length adjustments with either the PZT bender bimorph holding the back mirror, or via thermal expansion induced by varying the

laser coolant pressure. Measurements with the latter technique were found to be more reproducible.

The routine mixing of gases was performed in a gas mixing chamber, consisting of a $\sim$ 2 litre manifold and fan, with multiple gas inlet ports. The helium, nitrogen, carbon dioxide and xenon gases used were all research grade. Prior to operation the laser and mixing chamber were evacuated by a rotary and diffusion pump combination. Vacuum pressures as low as 1×10^{-5} torr were readily obtained, athough occasionally, and particularly after a dormant period, it was necessary to pass hot water through the laser coolant network to accelerate the removal of accumulated outgassing products and condensed water. Any vacuum leaks apparent at this stage were located with a leak detector (Edwards Model LT205) and repaired.

The addition of the desired partial gas pressures to obtain the required laser mix was monitored with a precision absolute pressure gauge; a typical mixture was 30 torr Xe + 120 torr CO_2 + 120 torr N_2 + 360 torr He, or $3He:1N_2:1CO_2$ + 5% Xe. The gas pressure in the laser vessel was monitored with a digital differential pressure gauge with a resolution of 0.1 torr. The gas pressure during laser operation would always increase slightly owing to gas heating and dissociation.

The RF forward and reflected power measurements were performed with an in-line bi-directional power meter (Bird 'thru-line' Model 4431). The net RF power, or the power

dissipated, was given by the difference reading. Reflected power levels of only a few watts were readily obtained by careful tuning of the impedance matching network. Occasionally, during laser operation over a wide range of RF power levels, it was necessary to retune the RF generator for maximum power transfer or to minimise its 'main hum' component. Precise frequency measurements were made with an RF frequency counter (Black Star Model Meteor 600).

During laser operation it was common to 'tweak' the laser mirror alignments to obtain the maximum output power. This was an iterative process of going from mirror to mirror until it was judged that no further improvements were possible. These mirror adjustments were very slight, typically less than one milliradian (optical tilt), and considered necessary because of the inevitable residual errors incurred during the pre-alignment process described in Chapter 4. The alignment of the folding mirrors was controlled by micrometre adjusting rods; four of the twenty-five micrometre divisions per unit gave approximately one milliradian tilt. There were two micrometres per folding mirror, for 'nearly' independent rotation about the X and Y-axis.

5.2 Experimental Results

5.2.1 Longitudinal Electrode Voltage Variation

As already mentioned in Chapter 4, the mode of RF excitation used throughout the experimental investigations

was that of the parallel resonant distributed inductance excitation technique [54]. Measurements of the voltage across the electrodes at various points along their length were performed in the absence of a discharge, with a few milliwatts of RF power delivered via an LC impedance matching network. The voltage measurements were carried out using a vector voltmeter (Hewlett-Packard Model 8405A: a two channel sampling RF millivoltmeter-phasemeter) which measured the voltage of two RF signals and simultaneously displayed the phase-angle between them. Probe A (the automatic phase control lock input) was fixed across the electrodes at the centre feed-point. Probe B (the mobile probe) was moved in turn to each of the measurement points. The voltage amplitude and relative phase measurements were extremely sensitive to movements of the probe leads and the pressure of the tip of probe B on the top electrode surface. To minimise the 'jitter' that accompanied the measurements the probe leads were taped down to the test bench; nevertheless the relative phase determinations were too sensitive to even the slightest probe movements and were consequently abandoned. The voltage amplitude measurements, on the other hand, were reasonably reproducible.

The average of several sets of electrode longitudinal voltage variation measurements is presented in Figure 5.1 for the resonant excitation frequency of 145 MHz. As can be seen, the maximum voltage deviations from the mean are only a few percent. The active (i.e. in the presence of a

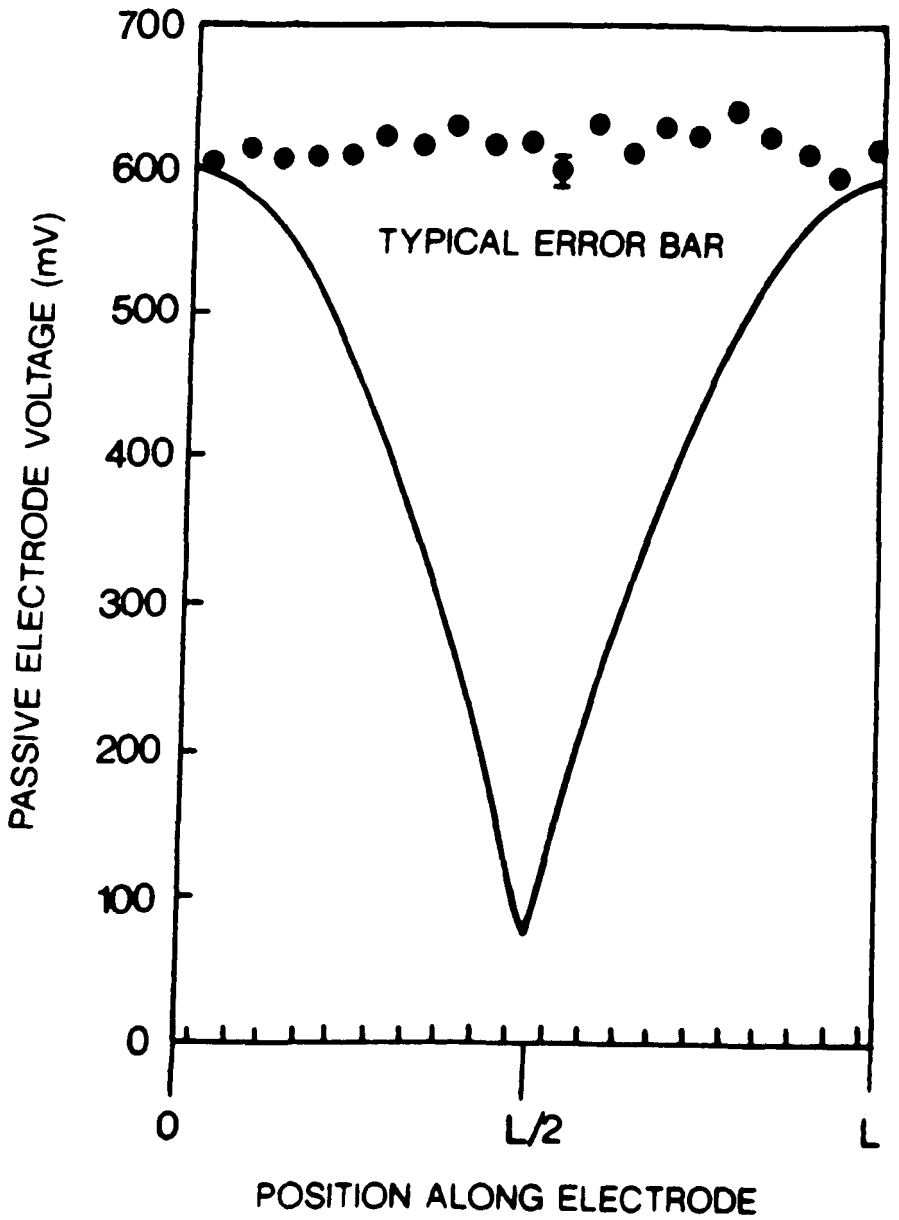

Figure 5.1. Electrode longitudinal voltage variations. The circles are experimental data points for parallel resonant distributed inductance excitation at 145 MHz (centre feeding). The solid line is the predicted voltage variation for the open electrode configuration (no inductors).

discharge) voltage variations were expected to resemble the trend observed for the passive case [29,76], and hence be conducive to a uniform discharge,. The solid line in Figure 5.1 represents the predicted voltage variations for the open electrode configuration (no distributed coils). The voltage deviations arise from the transmission-like properties of the electrode structure, approximately described by a cosine function [28], viz:-

$$V(x) = V_e \cos(\beta x) \qquad (5.1)$$

where V_e is the voltage at the open end ($x = 0$) and β is the phase constant given by

$$\beta = 2\pi f\sqrt{LC} \qquad (5.2)$$

where L, C and f are the lumped electrode mutual inductance and capacitance, and the operating frequency, respectively. For the measured values L = 200 nH and C = 350 pF and f = 145 MHz, equation (5.2) gives $\beta = 7.6/m$.

The open electrode voltage variation predictions (solid line in Figure 5.1) indicate deviations of almost 100%. A discharge sustained by a voltage varying as this one does would have a non-uniform RF power density distribution and hence 'hot' and 'cold' discharge regions associated with an inefficient laser pumping system.

5.2.2 Laser Output Power

In this section measurements of the well-aligned Z-fold laser output power as a function of RF excitation power and gas pressure are presented. In particular, comparisons are made between the power characteristics of the Z-fold laser for the plane, curved and partial waveguide folding geometries.

Prior to the modifications to the laser design (described in Chapter 4), namely, the introduction of externally adjustable mirror mounts and a water cooled top electrode, the maximum laser power recorded was 14.0 W at 3.3% efficiency (laser output power/net RF input power). Figure 5.2 shows the power characteristics of the Z-fold laser with plane folding mirrors, for a range of RF input powers at 145 MHz and pressures of the $3He:1N_2:1CO_2$ gas mixture. The power readings all corresponded to an output on the P20 rotational line and a single dot beam profile.

The power characteristics of the modified Z-fold laser with plane, curved and partial waveguide folding mirrors are presented in Figures 5.3, 5.4 and 5.5 showing peak powers of 30.0, 34.5 and 53.4 W, respectively. For these measurements the laser operated with a single-dot output beam profile on line P20 with a $3He:1N_2:1CO_2$ + 5% Xe gas mixture excited by RF power at 125 MHz. The plane and curved folding mirrors used in each case were supplied by the manufacturer with identical dielectric high reflectivity coatings (same batch), thus permitting a direct comparison between the folding geometries.

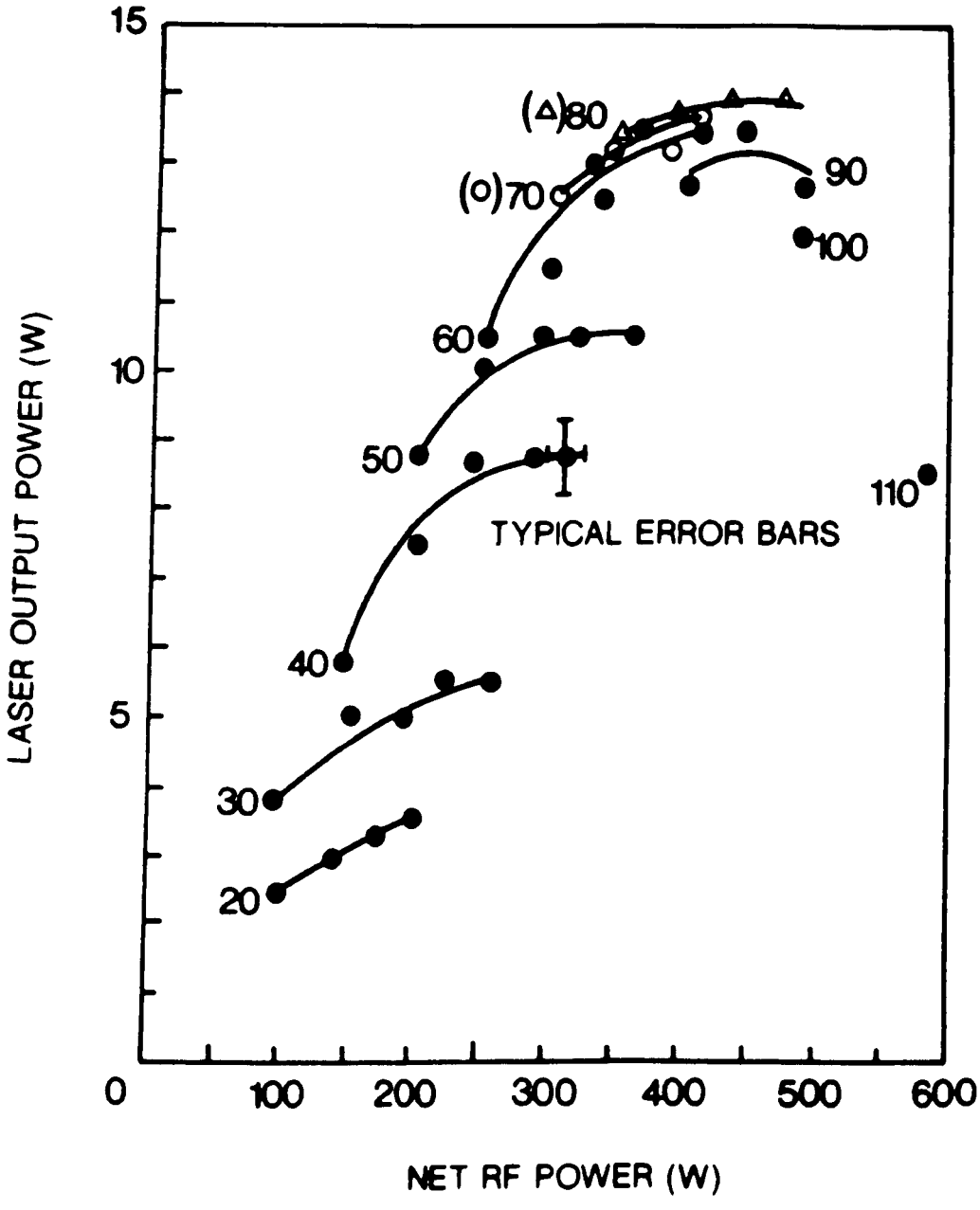

Figure 5.2. Plane mirror z-fold laser (pre-modification) input/output power characteristics for discharges in a $^3He:1N_2:1CO_2$ gas mixture at pressures between 20 and 110 torr, and rf-excited at 145 MHz.

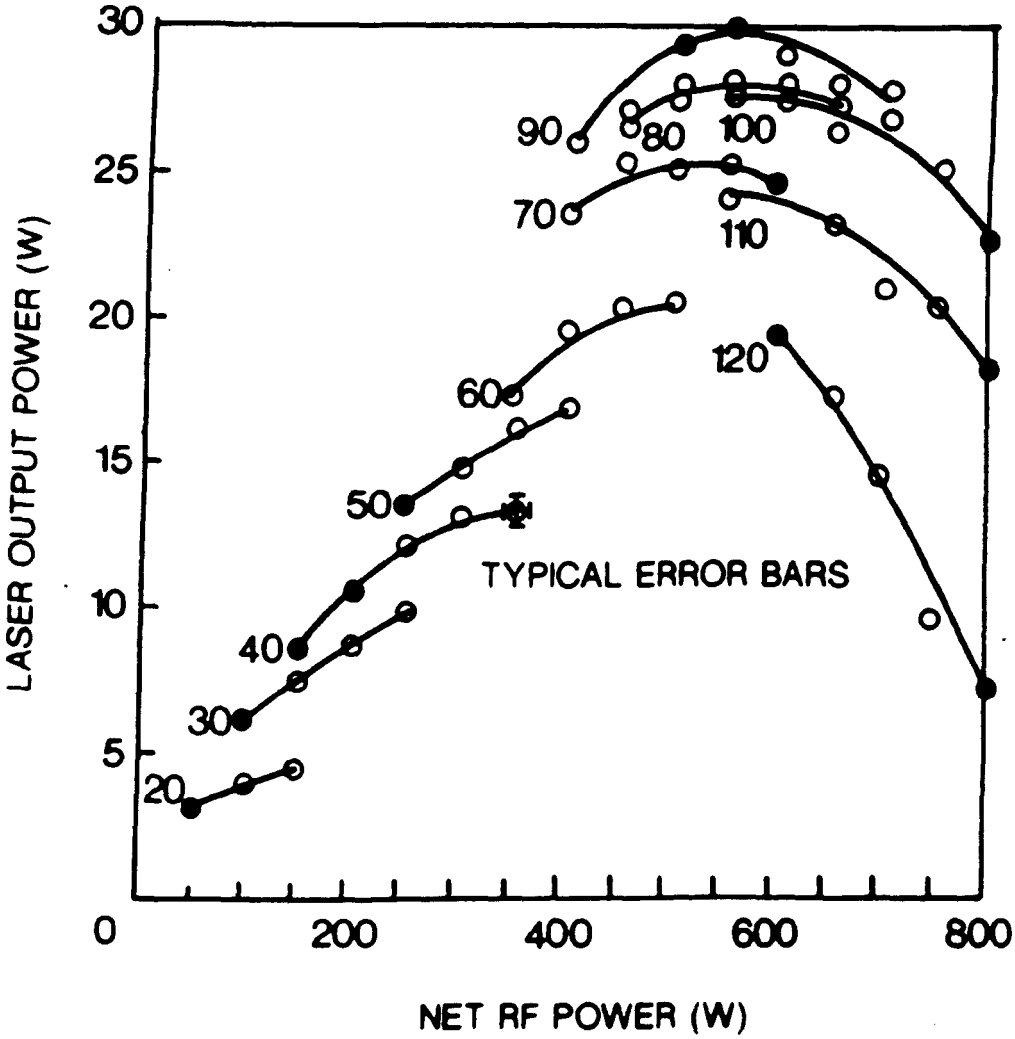

Figure 5.3. Plane mirror z-fold laser (post-modification) input/output characteristics for discharges in a $3He:1N_2:1CO_2$ + 5% Xe gas mixture at pressures between 20 and 120 torr, and rf-excited at 125 MHz.

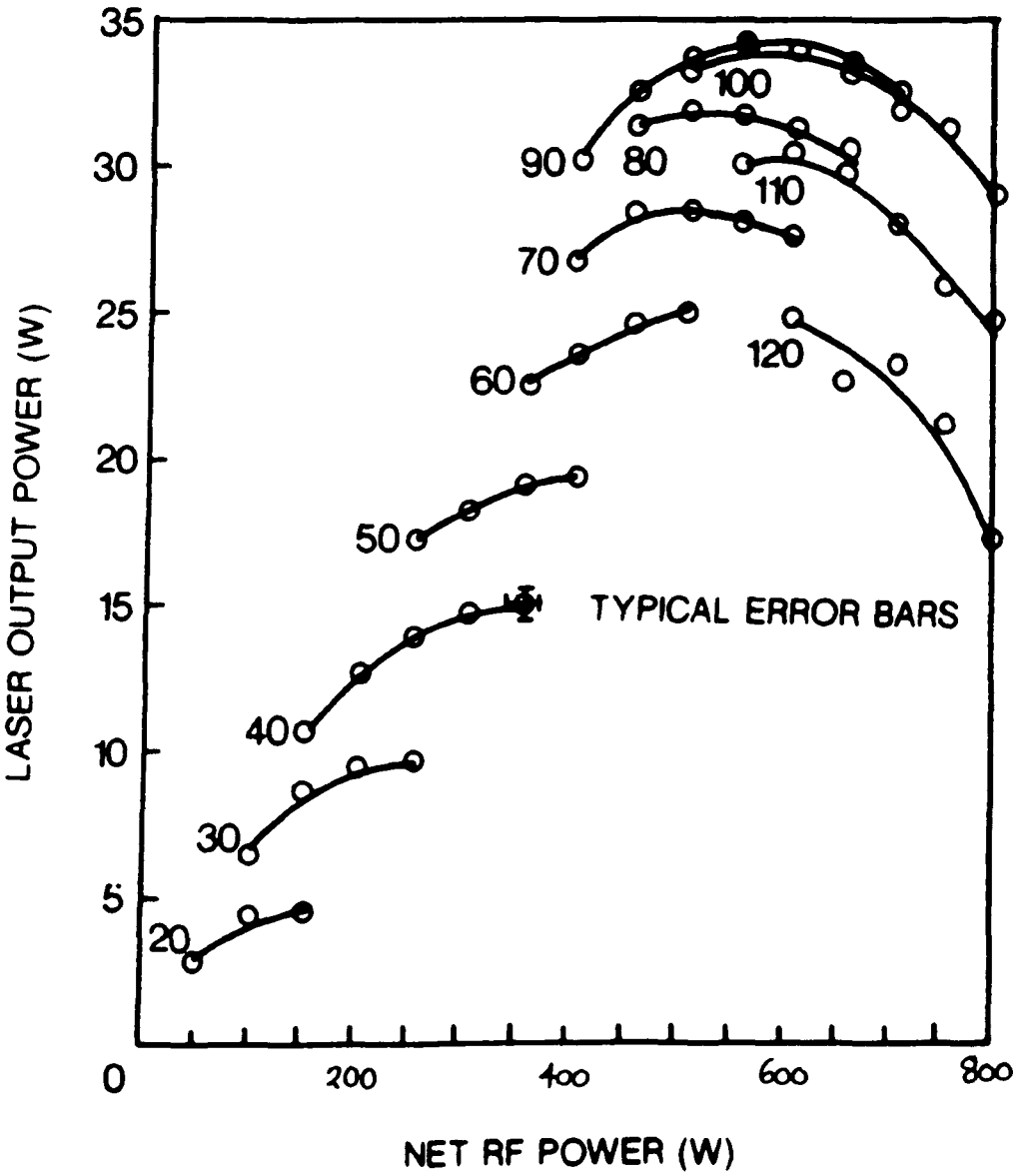

Figure 5.4. Curved mirror z-fold laser input/output power characteristics for discharges in a $3He:1N_2:1CO_2$ + 5% Xe gas mixture at pressures between 20 and 120 torr, and rf-excited at 125 MHz.

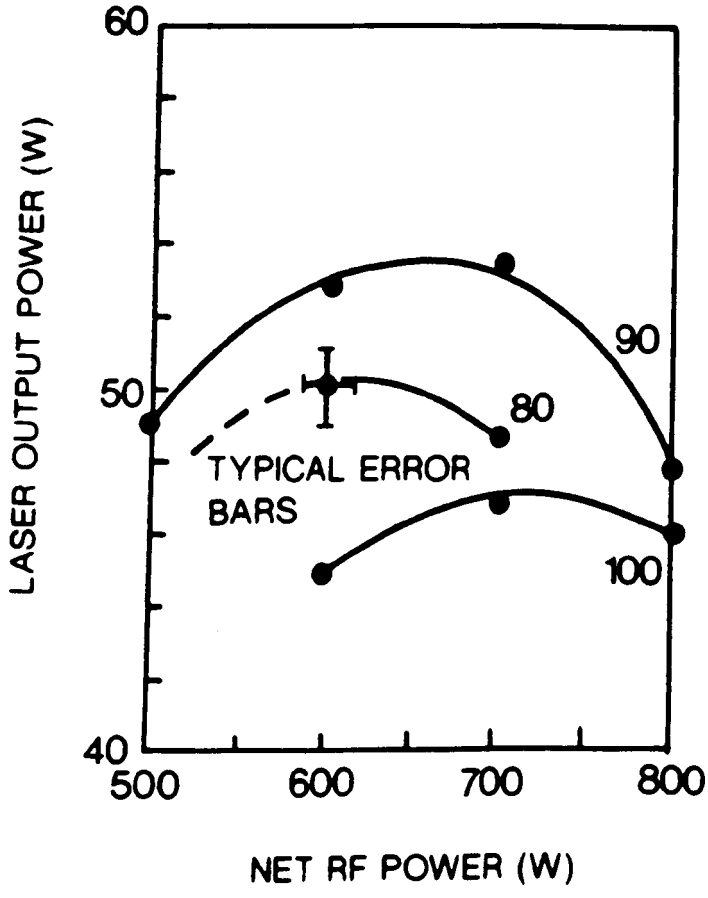

Figure 5.5. Partial waveguide z-fold laser input/output power characteristics for discharges in a $^3He:1N_2:1CO_2$ + 5% Xe gas mixture at pressures between 80 and 100 torr, and rf-excited at 125 MHz.

The 16 W increase in power for the plane folding mirror geometries (i.e. from 14 W to 30 W), is mostly attributed to the introduction of the resonator mirror alignment external controls and their adjustment during laser operation; although the comparison is cluttered by the many simultaneous modifications. An independent study of the dependence of the laser output power on folding mirror mis-alignment is presented in section 5.2.5. The power gain that arises through the extension of the water cooling network to the top electrode is assessed in section 5.2.4, while the boost in laser output power provided by the xenon gas additive is well documented (see for example ref. 36) and is typically 15-25%.

Figures 5.6 and 5.7 show comparisons of the laser power and efficiency performances of the three (post-modification) folding geometries. As expected, both the laser power and efficiency curves show a peak against gas pressure, in these cases around 90 and 70 torr, respectively. The enhancements in output power and efficiency provided by the curved and partial waveguide folding geometries were as high as 5 W and 1%, and 25 W and 4%, respectively. A summary of the laser performances for the various folding gemetries is presented in Table 5.1.

5.2.3 Laser Beam Profiles

The signal-averaged transverse intensity profiles of the well-aligned Z-fold laser beams under conditions giving the maximum output power, for the plane and curved mirror folding

Folding Geometry	Maximum Power (W)	Fold mirror tilt width at half max. power (mrad)	
		X	Y
Plane Mirror	30.0	5 $^{1}/_{3}$	3 $^{2}/_{3}$
Curved Mirror	34.5	6 $^{2}/_{3}$	6 $^{1}/_{3}$
Partial Waveguide	53.4	13 $^{1}/_{3}$	10

Table 5.1. Comparison of the z-fold laser maximum output powers observed with the three folding geometries, and the tolerance to angular misalignment of one of the folding mirrors.

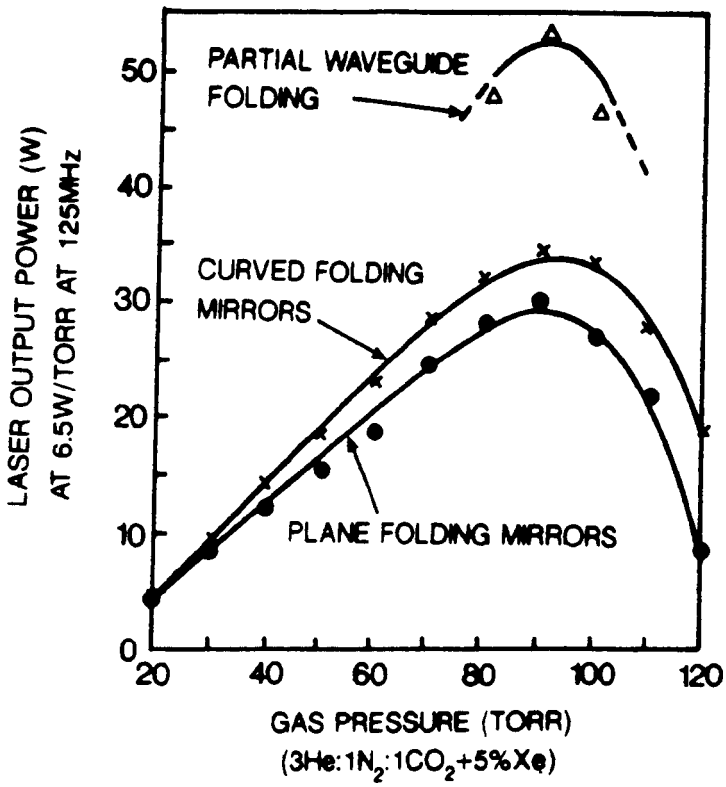

Figure 5.6. Comparison of the z-fold laser output powers for the three folding geometries.

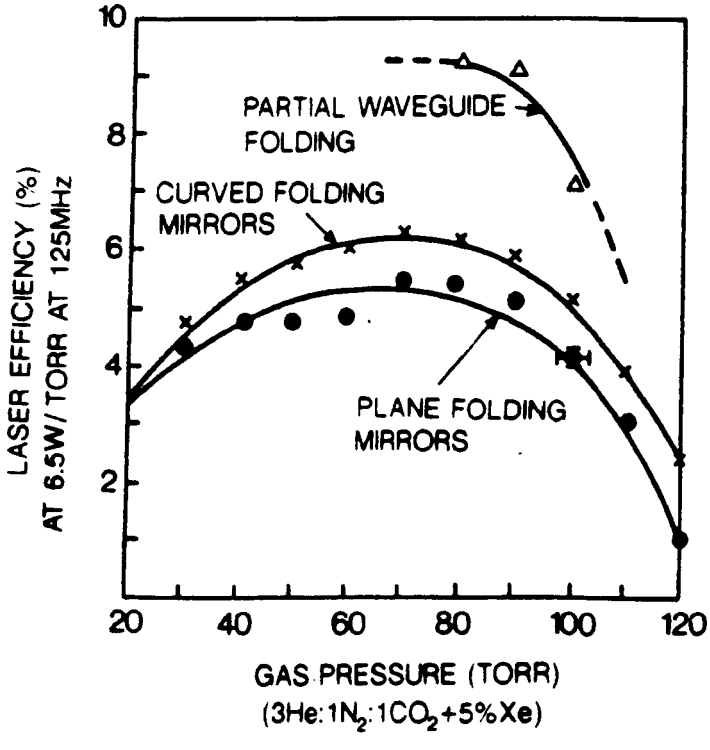

Figure 5.7. Comparison of the z-fold laser efficiencies (laser power/ rf power) for the three folding geometries.

geometries, are shown in Figures 5.8(a and b) respectively. As can be seen, the laser output beam profiles seem quasi-Gaussian. The 'transverse beam profiler' detector was placed at a distance of 2 m from the plane of the laser output coupler, with the same sensitivity and resolution settings in each case. Evidently, the diameters of the laser beams are different; this is seen more clearly in Figure 5.9, where Gaussian fits to the through-the-diameter line profiles are shown. There was no reason to expect that the laser beam profiles would be the same considering that the resonator configurations, and more specifically the folding geometries, were different in each case; as would be the resonator mode contents. The Gaussian fit beam diameter to the plane folding mirror geoemtry was 131% larger than that for the curved mirror geometry.

At the time it was not convenient to measure the transverse intensity profile of the Z-fold laser with partial waveguide folding in the same manner described above. Burn pattern profile evaluations at maximum laser output power did, however, reveal a single-dot output mode pattern almost, but not quite, as symmetric as those observed with the other folding geometries.

Although there are many scientiic and medical applications that require high raw laser output powers, they nearly always also require an accompanying 'good' laser mode quality. For example, beam delivery applications for material processing generally involve the focussing of a

(a)

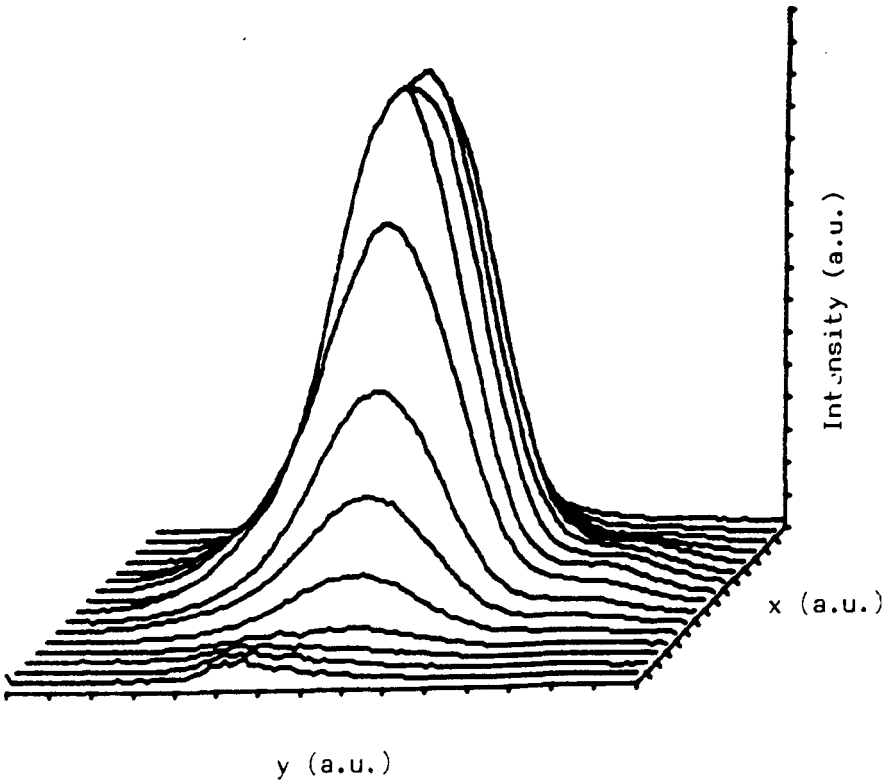

(b)

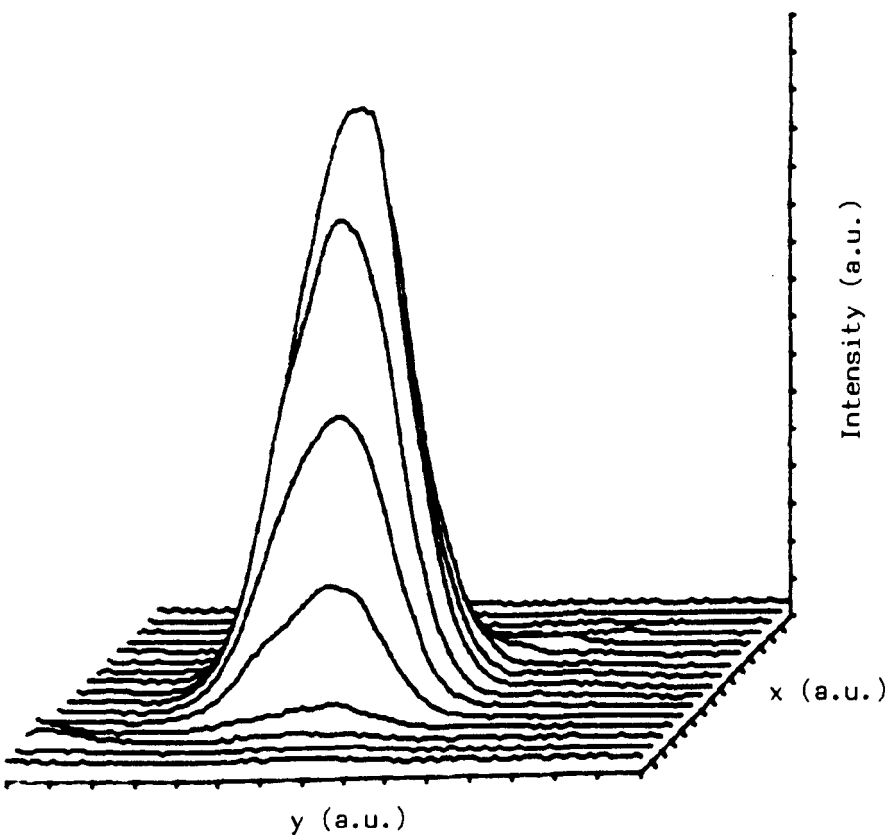

Figure 5.8. z-fold laser output mode profile at maximum power for the plane mirror (a) and curved mirror (b) folded resonator configurations.

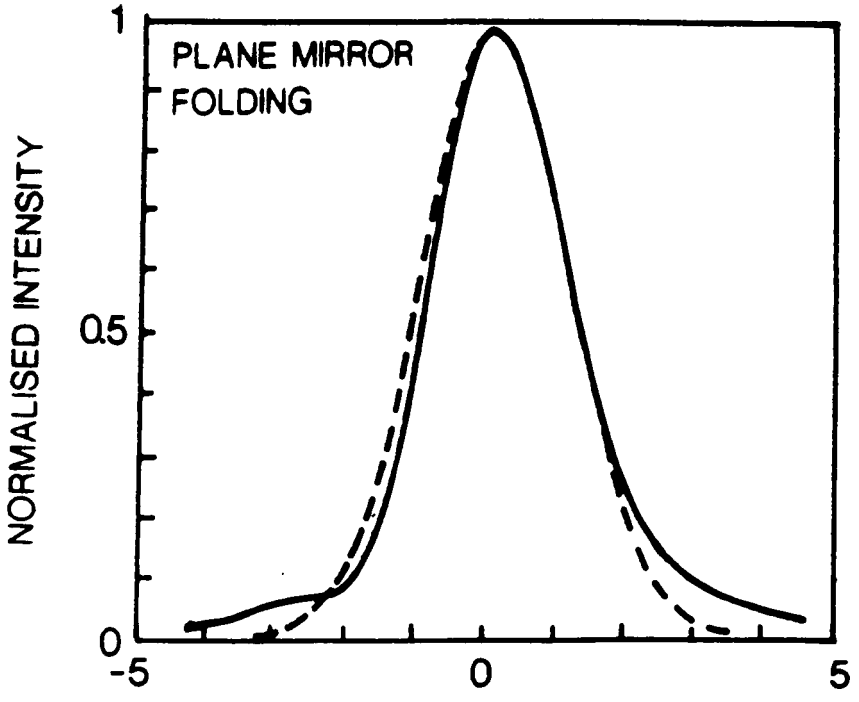

(a)

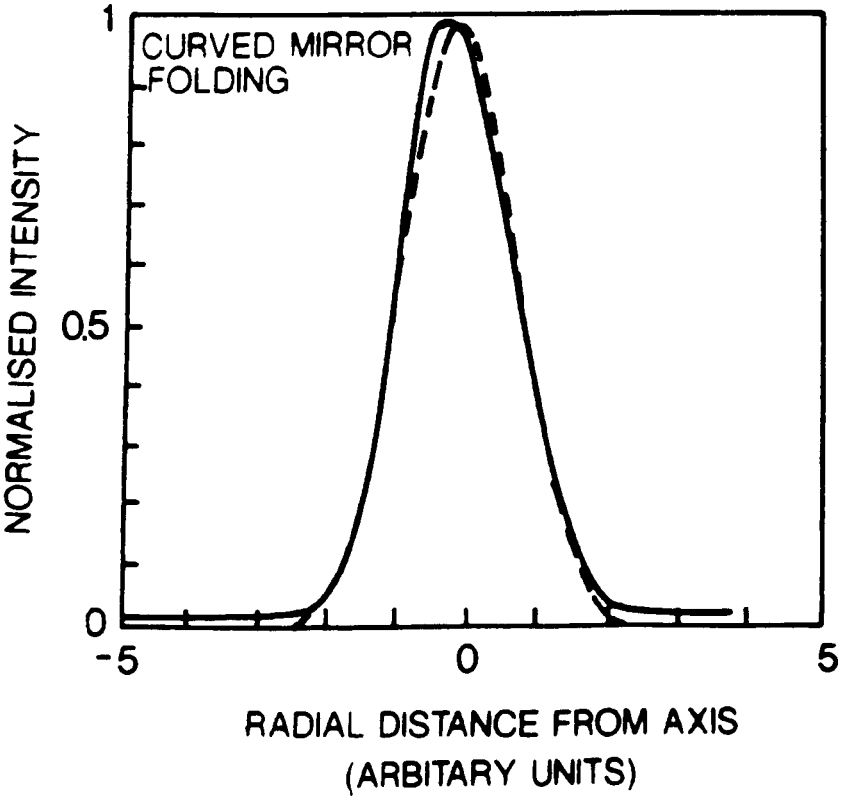

(b)

Figure 5.9. Gaussian fits to the through-the-diameter line profiles of the z-fold laser output modes (shown in Figure 5.8) produced with the plane mirror (a) and curved mirror (b) folded resonator configurations.

laser beam to a 'tight' spot, the minimum diameter of which is limited by diffraction effects; a focussed laser beam with a high-order mode content will produce an undesirable irregular and oversized spot. LIDAR applications involving transmitted laser beams often require highly directional and high on-axis intensity far-field laser patterns; these conditions are generally satisfied by well controlled laser transmitter sources exhibiting outputs with only the simplest (lowest order) transverse mode.

5.2.4 Laser Signature

There are at least two frequency selective elements in every CO_2 laser, the laser medium which exhibits gain over a 'comb' structure of vibrational-rotational bands, and the optical cavity which exhibits high Q axial modes at integer multiples of c/2L (free-spectral range); where c is the phase velocity of light in the optical medium and L is the length of the optical resonator. In general, several resonator mode frequencies lie within the range of laser medium frequencies for which optical gain exceeds optical loss and the laser can oscillate.

A waveguide laser resonator possesses a set of transverse modes, and for those lasers with a quasi-Gaussian output beam these range from the lowest-order lowest-loss EH_{11} mode, upwards through higher-order higher-loss modes. The same set of transverse modes is associated with each axial mode of the laser. For a square bore dual-Case I

waveguide laser the complete set of resonator mode frequencies is adequately described by the relation [77].

$$\nu_{q,mn} = \frac{qc}{2L} + \frac{c\lambda}{32a^2}\,(m^2 + n^2) \qquad (5.3)$$

where q is the axial mode number (a positive integer typically of the order of 10^5), λ is the optical wavelength, a is the guide half-width, and m and n are the transverse mode numbers (positive integers typically between 1 and 5). For an ideal homogeneously broadened laser only the mode with above threshold gain and the highest gain-to-loss ratio will lase.

Several points are in order here; equation (5.3) only applies to waveguide lasers with a resonator mode comprised predominantly of the EH_{11} waveguide mode. The resonator field is given by

$\sum_{mn} a_{mn} E_{mn}(x,y)$, where a_{mn} is the amplitude of EH_{mn} (a complex number), and $EH_{mn}(x,y)$ are the fields of the EH_{mn} modes. The field of the lowest-loss resonator mode is given by this coherent sum of amplitudes; its associated round-trip loss can be much lower (or higher) than the pure EH_{11} loss. It is the phases of the a_{mn} that greatly determine the resonator mode and its loss (more so than the waveguide attenuation terms); consequently, a resonator with a considerable unguided path (such as the Z-fold laser) may have a mode with significant non-EH_{11} content, in which case

the resonator mode frequencies are less easily determined. The fact that a resonator mode is not quasi EH_{11} does not imply that the laser output is not quasi-TEM_{00}: this was apparent in the previous section where the output beams of the z-fold laser for the plane and curved mirror folding geometries were both 'good' Gaussians but with different waist values; evidently, the mode compositions were different, which implies there must have been significant non-EH_{11} content. Despite these complications and apparent invalidation, the use of equation (5.3) can be justified inasfar as the different frequencies of the resonator modes and their functional dependences on wavelength and cavity length, etc. are likely to be intact, so that the inference that follows is reasonable.

Figure 5.10 shows the resonator mode spectra (up to EH_{13}) calculated using equation (5.3), for the 124 cm long z-fold square bore (1.125 mm) waveguide laser resonator. The rotational lines chosen are those in the R and P branches of the 00°1-02°0 and 00°1-10°0 CO_2 vibrational bands offering the highest gains (Figure 5.11). Evidently, there are several bunches of overlaced resonator modes lying under the Lorentzian (pressure broadened) gain profile: a 480 MHz linewidth (corresponding to a $\sim$ 90-100 torr laser gas mixture pressure) was assumed throughout. The inter- and intra-bunch spacings are wavelength dependent, as are their relative detuned (from line centre) frequencies. As the length of the z-fold laser resonator changes, either by deliberately

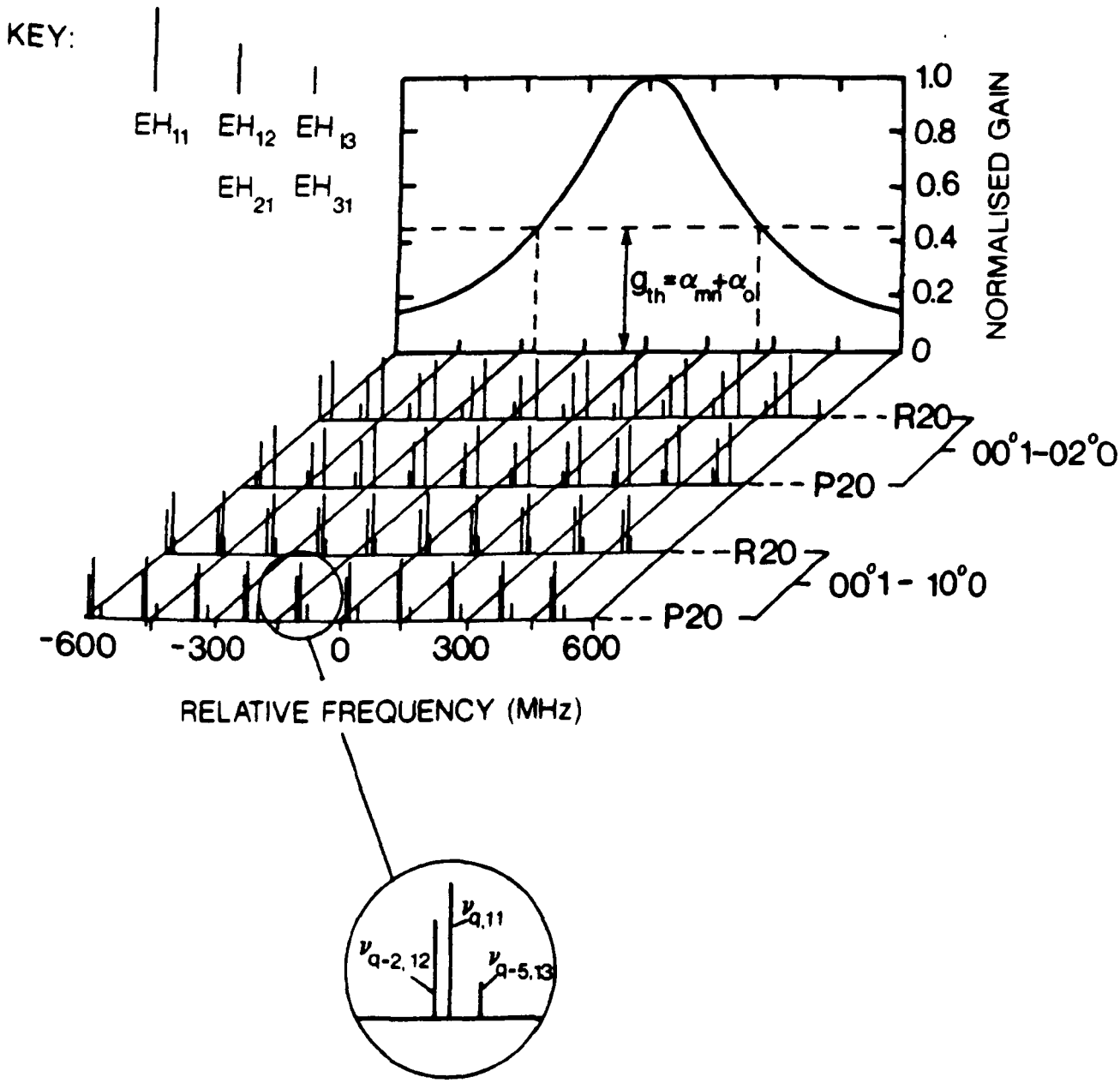

Figure 5.10. Plane mirror z-fold laser resonator mode spectra for various CO_2 rotational line wavelengths.

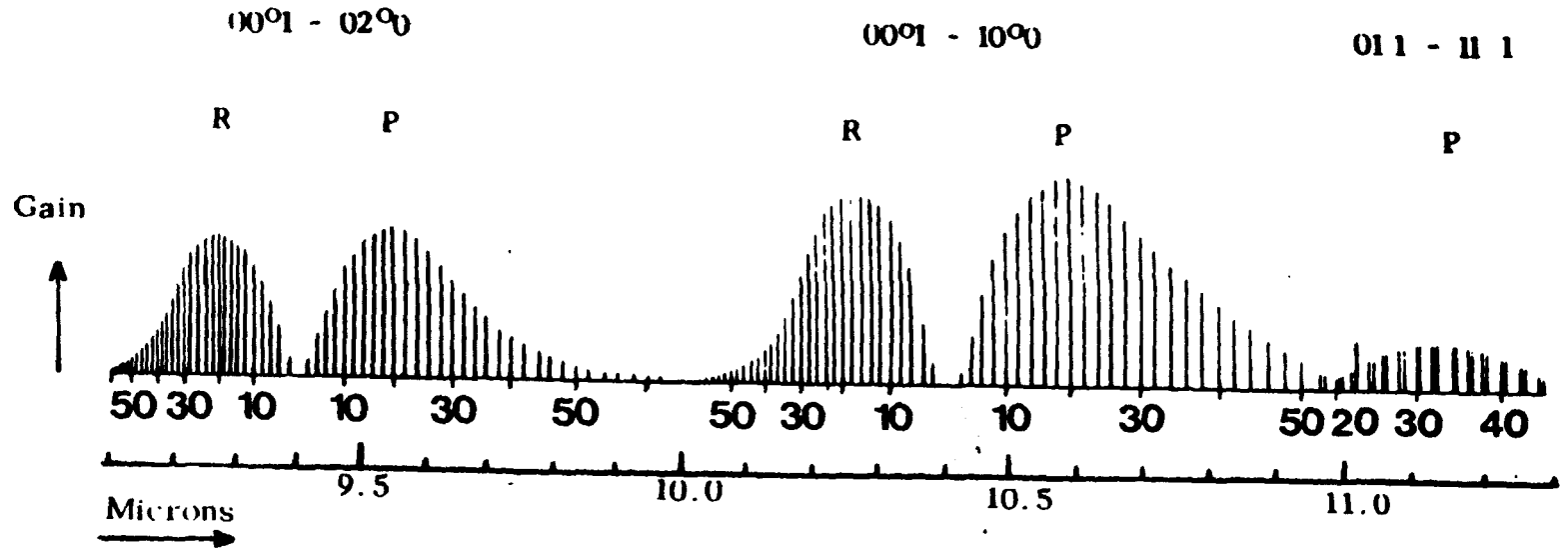

Figure 5.11. CO_2 laser gain curve.

applying a voltage to the PZT bimorph holding the back mirror or through thermal drift, the entire set of modes is shifted along the frequency axis at a rate of one free spectral range (in this case ∿ 120 MHz) per half-wavelength change in L. Thus as the resonator length is varied the lasing mode 'sweeps' over the gain region presenting varying power at the laser output (the laser signature). Throughout the laser signature the original lasing mode might be replaced by another mode (mode-hopping) with a higher gain-to-loss ratio, perhaps one falling under a different rotational line (line-hopping), or one nearer line centre. There may even be spates of no-lasing if none of the modes experience gain above the threshold for laser oscillation. Hence, throughout the laser signature the laser output may change transverse mode or line or fall to zero power.

The repeated z-fold (plane mirror) laser signature produced through thermal drifts in the resonator length (by three times the laser box length variations) and induced by deliberately isolating sections of the cooling network, is presented in Figure 5.12. Throughout the observation the laser did not change from the P20 (10.59 μm) line nor was there a discernible change in its quasi-Gaussian output beam transverse profie. This laser signature, although possibly uninteresting, is identified with a well-behaved single-line, single-transverse-mode laser operation; a performance often required by users and applications. The laser was only encouraged to transverse-mode-hop and

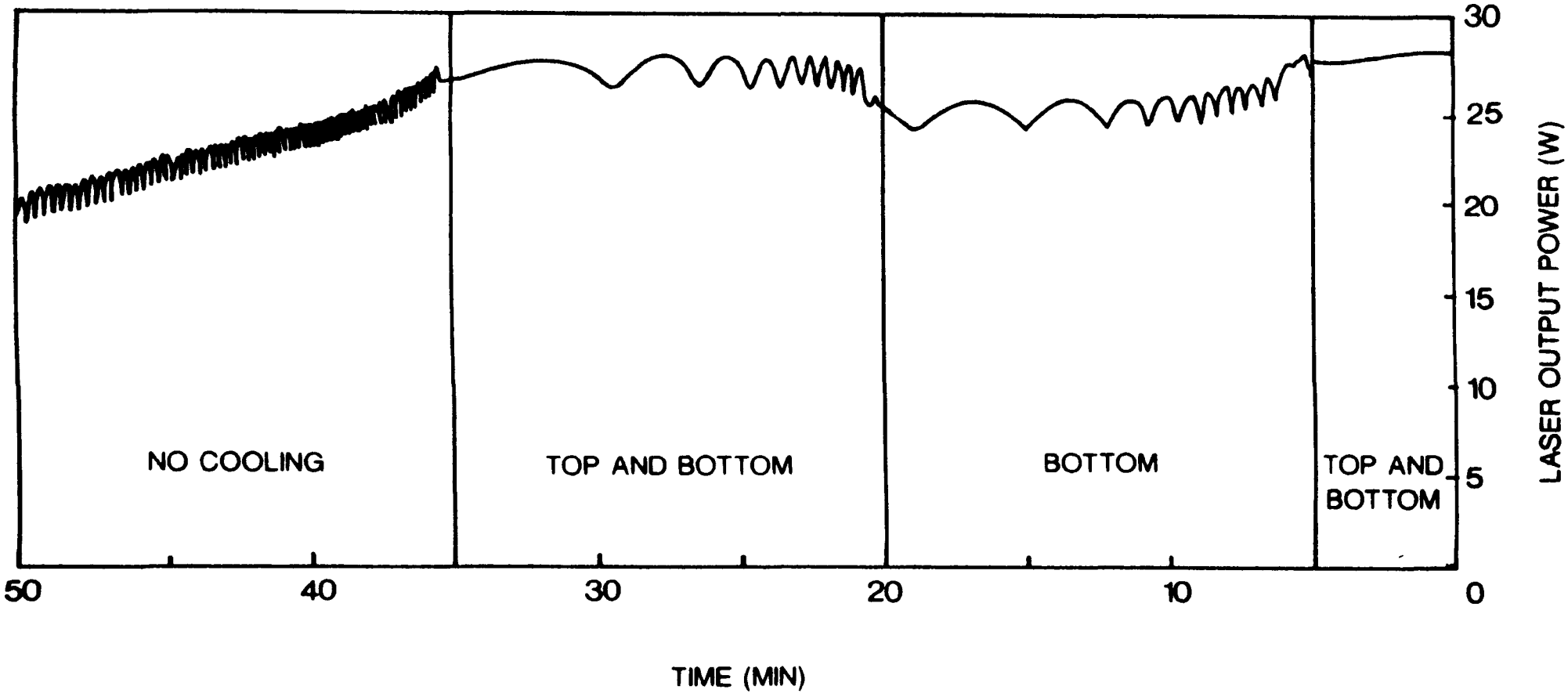

Figure 5.12. Plane mirror z-fold laser signature produced through thermal drifts in the resonator length and induced by deliberately isolating sections of the RF electrode coolant network.

line-hop by severely mis-aligning its folding mirrors: a topic addressed in the next section.

The z-fold laser single-line operation is most easily explained by the small axial mode spacing that results from its considerable resonator length; that is, by assuming that the minimum gain-to-loss ratio experienced by a mode under the P20 gain profile, which probably coincided with the minimum gain at $\sim$ 60 MHz (half the free-spectral range) frequency off-set from line centre, was always greater than that associated with any of the modes under the remaining rotational lines.

The single-transverse mode operation suggests that there was a one-sided competition between the modes under the P20 gain profile: one dominated by the $EH_{q,11}$ mode. The P20 mode spectrum in Figure 5.12, shows the almost coincident frequencies, differing only by 4.2 MHz, of the $EH_{q,11}$ and the $EH_{q,12}$ modes. Hence, considering that the z-fold laser waveguiding losses and coupling losses discriminate against higher order modes, the lower loss EH_{11} mode, with gain and all other things bar loss being equal, must be preferred. The design of a class of waveguide lasers with an inherent modal frequency coincidence as a means of improving mode purity was formally suggested in [59] some time after the construction of the z-fold laser, and in this case the conditions supporting mode discrimination were satisfied inadvertently. For a square bore dual-Case I waveguide laser the condition for discrimination against the higher-loss

mode $EH_{m'n'}$ in favour of the lower-loss mode EH_{mn} is

$$L = 165\ a^2/\lambda\Delta \qquad s = 1,2,3\ \ldots \qquad (5.4$$

where $\Delta = m^2 - m'^2 + n^2 - n'^2$. The condition may vary a little for lasers containing considerable free-space propagation, or mis-aligned mirrors. Although there is every reason to suggest that by careful design, modal coincidence as a means of improving mode purity can be achieved in all but a few waveguide laser resonators.

The dependence of the plane folding mirror laser output power on changes in the coolant paths, shown in Figure 5.12, indicates a drop in the steady-state maximum power of ∿ 5 W and ∿ 10 W over a 15 minute period induced by the isolation of the top electrode, and the top and bottom electrode cooling networks, respectively. The laser was not deprived of its water cooling for too long for fear of permanent damage caused by hot gas interaction with the Case I mirrors, or by rupturing of the coolant pipe vacuum seals in the top electrode. The 'worst case' power stability associated with the 'steady-state' maximum laser power produced by thermal drift over one free-spectral range, was ± 0.75 W in 30 W, or 1 part in 20; although power stabilities of 1 part in 100 over time periods of a few minutes were observed.

5.2.5 Laser Folding Mirror Tilt Experiment

The single-line and single-transverse mode operation observed with the well-aligned z-fold laser would not be

expected to persist if one or both of the folding mirrors were mis-aligned by introducing a finite tilt about either or both of the X and Y axes. On the contrary, if the second lowest-loss resonator mode suddenly becomes the lowest-loss mode with the highest gain-to-loss ratio, then one might expect to observe line-hopping, or transverse-mode hopping, or both. At the cross-over point, there may be mode beating or multi-line operation. The major resonator mode discrimination is provided by the folding mirror coupling coefficient matrices, which for the well-aligned laser strongly favours the quasi-Gaussian EH_{11} mode.

In this section observations of the deviations of the z-fold laser power from the well-aligned power are presented for the cases where a controlled and measurable mis-alignment had been introduced to one of the folding mirrors associated with the plane, curved and partial waveguide folding geometries. To simplify the interpretation of the results the single folding mirror was independently tilted about either the X or Y axis. The X- and Y-tilts refer to tilts about the vertical and horizontal axes; and the optical tilt is twice the mirror tilt, in this case continuously adjustable with a micrometre resolution corresponding to $\sim$ 1/3 of a milliradian. Also included in this section are some preliminary computer predictions of the resonator mode losses as a function of tilt for the z-fold laser with mis-aligned plane folding mirrors, derived from a theoretical resonator model [78]. The author does not claim to be able

to predict the precise behaviour of the mis-aligned laser; there is, however, qualitative agreement between the theoretical predictions and the experimental results.

Figures 5.13(a and b) show the z-fold laser power dependences on the plane folding mirror X- and Y-tilts respectively. The continuous power readings were recorded with a beam splitter/thermopile power meter/chart recorder arrangement while manually rotating the micrometer tilt control at a steady rate (at about 1 mrad every 2 s), and triggering an event marker for every micrometre division turned. Evidently, the laser is still oscillating with several milliradians of tilt. The power curves are asymmetric about the X- and Y-zero tilt axes, although the succession of sharp power maxima for the opposing tilts occur at tilt angles roughly equi-distant from the origin. The power curves were reproducible with only slight variations in the positions of the maxima and their power levels. The beam splitter was used to send most of the laser power to the thermopile power meter and the remainder to the 'transverse beam profiler'. A sample of the many different beam profiles encountered throughout the tilt experiment, and recorded at 2 mrad Y-tilt intervals is presented in Figure 5.14. As can be seen, there are various modes that vaguely resemble EH_{11}, EH_{12} or EH_{13}. The beam profiles for the X-tilt showed similar mode variations that closely resembled EH_{11}, EH_{21} or EH_{31}.

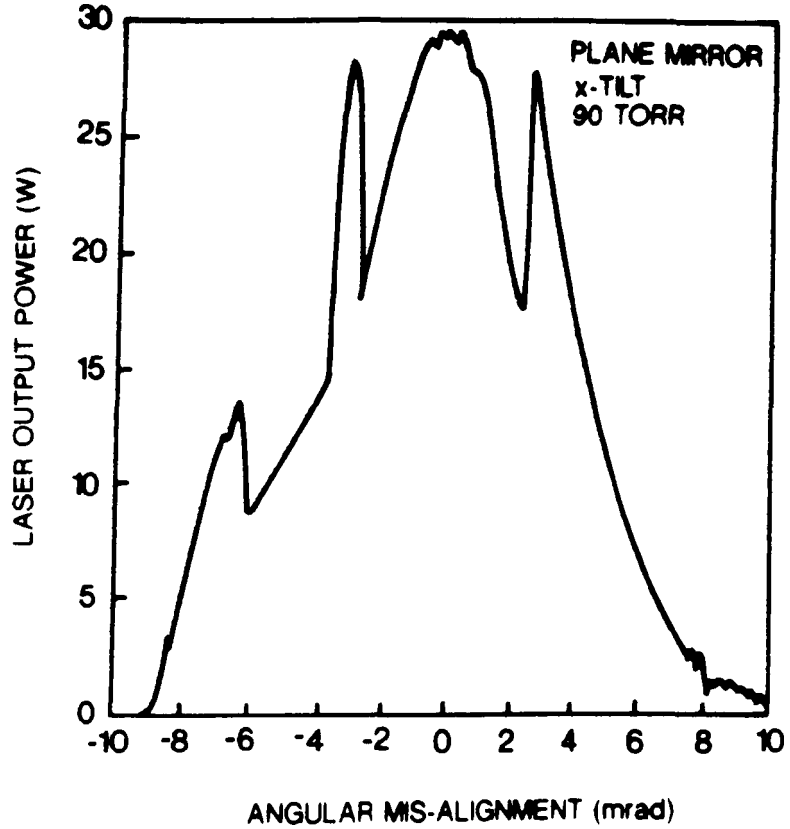

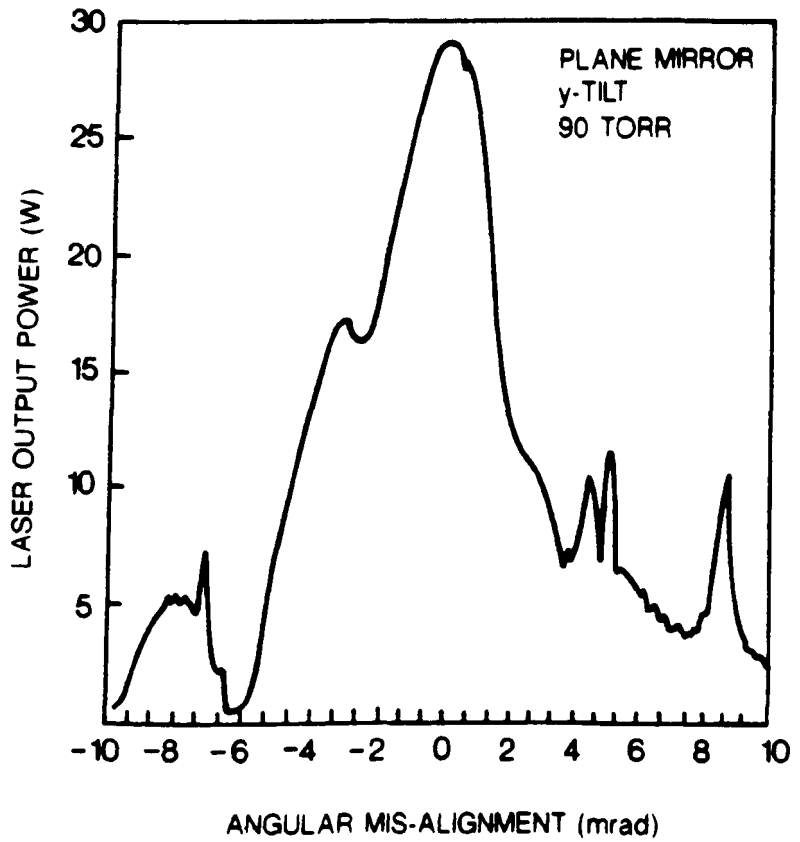

Figure 5.13. Plane mirror z-fold laser output power as a function of the angular misalignment of one of the folding mirrors (with a beam splitter in the path of the laser output beams).

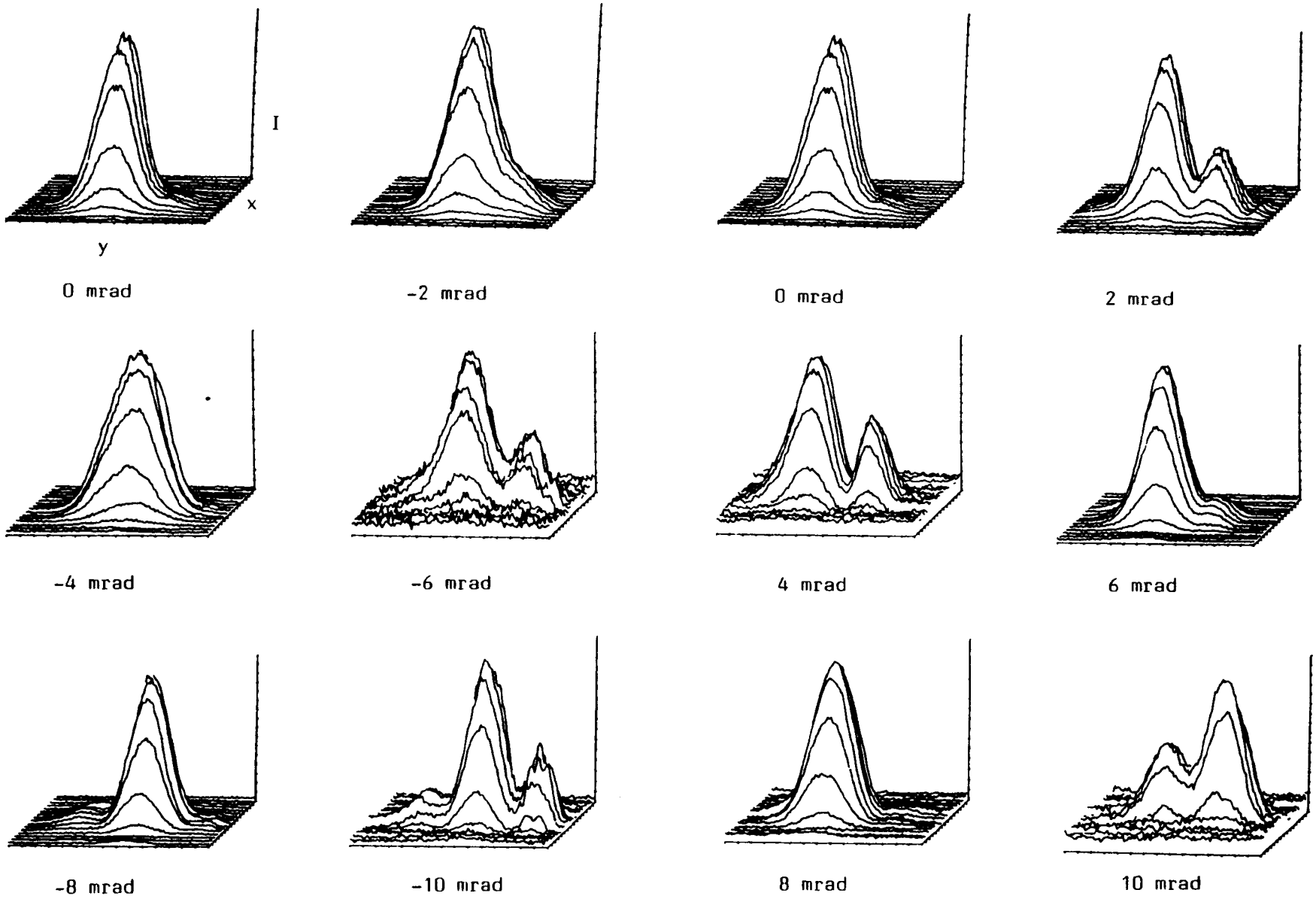

Figure 5.14. Normalised laser beam transverse intensity profiles observed during the angular misalignment (y-tilt) of one of the plane mirror *z*-fold laser folding mirrors (Figure 5.13).

Although the experiment described above produced an interesting power structure with tilt there are two experimental complications that disguise the 'true' behaviour. Firstly, the nearly well-aligned laser has little inherent polarisation selectivity, so the laser output is apt to flip from the X to Y polarisations unpredictably. Consequently, the power reflected onto the thermopile power meter by the beam splitter with its polarisation (and incidentally wavelength) dependent reflectivity is not directly proportional to the total laser output power. Secondly, the laser output power for a given mirror tilt changes because of thermal drift.

Hence the interpretation of the power curves in Figure 5.13 is cluttered by secondary effects peculiar to the diagnostics, there is, however, an interesting features that is worth pointing out that justify their inclusion: this is the coincidence between the polarisation flips and the total power (both polarisations) maxima (as verified below).

Having realised the importance of the diagnostic complications, which would vitiate any theoretical attempt to model the power behaviour, the experiment was repeated, this time measuring the laser power directly and tuning the cavity length with the PZT bimorph to record the peak powers. Experimental power versus X- and Y-tilt data collected in this way for the plane, curved and partial waveguide folding geometries are presented in Figures 5.15, 5.16 and 5.17(a and b) respectively. The common operating conditions were those

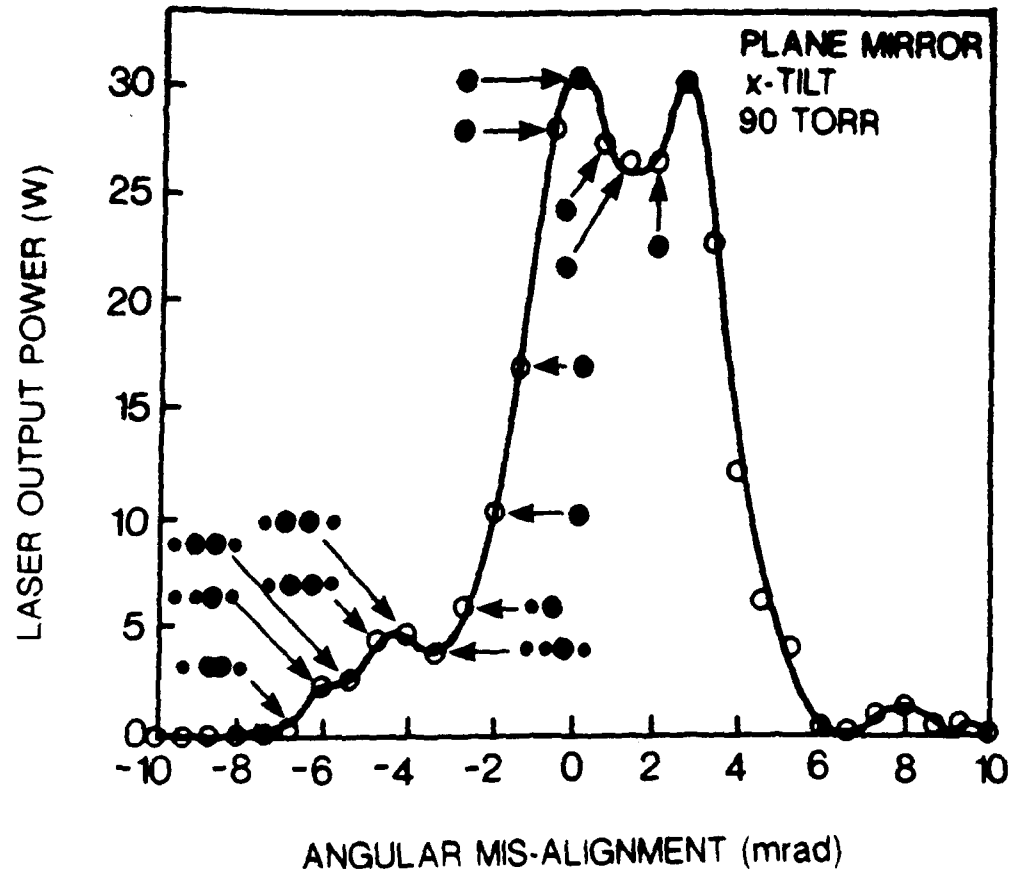

(a)

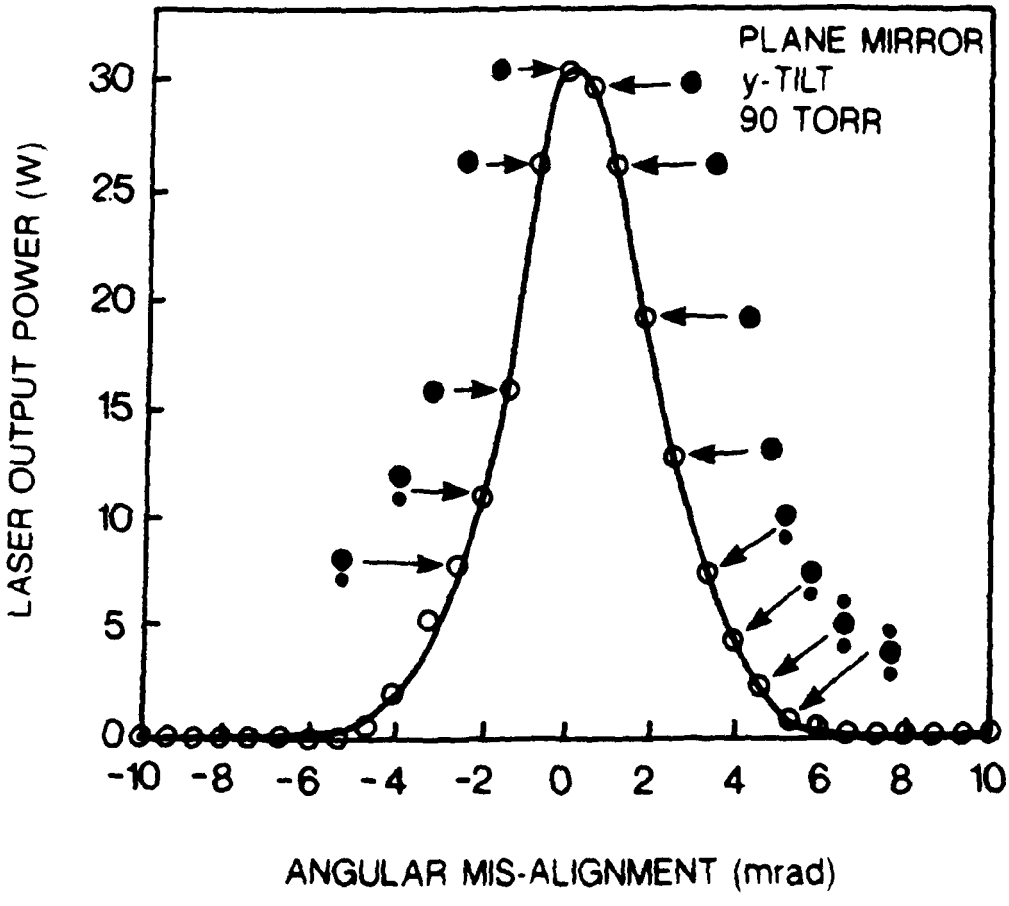

(b)

Figure 5.15. Plane mirror z-fold laser output power as a function of the angular misalignment of one of the folding mirrors (with the beam splitter removed). The solid dots represent the laser output mode patterns at the observation points (circles).

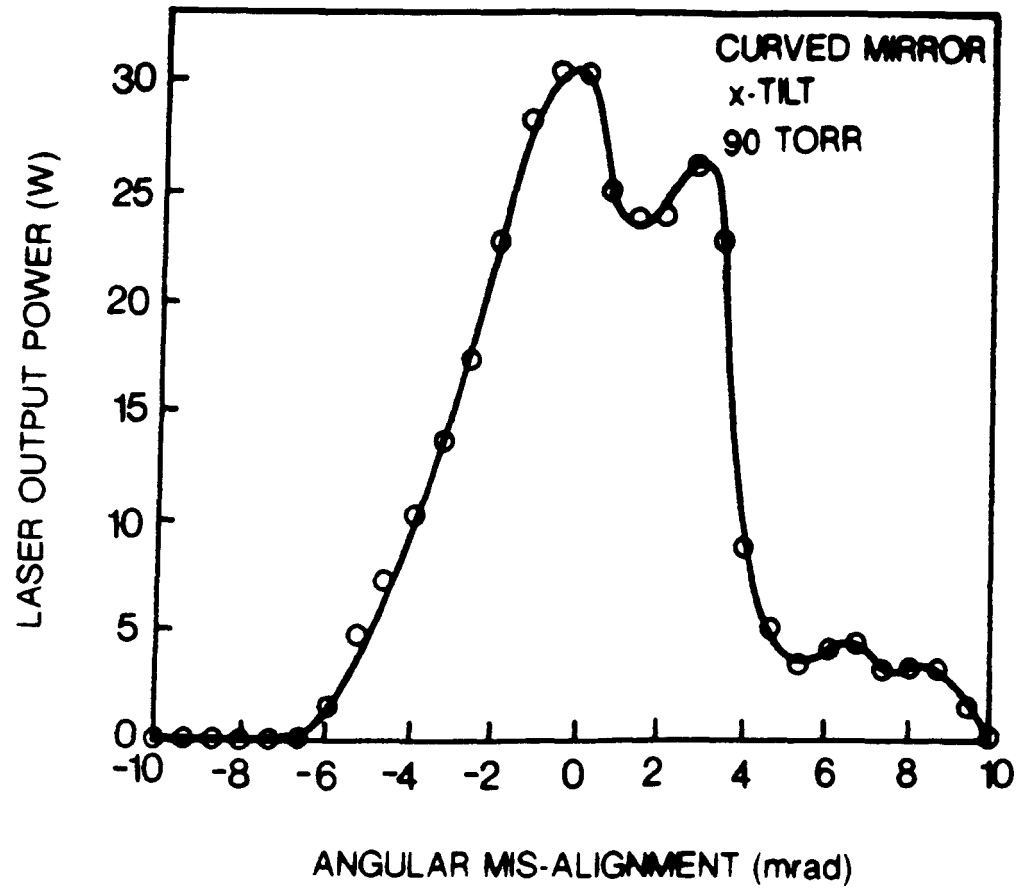

(a)

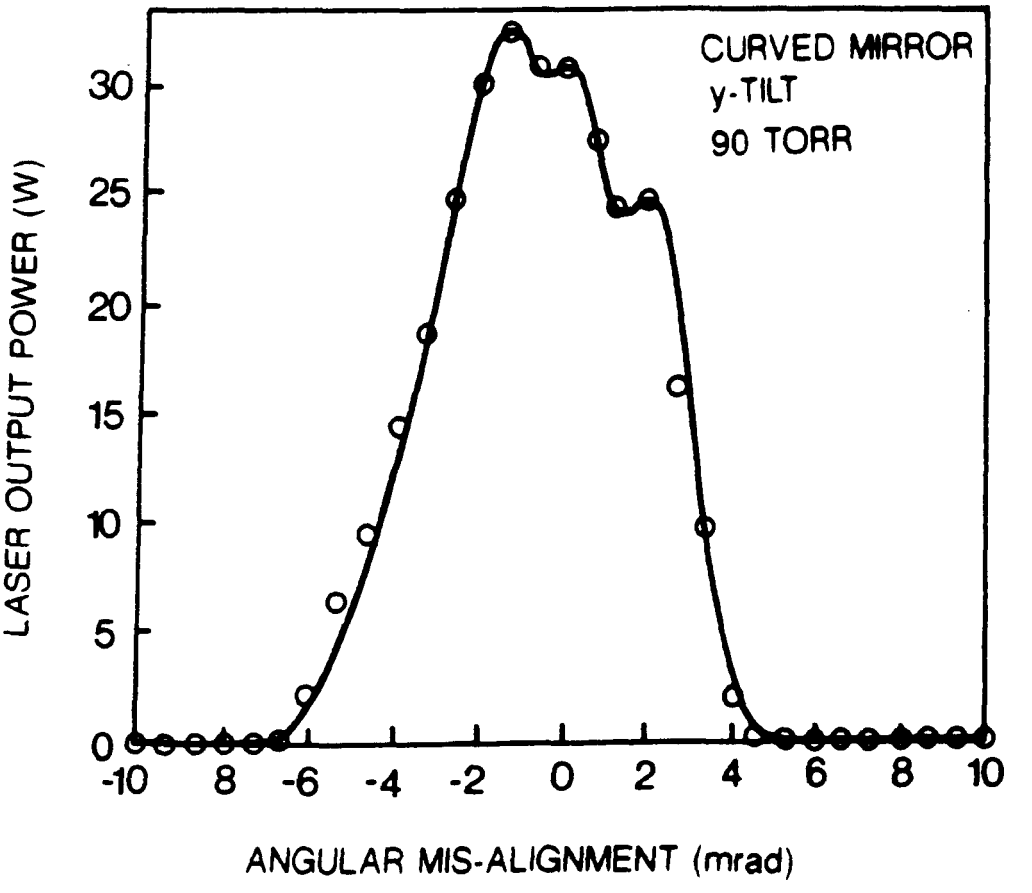

(b)

Figure 5.16. Curved mirror z-fold laser output power as a function of the angular misalignment of one of the folding mirrors.

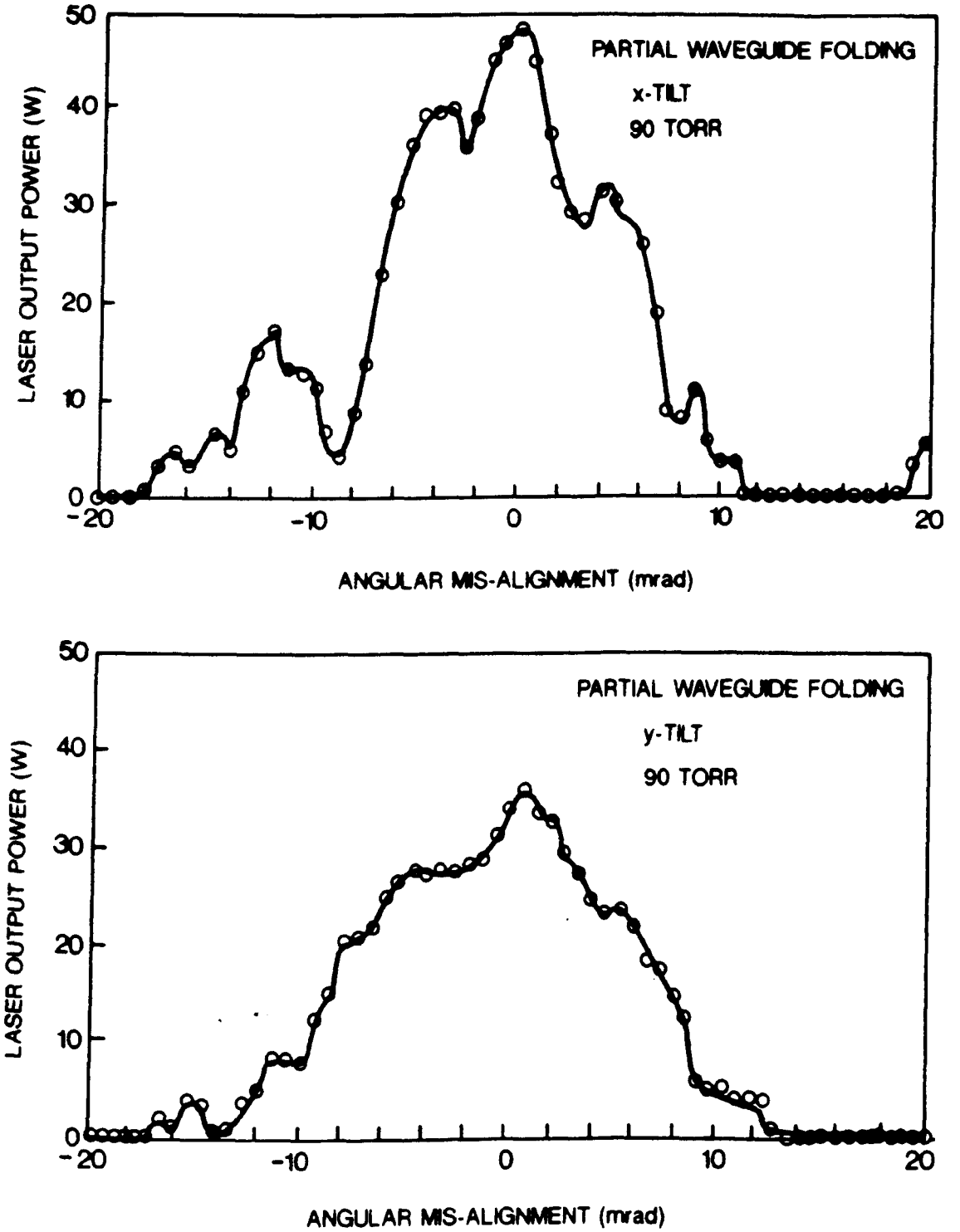

Fig. 5.17. Partial waveguide z-fold laser output power as a function of the angular mis-alignment of one of the folding mirrors.

for near maximum output power, namely, with 90 torr of $3He:1N_2:1CO_2$ + 5% Xe excited by 550 W net RF power at 125 MHz (except by 700 W for partial waveguide folding).

The power curves in Figure 5.15 show only a slight resemblance to those presented in Figure 5.13. The successive sharp power maxima previously observed now appear either as 'wobbles' in the laser power or are not apparent at all. Also, for large tilt angles the power drops to near zero where in Figure 5.15 a few watts of power was available. This latter anomaly may be explained by a difference in the laser gain provided by the discharge media for the apparently identical, yet invariably slightly different, operating conditions. This explanation is supported by the results in Figure 5.18, that show available powers for mirror tilts almost twice the angle of those in the previous case, provided by the higher gains at the lower gas operating pressure (45 torr as opposed to 90 torr).

The width of the power versus tilt curves at the half-maximum power points for the plane, curved and partial waveguide folding laser geometries was 5 1/3 and 3 2/3, 6 2/3 and 6 1/3, and 13 1/3 and 10 milliradians for the X- and Y-tilts respectively, at the 90 torr (maximum power) operating pressure. Evidently, the tolerance to mis-alignment differs in each case, and is worst for the plane mirror folding, as one might have expected considering that the divergence of its reflected beam is not checked in any way. The curved mirror folding does provide some

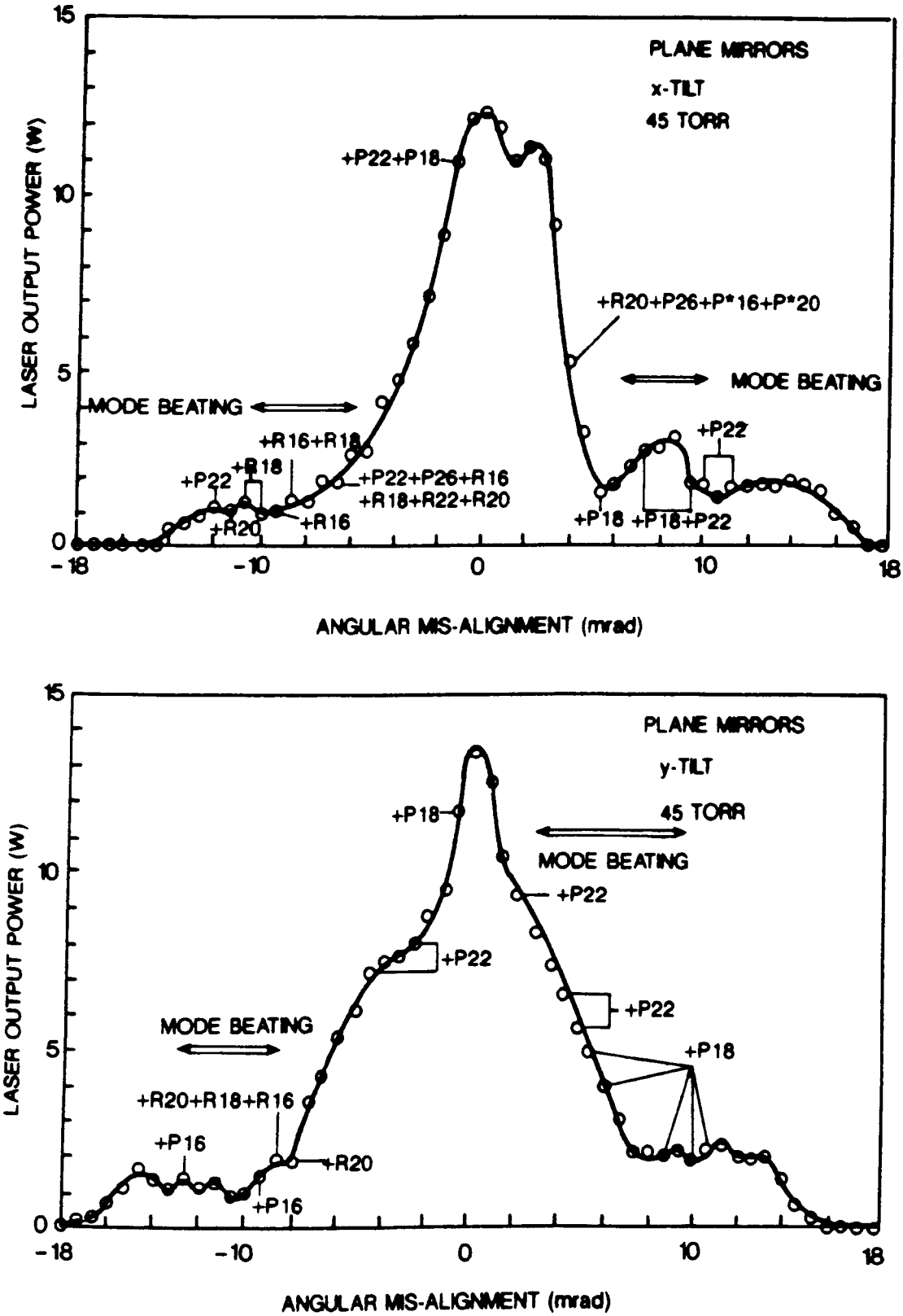

Fig. 5.18. Plane mirror z-fold laser output power at low gas pressure as a function of the angular mis-alignment of one of the folding mirrors. Also shown in the figures are points at which multi-line lasing occurred, and regions where mode beating was observed.

focussing, while the unguided portion of the partial waveguide folding is less than an eighth of that associated with the other two geometries. The efficiency with which the re-entrant beams couple into the various waveguide modes is, of course, a complex process to model and not one as straightforward as suggested above; the sense of the changes in tolerance associated with the three folding geometries is, however, intuitively correct.

A theoretical model of the laser resonators with tilted mirrors would need to include the evaluations of the waveguide mode propagation constants and 'tilt' coupling coefficient matrices for many modes perhaps at least 5 x 5 waveguide modes and 10 x 10 free-space modes, for several wavelengths in the CO_2 vibrational-rotational spectra. As yet, no attempt has been made to evaluate the partial waveguide folding coupling coefficient matrices, or the mis-aligned curved mirror folding matrices. Although the matrices in the latter case could be extracted from the theoretical analysis presented in Chapter 2 by introducing suitable modifications, the computer time needed to perform the appropriate algorithms renders it impracticale. The complications in the analyses for the curved and partial waveguide folding geometries arise from the lack of symmetry about the Y-plane; thus preventing, for example, the reduction of the multiple scalar diffraction integrals via symmetry considerations to simple integral or closed form solutions. The plane mirror folding treatment, however, is

greatly simplified by the preservation of symmetry which also permits the analysis of the positive and negative angular mis-alignments of the folding mirror to be treated as one case. Although relatively simplified, the iterative and numerical evaluations of the competing resonator mode compositions and round-trip losses are by no means trivial ones. The interpretation of the data by incorporating them into a Rigrod analysis to allow a direct comparison between the experimental and theoretical results is prone to many sources of error.

Figure 5.19 shows the preliminary results of a computer model of the plane folding mirror z-fold laser resonator, due to Hill [78], that predicts the variations of the competing resonator mode round-trip losses as a function of angular mis-alignment of one of the folding mirrors, for the P20 (10.59 μm), R20 (10.25 μm) and P20 (9.55 μm) rotational lines. Here 10 x 7 guide modes and 20 x 14 free-space modes were included in the X and Y direction respectively. The dominant line (the one with the highest gain-to-loss ratio) is reliably P20 for mirror tilts (either sense about the X- or Y-axes) up to about 6-8 mrad, after which there is strong competition from the rotational lines R20 and P20 lines, conducive to multi-line lasing. The tilted plane mirror experimental results presented in Figure 5.18 do bear a surprisingly good resemblance to the theoretical predictions, inasfar as the observed multiline behaviour occurs with roughly the same angular mis-alignment. Although a direct comparison between the predicted and experimental

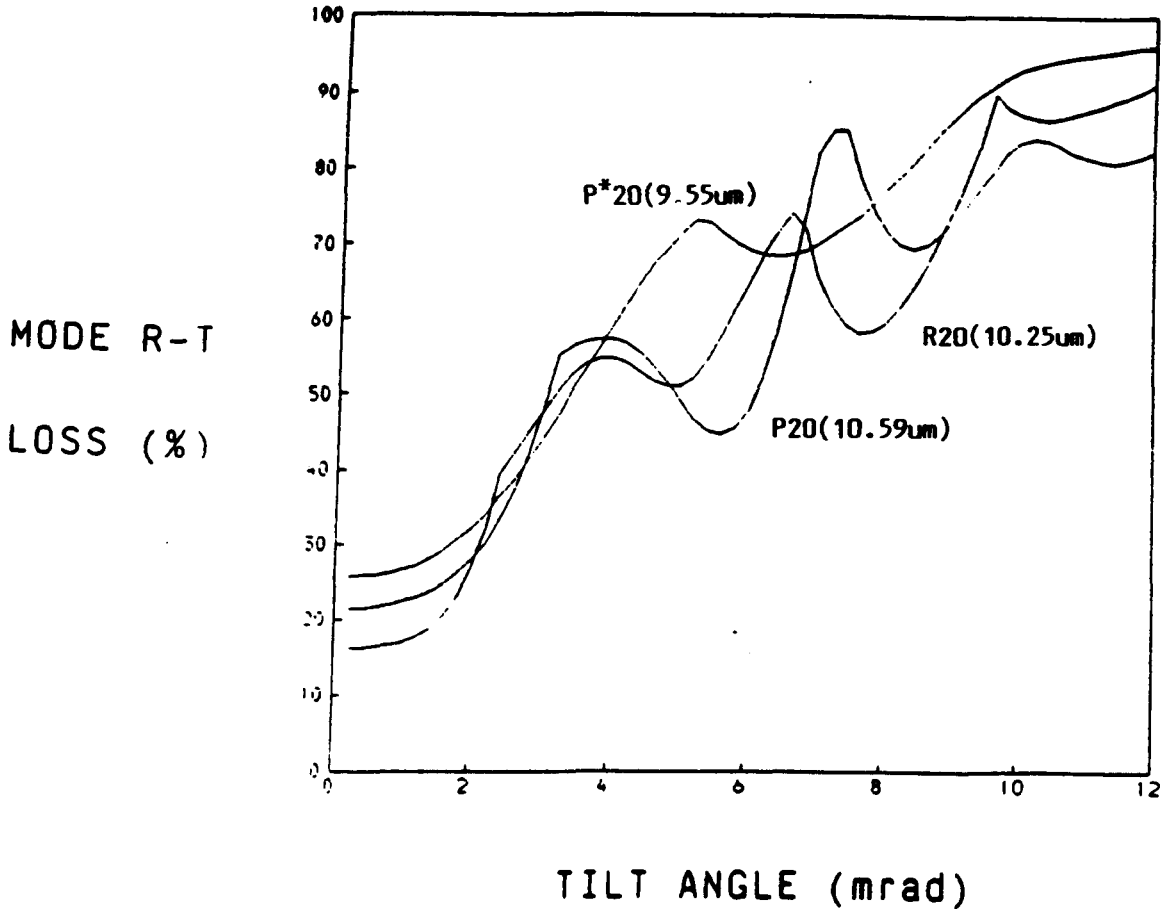

Figure 5.19. Predicted plane mirror z-fold laser resonator mode round-trip loss as a function of the angular misalignment of one of the folding mirrors for various CO_2 rotational line wavelengths. The waveguiding loss factors used in the derivation of these curves were as follows:-

Parallel loss factor (Al_2O_3) : 0.5 for P20 and R20
1.5 for P*20

Perpendicular loss factor (Al_2O_3) : 0.8 for P20 and R20
2.4 for P*20

power variations with tilt is not provided, there is a reassuring coincidence between the 'wobbles' in the envelope of the loss curves and those in the power data points.

Throughout the multi-lining region (here the term multi-lining is used loosely since the laser line measurements were conducted with a broadband spectrum analyser which did not provide short-time line information) the laser output mode pattern changed many times and was accompanied by mode beating (monitored with a fast CMT detector/RF spectrum analyser) at apparently random frequencies between 0 and 70 MHz. The beat frequencies, sometimes several at once, would jump over several megahertz with the slightest tilt adjustments, moving towards zero with decreasing tilt and disappearing at 4 or 5 MHz. An analysis of the mode beating behaviour for this relatively complicated resonator geoemtry was not attempted; instead, and in order to further the understanding of the physics behind mode beating (or hooting) in waveguide lasers, a separate experiment was undertaken (described in Chapter 6) with a deliberately simple and hoot-prone dual-Case I waveguide laser.

5.2.6 Laser Output Power Versus Gain Length

Experimental measurements of the output power of the z-fold laser described in Chapter 4, were taken when one, two and all three of its discharge segments were lit, while maintaining constant conditions of RF excitation power

density. The data consists of five sets of three power readings at gas pressures between 60 and 80 torr.

A BASIC computer program incorporating the solutions to the simultaneous Rigrod equations presented in section 3.2 was written to perform the functions of least squares and compound standard errors. An example of the least squares fitting to the experimental data points is presented in Figure 5.20, for the data set at 70 torr. The data points have been corrected to take into account the laser output window absorption losses (approximately 3% in this case). The window absorption does not affect the evaluation of the line gradient, it does, however, affect the evaluation of the saturation intensity, and if not taken into account would give an over-estimation (albeit very slight in this case).

Another correction would be the inclusion of the additional resonator round-trip loss through the attenuation of the circulating laser power by resonant gas absorption in the unlit discharge sections. The gas absorption which for 10.6 μm laser operation, occurs beween the 100 and 001 vibrational levels, would only be significant if the 100 lower laser level was heavily populated via the thermal excitation of the 000 ground state (both directly and via the 010 level). Considering that the discharge segments are separated by large slabs of alumina and that the top and bottom RF electrodes are water cooled, it seems reasonable to assume that the gas in the unlit segments would be at near-room temperature. The calculated P20 absorption of CO_2 is $< 0.0001\%\ cm^{-1}$ at 302 K [79], which is four orders of

magnitude less that the gain coefficient in the excited gas regions, and hence represents a negligible additional loss (or negative gain). In some lasers, however, with less cooling power it is conceivable that gas absorption could be a significant factor; indeed the reported successful frequency stabilisation of a CO_2 gas laser by intra-cavity optoacoustic absorption [80] indicates that in some cases gas resonant absorption is significant.

A 0.5 W error bar was assigned to each data point in Figure 5.20 for plotting purposes only, and are not included in the least squares fit. The inclusion of the power error bars by weighting the regression line equations is possible, but was considered to be an unnecessary complication. The line coefficient errors for a three point un-weighted fit are likely to be the dominant source of error. A ± 1% reflectivity error, deduced from infrared spectrometer measurements at the 10 μm wavelength, was assigned to the output mirror reflectivity. The effective laser resonator mode beam area was taken as 1 mm^2, using equation (3.5) and 2a = 2.25 mm. For the 70 torr example data set, the saturation intensity was calculated as 7.92 ± 0.80 kW/cm^2. The ∿ 10% error figure comprised approximately 4/5 least square fit variance and 1/5 output mirror reflectivity variance.

The least square fits to the data sets are plotted in Figure 5.21 without the data points (for clarity). In general, the line gradient increases with pressure, greatly

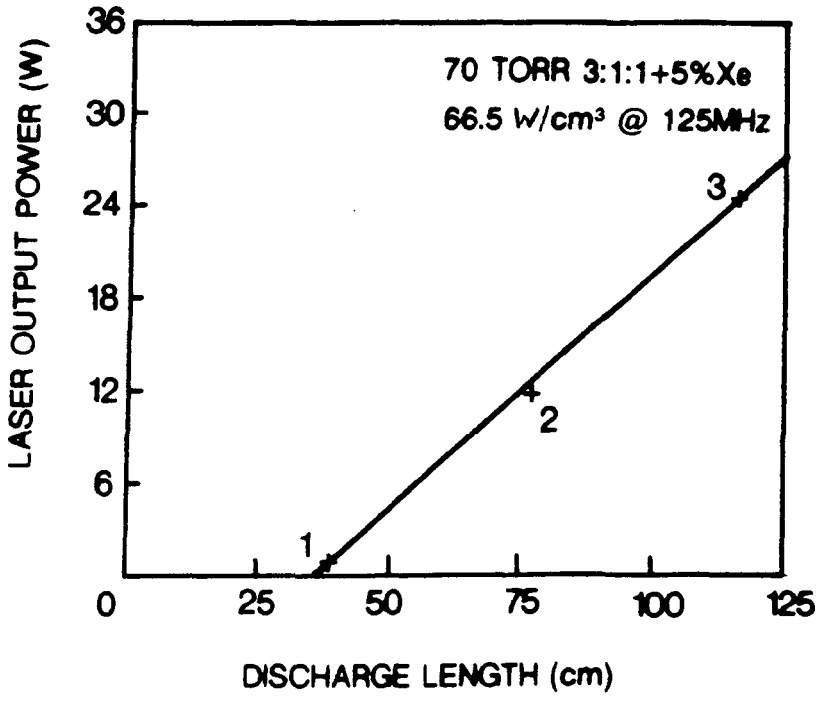

Figure 5.20. Least square fit to the plane mirror z-fold laser output power measurements at the 70 torr gas operating pressure.

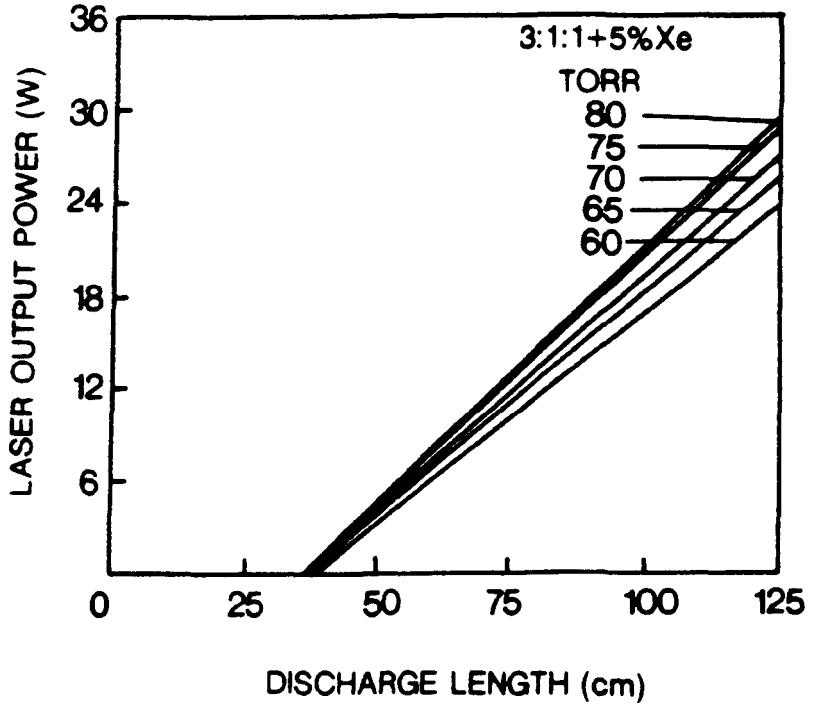

Figure 5.21. Least square fit to the plane mirror z-fold laser output power measurements for various gas pressures (the data points have been omitted for clarity).

at first and then less so, until the optimum pressure (for maximum output power) is reached, followed by a gradual decrease and eventual plummet. The 80 torr gas pressure falls a little short of the optimum pressure at this RF power density. The range of pressures was restricted by practical considerations. The corresponding line coefficients, and their associated standard errors, are presented in Figure 5.22. The percentage errors are quite large, between 4 and 7% for the gradients, and between 9 and 17% for the power intercepts. There are many possible sources for experimental error, although the greatest reduction in these fitting errors will inevitably be achieved with a larger number of data points per set. In this case the number of discharge sections (and hence the number of data points) was restricted to three, which was governed by other practical considerations (Chapter 4).

The calculated saturation intensities and their standard errors, are presented in Figure 5.23. Their values lie between 7.5 amd 8.25 kW/cm^2 with percentage errors between 20 and 30%. The increase in intensity with pressure was expected from the scaling relations of [11] and the single pass amplifier measurements of [47]. A direct comparison of the saturation intensities for this gas mixture and these pressures, at the RF power density and frequency used, for a similar size waveguide has not been found in the literature - although waveguide lasers with saturation intensities of between 5 and 10 $KW/cm,^2$ have been reported [81].

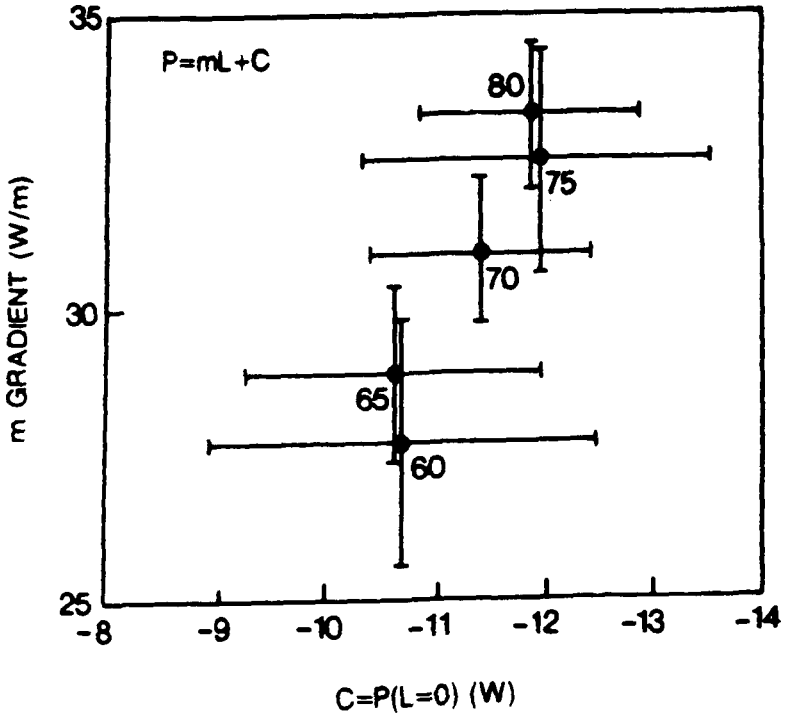

Figure 5.22. Linear least square fit coefficients and their associated errors for the straight lines through the data points (Figure 5.21).

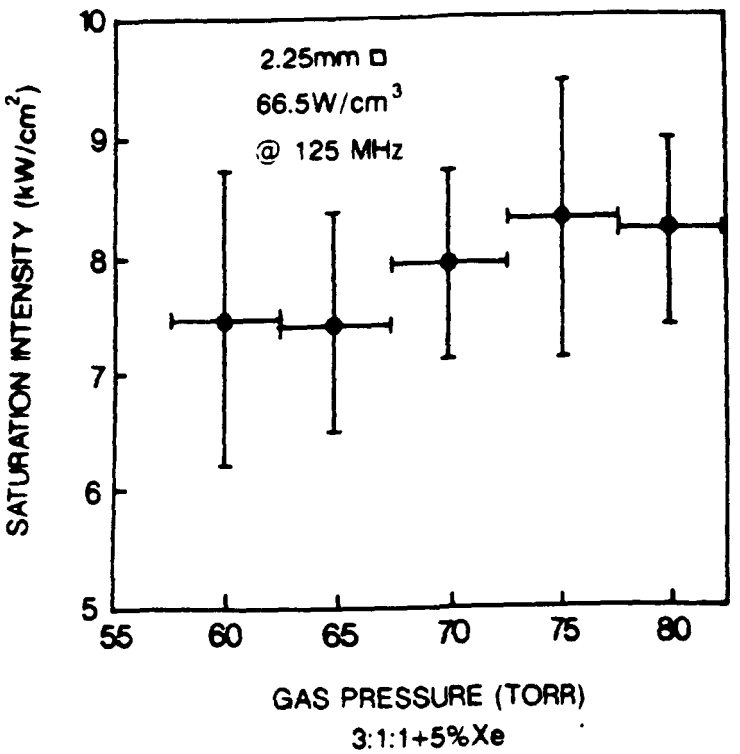

Figure 5.23. The calculated saturation intensities and their standard errors for various gas pressures.

As already mentioned in section 3.2, a complete Rigrod solution for the remaining unknown parameter values (gain and round-trip loss) is not possible. If one of these is known or estimated then the other parameter can be calculated and assigned a standard error through the same error analysis used above for the determination of the saturation intensity. Figure 5.24 shows a solution curve for the 70 torr data set. Also included in the figure are curves showing the bounds of the standard errors associated with the solutions, and histograms displaying the relative error contributions (at η^e = 25%) of the line parameter variances and the output mirror reflectivity variance. The relative error sharing varied only slightly over the parameter space considered. As expected the contributions of the weighted parameter variances are the same for the gain coefficient and the round trip loss evaluations. The coincidence between the standard error boundaries was unexpected, and in general suggests that σ_g/σ_{η^e} is a constant. Hence if η^e = 20.0 ± zero%, then g = 0.70 ± 0.05%, or alternatively for g = 0.70 ± zero%, then η^e = 20.0 ± 2.5%; with percentage errors of ∿ 7% and ∿ 12% respectively. The choice of η_e = 20% was not arbitrary but considered to be a suitable estimate for the plane folding mirror geometry used in this experiment (Chapter 2). Similar values of g and η^e, and their associated standard errors, taken from the solution curves for the remaining pressure data sets are presented in Figure 5.25(a and b) respectively. Evidently, the least percentage

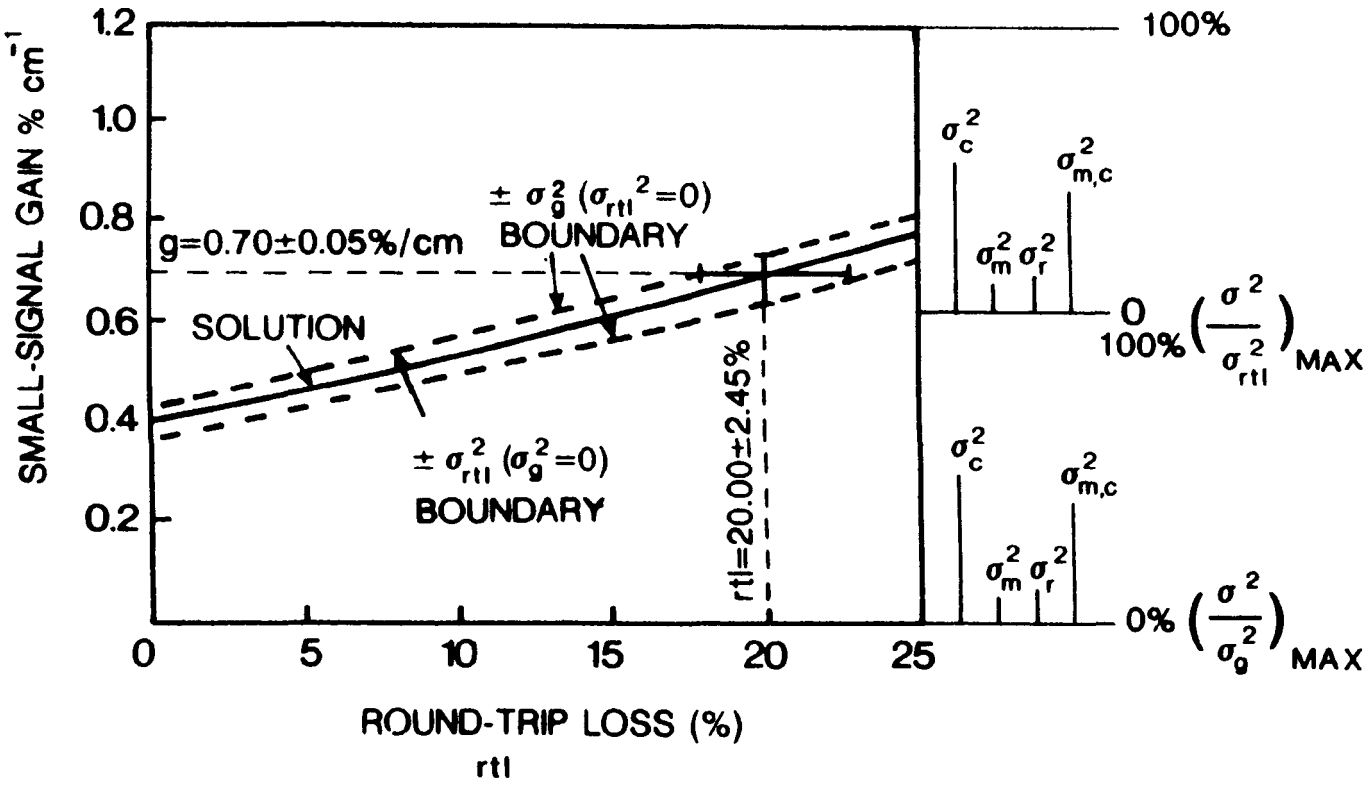

Figure 5.24. Simultaneous Rigrod solution curve for the 70 torr gas pressure data set.

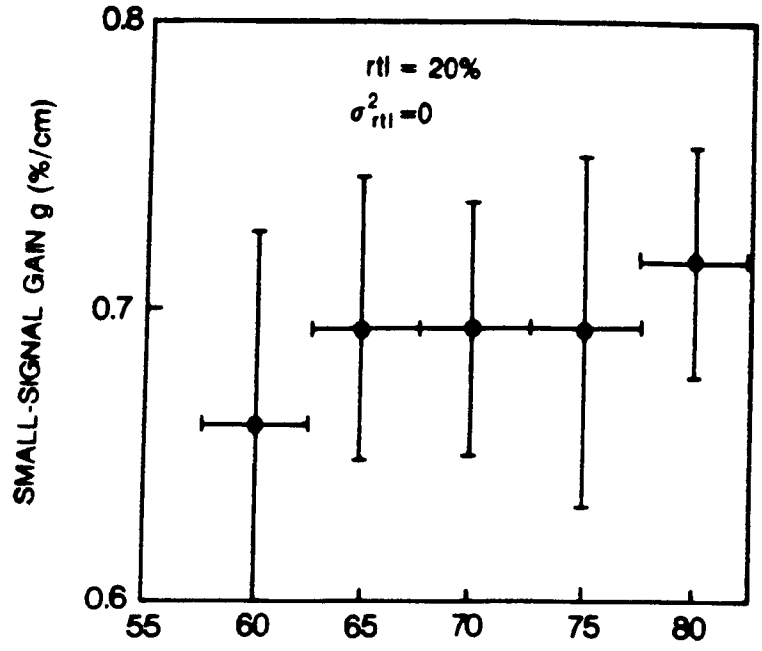

(a)

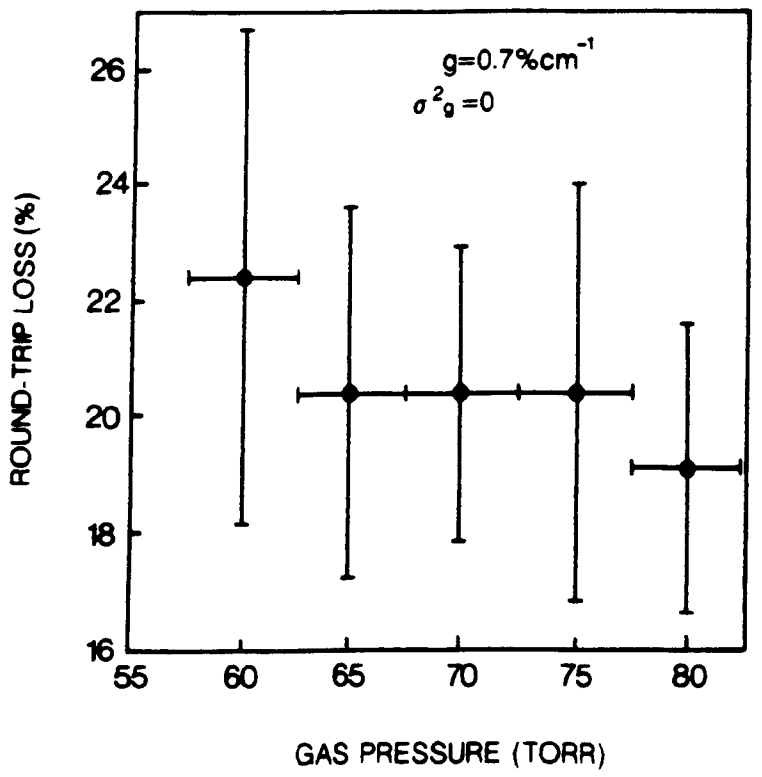

(b)

Figure 5.25. Small-signal gain (a) and round-trip loss (b) for various gas pressures, evaluations and their associated standard errors, derived using solution curves to the data sets (such as the one in Figure 5.24).

error is achieved by estimating the resonator round-trip loss to determine the gain coefficient (as opposed to the other way round). If the estimated parameter (whichever approach is used) has a finite standard error (assumed to be zero in Figures 5.24 and 5.25) then equation (3.48) or (3.49) will give the complete standard error of the remaining parameter.

The laser parameters for the curved mirror folding and the partial waveguide folding laser geometries could be determined using the simultaneous Rigrod solution method described above. Alternatively , the gain coefficient and saturation intensity values obtained for the plane mirror folding geometry can be incorporated into the Rigrod equations describing the aforementioned laser configurations, provided that the lasers operate with identical conditions of gas mixture and pressure, RF excitation frequency and power density, etc. Variations in gain length, effective beam area and output mirror reflectivity can be tolerated provided that their values can be determined, and their changes do not destroy the parallelism of the gas parameters (g and I_s). Since the Rigrod parameters are generally interdependent, the difference between the laser operating conditions is best restricted to the change in the parameter to be determined. In this case, a comparison of the effective resonator round-trip loss parameters for the three laser configurations was desired to test the theoretical coupling loss predictions derived in Chapter 2.

An experiment was performed to determine the gas parameters (g and I_s) of the z-fold laser with plane folding mirror at 90 torr and 94 W/cm³ RF power density. These common operating conditions produced laser outputs with close to the maximum power extraction

observed with each laser configuration. Operating at near maximum power extraction conditions was not essential, but provided a useful repeatability check to confirm that a good state of re-alignment of the laser mirrors had been achieved. The simultaneous solution of the plane folding mirror equations for the 90 torr data set gave I_s = 10.21 ± 0.75 KW/cm², and g = 0.68 ± 0.03 %/cm for η^e = 20.0 ± zero%.

The output powers for 115 cm of gain length for the plane mirror, curved mirror and partial waveguide folding geometries were P_p = 30.0 ± 0.5 W, P_c = 34.5 ± 0.5 W and P_{pw} = 51.4 ± 0.5 W respectively. The corresponding round-trip loss values, obtained by re-arranging equation (3.6) and using the gas parameter values above, are η^e_p = 19.53 ± 0.67%, η^e_c = 15.70 ± 0.50% and η^e_{pw} = 5.15 ± 0.13% (with compound standard errors). The reductions in the round-trip loss values provided by the curve and partial waveguide folding geometries to the plane mirror case, are η^e_{p-c} = 3.84 ± 0.84% and η^e_{p-pw} = 14.39 ± 0.68%, respectively. The difference between the calculated plane mirror folding round-trip loss

figure and the one above, namely 0.47%, occurs, because the power data point at 115 cm does not lie exactly on the least square fit line to the data points.

The 20.0% estimate of the plane mirror folding round-trip loss figure was based on the fundamental waveguide mode coupling coefficients derived from existing theory (Chapter 2), namely η^e_p = 20.11% (scalar-diffraction theory) and η^e_p = 21.92% Gaussian theory). A more comprehensive numerical multimode and iterative computation of the round-trip loss was described in section 3.3 and gave a value of η^e_p = 18.8 ± 2.0% (taking 3 x 3 waveguide modes and 13 x 8 Hermite-Gaussian free space modes). Although the 'actual' round-trip loss values may be a little different to those above, the difference values are weakly dependent on the choice of η_p. The round-trip loss reduction predicted for curved mirror folding was 4.82%, 3.01% and 0.5% depending on the value of η^e_p chosen (20.11, 21.92, 18.8 respectively). The first two figures are reassuringly close to the one above (3.84%). The lack of error bars with these figures arises from the complex and cumbersome nature of the coupling theory treatments, and the subsequent omission of error treatments. The reasonably assumed large error bar assigned to the multimode evaluation possibly accounts for the low reduction figure associated with it. The round-trip loss reduction provided by the partial waveguide folding has not been predicted quantitatively, but was expected from the curve in Figure 3.2.

A summary and comparison of the z-fold laser round-trip loss predictions for the three-folding geometries, derived with single mode and multimode coupling loss theoretical treatments (Chapter 2 and Section 3.3), and with the experimental evaluations of the Rigrod solutions (Chaper 3 and this section), is presented in Table 5.2: these results will be discussed further in Chapter 9.

ROUND-TRIP LOSS (%)			
Plane Mirror	Curved Mirror	Partial Waveguide	Folding Geometry / Method
20.11	17.10	-	Scalar diffraction single mode theory
21.92	-	-	Hermite - Gaussian single mode theory
18.8 ± 2.0	19.8 ± 2.0	-	Hermite - Gaussian multi-mode iteration
19.53 ± 0.67	15.70 ± 0.50	5.15 ± 0.13	Simultaneous Rigrod analysis

Table 5.2. Comparison of the z-fold laser round-trip loss predictions for the three folding geometries. The Rigrod loss estimates include dissipative losses (eg. absorption and scattering) at the mirror surface.

CHAPTER 6

LASER EFFICIENCY AND FREQUENCY STABILITY

Summary

This chapter contains descriptions of four short experiments related to laser efficiency and frequency stability. These investigations were prompted by often unexpected observations during other experiments and ideas developed en route that were considered interesting and worth pursuing.

6.1 Introduction

The use of radiofrequency discharges is now a well established technique for the excitation of molecular gas lasers, over a wide range of laser average power levels from milliwatts to kilowatts. One important consideration, particularly for high power devices, relates to the necessity of ensuring that RF power is transferred efficiently from the radiofrequency generator to the discharge load. To accomplish this task, it is necessary to transform the complex impedance of the load, which here consists of the combination of the passive electrode structure and the discharge itself, to match the impedance of the generator which is often real and equal to 50 Ω. The necessary impedance transformation may be achieved by the use of a number of possible inductor/capacitor (L/C) combinations which can efficiently transform a given discharge load over some limited range of generator frequencies. However, to maintain efficient impedance matching and a minimum in reflected RF power, in the face of changes in the discharge load conditions, it is usually necessary to change either values of L and C in the matching network and/or to adjust the generator frequency.

Sections 6.2 to 6.3 describe experiments on two effects which are linked insofar as each involves induced changes in the impedance of the discharge gain medium; the first caused by changes in RF input power and the second due to modulation of the intra-cavity circulating flux. The first effect relates to the fact that under constant

conditions of discharge geometry, gas pressure and mixture, and generator frequency, the magnitude of the impedance of the discharge is a function of the power which it absorbs from the generator. Thus, attempting to vary the RF power input to a laser disharge as a means to adjust the output infrared power will result in variable efficiency of power transfer. Section 6.2 describes a technique which provides real-time automatic impedance matching (AIMing) [82] in the face of varying drive powers and which has allowed efficient RF power delivery to an RF excited CO_2 waveguide laser over a wide range of input power. Section 6.3 describes experiments to detect the opto-Hertzian effect - the RF equivalent of the opto-Galvanic effect in DC discharges, which manifests itself in changes in RF power reflected by the discharge as a consequence of variations in the plasma impedance caused by modulation of the optical flux circulating inside the laser cavity.

It is proposed that these two effects may be combined to allow laser frequency stabilisation and laser efficiency optimisation.

Section 6.4 describes an experiment to demonstrate the operation of an RF-excited CO_2 waveguide laser by the parallel-resonant distributed inductance excitation technique [54] using a novel multi-start solenoid configuration. Also included are design proposals for a compact laser structure relieved of the multiple discrete inductors common to existing designs.

Many applications of CO_2 waveguide lasers, for example, in coherent LIDAR, require a laser output with a 'clean' intermediate frequency spectra. However, mode beating, or 'hooting', due to interference between two different transverse modes of a laser resonator is common in waveguide devices, especially those with slight cavity mis-alignments. Section 6.5 presents measurements of laser output power and hoot frequency as a function of mirror tilt for a dual-case I square bore waveguide laser. The experimental results are in reasonable agreement with a multimode resonator-matrix computer model [83].

The experiments described in this chapter were not performed with the z-fold laser described in Chapter 4. The reasons for this are two-fold; firstly, the experiments described here, and the ones with the z-fold laser described in Chapter 5 were conducted in parallel; secondly, the relatively complex nature of the z-fold laser resonator and RF excitation scheme, made it an unsuitable candidate for the experiments mentioned above, both in terms of extracting the experimental data and modelling the results. Despite this, the benefits observed with the automatic impedance matching technique made it a viable excitation scheme for folded waveguide lasers with its associated high RF input powers. Also, the predicted high sensitivity in detection of the opto-Hertzian signal with the near 50 Ω combined discharge resistance of the z-fold laser, suggests this laser is particularly suitable for opto-Hertzian laser frequency

stabilisation. If the z-fold laser is to be used as, for example, a high power transmitter in a coherent LIDAR system, then among other things its IF spectrum will have to be devoid of hoot signals. The results obtained in section 6.5 are the first steps towards modelling the z-fold resonator mode behaviour to determine the conditions for the suppression of its mode beating.

6.2 Automatic Impedance Matching

RF-excited waveguide structures generally consist of precisely ground ceramic blocks sandwiched between metal electrodes, forming a high capacitance structure. RF power can be delivered to the discharge region via an appropriate matching network. In recent years, advances have been made to reduce the ohmic losses in the matching network and improve the uniformity of the discharge along the length of the laser [28,30,54]. The parallel-resonant distributed inductance excitation technique [54] is now commonly used because it allows a high degree of longitudinal gain uniformity coupled with efficient power transfer. Here an automatic impedance matching scheme has been introduced which, when applied to this technique, improves its versatility and efficiency in practical usage.

The laser used in the experiments consisted of a four-walled alumina waveguide (2.25 x 2.25 x 386 mm) sandwiched between two aluminium electrodes. The capacitance of the overall structure was approximately 150 pF. Twelve

parallel inductors placed across the electrodes at equal intervals were chosen to form a resonant transmission line at ∿ 90 MHz. Up to 200 W of RF power close to this frequency was delivered to the centre of the top electrode via a 50 Ohm cable and LC impedance matching network. The water-cooled lower electrode was electrically grounded to the vacuum envelope which consisted of an aluminium box structure. A Ge total reflector of reflectivity 99.6% and a 95% ZnSe output coupler were used in a dual-Case 1 resonator configuration. An unoptimised gas mixture of $3He:1N_2:1CO_2$ + 5% Xe at 80 Torr gave laser output powers of up to 17 W with a quasi-TEM_{00} output mode.

The AIMing technique was used to maintain efficient RF power delivery to the laser over a wide range of input powers. The laser head impedance changes with the level of RF power, producing various degrees of impedance mismatch to the 50 Ohm line. To correct this, a feedback loop (Figure 6.1) continuously adjusts the RF drive frequency to minimise the reflected power.

A lock-in stabiliser is at the heart of the feedback loop, using phase sensitive detection to continuously monitor the reflected power resulting from the mis-match between the RF source and its load. The lock-in signal is produced by frequency modulating the RF generator signal, and detected with a reflectometer and RF detector. The home-made reflectometer is of a simple construction [84]; a subsidiary line coupled to the main power cable and terminated by its

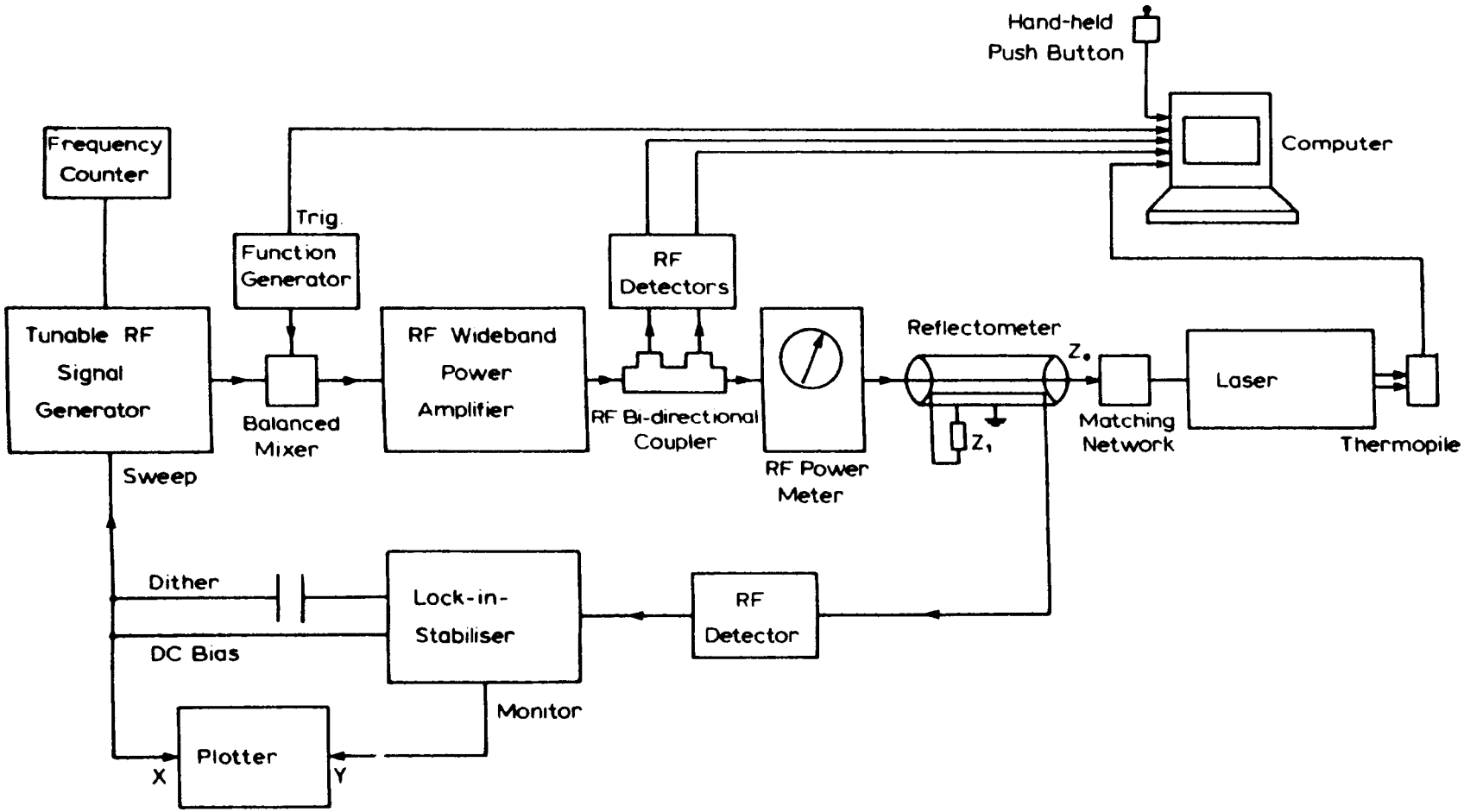

Figure 6.1. Schematic of the automatic impedance matching systems.

characteristic impedance produces a sample RF voltage proportional to the reflected power. Half-wave rectification of this signal produces a DC voltage containing an audio frequency component caused by the periodic mis-match induced by the frequency modulation of the RF generator signal. The error signal derived fom this input to the lock-in-stabiliser is used to adjust the RF drive frequency to a value giving the least reflected power, so completing the feedback loop.

To determine the depth of RF frequency modulation needed for successful "AIMing" the discriminator function of the lock-in stabiliser was investigated. An automatic linear sweep through the full range of the RF frequency sweep DC bias, centred near the laser resonant frequency and extending over approximately 1 MHz, allowed the discriminator signal versus RF frequency to be displayed on a graph-plotter for several depths of RF frequency modulation. The discriminator functions and the reverse RF power were measured simultaneously. The results obtained under typical lasing conditions are presented in Figure 6.2(a) with their calculated through-zero phase gradients (Figure 6.2(b)) for depths of modulation between 0.5-7.0 kHz peak-to-peak at 512 Hz dither. In general, a feedback control system trades discrimination against disturbance. In this case, the discriminator function signal-to-noise ratio is poor for small modulation depths, but improves significantly with larger depths. All curves pass through the zero-phase point

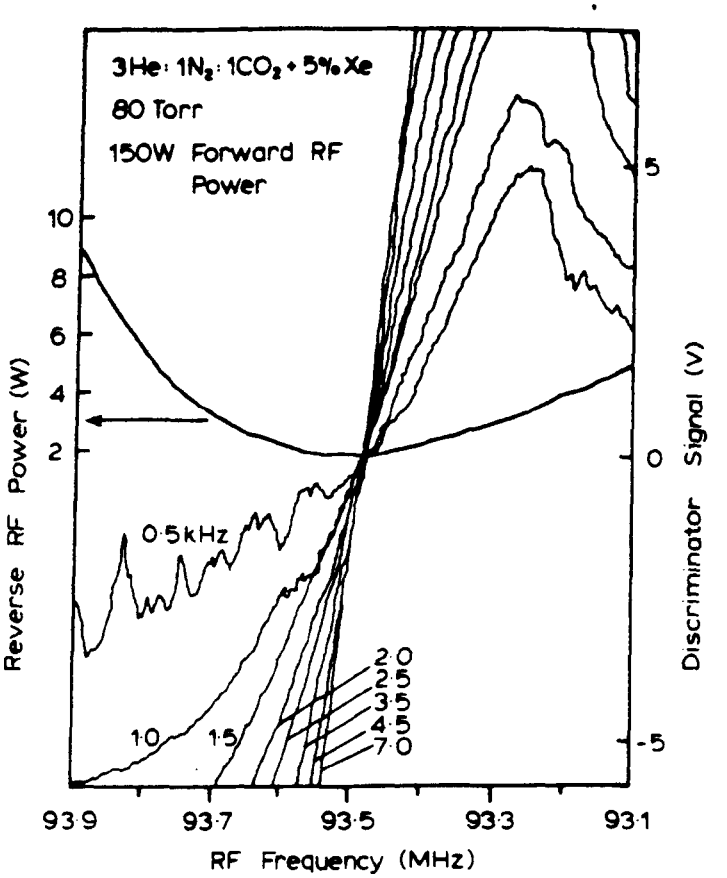

(a)

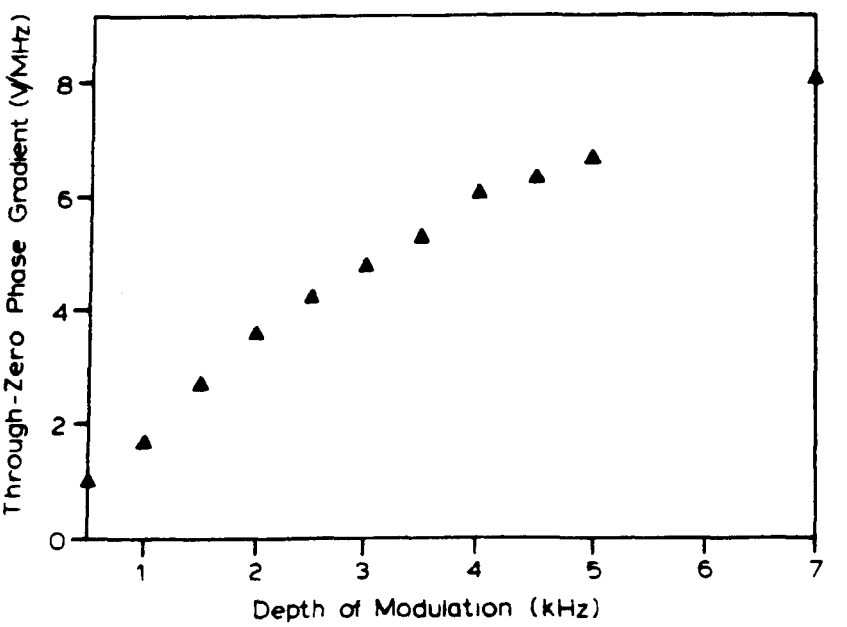

(b)

Figure 6.2 (a) Reverse RF power and lock-in stabiliser discriminator function versus RF frequency for various depth of RF frequency modulation.

(b) Through-zero phase gradients for the discriminator functions shown in Fig. 6.2(a).

corresponding to a minimum reverse power. The modulation depth of 2.5 kHz pp. was chosen as the standard for the rest of the investigation. The laser power disturbance resulting from this modulation depth was measured with a sensitive photo-detector and lock-in amplifier and found to be less than 0.2%.

To characterise the laser performance with and without the AIMing technique the following diagnostic components were introduced; a thermopile to measure the laser output power, a function generator and a balanced mixer to control the RF power level (linear RF voltage ramp) and a commercial bi-directional coupler to monitor the forward and reflected RF powers. The experimental data were sampled by a 12 bit analogue to digital (A to D) microcomputer interface which facilitated the continuous measurement of up to four voltages. The four analogue inputs were proportional to the laser power, forward and reflected RF powers, and the trigger produced by the function generator respectively. A real-time BASIC program was written to access the A to D conversion, refer to calibration data, perform a few simple calculations and display graphically the laser power/efficiency (Figure 6.3(a,b)) and RF reflected power/VSWR (Figure 6.3(c,d)) as a function of forward RF power for a variety of operating conditions. A hand-held push button was used to record the best RF impedance match frequencies observed on the digital frequency meter and their corresponding values of forward and RF power at specific frequency increments (Figure 6.3(e)).

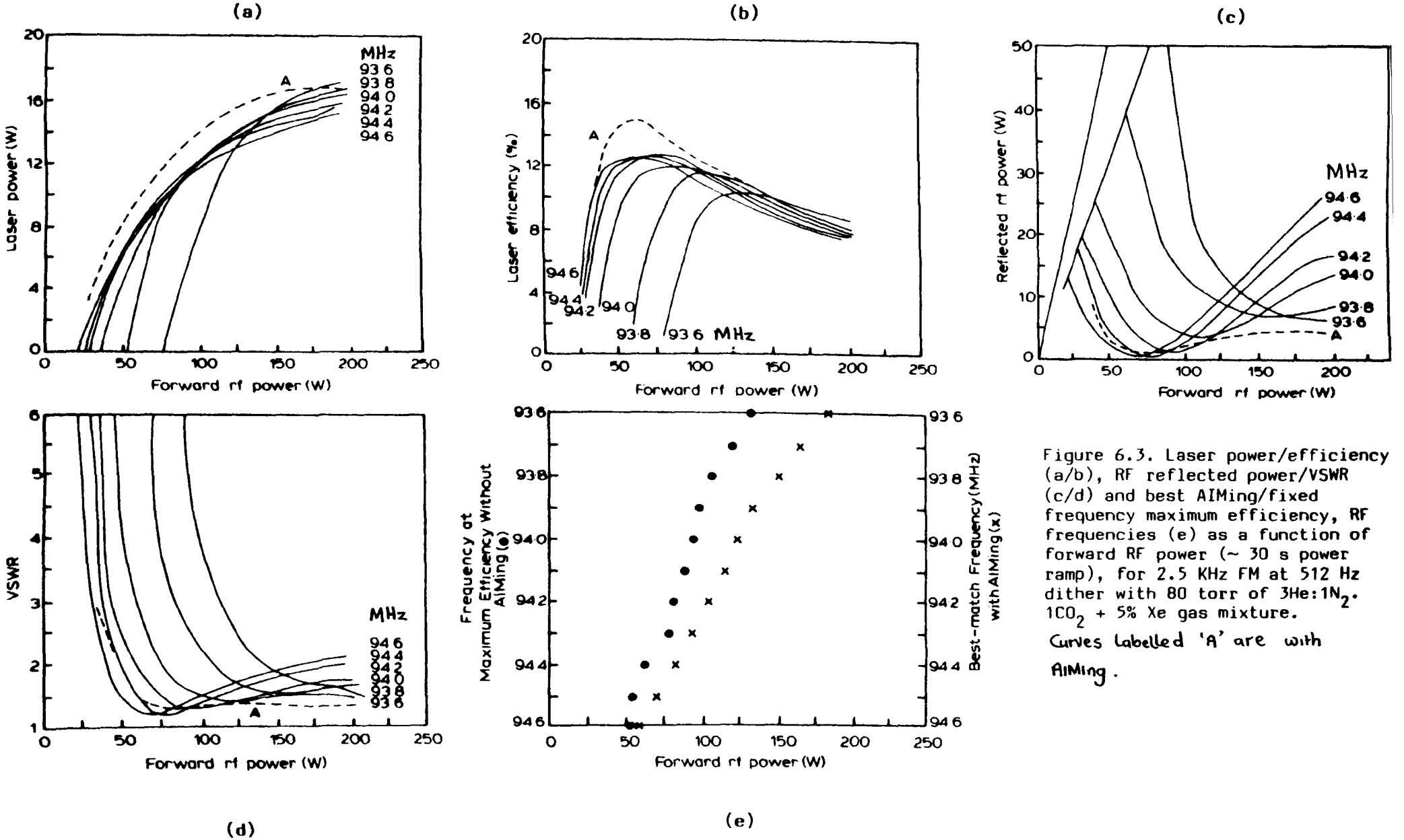

Figure 6.3. Laser power/efficiency (a/b), RF reflected power/VSWR (c/d) and best AIMing/fixed frequency maximum efficiency, RF frequencies (e) as a function of forward RF power (~ 30 s power ramp), for 2.5 KHz FM at 512 Hz dither with 80 torr of 3He:1N_2:1CO_2 + 5% Xe gas mixture. Curves labelled 'A' are with AIMing.

When the laser was operated with AIMing, output powers in the range 2 to 17 W were observed with RF forward powers between 25 and 200 W, at efficiencies (laser output power/RF forward power) as high as 15%. To maintain efficient RF power delivery during the power ramp the operating frequency changed fairly linearly at ∿ 8 kHz/W between 93.6 MHz at high power to 94.6 MHz at low power.

To demonstrate the advantages of the AIMing system these measurements were repeated for fixed RF frequencies lying within the bandwidth swept during the AIMing operation. The advantages can be clearly seen, at all values of RF forward power, the AIMing performance gives the greatest laser output power with the highest efficiency. The AIMing properties responsible for this are visible in the matching trends shown by the reflected RF power/VSWR plots. The parameters recorded during the AIMing operation essentially form the envelopes of the optimum parameters associated with the fixed frequency operations.

The discrepancy between the forward RF power (F; reverse RF power, R) levels corresponding to the optimum laser efficiency (E) for fixed frequency operations and the best-match frequencies observed with the AIMing operation is a consequence of the way that the laser efficiency has been defined, i.e. E = P/F and not P/(F-R).

With poor matching at low RF forward power levels, there was insufficient net RF power available for discharge excitation. In these cases the reflected RF power fell short of the R = F 'no-load line' (Figure 6.3(c)), with the lost

power appearing as heat in the matching network. This hazard did not occur under AIMing conditions, where the discharge was maintained with good matching for forward RF power levels below that capable of causing damage to the matching network components.

To determine the dynamic response of the AIMing loop the period of the RF power ramp was decreased while empirically optimising the DC loop gain by varying the sensitivity of the lock-in stabiliser. In this way stabilisation for RF power changes greater than 100 W/s were maintained, without considerable laser power/reverse RF power versus forward RF power hysteresis.

6.2.1 Conclusions

Existing matching techniques involving reactive networks are limited because they do not have mechanisms to compensate for changes in laser head input impedance variations, resulting from, for example, RF drive power adjustments. Often, in commercial lasers, the pre-set matching network components are chosen for easy discharge 'striking' and good overall RF power delivery. Any desired change in laser output power achieved by manual adjustment of the RF drive power, generally, produces an impedance mis-match causing power to be reflected into the RF generator. This reflected power can be tolerated in low RF power devices, but with higher power devices it presents a hazard.

Here the operation of an automatic impedance matching technique (AIMing) which maintains efficient RF power deivery to an RF-excited CO_2 waveguide laser over a wide range of operating conditions has been successfully demonstrated. This system contains a feedback loop which continuously monitors the reflected RF power level using phase sensitive detection and automatically adjusts the RF drive frequency to a value giving the least reflected power. A useful feature of this system, is that its pre-strike state is one for easy discharge initiation. Prior to discharge strike, the RF drive frequency is 'relaxed' at one of its extreme values. Consequently, a power turn-on produces an initial mis-match and high electrode potential suitable for gas breakdown. The post-strike RF drive frequency is automatically tuned for optimum matching conditions.

6.3 Opto-Hertzian Effect

The phenomenon of static resistance fluctuation in a DC-excited cw laser discharge due to the intra-cavity coherent radiation power fluctuation is well known as the opto-Galvanic or opto-Voltaic effect [85,86]. This section describes observations of a similar effect pertaining to RF-excited cw laser discharges, termed the "opto-Hertzian" [87] effect to distinguish it from its DC counterparts. Here the radiation flux induced changes in discharge impedance manifests itself, not as voltage or current fluctuations as for DC discharges, but in terms of changes in reflected power.

ERRATA

An alterative mechanism for the occurrence of the opto-Hertzian signal (or its d.c. counterparts) is as follows: In the presence of laser action there is a removal of energy (heat) from the gas discharge by the extraction of optical power. The cooling of the discharge is accompanied by an increase in gas pressure and hence the E/P or E/N (E-electric field, P-pressure, N-density of neutral gas molecules) is decreased. Since the production of electrons in a volume ionisation process (giving rise to N_e) is roughly proportional to E/N and the collisional frequency (v) is proportional to the gas pressure, this implies that the quantity v/N_e in equation 6.1 is increased. Hence, the discharge resistance is larger in the presence of laser action.

A simple transverse RF plasma model describing the characteristics of CO_2 waveguide laser discharges in terms of analogous RF circuit elements has been proposed by Griffith [7]. The dominant impedance component for the discharge is the resistive term R_d, given by

$$R_d = \frac{m\ v\ d}{1\ w\ N_e\ e^2} \qquad (6.1)$$

where m is the mass of an electron, v is the collisional frequency of the gas molecules (given by $v = e/2\ \mu m$; where μ is the electron mobility), d and lw are the electrode separation and common area, N_e is the electron density and e is the electron charge.

Electrons periodically gain energy from the RF electric field and lose energy by collisions. The mobility and electron density product increases with higher electron energies [88]. In a molecular discharge there is also a balancing of energy between the molecular excitation and electron cooling. The energy transfer flow to the molecules depends on the molecular transition losses such as spontaneous decay, molecular relaxations and stimulated emission. In the presence of laser action there is thus a larger cooling effect on the electrons and this in turn decreases μN_e. This cooling effect can also be explained in a simple fashion by the conservation of energy, where the balance of energy mostly appears in the form of laser output power. Consequently, from equation (6.1), the discharge resistance is larger in the presence of laser action.

To investigate the opto-Hertzian effect the laser described in Section 6.2 was modified. A light chopper inserted between the back mirror and waveguide, preserving the Case I geometry, allowed 100% modulation of the circulating laser flux. A PZT bimorph attached to the back mirror allowed frequency tuning through the laser signature and modulation of the cavity length. A schematic diagram showing the laser configuration and diagnostic apparatus is presented in Figure 6.4.

The correlations between the laser output power fluctuations, measured with a sensitive photodetector, and the opto-Hertzian signal detected in the forward and reverse RF powers, induced by 100% modulation of the circulating flux provided by the light chopper, and observed with an oscilloscope are shown in Figure 6.5. As can be seen, the optical waveform is reproduced in the RF voltage signal envelopes, with modulation depths of 0.9% and 14.0% for the forward and reverse power samples respectively. The wave shapes are determined by the chopper blade mark-to-space ratio, mark- and space-to-waveguide bore size ratios and chopping frequency; in this case these were 1:1, 3:1 and 300 Hz respectively. The anti-phase relation between the RF signals is predictable, although their phase relationship with the optical signal is dependent upon the matching conditions, as discussed later.

If the input impedance to the laser head is assumed to be purely resistive, then the analysis of the matching

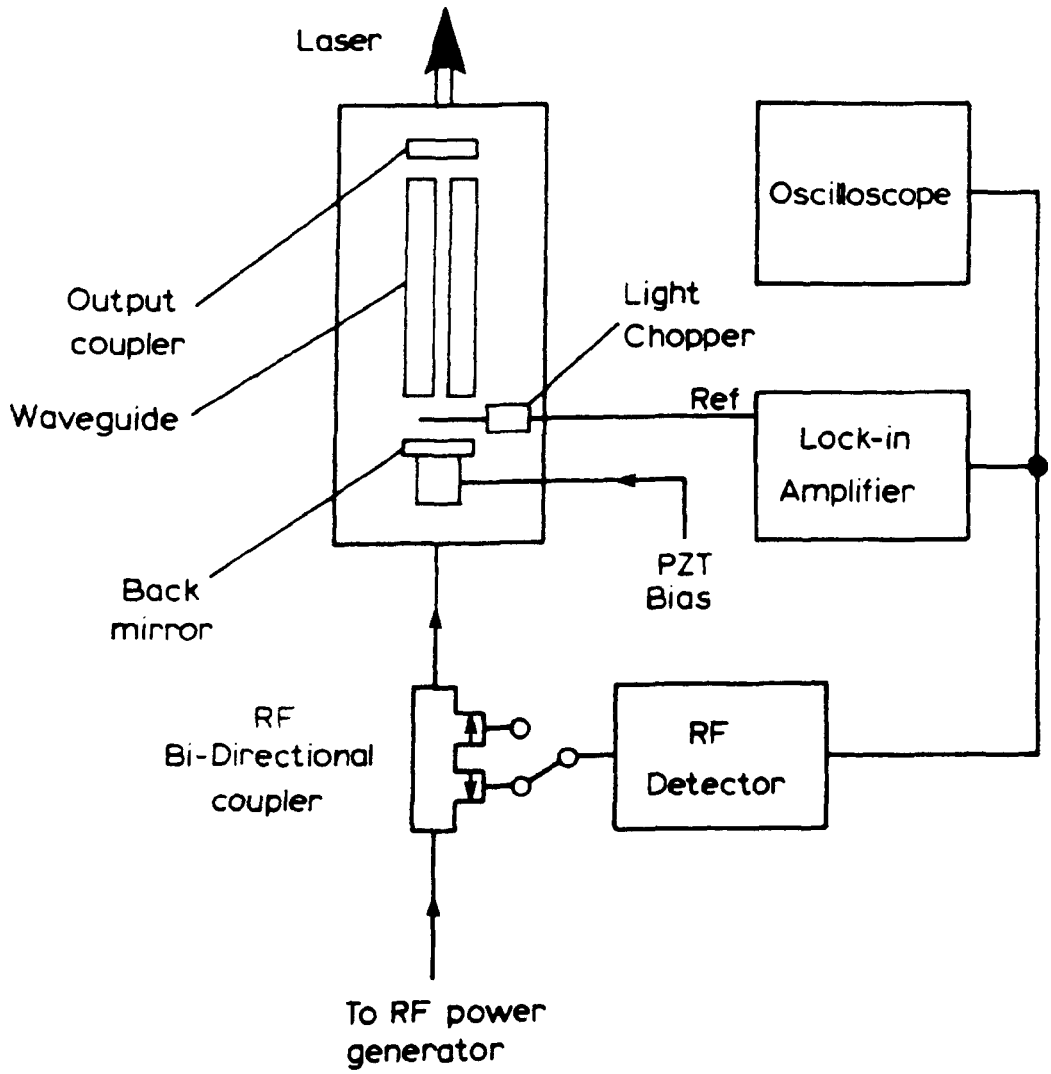

Figure 6.4. Schematic of the apparatus used to observe the opto-Hertzian effect.

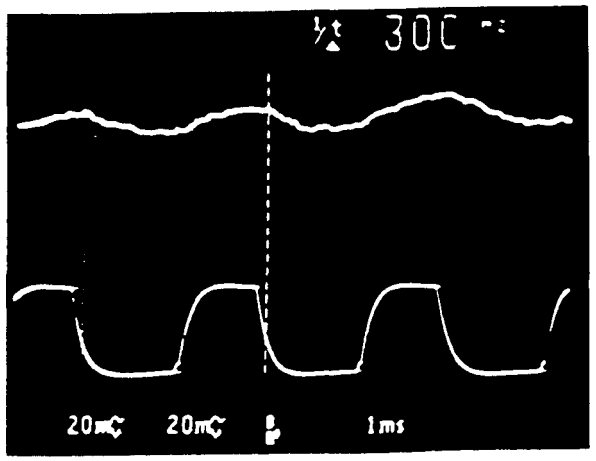

a

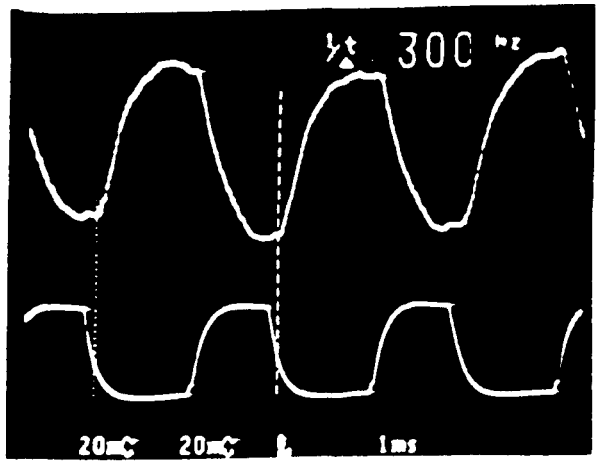

b

Figure 6.5 Oscillograms showing the correlation between the laser output power (bottom traces) and the opto-Hertzian signals (top traces) detected in the forward (a) and reverse (b) RF powers, induced by 100% modulation of the circulating laser power. The laser operated at 93.6 MHz with 100 W forward and 3 W reverse RF power, with 80 Torr of $3He:1N_2:1CO_2$ + 5% Xe gas mixture.

network function is greatly simpliifed. In making this assumption it is presumed that the laser operates with parallel-resonant distributed inductance excitation. In general, however, the resonant discharge channel has a high quality factor, Q, so that if the laser operates at a frequency sightly removed from the resonant value there will be non-zero reactive components. In this case, the Q was about 18.5 and the calculated reactance for a detuning of ± 0.5 MHz about 95 MHz is ∓ 45 Ohms, although the modulus of the input impedance differs only by 10 Ohms from 200 Ohms. The effects of detuning are ignored in the following estimate of the sensitivity of opto-Hertzian detection.

The input impedance of an LC matching network (Figure 6.6), such as the one in the experiment, used to transform a pure resistance (R_d) to the line characteristic impedance (Z_0) is given by

$$Z = Re(Z) + jIm(Z) \tag{6.2}$$

$$Re(Z) = \frac{X_c^2 R_d}{R_d^2 + X_c^2} \tag{6.3}$$

$$Im(Z) = jX_1 + \frac{jX_c R_d^2}{R_d^2 + X_c^2} \tag{6.4}$$

where $X_C = 1/\omega C$, $X_1 = \omega L$ and ω is the angular RF frequency., For 'perfect' matching Re(Z) = 50 Ohms and Im(Z) = 0.

Values for the resistance of the discharge, pertaining to a waveguide geometry similar to the one described above, have been determined experimentally by co-workers [12]. In this case, their results imply that a suitable value for R_d would be about 200 Ohms.

For R_d = 200 Ohms, equations (6.3) and (6.4) give X_c (Re(Z) = 50 Ohms) = -115.5 Ohms and X_l (Im(Z) = 0) = 86.6 Ohms. Hence, the reactive components needed to perform the matching function at the ∿ 95 MHz operating frequency are C = 14.5 pF and L = 145 nH.

If this pre-set matching condition is upset by changes in R_d, then Z differs from 50 Ohms and there will be a mis-match giving rise to a non-zero reflection factor defined as

$$\rho = \frac{V2}{V1} = \frac{Z - Z_0}{Z + Z_0} \qquad (6.5)$$

where V1 and V2 are the complex voltages of the forward and reflected waves in the transmission line.

It can be shown that the ratio of the rates of change of the real and imaginary components of Z with respect to R_d is given by $X_c/2R_d$ or 1/4Q. 'Q' is the quality factor of the matching network.

It is convenient to express the input impedance to the mis-matched network in exponential form, viz.

$$Z = M \exp(j\theta) \qquad (6.6)$$

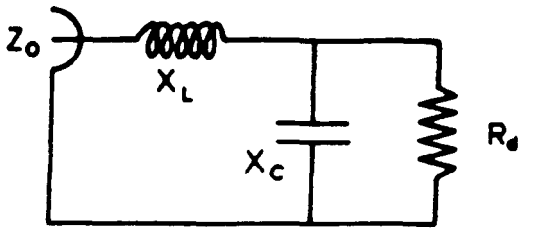

Fig. 6.6. LC impedance matching network.

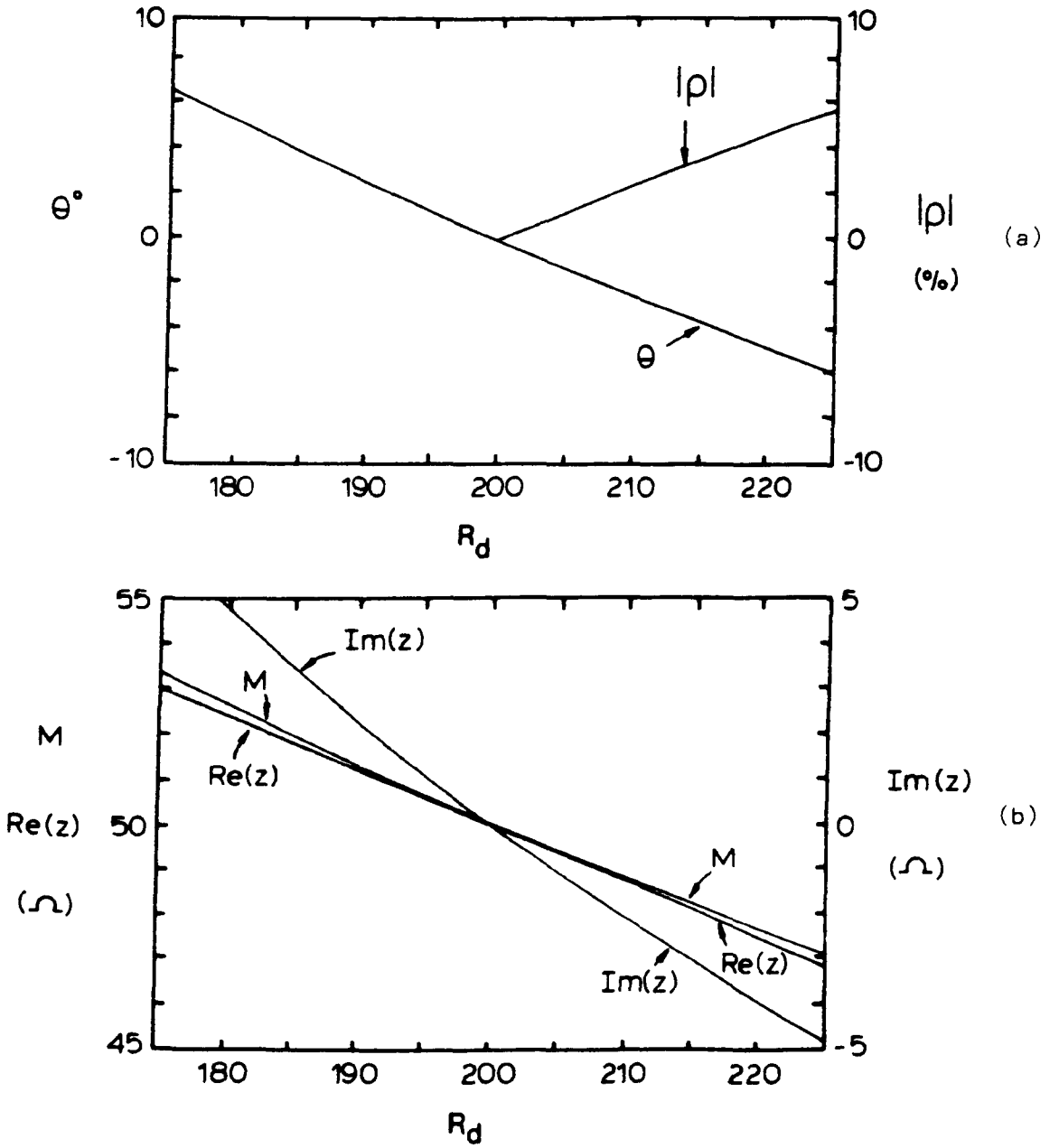

Figure 6.7. The dependence of Re(Z), Im(Z) and M(Z) (a), θ and ρ (b) on Rd for mis-matching condition such as those induced by the opto-Hertzian effect.

$$M = \mathrm{sqrt}(\mathrm{Re}(Z)^2 + \mathrm{Im}(Z)^2) \qquad (6.7)$$

$$\theta = \arctan(\mathrm{Im}(Z)/\mathrm{Re}(Z)) \qquad (6.8)$$

where M is the modulus of Z and θ is the difference between the phase angles of Z and Z_o.

The dependence of Re(Z), Im(Z), and M on R_d, and θ and ρ on R_d, for our values of X_c, X_i and Rd are shown in Figures 6.7(a and b) respectively. As can be seen, these parameters vary fairly linearly over the range of R_d considered. Also, there is a coincidence between the magnitude of the gradients of the reflection factor and mis-match phase angle lines. Essentially,

$$\frac{dM}{dR_d} = \frac{1}{8} \quad , \quad \frac{d\rho}{dR_d} = \frac{1}{4}\ \%/\mathrm{Ohm} \quad \text{and} \quad \frac{d\theta}{dR_d} = \frac{1}{4}\ \mathrm{deg/Ohm} \qquad (6.9)$$

For V1 = 2.2 Volts, as was the case for the results presented in Figure 6.5,

$$\frac{dV2}{dR_d} = V1\,\frac{d\rho}{dR_d} = 5.5\ \mathrm{mV/Ohm} \qquad (6.10)$$

where it is assumed that V1 is constant.

The opto-Hertzian signal shown in Figure 6.5(a) is 60 mV pp. which corresponds to a change of R_d, estimated from 10, or 10.9 Ohms, corresponding to a $\sim$ 5% discharge resistance variation with 100% circulating flux modulation. The laser output power (L), with $\sim$ 100 W RF input power, was 9 W. The

discharge resistance span estimated above, suggests that R_d (lasing) = 210.9 Ω and R_d (no lasing) = 200.0 Ω. Assuming that the rms voltage across the electrodes (V) and the net RF power (P) are unchanged during modulation, gives

$$P = \frac{V^2}{R_d(\text{lasing})} + L \quad , \quad P = \frac{V^2}{R_d(\text{no lasing})} \qquad (6.11)$$

This very simplified calculation gives L =5.2 W, which is of the same order of that observed.

It has been show theoretically and experimentally that a 5% change in the 200 Ohm discharge resistance of the laser manifests itself as a change in reflected RF voltages of typically 50 mV. An equivalent percentage change in the 1 MΩ discharge resistance of a DC-excited laser, produced a change in the voltage dropped along the discharge tube of as much as 500 V. Hence the sensitivity of the RF excited system to a 5% change in discharge resistance was four orders times less sensitive than for an equivalent change in the DC-excited system, athough the voltage change per Ohm in each case was comparable.

Phase-sensitive detection was used to observe the magnitude and sign of the opto-Hertzian signal as a function of foward RF power for various fixed RF frequency operations. The computer arrangement described in the preceding section was used to monitor the forward and reverse RF powers, lock-in amplifier output and laser output power. The results obtained are presented in Figure 6.8(a-c). There are a few

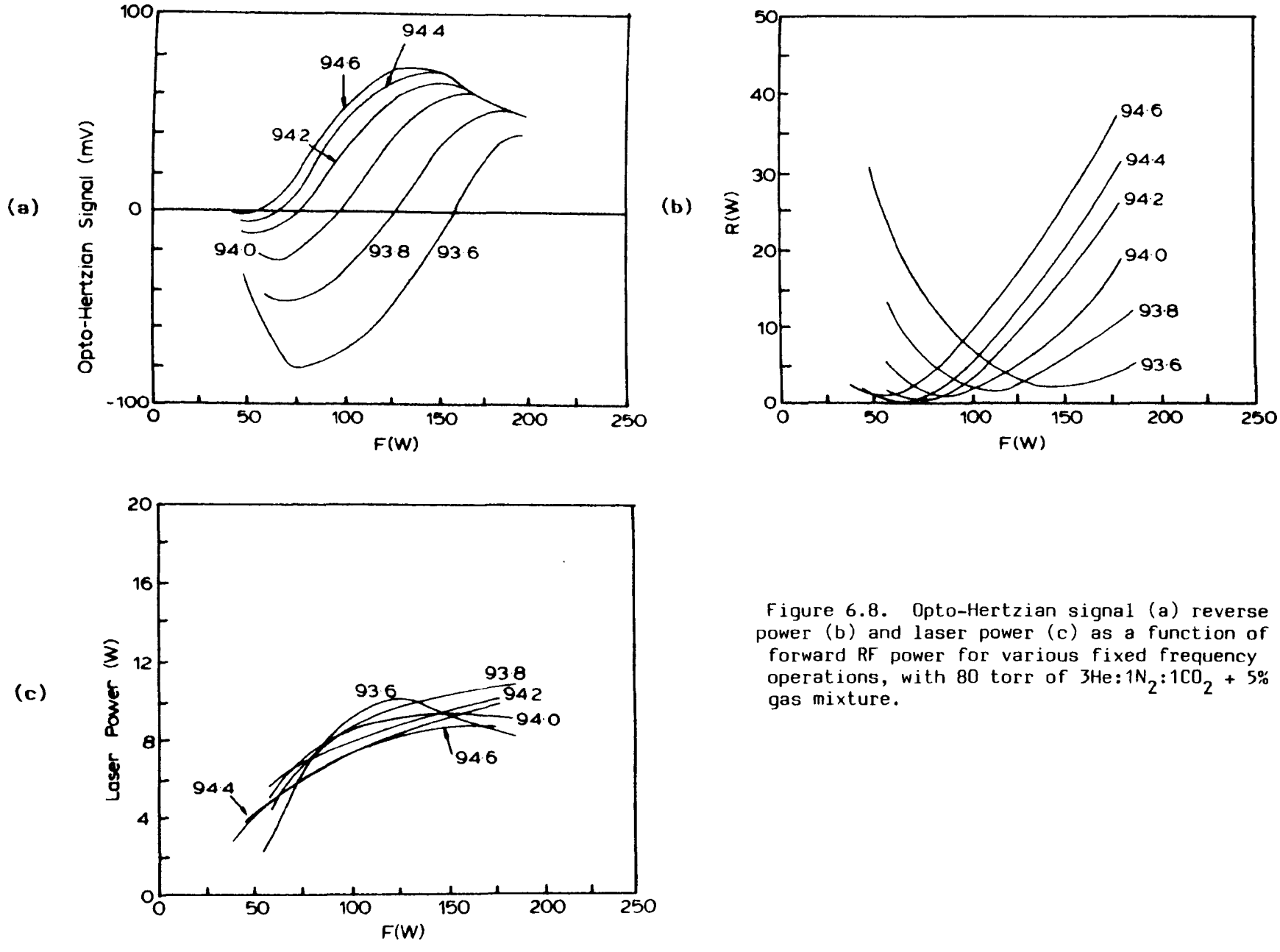

Figure 6.8. Opto-Hertzian signal (a) reverse RF power (b) and laser power (c) as a function of forward RF power for various fixed frequency operations, with 80 torr of 3He:1N_2:1CO_2 + 5% Xe gas mixture.

points of interest; firstly, there is a strong correlation between the reflected RF power and opto-Hertzian signal trends, with no apparent relation to laser output power. This confirms the earlier predictions that the opto-Hertzian signal is strongly dependent on matching conditions. Secondly the null point sign reversal of the opto-Hertzian signal is coincident with the minimum reflected RF power corresponding to the best-matching point. Consequently, it is necessary to operate with finite mis-matching to observe a non-zero signal. The sign of the opto-Hertzian signal depends on which side of the best-matching point the laser operates, and whether the reactance of the input impedance is more capacitive or inductive. Finally, the opto-Hertzian curve ends, at low and high RF forward powers, tend towards the base line and an envelope respectively. The former is a consequence of insufficient laser power for significant opto-Hertzian effect, and the latter may be due to heating/saturation effects.

To determine the dependence of the opto-Hertzian signal on the level of circulating laser power, for fixed discharge conditions, the output coupler was mis-aligned to change the laser output power, whilst maintaining a predominantly single-dot output mode. The measurements of the opto-Hertzian signal for laser powers between 0-10 W illustrating saturation is shown in Figure 6.9.

Laser frequency stabilisation on a single CO_2 line has been achieved for DC-excited lasers using the opto-Galvanic

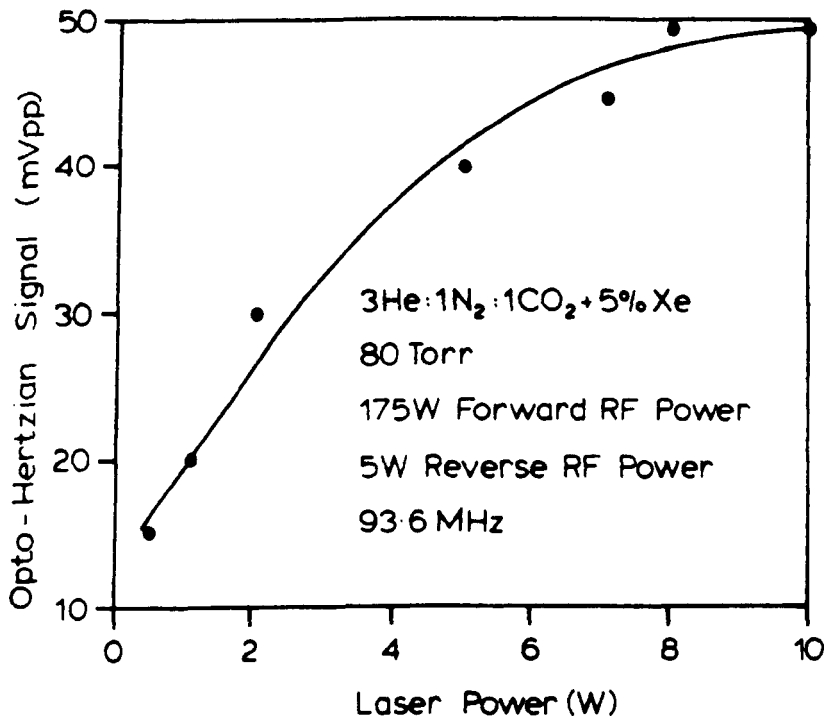

Figure 6.9. Opto-Hertzian signal versus laser power output power, showing saturation.

effect [85]. Frequency stabilisation of the RF-excited laser was attempted using the opto-Hertzian effect. Initially frequency stability was achieved using a pyro-electric detector/beam splitter configuration. Successful lock-in stabilisation was achieved with 0.5 V pp. dither (200 V swept through 1 free-spectral range) on the bimorph holding the back mirror. When the opto-Hertzian signal was used for feedback for otherwise identical conditions, it was found that it was necessary to increase the dither signal to 50 V pp. to discern the error signal above the noise. Obviously, this dither is far too large for accurate frequency stabilisation. Successful lock-in stabilisation will only be achieved if the sensitivity of the detection of the opto-Hertzian effect can be markedly improved.

6.3.1 Conclusions

Modulation of the reflected RF voltage (opto-Hertzian signal) has been observed by 100% modulation of the circulating laser power in an RF-excited CO_2 waveguide laser. The relationship between the reflected voltage modulation and the discharge resistance variations producing it, has been analysed in terms of a simplified RF network analysis. It was found that the sensitivity of the opto-Herzian signal is strongly dependent on the properties of the matching network used, and estimated that the change of discharge resistance needed to produce signals at the level observed, was of the order of 5% at a rate of $\sim$ 5 mV/Ohm. This rate is comparable

to that giving rise to the opto-voltaic signals observed in DC-excited lasers, although the sensitivity in this case is four orders greater than that observed here.

If the opto-Hertzian signal is to be used in a feedback system for laser frequency stabilisation then the sensitivity of its detection must be improved by at least one hundred fold. It is clear from the network analysis that this may be achieved by using impedance matching network with high Q. For example, if the laser discharge resistance is near the 50 Ohms line characteristic impedance as is often the case for multi-channel waveguide lasers, then a series resonant circuit would provide the highest Q. Notice that it is 'near 50 Ohms' because the opto-Hertzian signal null sign reversal occurs under 'perfect' matching conditions.

Ultimately, one can envisage an RF-excited CO_2 laser simultaneously using automatic impedance matching and opto-Hertzian laser frequency stabilisation using the same error signal detected with a simple reflectometer.

6.4 Parallel-Resonant Distributed Inductance Excitation Technique using a Multi-Start Solenoid

The parallel-resonant distributed inductance excitation technique [54] is now common-place because of its overall laser efficiency. Here, a large number (typically 30-60 per metre) of equal-value parallel inductors are placed at equal intervals across the electrodes and along their length. These discrete, or 'lumped' inductors approximately form a

uniformly distributed inductance. Here, 'discrete' implies that each inductor has its own isolated magnetic flux (albeit produced by the same RF source). Conversely, 'distributed' implies that the components forming the inductor have a common magnetic flux. Examples of the distributed inductor are the Rogowski coil (or single-turn sheet inductor) and the multi-start solenoid (MSS). Unfortunately, the value of inductance needed to resonate with the capacitance of typical electrode stuctures at their VHF operating frequencies generally precludes the use of Rogowski coils because of the large cross-sectional area needed; and high permeability compounds which might allow for more compact inductors are not readily available at these frequencies. Multi-start solenoids, on the other hand, are inherently more widely scalable and with geometries more in accordance with compact structure design criteria.

As already mentioned, the multi-start solenoid (shown schematically in Figure 6.10) is an example of a distributed inductor. The value of inductance for this solenoid is given by [69]

$$L = \frac{n^2 \mu S}{l} \qquad (6.12)$$

where n is the number of turns associated with each coil, μ is the permeability of the coil former, S is the solenoid cross-sectional area (arbitary shape), and l is its length.

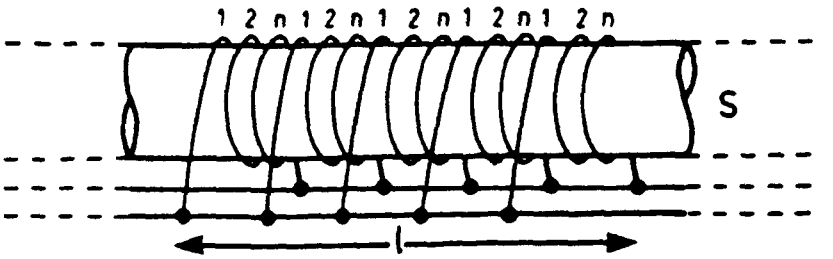

Figure 6.10. The multi-start solenoid.

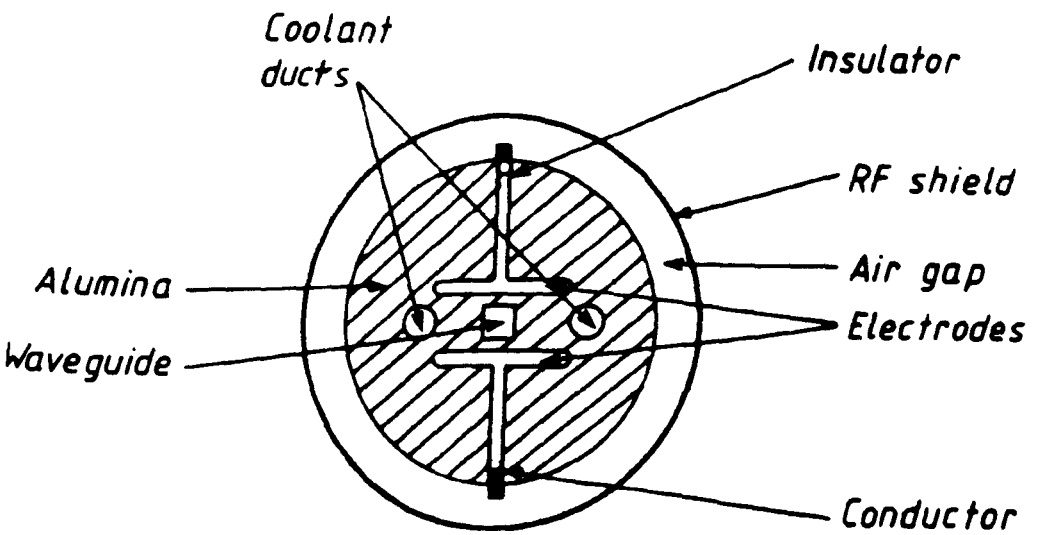

Figure 6.11. (a) Schematic of a proposed laser configuration for MSS distributed inductance resonant excitation (end view).

To investigate the performance of the MSS, the laser described in Section 6.2 was modified; it comprised a four-walled alumina waveguide (2.25 x 2.25 x 386 mm) sandwiched between two aluminium electrodes forming a capacitance C ≈ 150 pF. A Ge total reflector and a 95% ZnSe output coupler were used in a dual-Case I resonator configuration.

The MSS was made by winding 24 SWG copper wire into grooves cut along a 1" PTFE bar at a pitch of 20 turns per inch, giving a total of 86 adjacent 3 turn coils over 13". The common loose ends of the coils were soldered onto copper strips which were bolted to the top and bottom electrodes respectively. For this solenoid, with n = 3, $\mu = \mu_0 = 4\pi \times 10^{-7}$ H/m, $S = \pi\ (12.5 \times 10^{-3})^2$ m^2 and 1 = 0.33 m, equation (6.12) gives L = 16.8 nH. The resonant frequency of a parallel LC network is given by [69]

$$f = \frac{1}{2\pi\sqrt{LC}} \qquad (6.13)$$

and for C = 150 pF and L = 16.8 nH this gives f = 100 MHz. The actual (passive) resonant frequency was measured with an RF 'dip' meter and found to be ≈ 80 MHz. The discrepancy between the calculated and measured value is thought to be due to additional distributed capacitance associated with the MSS and its fixing, and solenoid end effects.

RF power was delivered to the centre of the top electrode via a 50 Ohm power cable and LC matching network.

The laser head input impedance (passive), observed with an an RF sweep generator and AC bridge, approached 50 Ohms, close to the resonant frequency at 83 MHz.

The transverse voltage at points along the length of the resonant (or near resonant) electrode structure were measured with a vector-volt meter at low RF input powers (a few mW), deliverd via the matching network. Voltage and phase variations along the electrodes of approximately 10% and 0.4 deg, 4% and 0.3 deg, 12% and 1.0 deg at 60, 80 and 100 MHz were observed respectively. As expected, the most uniform RF voltage distribution, which is conducive to a uniform discharge and hence an efficient laser pumping scheme, occurred with the 80 MHz RF signal (the one nearest to the 83 MHz resonant frequency).

Up to 200 W of RF power supplied by a wideband amplifier was available for laser operation. A discharge in $3He:1N_2:1CO_2$ + 5% Xe at 80 torr was maintained with 100 W RF power at 79.6 MHz, producing several watts of laser power in a 'good' single-dot mode. There was no problem striking the discharge and the RF power reflected from the laser head was reduced to less than 1 W by varying the matching network components and by making minor adjustments (typically $\leq$ 0.5 MHz) to the RF frequency, suggesting that there was a very good impedance match between the RF source and its load. At higher RF power levels ($\geq$ 150 W) a minor discharge leak occurred between two adjacent turns on the MSS. This was always between the same two turns and may have been caused by a poor solder contact or solder spike.

6.4.1 Discussion

The operation of a CO_2 waveguide laser excited by the parallel-resonant distributed inductance excitation technique using a 'novel' multi-start solenoid arrangement, as opposed to the multiple parallel discrete inductors commonly used in existing designs, has been successfully demonstrated.

The potential usefulness of the MSS becomes apparent when one realised that the laser discharge structure itself can be housed inside the coil. Furthermore, the coil turns do not have to be made of wire, but instead could be deposited as tracks on the waveguide ceramic. Schematic diagrams showing a possible design for this type of structure are presented in Figures 6.11(a and b).

The capacitance of the electrodes shown in the figure is approximately given by

$$C = \frac{\epsilon_0 \, \epsilon_r \, A}{d} \qquad (6.14)$$

where ϵ_0 is the free-space permittivity (8.8542×10^{-12} F/m), ϵ_r is the relative permittivity of the alumina substrate ($\simeq 9.0$), A is the electrode common area, and d is their separation.

For, say, 10 mm wide electrodes separated by 4 mm, equation (6.14) gives C = 200 pF/m. A suitable MSS might have the following parameters:- n = 4, $\mu = \mu_0$, and $S = \pi (10 \times 10^{-3})^2$ m^2, for which equation (6.12) gives L = 6.3 nHm.

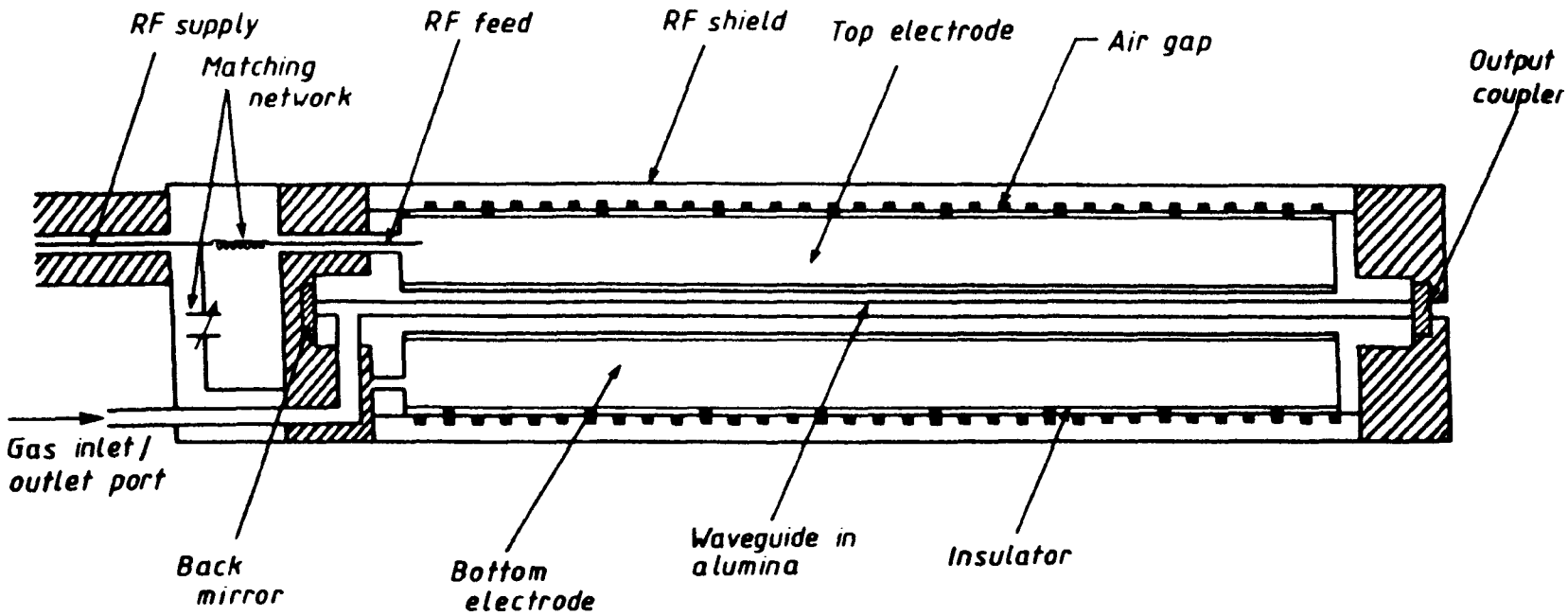

Figure 6.11. (b) Schematic of a proposed laser configuration for MSS distributed inductance resonant excitation (side view).

The resonant frequency of this structure, given by equation (6.13) is 142 MHz, lying within a band of frequencies considered to produce near optimum laser performance for waveguide bore dimensions between 1 and 3 mm [12]. The quality factor of the active discharge structure is given by

$$Q = 2\pi f C R_d \qquad (6.15)$$

where R_d is the discharge resistance.

For R_d = 200 Ohms (typical plasma resistance) for a 30 cm channel, and C = 800 pF/m equation (6.15) gives a Q of about 10; a suitable value for efficient power transfer between the RF source and its load.

There are a few points of interest regarding the RF properties of this device and the technology needed for its fabrication. Until now the electrode structure and the MSS were considered to be spatially independent. If, however, the electrodes are housed within the solenoid there will be an interaction between the H-field associated with the inductance and the E-field exciting the discharge; furthermore, the sense of the field directions are compatible and constructive. The H-field will tend to cause the gas electrons in the discharge region to spiral about the magnetic lines of force that are parallel to the waveguide axis (see, for example, ref. [89]). This may have a beneficial effect because it would invariably increase the electron collision rate for a given distance travelled radially, reducing the collision losses to the wall

boundaries, and hence the mean electron temperature may fall to nearer the optimum value for laser pumping. Currents will be induced on the surface of the metal electrodes constituting a loss, but because of the small skin-depth at VHF frequencies this is unlikely to be significant.

At resonance the total maximum instantaneous current flowing through the coils forming the MSS is given by [69]

$$I = \frac{V}{\sqrt{L/C}} \qquad (6.16)$$

where V is the maximum instantaneous potential across the electrodes. Here it is assumed that the total series resistance associated with the MSS is negligible compared to its reactance. For V = 150 V (typical electrode potential) and for the distributed capacitance and inductance values given above, equation (6.16) gives I = 8.0 A.

The magnetic field inside and along the axis of the MSS is given by [69]

$$H = \frac{N_t\ I}{N_c} \qquad (6.17)$$

where N_t is the number of turns per unit length along the solenoid, and N_c is the number of coils. For I = 8.0 A, N_t = 800 and N_c = 60, equation (6.17) gives H = 107 A/m. This magnetic field will tend to cause the gas electrons in the discharge to spiral about the magnetic lines of force that are parallel to the waveguide axis. The electron

ERRATA

Equation 6.18 should read

$$r = \frac{mv}{eB}$$

where $B = \mu_0 H$ (SI units). Consequently equation 6.20 and 6.21 are a factor u $(4\pi X\ 10^{-7})$ too small. Although the discussion is in essence correct, the influence of the magnetic field on the electron motion in the gas discharge has been over-estimated.

displacement radius is found by balancing the Lorentz force with the centripetal force, giving

$$r = \frac{mv}{eH} \tag{6.18}$$

where m and e are the electron mass and charge (9.1091×10^{-31} kg and 1.6022×10^{-19} C) respectively, and v is the component of electron velocity perpendicular to the magnetic lines of force. A typical electron energy of 1 eV would give

$$V = \sqrt{\frac{e}{m}} \tag{6.19}$$

For this case equation (6.18) becomes

$$r = \frac{\sqrt{m/e}}{H} \quad \text{or} \quad r = 2.38 \text{ μm per A/m} \tag{6.20}$$

The period of one revolution is given by

$$t = \frac{2\pi r}{V} = \frac{2\pi m}{eH} \quad \text{or} \quad t = 35.7 \text{ ps per A/m} \tag{6.21}$$

For H = 1 to 107 A/m from above, equations (6.20) and (6.21) give r = 2.38 μm to 22.3 nm with periods 35.7 ps to 0.33 ps (or 28 GHz to 3 THz) respectively. This suggests that there would be time for several hundred spiral orbits with a mean radius of hundreds of nanometers (which is comparable to the

mean free electron path at these gas pressures) during the 142 MHz RF cycle.

For this case, the magnetic field producing the electron spiral motion is time-dependent and 90 degrees out of phase with the electric field. Consequently, the sense of radius of arc traced by the electron vary with the RF field, and is superimposed on to the transverse motion induced by the electric field. The time-averaged electron path envelope is thus described by the surface of an 'hour glass' sitting between the electrodes.

The technology needed for the fabrication of the proposed structure already exists [55]. The thermo-diffusion bonding techniques developed at RSRE (Malvern, U.K.) permit the joining together of ceramic pieces to form waveguide channels allowing long or irregular channels to be manufactured in two halves before they are joined. Brazing techniques that allow the laser mirrors to be vacuum sealed on to the end of the ceramic structure have also been developed at RSRE. The exclusion of the MSS from the low-pressure gas region greatly reduces the probability of breakdown between adjacent coil elements. Lithographic masking and projection or laser deposition of insulating and conducting compounds are methods which permit the precise 'drawing' of tracks, such as the one needed to form the MSS and its fixing.

6.5 Hooting Modes in a CO_2 Waveguide Laser

The experimental work described in this section was a joint undertaking in collaboration with Dr. Christopher Hill (RSRE, Malvern, U.K.) who was visiting Hull University. The multimode resonator-matrix computer model outlined here and used for hooting mode identification, is due to Hill; for a detailed account the reader is referred to [83].

CW CO_2 waveguide lasers 'hoot' when, instead of the solitary resonator mode expected from a homogeneously broadened gas laser, two or more resonator modes lase simultaneously on a common laser line. The unwanted mode or modes, even if very faint and present only occasionally, can impede heterodyne measurements when a 'clean' frequency spectrum is required. 'Hooting', or mode beating, is due to interference between different transverse modes of a laser resonator (not to be confused with multi-line lasing). The CO_2 waveguide laser linewidth is pressure broadened at $\sim$ 4-5 MHz/torr [90], and at typical operating pressures of 50-250 torr is often broad enough to include more than one resonator mode under its lineshape. In general, for homogeneously broadened lasers, only the resonator mode with above threshold gain and the highest gain/loss ratio will lase, yet stimultaneous lasing of more than one mode within a single line has been reported [91].

A batch of apparently 'identical' waveguide lasers producing single line (say, P20), and predominantly single mode (say, quasi-TEM_{00}) outputs may produce outputs

with very different spectral contents. These might include:- no hoot signal even during small perturbations, such as slight cavity length adjustments or mirror misalignments; a hoot signal when perturbed; a hoot signal even when unperturbed. A hooting laser has a characteristic frequency spectrum, most noticeably within the bandwidth of a CMT detector, typically between 0-100 MHz, although the precise values seem unpredictable. In the simplest case of a single beat note, arising through interference between a strong principle mode and a weak (unwanted) mode, tuning through the laser signature may affect the presence of the beat note (it is either there or not), but not to any great extent its frequency.

A hoot-free waveguide laser might be one with mode-discriminating elements such as a long and small bore waveguide, or a Case III reflector [43], although the conditions that support mode beating are not so well understood. In this section the tranverse modes of a deliberately simple and hoot-prone RF-excited CO_2 waveguide laser are derived by solving a matrix equation for the resonator modes. In this way the beat notes between the possible mode pair combinations are determined as functions of mirror angular misalignment and compared to experimental determinations.

The experimental apparatus is shown in Figure 6.12. The laser construction was similar to that of the z-fold laser described in Chapter 4, except here the resonator consisted

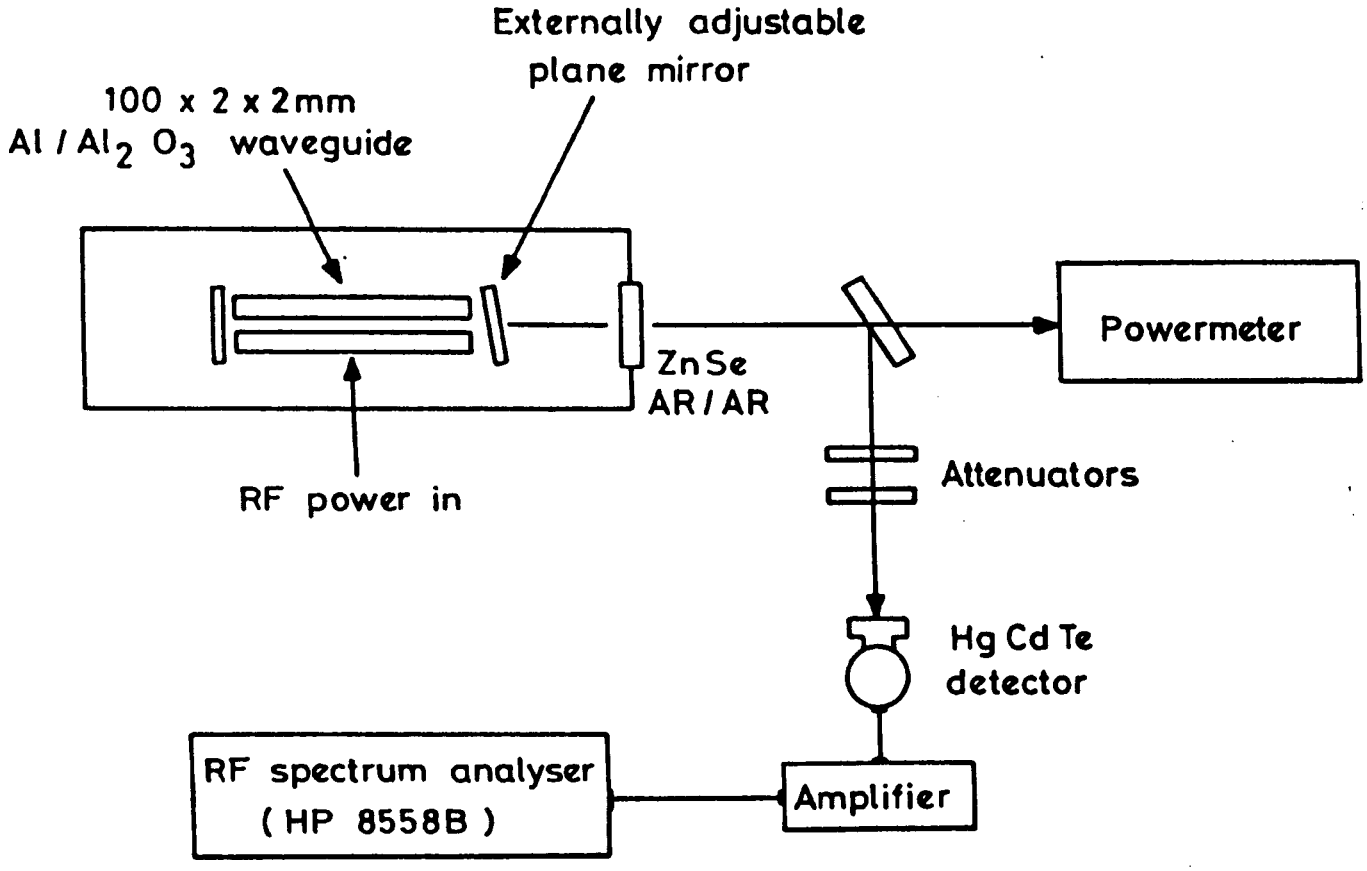

Figure 6.12. Experimental apparatus.

of a single segment hybrid waveguide (2 x 2 x 100 mm) placed equidistantly between two Case I reflectors separated by L = 104 mm. The germanium back mirror total reflector was mounted on a bender bimorph, and the zinc selenide 95% reflectivity output mirror was held in an externally adjustable mount. Both mirrors were pre-aligned on a He-Ne laser aligment bench using the technique described in Chapter 5. A 145 MHz RF generator (Dressler model D200s), with an impedance matching network and RF feed-through, suplied typically 20-40 W to the discharge in a $3He:1N_2:1CO_2$ gas mixture. Laser power up to 1.3 W was measured with a thermopile (Coherent Model 201) placed close enough so as to avoid aperturing of the beam. The presence and frequency of a beat signal was detected with a liquid nitrogen cooled HgCdTe (SAT) detector placed in the path of a greatly attenuated beam portion, and displayed on an RF spectrum analyser (Hewlett Packard Model HP855B).

The laser waveguide mode discrimination was expected to be fairly weak, firstly because of the large guide Fresnel number N = 1 [92], and secondly because of previous observations of high-order modes in the laser output [93]. Initial determinations of the beat signals as functions of the output mirror 'optical' tilt angle (i.e. twice the angle of mirror rotation) were hindered by the poor angular resolution of 0.4 mrad, and by an inherent tilt with translation of the imperfectly mounted bimorph. The slightest adjustment of the output mirror tilt produced beat

note shifts of ≥ 10 MHz. The bimorph cavity length translations were performed to tune a mode to line centre and maximise the laser output power. The smooth beat note changes of tens of megahertz observed with the voltage ramp applied to the bimorph, corresponding to translation over approximately one free-spectral range, were much greater than the expected (almost negligible) mode-pulling effects [94].

Modifications of the output mirror mount greatly improved its angular resolution to 0.007 mrad, this time measured with a He-Ne laser back reflection on a graticule screen. The bimorph was remounted and found to be tilt-free during translation (confirmed by observing the He-Ne laser reflection during the aligment process as the voltage ramp was applied). The modified 'well'-aligned laser hooted only occasionally, although persistent hooting was easily induced with small output mirror tilts. The nearly linear variation of hoot frequency with mirror tilt (about the Y-axis) is presented in Figure 6.13, and shows a surprisingly steep slope of 65-70 MHz/mrad. The transverse beam profile was double-dot (EH_{21}-'like').

Measurements of the bimorph tuned maximum laser output powers as a function of tilt about the X axis, for near zero Y-tilt are presented in Figure 6.14. The peak laser power occurred at what appeared to be zero X-tilt which corresponded to the same micrometer tilt control reading that gave the minimum beat frequency. The minimum beat frequency did not reach zero, but turned around at 1.5 MHz (the

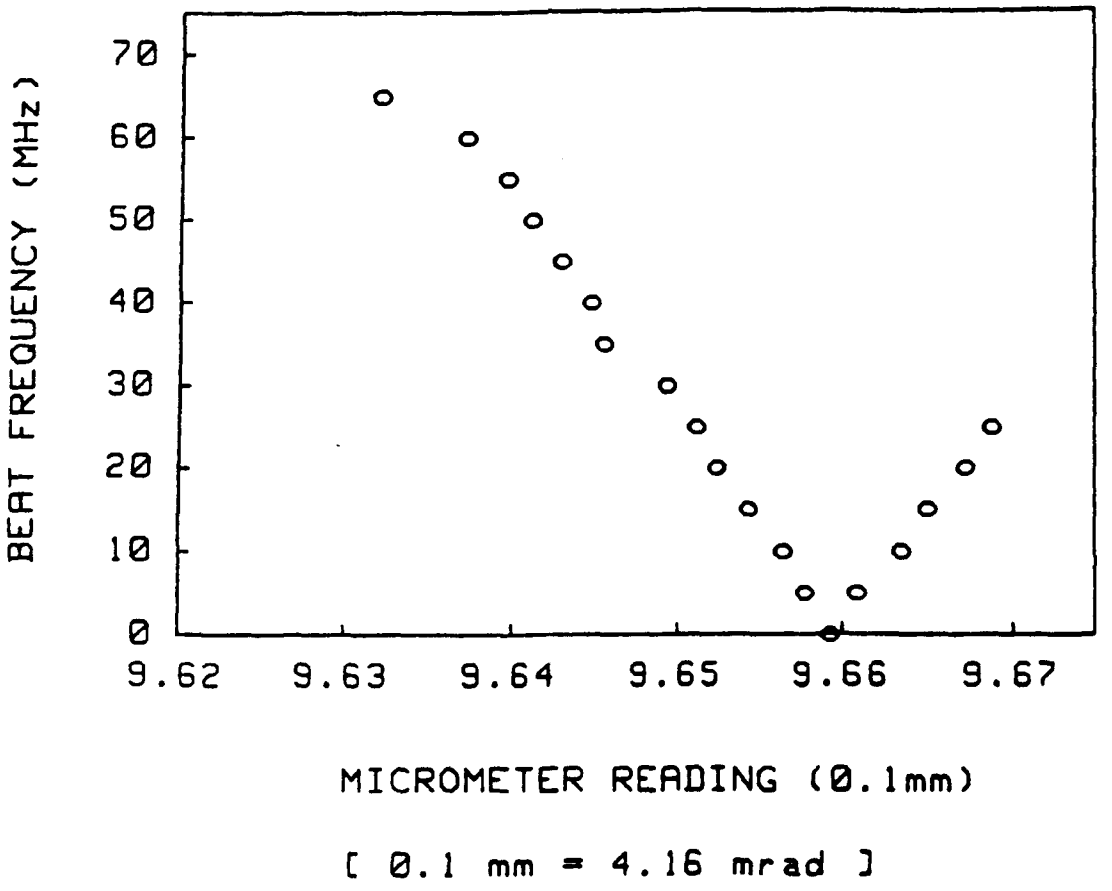

Figure 6.13. Hoot frequency as a function of mirror x-tilt. Hooting occurs over the range ≈ 4.6-6.4 mrad (50 torr 3He:1CO_2:1N_2, RF frequency 145 MHz, λ = 10.6 μm).

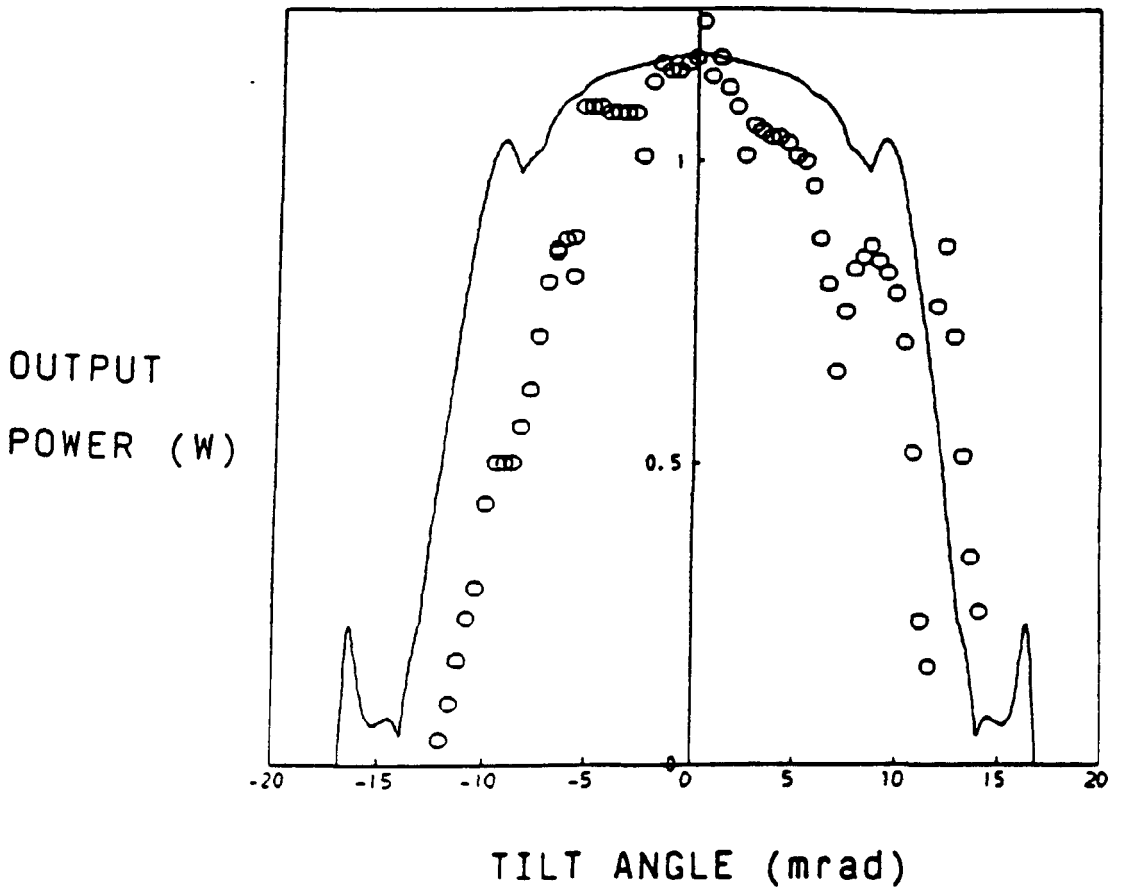

Figure 6.14. Circles: measured laser output power as a function of mirror x-tilt (50 torr 3:1.1, 145 MHz, input power ≈ 26 W, y-tilt ≈ 0, λ ≈ 10.6 μm). Solid line: laser power predicted by distributed-loss Rigrod equation [62]. We take the beam area as $A_b = \pi a^2/4$ and estimate the effective mirror reflectances as $R_1 \approx 0.99$ and $R_2 = 1 - T_2 \approx 0.95$; we take a small-signal gain of 0.9 cm^{-1} and a distributed loss coefficient $2\alpha = -(1/L) \ln(|\gamma|)$ where γ is the eigenvalue of the lowest-loss resonator mode at 10.6 μm. A saturation intensity $I_s = 3.1$ KW cm^{-2} then gives reasonable fit to the measured power.

extremum at the zero tilt position was expected from symmetry) with a single-dot (EH_{11}-'like') transverse beam profile as expected. It seems that minimising the beat frequency produced laser mirror alignment to within ± 0.05 mrad.

6.5.1 Theory and Discussion

A passive waveguide resonator has a spectrum of resonator modes each with its own round-trip loss and frequency, and associated with an axial mode integer $q = 2L/\lambda$ (often dropped when the wavelength (λ) dependence is not crucial) and two transverse mode integers r and s, for the X and Y directions respectively. The transverse modes of an 'ideal' dual-Case I waveguide laser should be pure EH_{mn} waveguides modes, with well defined losses and frequencies. In general each resonator mode can be described as a linear combination of waveguide modes, with a specific, yet not so easily determined, loss and frequency.

The theoretical treatments that follow assume that the presence of the active medium does not greatly affect the transverse form of the resonator modes, or the weighting of their waveguide mode components, or their relative (not absolute) frequencies. Further, it is assumed that the presence of a weak hooting mode implies no great change in the composition or loss or frequency of the main mode. In addition, non-uniformities and imperfections of the laser structure and its active medium, although they are invariably

responsible for the incompleteness of the mode competition giving rise to the hoot signal, are ignored. As regards tilting, the results of previously reported [95] passive resonator treatments and their associated assumptions are applied.

The waveguide mode frequencies for an 'ideal' passive dual-Case I resonator are approximately given by [92]

$$\nu_{q,mn} \simeq \frac{qc}{2L} + \frac{c\lambda}{32}\left[\frac{m^2}{q^2} + \frac{n^2}{b^2}\right] \qquad (6.22)$$

where 2a and 2b (in this case 2.00 and 1.98 ± 0.02 mm) are the guide width and height respectively. The beat frequencies for several likely mode combinations with a = 1.00 to 1.10 mm, b = 1.00 mm, and λ = 10.6 μm are presented in Figure 6.15. Evidently, the difference frequency $|\nu_{q\ 4\ 1} - \nu_{q\ 1\ 1\ 1}|$, lying within the CMT detector bandwidth, is a strong candidate. It should be almost zero for 2a = 2.00 mm and λ = 10.25 μm (R20 on 001-100), and can be reasonably expected to lie below 100 MHz whatever the common line.

Other less likely candidates include beating between degenerate pairs of modes (for example between $EH_{2\,1}$ and $EH_{1\,2}$) in an asymmetric waveguide, and between modes polarised parallel with the aluminium waveguide walls and high loss, not quite orthogonal (would be perpendicularly) polarised modes. The list of possible 'hooting pairs' ends when waveguide losses (rising as $m^2 + n^2$) drive them below the gain threshold for lasing.

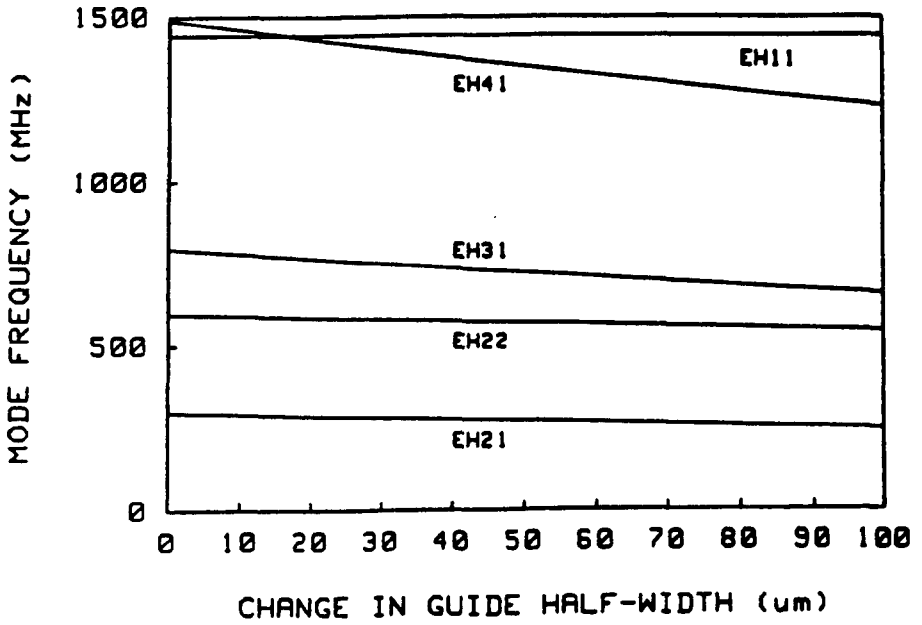

Figure 6.15. Relative transverse mode frequencies $\nu_{mn} - \nu_{11}$ of the well-aligned passive resonator, as functions of waveguide half-width a = 1.00 mm + δa (b = 1.00 mm, λ= 10.59 μm). The x-axis and the horizontal line at ≈ 1440 MHz refer to the EH_{11} modes of adjacent axial modes.

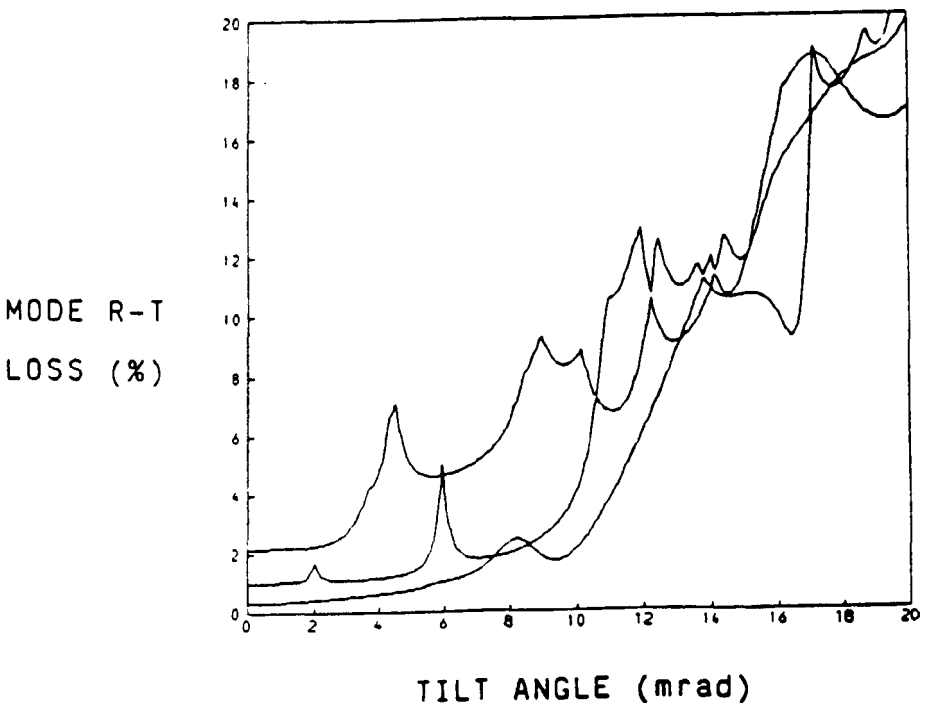

Figure 6.16. Predicted round-trip losses $(1 - |\gamma_{r1}|^2)$, as functions of mirror x-tilt, for three lowest-loss resonator modes formed from EH_{m1} guide modes (m = 1,2,....20).

The treatment below predicts only the dependence of the beat signal on tilt, without positive identification of the beating pair. A complete model of the hooting behaviour of a waveguide laser would include several mode pair candidates, extremely accurate waveguide dimension determinations (to within a fraction of a wavelength), complex calculations of resonator mode gain/loss ratios, and laser rate equations.

The hooting laser computer model due to Hill [83] may be summarised as follows:- The eigenvectors (resonator modes) and eigenvalues (complex round-trip propagation coefficients) are extracted from the resonator round-trip matrix (product of waveguide mode propagation matrices). With these the EH_{mn} guide propagation coefficients k_{mn} and the tilt coupling coefficeints $C^{m'n'}_{mn}$ are determined. Neglecting the Y-tilt (always $<< \lambda/a$), the resonator mode difference frequencies between the sets formed from combinations of EH_{m1} ($m = 1,2,3, \ldots.$), EH_{m2}, etc. respectively, are evaluated as a function of X-tilt.

The measured output power and several resonator modes predicted losses (with the model including up to EH_{20}) as a function of X-tilt are presented in Figures 6.14 and 6.16 respectively. The envelope values obtained from Figure 6.16 were incorporated into a Rigrod-type model [62] to give the solid line in Figure 6.14. Since in the experiment the laser output power was maximised (with bimorph translations) for every power reading taken, its performance should be governed

by the envelope behaviour, and so a direct comparison between the measurement points and the solid line is possible. There is reasonable agreement, much as in [95] for one half of the curve at least. The change in the predicted hoot frequency, over the tilt range covered in Figure 6.13, is shown in Figure 6.17. The slopes are all between 50 and 70 MHz/mrad, and, in view of the many possible flaws in the experimental and theoretical determinations, are surprisingly close to the measured value of 65-70 MHz/mrad. The choice of guide width was a little unfortunate insofar as there is little discrimination between the slopes of the various mode pairs; unlike a second set of curves in Figure 6.18 for 2a = 1.6 mm, for example. Consequently, the mode pair responsible for the hoot signal could not be positively identified.

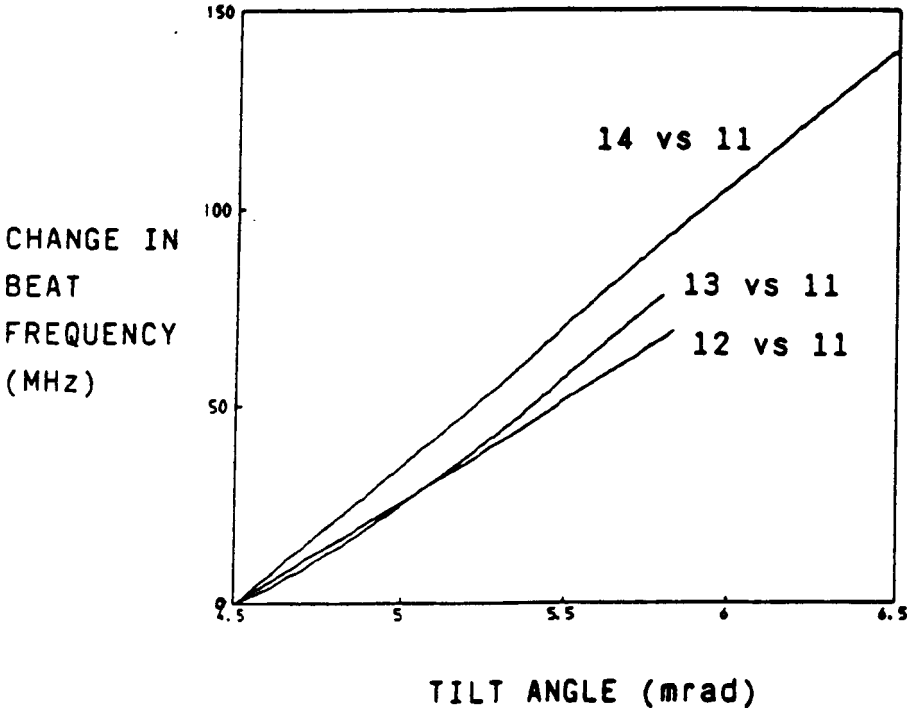

Fig. 6.17. Predicted changes, as functions of mirror x-tilt, of the beat frequencies $\nu_{21} - \nu_{11}$, $\nu_{21} - \nu_{11}$, and $\nu_{41} - \nu_{11}$ (L = 104 mm, 2a = 2.00 mm). The slope for $\nu_{41} - \nu_{11}$ reaches $\approx$ 70 MHz mrad^{-1} (compare with Figure 2) but is not very different from the others.

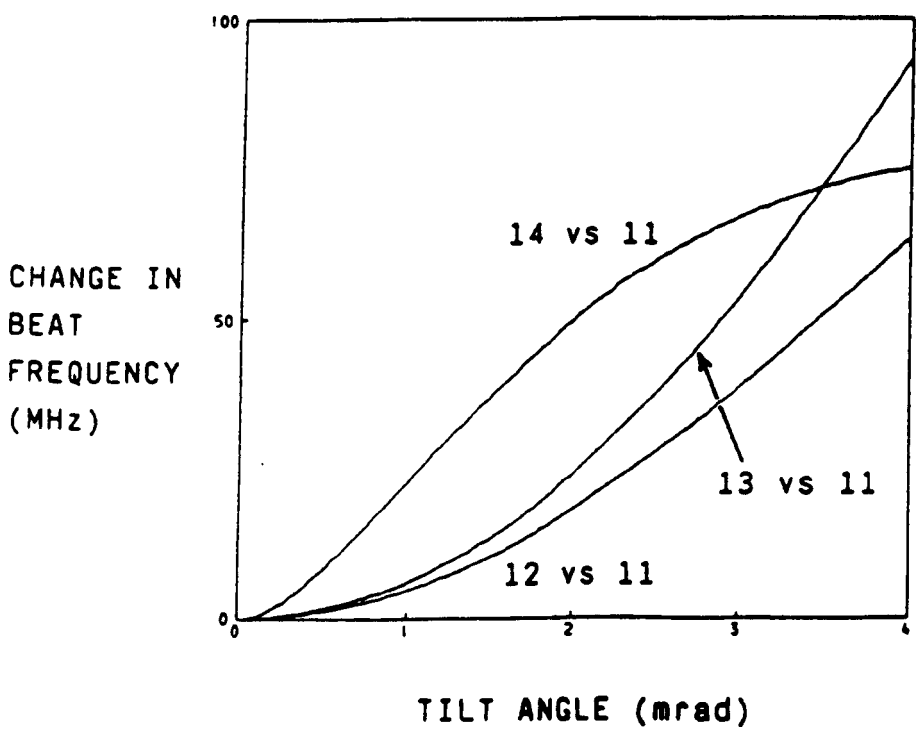

Fig. 6.18. As Figure 6.17 but 2a = 1.6 mm; over this tilt range the hoot slopes should be easy to tell apart.

CHAPTER 7

LASER AMPLIFICATION

Summary

This chapter outlines the fundamental principles of optical amplification and investigates the renewed interest in laser amplifiers for LIDAR applications. Of particular interest is the amplification of chirp pulses, such as the ones used in heterodyne range finders and velocimeters, and their distortion resulting from the inherent frequency dependent gain and saturation behaviour, and anomalous dispersion in the active medium. Practical schemes are examined for the injection of a probe beam into a waveguide amplifier, and the spatial filtering and reduction of amplified spontaneous emission noise at the output of a pre-amplifier: these techniques will be applied in the experimental determinations described in Chapter 8.

7.1 Laser Amplifiers for Coherent LIDAR: An Overiew

Optical amplification can be considered in two main categories, namely, power amplification and small signal amplification. The two differ in the intensity level of the input signal to be amplified. Power amplification, as it suggests, involves the amplification of high intensity signals where gain saturation is an important consideration. On the other hand, small signal amplification (or pre-amplification) involves the amplification of low intensity signals where the signal to noise ratio is important. The design of an amplifier is therefore very much dependent on its intended application and the priorities attached to gain, saturation of gain, gain bandwidth and noise.

In this section the discussion is confined to a review of laser amplification techniques in the infrared, namely with the carbon dioxide molecule, as the active species. Laser action occurs between vibrational modes at wavelengths around 10 μm. It is, however, worth comparing the fundamental amplifier characteristics of the CO_2 molecule with a few alternative laser gas media lying in the infrared spectrum. A typical low pressure (10-200 torr) static CO_2 laser gas mixture may exhibit small-signal gain coefficients of up to 1%/cm (cw) and 5%/cm (pulsed), saturating between 10 W/cm² to 10 kW/cm² with pressure broadening coefficients of about 5 MHz/torr. These gains are rather modest when compared to the gains available with He-Ne, He-Xe or CO gas mixtures. The He-Ne and He-Xe neutral gases lase around 3 μm with gains of 50-100%/cm saturating at less than 100 mW/cm².

The CO molecule lases around 5 μm with pressure-broadened gains similar to CO_2 at room temperature, saturating between 1 W/cm² - 1 kW/cm², but with gains up to 10%/cm at cryogenic temperatures.

Although the high gains available with these gases are desirable, it should be noted that in laser systems an amplifier is often used to amplify laser light. Consequently, the laser and its amplifier need to operate at the same wavelength, either by using a common atomic or molecular laser transition, or by tuning the laser to lie within the amplifier bandwidth. The implication is that either the laser or the amplifier must operate to complement the other. The He-Ne and He-Xe gases offer high gains but do not provide for a powerful laser. Also, the narrow linewdith associated with their atomic transitions does not cater for large frequency shifts incurred by the signal to be amplified, as is often the case for the Doppler shifted return signals in LIDAR systems. The CO and CO_2 gases, on the other hand, offer a compromise, whereby a subtle difference in the operating conditions of the laser and amplifier can permit high power extraction for the laser with moderate unsaturation gain for the amplifier. The difference need not be that subtle; for example, the laser could be a TEA laser and the amplifier could be a low pressure cw discharge cell. This versatility is not accommodated by other laser media in this spectral region. The application of the CO gas mixture, although as versatile as the CO_2

mixture, is hindered by the need for cryogenic operation conditions.

Among the solid media, the most important material for laser amplifiers is neodymium glass operating at 1.06 μm. The gain bandwidth in neodymium glass is of the order of 100 GHz, amply sufficient for the reception of LIDAR signals. High energy laser pulses at this wavelength (above eye damage threshold energies) are required to counter the effects of atmospheric absorption (1.06 μm lies outside the 3-5 and 8-14 μm atmospheric transmission bands). Consequently, a search has continued for materials which emit radiation beyond the tranmsission cut-off of the eye's vitreous humour, which is about 1.4 μm.

As mentioned above, there are essentially two types of laser amplifier, the power amplifier and the pre-amplifier. In LIDAR parlance the power amplifier is often associated with a transmitter system and the pre-amplifier with a receiver system. At this point we may ask, why bother with optical amplifiers at all, why not build more powerful lasers and use more sensitive detectors with larger antennas? There may be several answers to this question, but for example, consider a Heterodyne Chirp CO_2 Laser System (Hulme, 1984 [96]). This laser rangefinder system uses a few watts output to provide a local oscillator and transmitter beam. The transmitter beam is modulated by an acousto-optic modulator with 'chirp' pulses. The pulses are 4 μs duration and are repeated every 33 μs; the modulation frequency

swings linearly during the pulse from 53 to 67 MHz and back again in an up-down chirp fashion. If it were thought necessary to increase the range of the system, or improve the discrimination of its range and velocity determinations, one might consider the following options:- the transmitter beam power could be increased by using a more powerful laser or by placing a power amplifier in the path of the beam; alternatively, the signal to noise ratio at the detector in the receiver system might be improved by inserting a pre-amplifier between the receiver optics and the detector.

There are at least two reasons why a more powerful laser might be unsuitable. Firstly, the laser frequency stability and not power extraction is of prime concern where the laser is concerned and the two are not generally compatible. Secondly, in this system the acousto-optic modulator specifications do not permit higher power operation. The only suitable action with this option is to place a power amplifier after the acousto-optic modulator stage. This immediately puts several requirements on the amplifier design. The amplifier must provide gain at input power levels of a few watts at the 10.6 μm (P20) laser wavelength. This gain must be available at up to 67 MHz frequency offset from line centre for at least 4 μs duration. A likely candidate, for example, would be the waveguide laser amplifier [47] which accommodates a high pressure discharge with the required pressure-broadened gain linewidth. The amplifier bandwidth is afforded at the cost of the available

gain. A static gas device of this type with an unsaturated gain of 0.5%/cm would need to be nearly 1.5 m long to deliver twice the input power. Techniques to improve the gain, such as gas flow, generally increase the net gain to device volume (or weight) ratio, making this an undesirable option where compact field devices are required. There are additional complications associated with power amplification, namely power broadening [47] of the amplified signal, frequency/ temporal dependent saturation behaviour [97], anomalous dispersion [98] and distortion [99].

The second option involves the use of a pre-amplifier placed between the receiver optics and the detector. The same considerations that applied to the power amplifier are evident here also, with the additional criterion that the amplifier bandwidth be large enough to accommodate Doppler shifts in the incoming return signal in addition to the 67 MHz frequency offset from line centre. For 10 μm systems, Doppler shifts of around 200 kHz per m/s are observed. Hence a target travelling radially at the speed of sound in air would give ∿ 65 MHz Doppler shifted return signal.

A third option, not mentioned above, would be to use a common amplifier for both power amplification and pre-amplification [100]. Here the same gain medium is shared by the outward and inward bound signals. The obvious problems of synchronisation, and the trade-off between the unsaturated and saturated gains by the compromised operation conditions, may be outweighed by the efficiency use of space in this sharing arrangement.

So why not use more sensitive detectors? The variance in the detector element signal current is proportional to the optical power in direct detection, and to the field in heterodyne detection. In heterodyne receivers the local-oscillator-induced shot noise can be made to dominate all other noise sources at the output of the detector pre-amplifier circuitry, whereas in direct detection receivers Johnson noise dominates. Consequently the signal-to-noise ratio (SNR) is proportional to the signal power in direct detection and to signal field in heterodyne detection. Thus, under all conditions one would expect heterodyne detection to give a larger SNR [101]. The introduction of an optical pre-amplifier would not be beneficial for heterodyne receivers unless it amplified a signal above a minimum detectable energy. Optical pre-amplification in direct detection receivers would be advantageous if the noise-in-signal could be reduced.

Unfortunately an optical pre-amplifier is inherently noisy. Photons produced by energy transitions other than stimulated emission contributions to the signal gain, are themselves amplified by the gain medium to increase the noise-in-signal. This spontaneous emission noise is broadband, although the amplified spontaneous emission noise (ASE) has a structure determined by the amplifier passband. Both the unamplified and amplified noise powers (including thermal noise generated by the CO_2 discharge), travelling in the direction of the incoming signal and falling on the

detector, will create additional noise current at the detector output. Evidently, the effective noise figure is particularly high for amplifiers having broad gain profiles [102,103]. Considerable improvements are possible by housing the gain medium within a noise reduction structure [104,105] forming a low noise pre-amplifier. A typical noise reduction structure might consist of two aperture stops with a lens and polariser inserted between them. When these optical elements are arranged to form a system with an acceptance factor (defined in Section 7.4) equal to unity, common to a class of structures designed for optimum SNR, the noise emanating from the amplifier is contained within a solid angle occupied by a single black-body mode. This type of filtering takes advantage of the incoherence of the ASE and its random polarisation. Additional filtering may be achieved by the introduction of a narrow band transmission filter [106], or by cold shield coupling between the pre-amplifier and the detector. It turns out that the equivalent noise input power (NEP) is limited to a quantum noise level of about one photon per second per hertz. This represents an improvement of five orders of magnitude over the conventional direct detection limit in photoconductive HgCdTe detectors at 10 μm, and is comparable with the heterodyne noise equivalent power per hertz under ideal conditions. It should be appreciated, however, that the amplified noise reaching the detector is G times the NEP (where G is the amplifier net gain). Furthermore, the SNR associated with a direct-detection

receiver may be reduced appreciably by specular interference noise at the detector element.

A selection of previously reported laser amplifier design specifications and performance details, with the authors' comments, is presented in Appendix B for reference purposes and summarised in Table 7.1. These examples have been chosen to demonstrate the typical operating expectations of both power amplifiers and pre-amplifiers. After surveying this literature one might reasonably conclude that compact high net gain devices are associated with the following:

* Low pressure discharge
* Pulsed discharge excitation
* Gas flow
* Folded optical paths of several metres

It is also apparent that amplifiers enjoying large optical bandwidths, or unsaturated gain at high input powers, or continuous gain, or a combination of these, do so at the expense of the available gain. Pre-amplifiers without noise reduction structures tend to have noise equivalent powers at least two or three orders of magnitude greater than the theoretical minimum. Since the NEP is strongly dependent on the geometry of the pre-amplifier it is conceivable that an amplifier with a folded gain path could, by careful design, exhibit an inherent ASE noise reduction.

Although the gain figures displayed in Table 7.1 are encouraging, it should be appreciated that the experimenters

REFERENCE	DESCRIPTION	DEVICE SIZE	EXCITATION	GAS MIXTURE He	CO_2	N_2		GAS PRESSURE Torr	GAS FLOW CM./S	GAIN LENGTH CM	NET GAIN dB	GAIN COEFFICIENT %/CM	SATURATION INTENSITY W/CM^2	NEP Ph./S/Hz	POWER BROADENING $\frac{\Delta\nu_{3dB}}{\Delta\nu}$
KLEIN AND ABRAMS 1975	1.65mm Ø BORE IN BeO. WAVEGUIDE POWER AMPLIFIER. WIDEBAND GAIN LINEWIDTH	~1m LONG	CW DC 60-180 W/CM^3	3.3 7 1.5	1 1 1	1.1 1.1 1.3		0-200	0-600	77	2.5-17.5	1.2-3.7	1K-6K	-	150 AT 100 Torr 80W O/P
DEZENBERG AND MERRITT 1967	7.7CM Ø DISCHARGE TUBE MULTIPATH CELL LASER POWER AMPLIFIER	~1.5M LONG	CW DC ~10W/GM^3	3.5	0.5	1		5	1	4-30 x 150	1-9	0.05	65	-	
HIESLMAIR ET AL 1970	4.7 CM Ø DISCHARGE TUBE MULTIPATH LASER PRE-AMPLIFIER	~0.65M LONG	CW DC	2.9	1	1.4		5	?	16 x 65	17-39	0.4-0.7	50	~100	-
LOTSPEICH 1975	1.9CM Ø DISCHARGE TUBE TWO STAGE LASER PRE-AMPLIFIER	~0.72M LONG	CW DC	5	1	0.6		8	12	72	1.5-3.9	0.5-1.5		40-90	-
JACKSON ET AL 1987	4MM SQUARE BORE DISCHARGE CHANNEL. PRE-AMPLIFIER MODULE WITH NOISE REDUCTION STRUCTURE	~0.37M LONG	CW RF 5-40 W/CM^3	3	1	1	5% Xe	10-50	0	37	0.8-1.3	0.5-0.8		1-2	-
PSI LDP-30	RECTANGULAR DISCHARGE CROSS-SECTION. MULTIPATH LASER PRE-AMPLIFIER	14" x 9.25" x 7.25"	0-10Hz PRF DC	6.5 8.2	1.8 0.8	1.5 0.8	0.2 CO_2 0.2 CO	5-150	0.14l PER MIN.	7 x 30	28	3		~7000	-
MALOIA 1985	ANNULAR DISCHARGE CROSS-SECTION. SIMULTANEOUS LASER POWER - AND PRE-AMPLIFIER. MULTIPATH	~1.2M LONG	≤100Hz PRF RF							600		1.8-2.2			
XIN AND HALL 1987	ANNULAR DISCHARGE CROSS-SECTION. MULTIPATH HERRIOTT CELL LASER POWER AMPLIFIER/PRE-AMPLIFIER	8"x 8"x 24"x	RF 130 W/CM^3	3	1	1	5% Xe	10-50	0	19 x 26	7.5CW 30* PULSED	0.35 1.4*	850		

* PREDICTED

Table 7.1. CO_2 laser amplifier survey summary.

have used probe lasers to complement their amplifiers. To obtain the gains suggested and avoid gain narrowing, the laser signals being amplified must be generated by a laser with a linewidth less than or equal to the gain bandwidth of the amplifier gain cell.

A second consideration is the amplifier gain temporal distribution in pulsed amplifiers. The gain pulse duration is, roughly, inversely proportional to gas pressure. Evidently, there must be a coincidence between the input optical pulse and the gain pulse (ideally at maximum gain), and, in addition, the gain experienced by the optical pulse should be unchanged during its transit through the amplifier if gain modulation is to be avoided. The former criterion may present a problem if a high pressure pre-amplifier is incorporated into a laser rangefinder system, where the return pulse arrival is determined by the target range. The amplifier gain pulse-to-pulse stability and the optical pulse-to-pulse frequency stability influence the signal to noise ratio at the amplifier output. Gain fluctuations may be the limiting noise mechanism rather than ASE or background noise.

The amplifier gain linearity might be important if the returned LIDAR pulse amplitude is to remain undistorted. Other practical considerations include the optical coupling of the pre-amplifier input to the receiver optics and its output to the detector and their associated insertion losses, the reduction of the receiver field of view, anomalous

dispersion effects, mode distortion effects, and the suppression of self-lasing.

A more detailed analysis of the problems mentioned above can be found in the literature [107,108,109]. Despite these problems, signal to noise ratio enchancement in direct detection LIDAR systems has been reported. These examples involve the inclusion of the PSI laser pre-amplifier [110,111] in laser rangefinding systems, operating with a TEA [107] or hybrid-TEA [108] CO_2 laser. The pulse-to-pulse frequency shifts of the TEA laser axial mode relative to the gain cell centre frequency resulted in a lower SNR, albeit with a higher than anticipated amplifier gain of 25 dB. The hybrid TEA laser system, on the other hand, with its single frequency 3 MHz linewidth pulses, experienced gain in the signal level of the LIDAR return of approximately 29 dB. Taking into account the pre-amplifier optical insertion loss factor of 4, this gave a net sensitivity enhancement of 23 dB (200-fold improvement), with no increase in the measured noise level.

7.2 Laser Amplifier Theory

The principal parameters that describe a laser amplifier are its net gain, small-signal gain coefficient, saturation intensity, noise equivalent input power and transition frequency bandwidth. The frequency dependences of gain and saturation intensity give rise to the phenomena of 'gain narrowing' and 'power broadening' respectively. The temporal

behaviour of these frequency dependences, during for example the amplification of chirp pulses, is an important consideration in amplifier design for LIDAR applications. In this section the determination and the dependences of the basic amplifier parameters are discussed. In the following sections practical techniques are described for the injection of a laser signal into a waveguide amplifier, and the reduction of the amplified spontaneous emission noise at an amplifier output. Later, in Chapter 8, experiments (incorporating these techniques) with a waveguide power amplifier, and a non-waveguide pre-amplifier, are described.

The mechanisms of stimulated emission and the population inversion responsible for the properties of an amplifying media, namely its small-signal gain, its saturated gain, and the accompanying spontaneous emission noise, are described in standard text books (see, for example, ref. [112]). From the standard text and the overwhelming amount of literature on CO_2 lasers, the following relevant principles are summarised:-

Carbon dioxide is a linear triatomic molecule with three different modes of vibration, namely the deformational (bending), symmetric and asymmetric stretch. A simplified energy-level diagram for the CO_2 molecule showing its principal vibrational transitions is presented in Figure 7.1. The important upper-laser level excitation mechanisms in a CO_2 laser mixture are the direct-electron impact excitation, and the electron impact excitation of nitrogen and carbon

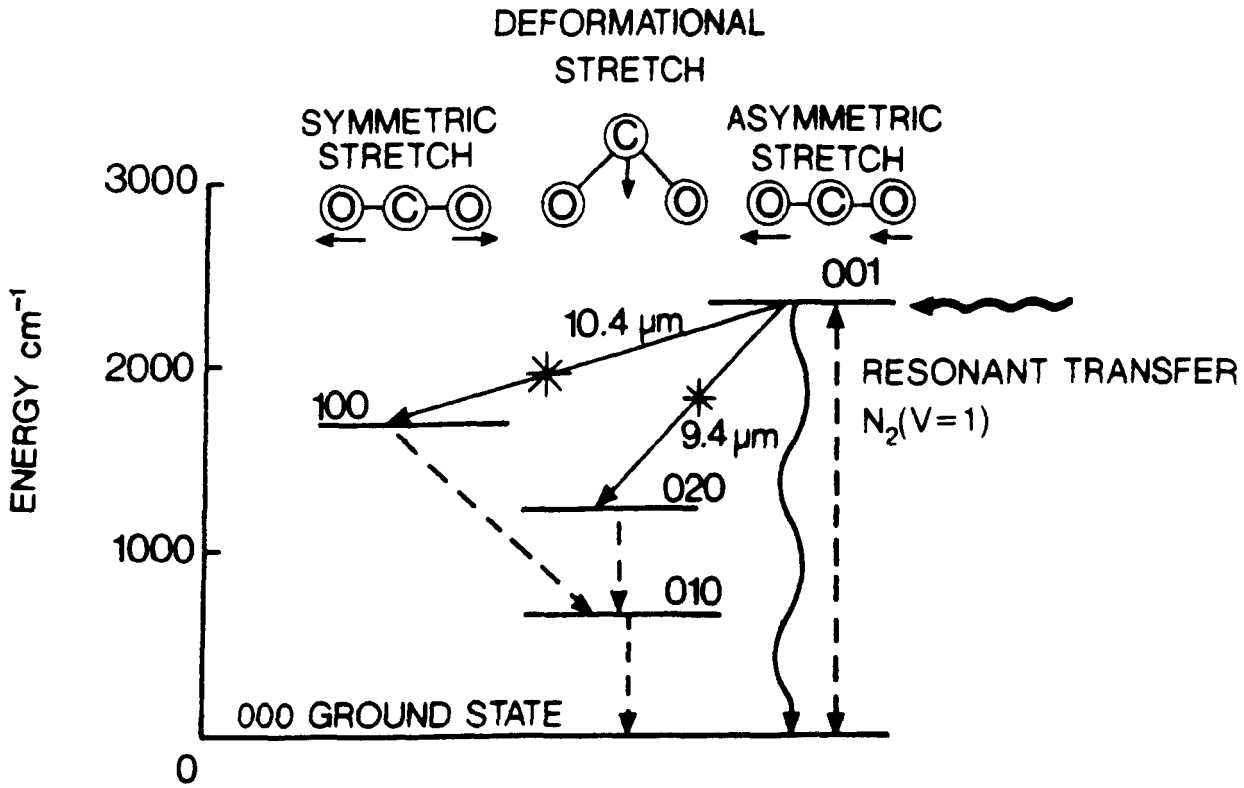

Figure 7.1. A simplified energy level diagram for the CO_2 molecule.

monoxide (dissociated from CO_2) resonant energy transfer. The lower laser level relaxation mechanisms are essentially those of radiative and collisional (via helium) relaxation. The CO_2 laser transitions are homogeneously broadened, that is, all the CO_2 molecules have identical Lorentzian line (gain) shapes that peak at the same frequency. The collision (pressure) broadened unsaturated linewidth ($\Delta\nu$) of the 10.6 μm, laser transition is approximately given by the empirical relation in [90]

$$\Delta\nu = 7.58\ (\psi_{CO_2} + 0.73\ \psi_{N_2} + 0.6\ \psi_{He})\ p\ \left(\frac{300}{T}\right)^{1/2}$$

where ψ is the fraction of the gas x, p is the total average pressure in torr and T is the absolute temperature of the gas. Hence at room temperature, a 3 He + $1N_2$ + $1CO_2$ typical laser gas mixture is pressure broadened at a rate of $\sim$ 5.4 MHz per torr.

Expressions relating independent amplifier parameters such as overall length, small-signal gain coefficient, and linewidth to system design requirements such as overall gain, output power, and output linewidth, including the effects of distributed loss and gain saturation, have been derived in [47].

The frequency-dependent saturation of small signal gain in a homogeneously broadened amplifier is described by

$$g(\nu) = \frac{g_0}{[1 + \frac{I(\nu)}{I_S(\nu)}]\ [1+\delta^2]} \qquad (7.1)$$

where $g(\nu)$ is the saturated gain at frequency ν, g_0 is the small signal gain at line centre, $I(\nu)$ and $I_S(\nu)$ are the beam intensity and saturation intensity at frequency ν, and δ is the normalised frequency detuning given by $\delta = 2(\nu-\nu_0)/\Delta\nu$, where $\Delta\nu$ is the unsaturated gain linewidth and ν_0 is the line centre frequency.

The mechanism of saturation is well known; transitions due to stimulated emission and absorption tend to equalise the populations in the pair of levels coupled by the radiation so the net inversion, and hence gain, tends to zero.

There are many techniques for measuring the saturation intensity using both oscillator (Chapter 3) and amplifier configurations. The saturation intensity can be estimated from experimental results on the dependence of the low-signal gain and the output power on the pressure in the active medium. Another way to measure I_S is to measure the gain of the active medium for various levels of the probing radiation.

Saturation flux increases with pressure (owing to molecule-molecule collisions) and with the magnitude and frequency of the applied electric field (owing to electron-molecule collisions).

The saturation intensity at line centre is given by [113]

$$I_s(\nu_o) = 8\pi^2 h\nu_o(\Delta\nu)\ t_{sp}\ \lambda^2\ \left(\frac{1}{\gamma^u_{eff}} + \frac{g_u}{g_l}\frac{1}{\gamma'_{eff}}\right) \qquad (7.2)$$

where $\Delta\nu$ is the full Lorenzian linewidth, t_{sp} is the spontaneous radiative lifetime between the upper and lower laser levels, λ is the wavelength. γ^u_{eff} and γ'_{eff} are the reciprocals of the upper and lower level lifetimes respectively, and g_u and g_l are the corresponding level degeneracies.

This equation is useful insofar as it gives the dependence of the saturation intensity but its use is limited by the lack of accurate values for γ^u_{eff} and γ'_{eff}.

The saturation intensity $I_s(\nu)$ is related to the saturation intensity at line centre by

$$I_s(\nu) = (1 + \delta^2)\ I_s(\nu_o) \qquad (7.3)$$

The incremental gain is

$$\frac{1}{I(\nu)}\ \frac{dI(\nu)}{dz} = g(\nu) - \alpha \qquad (7.4)$$

where α is the distributed intensity loss and z is the distance of propagation.

Combining (7.1,3-4) and solving by separation of variables gives

$$g_oL = (1+\delta^2)\ \mathrm{Ln}\frac{\gamma_2(\nu)}{\gamma_2} + [\gamma_2(\nu) - \gamma_1] \qquad (7.5)$$

where γ_1 and γ_2 are the normalised input and output intensities respectively, i.e. $\gamma(\nu) = I(\nu)/I_S(\nu_0)$.

Here it is assumed that the distributed loss is much less than the line centre gain coefficient, so that except in the far wings of the gain profile, the relationship $\alpha(1+\delta^2) << g_0$ is satisfied.

Measurements [26] have shown that alumina exhibits a guiding loss of typically $\sim 10^{-3}$ m^{-1} which is insignificant compared to the achievable gains of the order of 1 m^{-1} in a typical CO_2 waveguide laser, so that the assumption $\alpha(1+\delta^2) << g(\nu)$ is valid.

In order to design a laser amplifier with given performance characteristics, requires knowledge of the small-signal gain coefficeint g_0, the line centre saturation intensity $I_S(\nu_0)$, and the linewidth $\Delta\nu$, for a variety of discharge conditions including discharge geometry, gas pressure and mixture, and the magnitude and frequency of the RF drive input power. However, an analytical relationship derived from the equation (7.5) may be used to obtain the frequency dependence of the normalised output intensity for various values of the system gain and the output intensity at line centre, viz:-

$$\delta^2 = \frac{\gamma_2(\nu_0) - \gamma_2(\nu) - \mathrm{Ln}\,\dfrac{\gamma_2(\nu)}{\gamma_2(\nu_0)}}{\mathrm{Ln}\,\dfrac{\gamma_2(\nu)}{\gamma_2(\nu_0)} + 0.23\ G} \qquad (7.6)$$

where G is the system gain given by

$G = 4.34\ \mathrm{Ln}\ \frac{\gamma_2(\nu_0)}{\gamma_1}$ decibels. At line centre $\nu = \nu_0$ and $\delta = 0$; rearranging equation (7.6) in terms of the system gain gives

$$G = 4.34(g_0L-\gamma_2(\nu_0)+\gamma_1) = 4.34[g_0L+\gamma_1(1-\exp[G/4.34])] \quad (7.7)$$

An iterative and numerical solution to equation (7.7) has been used to determine the dependence of the system gain on the normalised input intensity for a 1 m ampliifer section with a typical small-signal gain coefficient of 1% cm^{-1}; the results are presented in Figure 7.2. As expected, the system gain is reduced to one half its small-signal value for an input intensity equal to the saturation intensity.

In Figure 7.3 the line profiles are plotted for the amplifier parameters labelled A to D in Figure 7.2. At low levels of saturation the output linewidth is reduced (gain narrowing). As saturation becomes important, the output is broadened again (power broadening), and the linewidth may even exceed the small signal linewidth. Power broadening is effective throughout the line profile. This is not true when distributed loss is present; in this case, the amplifier line shape is truncated at the frequencies where the unsaturated gain equals the distributed loss.

The results presented in Figures 7.2. and 7.3 will be used in the next section for a comparison to those obtained with the amplification of chirp pulses.

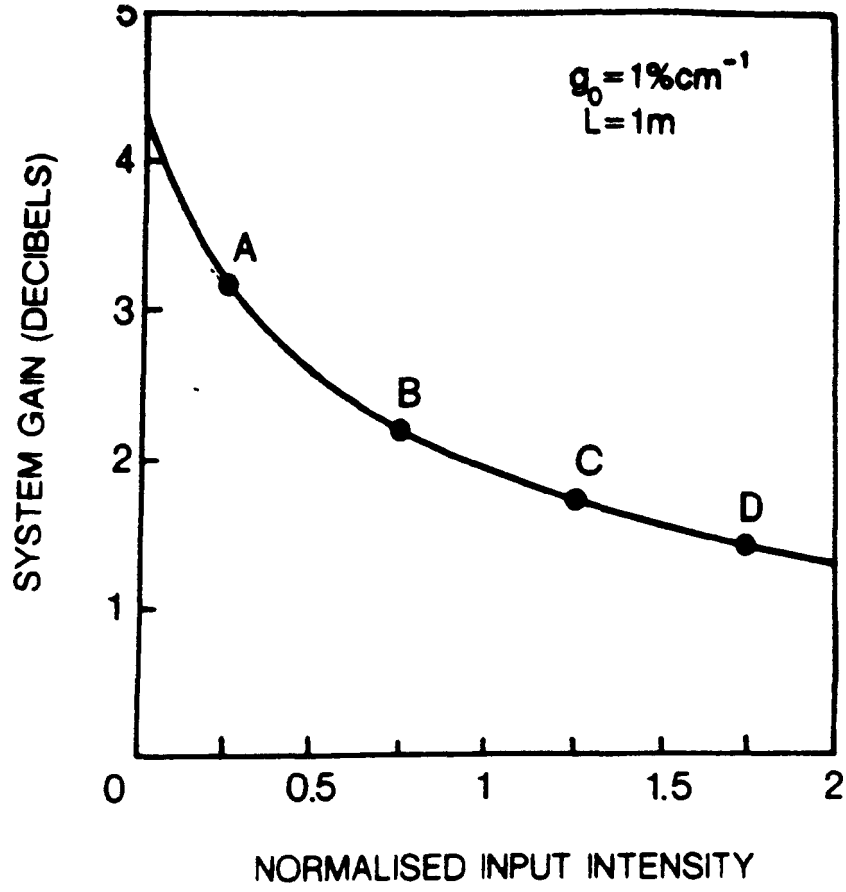

Figure 7.2. Gain saturation for monochromatic input signals.

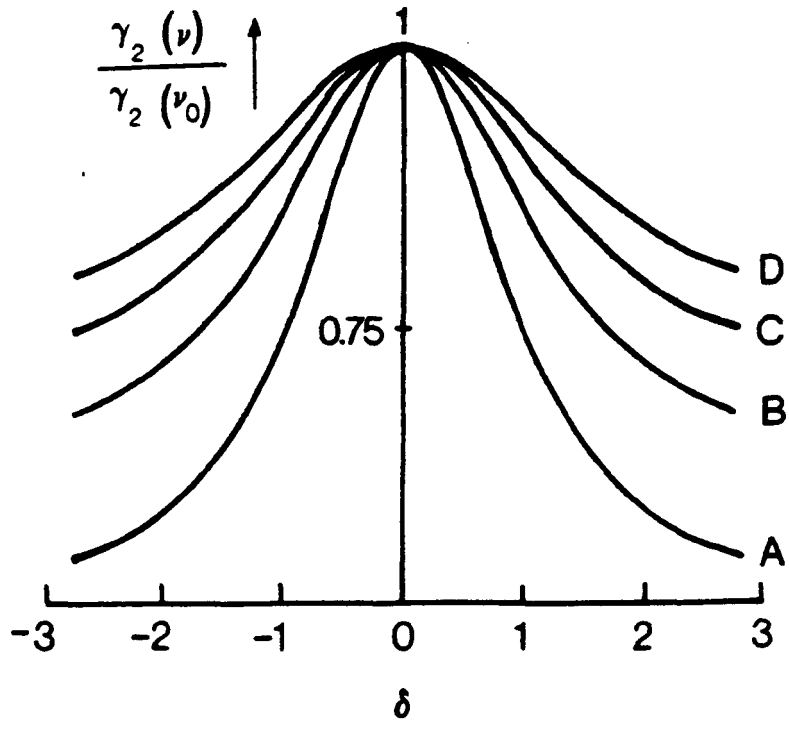

Figure 7.3. Power broadening. Curves A-D are the line profiles for the amplifier parameters labelled A-D in Figure 7.2.

In addition to the net gain measurements it would be useful to be able to calculate the gain coefficient per unit length. The amplified power exiting from a waveguide, P_a, is defined by the equation:

$$P_a = P_i \exp(g_o - \alpha)L \qquad (7.8)$$

where P_i is the power actually injected into the waveguide. Here it is assumed that the effects of gain saturation are unimportant.

It might appear at first sight that such a calculation would be difficult to perform as P_a or P_i are not measured directly and estimates of their values would involve taking into account, for example, window transmission coefficients, waveguide aperturing effects and for a folded design, coupling beween adjacent waveguide segments. However, it can be shown that [48]

$$g_o = \frac{1}{L_T} \mathrm{Ln} \frac{P_a}{P_p} \qquad (7.9)$$

where P_a and P_p are the measured output powers with the amplifier on and off respectively, and L_T is the total active length.

The net gain, G_n, is defined as the ratio of the input power to the output power.

7.2.1 Chirp Pulse Amplification

In a CO_2 LIDAR system the choice of transmitter waveform is affected both by the intended application and by the ever

advancing capabilities of lasers, modulators and receiver signal-processing systems. A heterodyne radar system aims to estimate two primary parameters from the target return signal: the range from the round trip delay, and the velocity from the Doppler shift. Recently, the application of modern microwave radar signal processing techniques [114] to the laser field has encouraged the development of heterodyne chirp CO_2 laser systems [49,96]. Here the transmitted signal contains a linear-frequency-sweep chirp-coding with a bandwidth a few times greater than the maximum Doppler shift.

Heterodyne detection results in superior sensitivity over direct detection in rangefinders and is in addition a fundamental requirement in Doppler velocimetry systems; however, stringent frequency control is required of the transmitted laser beam. The theory of the required frequency characteristics of such pulsed radars has been developed by Woodward [115]. He showed that range accuracy was proportional to the pulse bandwidth and Doppler accuracy to the pulse length, provided that the pulses are reproducible and that a suitable matched filter can be constructed.

It is the large frequency content of a short pulse that accounts for its high resolution capabilities. It follows, as a consequence of Fourier analysis, that a long pulse of constant carrier frequency contains a narrow bandwidth and therfore possesses poor range resolution properties. However, the spectrum of this long signal can be significantly broadened by introducing frequency modulation.

By this method one can introduce the frequency-spread characteristics of a short pulse within the envelope of a long-duration signal.

Within this envelope the instantaneous frequency is modulated in a linear manner covering a band of frequencies Δ, centred at some suitable carrier frequency f_0. This signal, shown in Figure 7.4, is described by the real part of the complex waveform $\epsilon(t)$, where

$$\epsilon(t) = \text{RECT}\left(\frac{t}{T}\right) \; e^{2\pi j(f_0 t + Kt^2/2)} \qquad (7.10)$$

thus, during the T second interval of the pulse the instantaneous frequency, $f_i = f_0 + KT$, changes in a linear fashion from $f_0 - Kt/2$ to $f_0 + Kt/2$.

An anaysis describing the propagation of a chirped optical pulse in an RF excited discharge gain media is desired in order that the appropriate degree of signal control may be exercised. Of particular interest are the effects of gain saturation, dispersion and mode distortion.

The phenomena known as "gain-narrowing" and "power broadening" have been discussed in detail by Klein and Abrams [47], and were examined in Section 7.2. However, the solution given in this previous analysis was by no means a general solution. With chirped radar applications the chirp rate must be considered before the frequency dependent saturation behaviour can be defined.

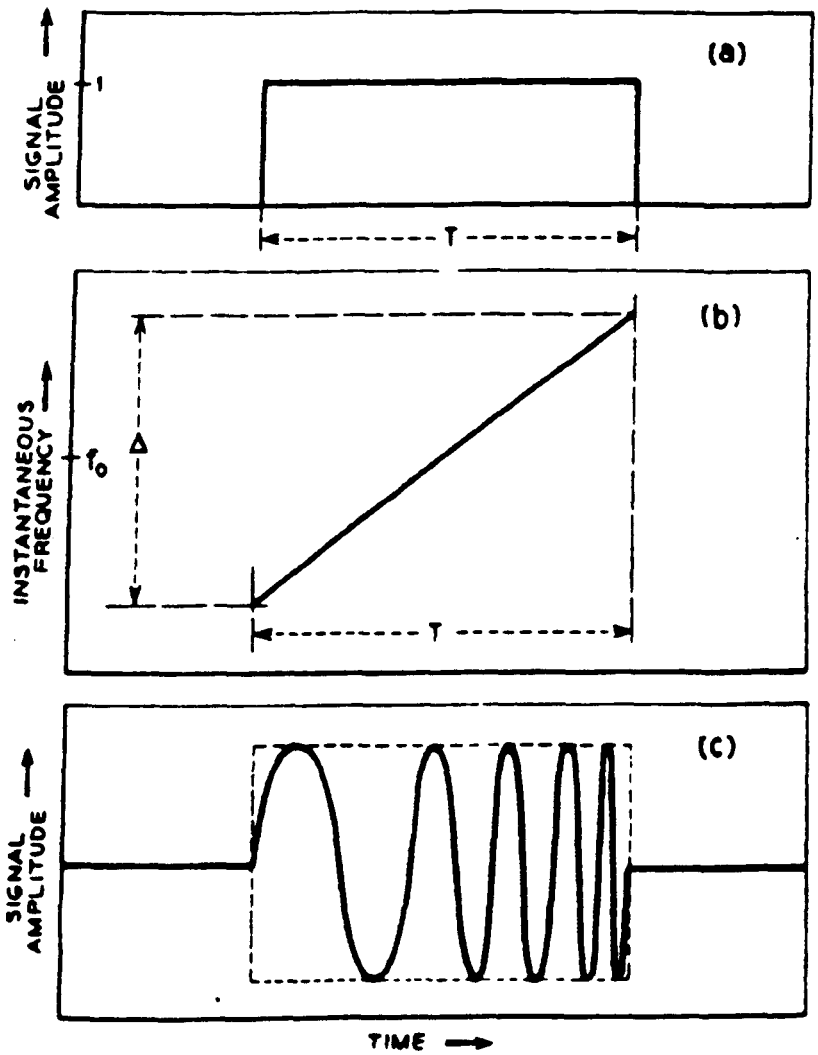

Figure 7.4. (a) Ideal envelope of actual Chirp signal, of T seconds duration and chosen to be of unit amplitude.
(b) Instantaneous frequency vs. time characteristic of Chirp signal; a band of frequencies, Δ, centred at f_0 is linearly swept during the pulse duration.
(c) Schematic diagram of a signal having the properties indicated in (a) and (b) (after Klauder [114]).

A closed-form solution of the rate equations for chirped amplifiers has been given by Laakmann [97]. In this analysis, two regimes were considered; the first was for slow-chirped inputs whose chirp period far exceeded the upper laser level lifetime and the second was for fast-chirped inputs in which the population inversion of the laser levels changed negligibly during the chirped period, viz.:-

slow chirp input:

$$\mathrm{Ln}\left(\frac{I_{out}(\nu)}{I_{in}(\nu)}\right) = \frac{G_0}{1 + \left(\frac{\nu-\nu_0}{\Delta\nu/2}\right)^2} - \frac{I_{out}(\nu) - I_{in}(\nu)}{I_s\left[1 + \left(\frac{\nu-\nu_0}{\Delta\nu/2}\right)^2\right]} \qquad (7.11)$$

Fast chirp input:

$$I_{out}(\nu) = I_{in}(\nu)\ \exp\left[\frac{G_{avg}}{1 + \left(\frac{\nu-\nu_0}{\Delta\nu/2}\right)^2}\right] \qquad (7.12)$$

where

$$G_{avg} = G_0 - \frac{\bar{I}_{out} - \bar{I}_{in}}{I_s} \qquad (7.13)$$

The nomenclature used in the equations above differs from that used in the expressions for the frequency-dependent saturation of a monochromatic input beam given by [47] in Section 7.2; the equivalent parameters are:-

$$I_{in} \equiv I_1$$

$$I_{out} \equiv I_2$$

$$G_0 \equiv g_0 L$$

$$\frac{\nu-\nu_0}{\Delta\nu/2} \equiv \delta$$

The slow-chirp saturation equation is identical to the monochromatic saturation equation given in Section 7.2.

The fast-chirp equation (7.12), written in the alternative nomenclature and rearranged, becomes

$$\alpha_0 L = (1 + \delta^2)\ \mathrm{Ln}\ [\frac{\gamma_2(\nu)}{\gamma_1(\nu)}] + \bar{\gamma}_2 - \bar{\gamma}_1 \qquad (7.14)$$

where

$$\gamma_2 = \int_{\nu_1}^{\nu_2} \frac{\gamma_2(\nu)}{(\nu_2-\nu_1)}\, d\nu \quad \text{and} \quad \bar{\gamma}_1 = \gamma_1 \qquad (7.15)$$

(for the top hat waveform given in equation (7.10)).

The frequency-dependent saturation behaviour for the fast-chirp input is clearly different from that of the slow-chirp monochromatic inputs. A direct comparison is possible by considering the linewidth saturation dependence by putting $\gamma_2(\nu) = \gamma_2(\nu_0)/2$ in each case. Hence,

$$\Delta\nu_{3dB} = \Delta\nu\ (\frac{\gamma_2(\nu_0)/2 + \mathrm{Ln}\ 2}{0.23\ G - \mathrm{Ln}\ 2}) \quad \left.\begin{matrix}\text{monchromatic}\\ \text{slow-chirp}\end{matrix}\right\}\ \text{input} \qquad (7.16)$$

$$\Delta\nu_{3dB} = \Delta\nu \left(\frac{\text{Ln } 2}{0.23\ G - \text{Ln } 2}\right) \quad \text{fast chirp input} \tag{7.17}$$

Evidently, the amplifier bandwidth with a fast-chirp input is independent of the degree of saturation and always less than for the slow-chirp system.

The implications of the above statement are, in order to achieve the same power gain as in the slow-chirped regime, the fast chirped amplifier requires a greater operating pressure (which is generally accompanied by a diminished small-signal gain coefficient) and consequently a longer length.

A numerical and iterative solution to equation (7.14) has been used to determine the system gain dependent on the normalised fast-chirp input intensity for the same amplifier section considered in Section 7.2; the iteration algorithm is given by

$$\gamma_2(\delta) = \gamma_1 \exp\left[\frac{G_1}{(1+\delta^2)}\right] \tag{7.18}$$

$$\bar{\gamma}_2 = \left[\sum_{\delta=-3}^{3} \gamma_2(\delta)\right]/\Delta\delta \tag{7.19}$$

$$G_1 = g_0 L - \bar{\gamma}_2 + \gamma_1 \tag{7.20}$$

$$G_{avg} = 4.34\ G_1 \tag{7.21}$$

The average system gain values derived in this manner are presented in Figure 7.5 for various normalised input intensities, with their corresponding lineshapes shown in Figure 7.6. The average system gain is reduced to about three quarters its small-signal value for an input intensity equal to the saturation intensity.

To summarise, the frequency-dependent saturation behaviour experienced by a slow-chirp input signal is identical to that experienced by a monochromatic input signal; a fast-chirp input signal, on the other hand, does not experience power broadening, instead the amplifier bandwidth stays constant as the degree of saturation increases. Further, the gain observed by a fast-chirp input signal is that associated with an average input intensity rather than an instantaneous intensity.

An optical pulse with a linearly chirped frequency may be temporally compressed or expanded upon propagating through a suitably dispersive medium. A well known source of refractive index variation is the resonant behaviour in the vicinity of a molecular transition, called anomalous dispersion. For a homgeneously broadened molecular transition this is given by [115]

$$n = n_0 + \frac{g(\nu)c}{\gamma\nu}(\nu - \nu_0) \qquad (7.22)$$

where $g(\nu)$ is the gain at frequency ν, ν_0 is the molecular transition frequency and $\gamma = 2\pi\Delta\nu$, where $\Delta\nu$ is the full width at half maximum of the Lorentzian spectrum.

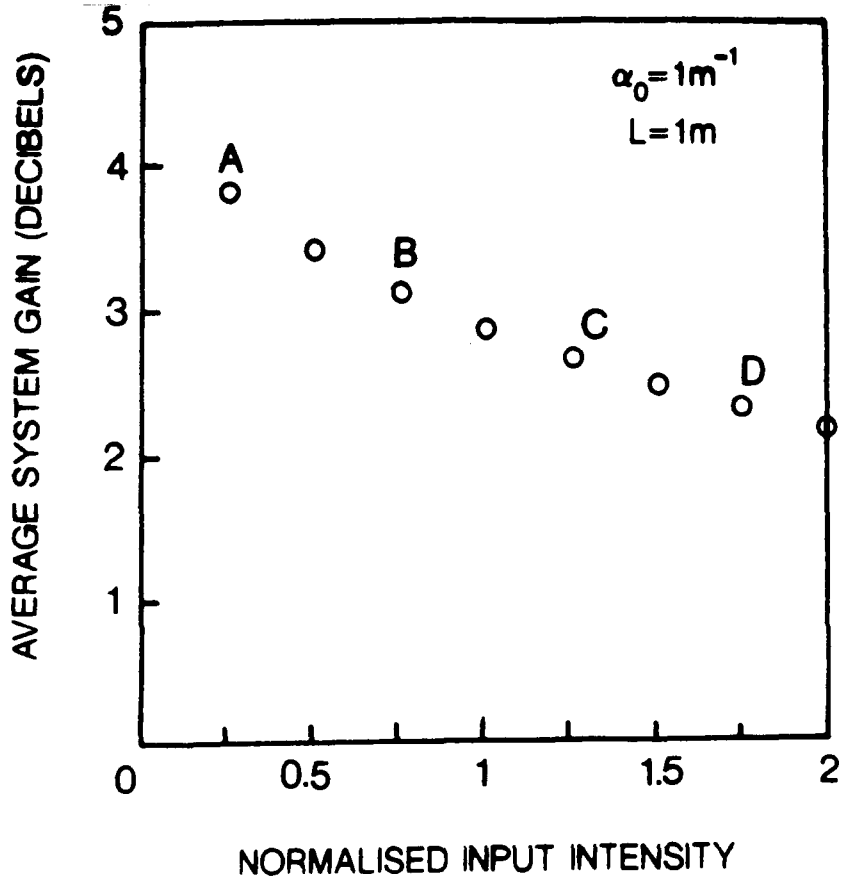

Figure 7.5. Gain saturation for fast-chirped input signals.

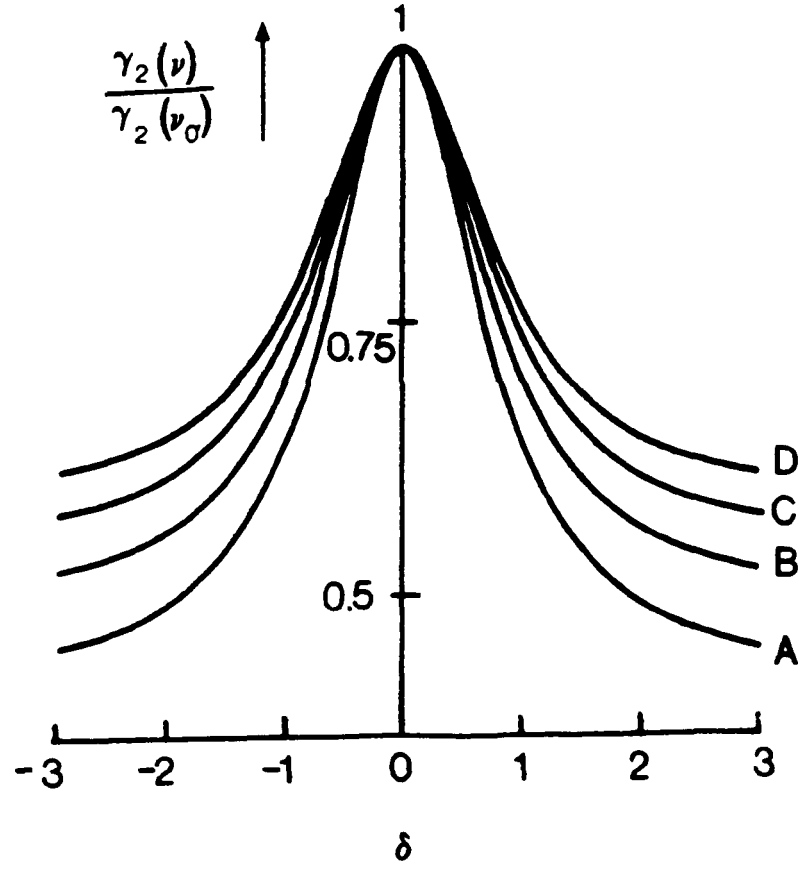

Figure 7.6. Line profiles for the amplifier parameters labelled A-D in Figure 7.5.

Substituting equation (7.1) into (7.22) gives the anomalous dispersion refractive index variation for a homogeneously broadened transition with a monochromatic (or slow-chirp) input, viz.:-

$$n = n_0 + \frac{g_0 \, \delta\lambda}{4\pi[1+\gamma_1][1+\delta^2]} \qquad (7.23)$$

In Figure 7.7 the term $(n-n_0)$ is plotted as function of δ at 10.6 μm for the small-signal gain of 1% cm^{-1} and the normalised input intensities labelled A to D in Figure 7.5. As expected the curves pass through the origin at $\delta = 0$, corresponding to resonance with the transition fequency. Evidently, the degree of anomalous dispersion is greater for low input intensities. The extrema occur at $\delta = \pm 1$, that is, at the half-maximum points of the Lorentzian spectrum. The maximum absolute value of $(n-n_0)$ for the example shown is less than 4×10^{-7}, which is very small when compared to the unity refractive index term n_0.

The amplifier travelling-wave velocity is related to the free-space wave velocity by the relation

$$v = \frac{c}{n} \qquad (7.24)$$

For an "up-chirp" input pulse (δ increasing) starting at $\delta \geq 1$, the gain media refractive index is always geater than unity and decreasing (as shown in the figure), thus from equation (7.24) the wave-velocity components are always less

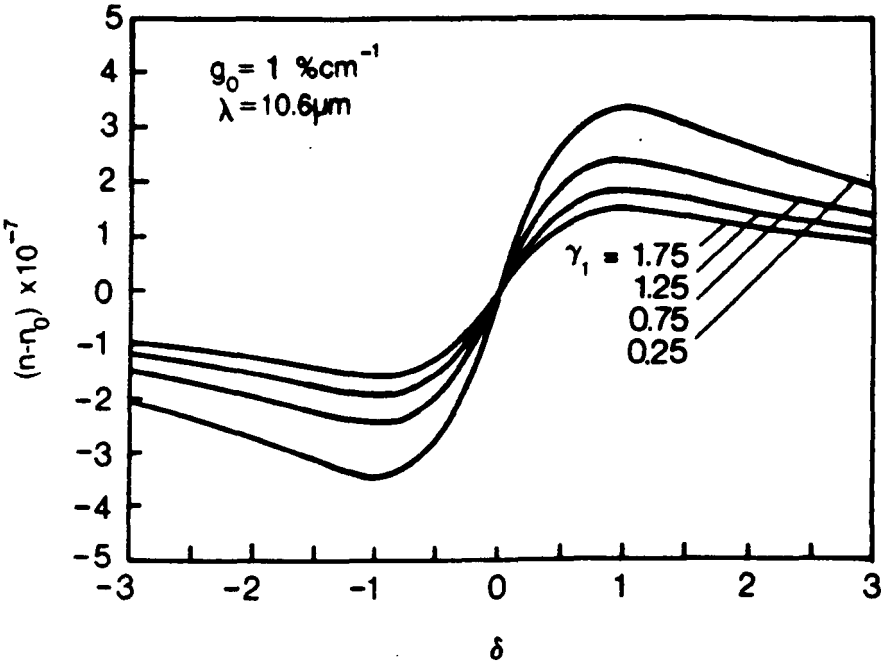

Figure 7.7. The anomalous dispersion refractive index variation for a homogeneous broadened amplifier transition with slow-chirp inputs.

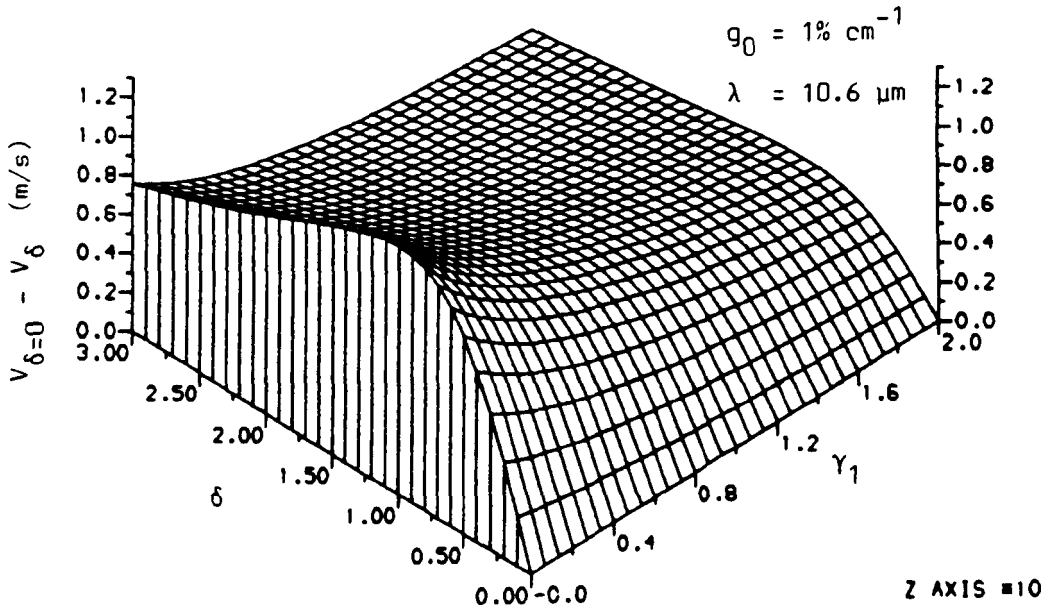

Figure 7.8. The amplifier travelling wave relative velocities as functions of the normalised input intensity and frequency detuning from line centre.

than c, but increasing; consequently, the pulse is temporally compressed. Conversely, for a "down-chirp" input pulse (δ decreasing) with $\delta \geq 1$, the refractive index is always greater than unity and increasing, thus the wave-velocity components are always less than c but decreasing; and the pulse is temporally expanded.

The inference from the above paragraph may be a little misleading, as although in the case of the down-chirp, for example, the refractive index increases as δ decreases, the rate of increase is suppressed as the pulse gains intensity on its travel through the amplifying media; and hence the wave-velocity components gather speed. It is the relative wave velocity components that determine the degree of pulse compression or expansion. This underlying trend is reflected in the quasi-three dimensional plot shown in Figure 7.8. Here the relative velocities across the line spectra are displayed as functions of the normalised intensity of the travelling waves. As their intensities increase the wave velocities tend towards the line-centre velocity. The maximum relative velocities occur at $\delta = 1$ (half-maximum point of the Lorentzian spectrum) and tend towards zero for frequencies further removed from line centre. For the example shown the range of velocities represent a change of less than 1 part in 2.4 million.

To illustrate the degree of distortion a pulse experiences on transit through a travelling wave amplifier in a realistic situation, it is convenient to consider an

example. As already mentioned in Section 7.1, there is growing interest in the concept of optical power amplification and pre-amplification for LIDAR applications. The CO_2 laser rangefinder using heterodyne detection and chirp pulse compression described in [96] is a system that might benefit by the introduction of an optical amplifier. This system is part of an ongoing research programme at RSRE (Malvern, U.K.) and has the following typical pulse characteristics. A cw waveguide laser and external acousto-optic modulator are used to produce a $\sim$ 1 W transmitted linearly chirped square pulse with, say, 1 μs duration and 50 MHz bandwidth centred at 100 MHz. The signal power returned from a distant moving target may be as little as 10 pW, with a fundamental Doppler shift of $\sim$ 200 kHz per m/s.

There are three possible ways to introduce optical amplification into the system; power amplification of the transmitted beam, pre-amplification of the return signal, or dual-amplification (in the same amplifier) of the transmitted and received signals. The choice of operating conditions associated with each amplifier is a trade-off between the available (un)saturated gain and linewidth, and influenced by the tolerance of the resulting pulse amplitude and chirp distortions. A suitable gain linewidth for the example above might be 500 MHz provided by a cw discharge in $\sim$ 100 torr laser gas mixture, with say, 1% cm^{-1} small-signal gain and 10kW cm^{-2} saturation intensity (or $\sim$ 100 W saturation power in a 2.25 mm square bore waveguide). The detuning associated

with the chirp is then 0.4 ± 0.1 (100 ± 25 MHz), and the normalised input intensities for the power- and pre-amplifiers are 0.01 and 1 x 10^{-13} (1 W and 10 pW) respectively. The chirp centre frequency net gains provided by amplifier gain lengths of between 0 and 5 m for these two amplifiers configurations (determined by solving equation (7.7) iteratively for 5 cm length increments) are presented in Figures 7.9(a and b). A small-signal gain of 2.5% cm^{-1} was assumed for the pre-amplifier, perhaps provided by a pulsed discharge with gain pulse durations greater than the chirp pulse duration. Pre-amplification is generally peformed at lower gas pressures (compared to power-amplification), since there is no trade-off between net gain and saturation intensity at the low input intensities and the gain lengths considered. In this case, however, to allow for a direct comparison, the amplifiers are assumed to be identical in all respects except that the pre-amplifier small-signal gain is 2.5% cm^{-1}.

Evidently, net gains of up to ∿ 20 dB (Figure 7.9(a)) and ∿ 50 dB (Figure 7.9(b)) are provided by the power- and pre-ampliiers respectively (over the parameter space considered). The chirp pulse shape (normalised amplitude) distortions arising as a consequence of the frequency-dependence of these gains are presented in Figures 7.10(a and b) respectively. Gain narrowing is present in both cases, although as the length of the power amplifier is increased the rate of gain narrowing is suppressed as power

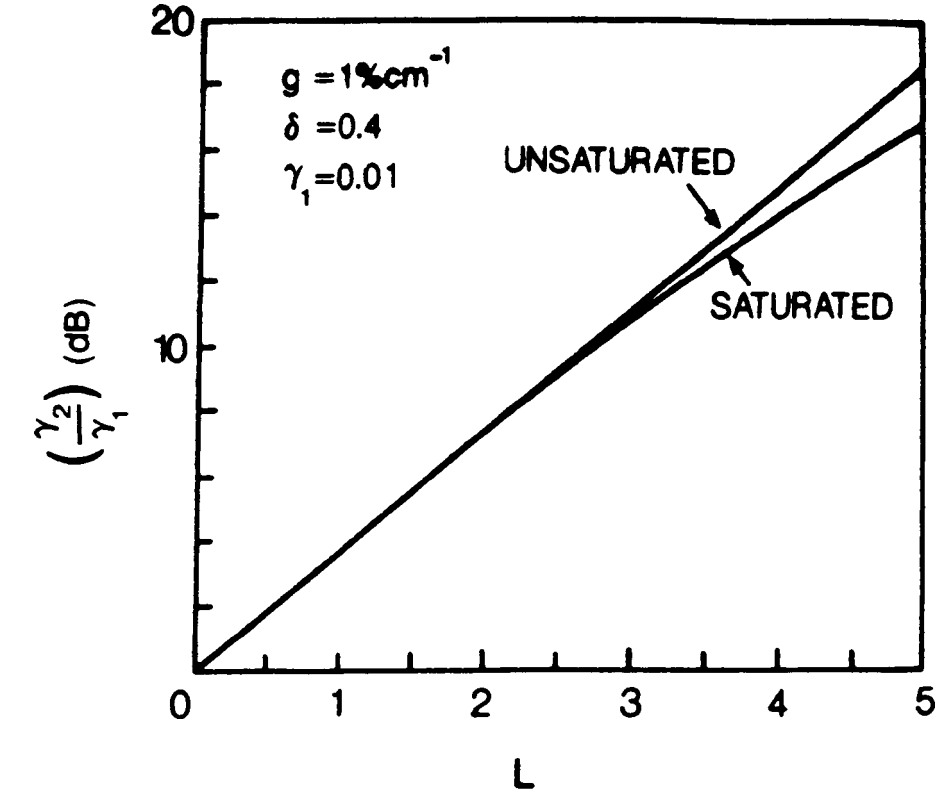

(a)

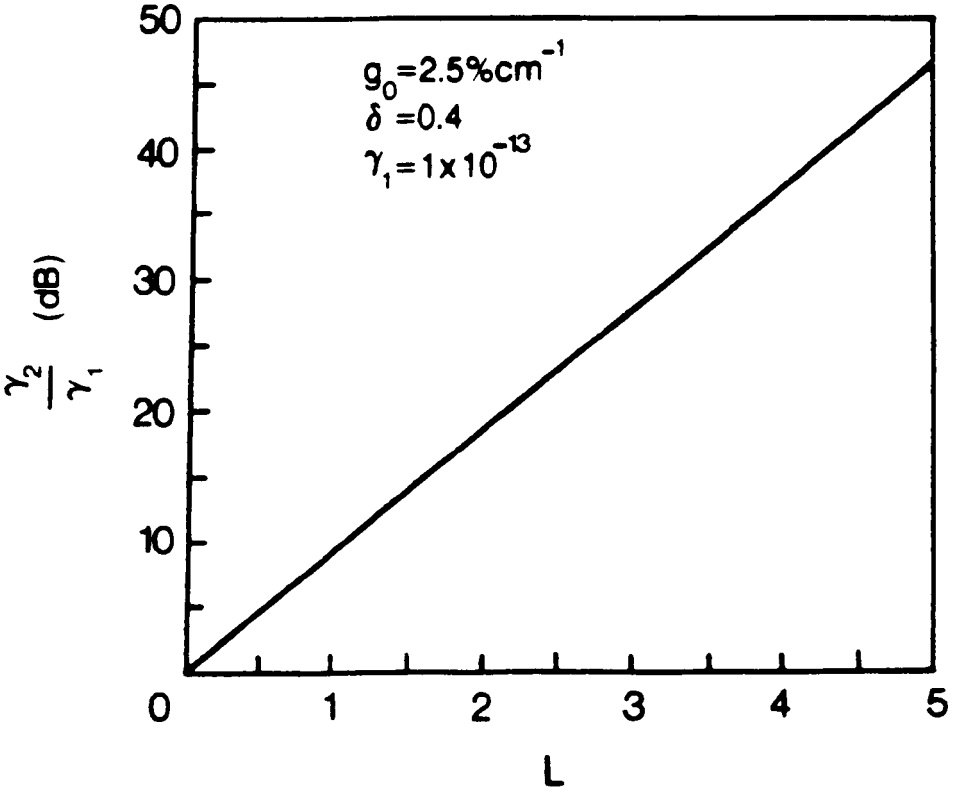

(b)

Figure 7.9. Net power amplification (a) and pre-amplification (b) as a function of gain length, for frequency off-set input signals with intensities typical of those in the transmitter and receiver stages of a CO_2 LIDAR system, respectively.

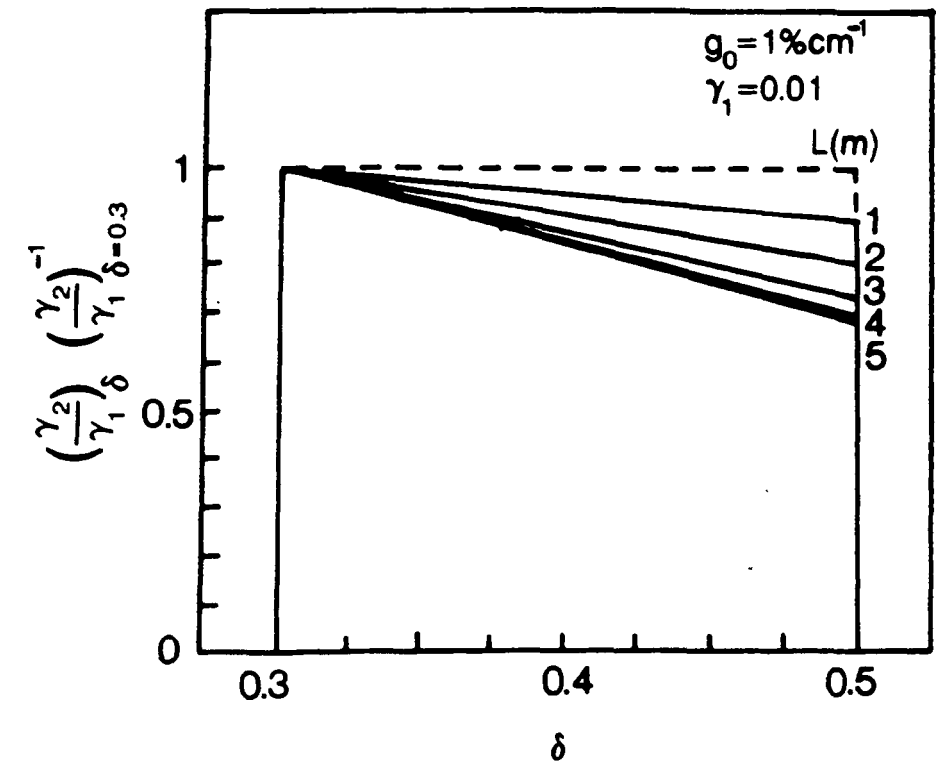

(a)

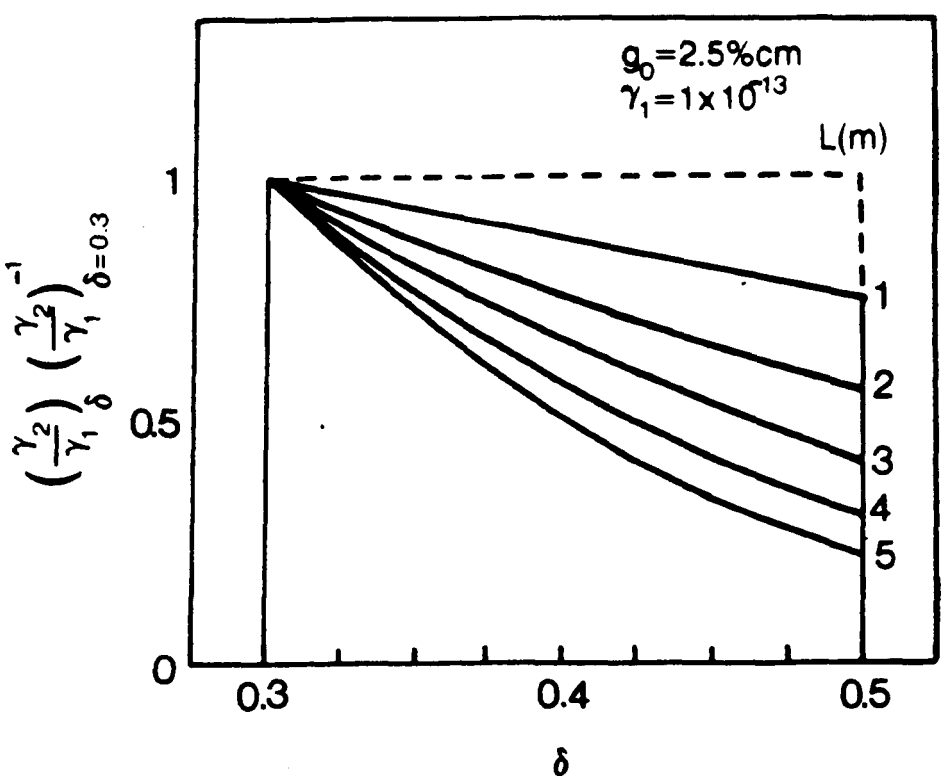

(b)

Figure 7.10. Slow chirp pulse shape distortions after power amplification (a) and pre-amplification (b) for various gain lengths.

broadening becomes significant. This trend is reflected in composite graph shown in Figue 7.11 where the degree of pulse distortion (percentage variance) is plotted as a function of gain length.

The time delays associated with the different frequency components of the chirp pulses for several amplifier lengths are shown if Figures 7.12(a and b), for the power and pre-amplifiers respectively. Hence, for the parameters considered the maximum time delays are a few femto-seconds (10^{-15} s), varying fairly linearly over the bandwidth. These delays represent a change in the chirp-rate (in this case 50 MHz per μs) of a few parts in 2.5 billion, and a frequency shift of a few tenths of a Hertz when overlapped with the input pulse. Obviously, time delays of these magnitudes are insignificant when compared to the pulse duration, and in a waveguide amplifier are comparable to the waveguide dispersion [116]. Figure 7.13 shows the spectral time delays across the lineshape for different lengths of pre-ampiifer sections possessing a small-signal gain of 5% cm^{-1}. Even here the maximum time delays which occur at $\delta = \pm 1$ are only a few tens of femto-seconds.

The time delays associated wth a fast-chirp pulse are given by [97]

$$\Delta t = \frac{G_{avg}\,\lambda\delta^2}{4\pi c\,(1+\delta^2)} \qquad (7.25)$$

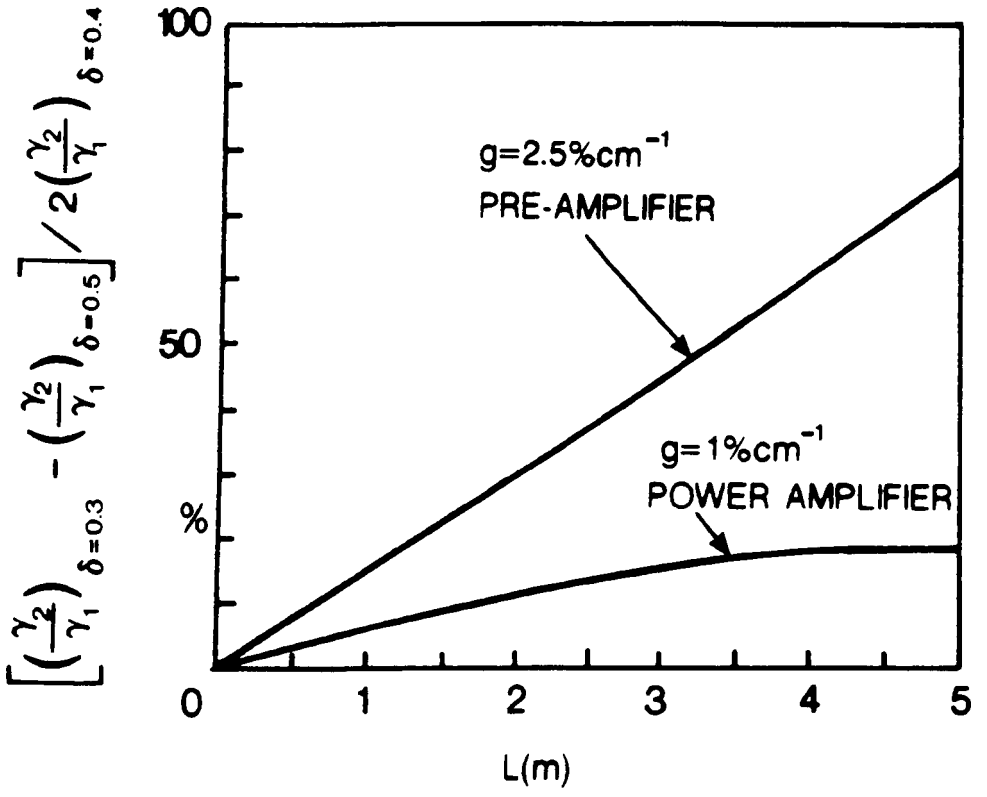

Figure 7.11. Slow chirp pulse distortion (percentage amplitude variation from the 'top hat' input pulse) as a function of gain length.

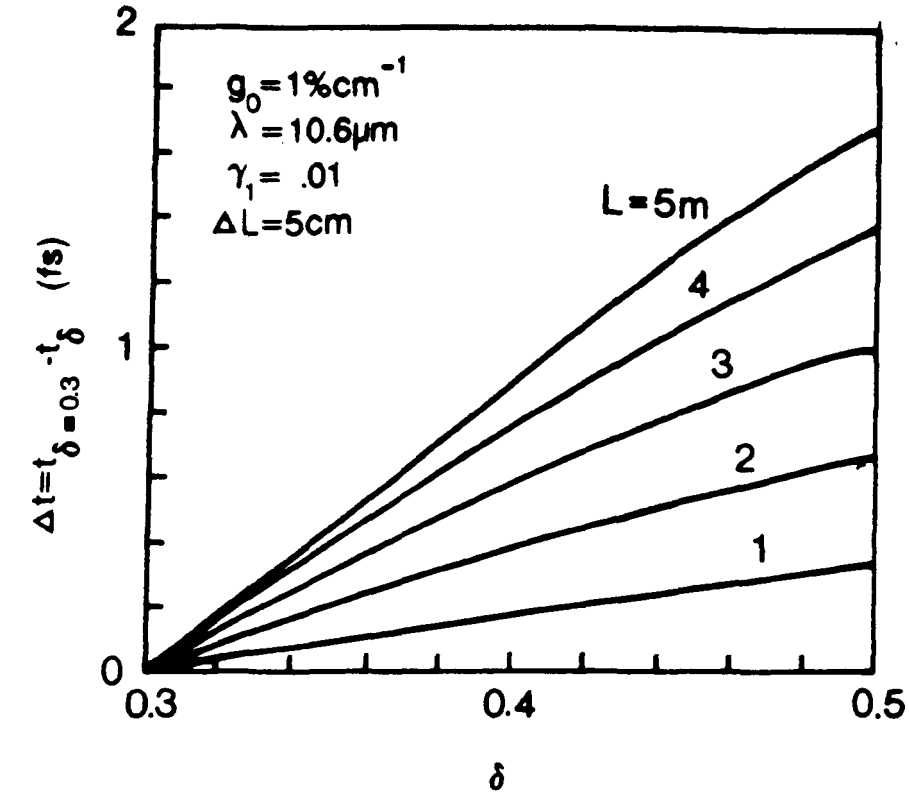

(a)

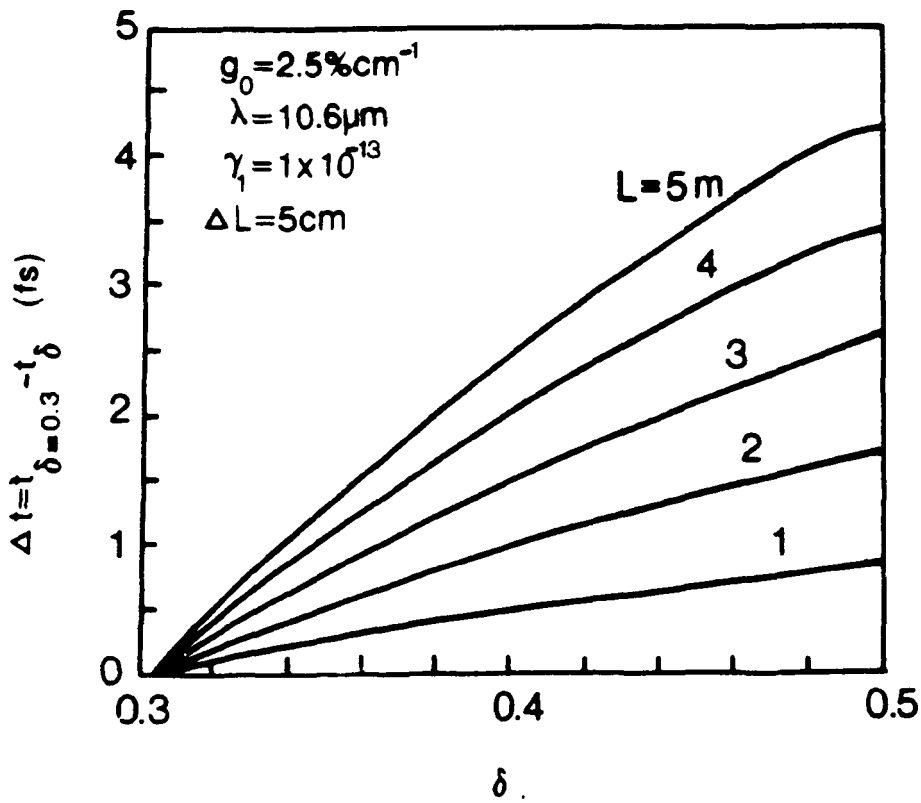

(b)

Figure 7.12. Propagation time delays associated with the frequency components of a slow-chirped input signal for various power amplifier (a) and pre-amplifier (b) gain lengths.

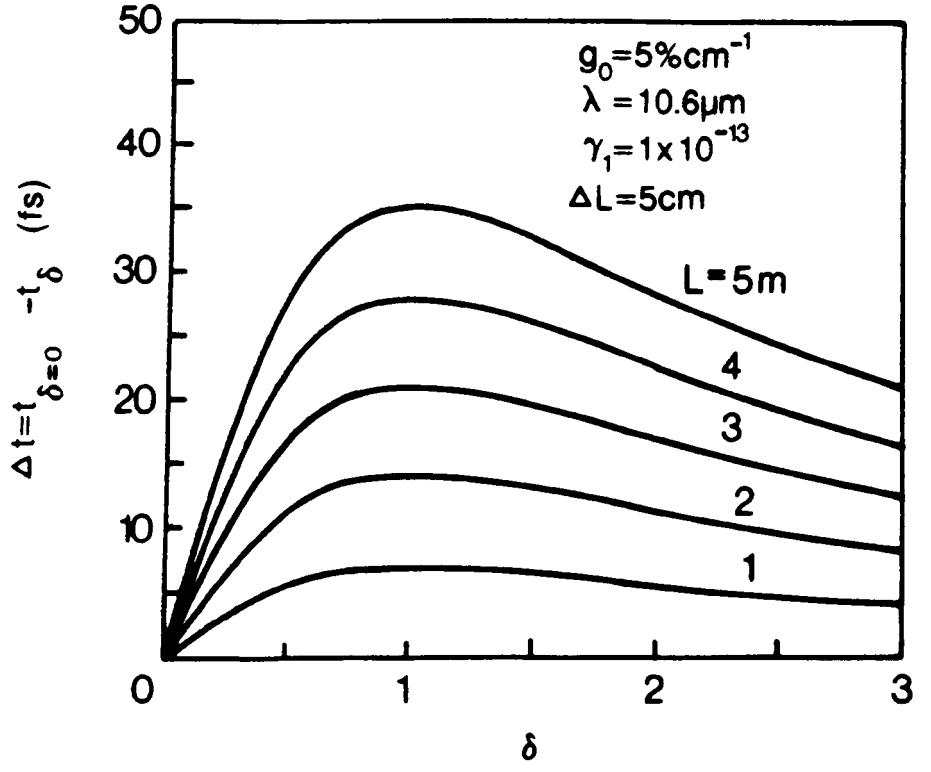

Figure 7.13. Propagation time delays across the transition linewidth for various gain lengths in a high gain pre-amplifier.

For a 50 dB amplifier and $\delta = 1$, this gives $\Delta t = 16$ fS; corresponding to a $\sim$ 1 kHz frequency shift when overlapped with the input chirp pulse of 1 ns duration and 50 MHz bandwidth. Chirp pulse rate changes and distortions of these magnitudes are not likely to influence the accuracy of range or velocity determinations in a CO_2 LIDAR system. The pulse shape distortions incurred during optical amplification, on the other hand, are significant, although it is conceivable that a square output pulse shape could be obtained by introducing a suitably distorted input pulse shape.

Further distortion of the optical pulse may arise fom refractive index pertubations; for example a non-uniform electric discharge will result in a variation in energy deposition and thus changes in density and refractive index. The presence of a non-uniform susceptibility profile causes the normal modes of an unperturbed waveguide to couple into one another. Normally the excellent mode discrimination exhibited by waveguide devices mean that the distortion of the lowest loss mode is generally quite small.

7.3 Mode-Matched Injection for Waveguide Amplifiers

This section considers ways of injecting a Gaussian profile laser beam into a wavguide laser amplifier. Practical injection schemes that satisfy the criteria for maximum coupling to the EH_{11} waveguide mode are particularly sought. The benefits of laser amplification may be undermined if the coupling to the waveguide excited multiple

waveguide modes, producing an undesirable far field beam intensity profile.

The injection of a linearly polarised Gaussian profiled beam into a hollow dielectric waveguide may be described in terms of the excitation of the EH_{pq} waveguide modes. The energy content of the coupled modes is determined from the square of an amplitude overlap integration in the plane of the waveguide entrance. Previous treatments, limiting the analysis to a linearly polarised plane wavefront TEM_{00} input beam and a square bore waveguide, predicted a maximum energy coupled to the EH_{11} fundamental waveguide mode for a beam waist (1/e amplitude locus) to waveguide half-width ratio of 0.69 [18]. Here it was assumed that the input Gaussian beam was aligned to the waveguide axis. This waist allows 98% of the energy of the Gaussian beam to be coupled into the EH_{11} mode. The propagation losses associated with this mode, among other things, depends on the plane of polarisation of the input Gaussian beam. For a hybrid waveguide, the lowest loss mode is polarised parallel to the metal walls, while in an all dielectric waveguide the lowest loss mode is degenerate and polarised orthogonally to either one of the guide axes.

Preliminary studies of single pass waveguide laser amplification are presented in Chapter 8. The probe laser used in the experiment had a conventional free-space resonator, comprised of a 3 m radius of curvature total reflector and a plane output coupler, separated by 75 cm.

For this geometry the waist is located in the plane of the output coupler with a radius (ω_0) given by [45]

$$\omega_0 = \sqrt{\frac{\lambda}{\pi}} \; (d(R-d))^{1/4} \qquad (7.26)$$

where R is the radius of curvature of the total reflector, λ is the laser wavelength, and d is the optical cavity length (approximately equal to the mirror separation). The values above, gives ω_0 = 2.09 mm.

The waveguide used in the experiment was a four-walled alumina square bore guide with a half-width (a) of 1.125 mm. To satisfy the criterion for maximum energy coupling to EH_{11} above, namely ω_0 a = 0.69, required a waist of 0.78 mm in the plane of the waveguide aperture. This condition could only be satisfied by a suitable transformation of the probe beam.

Mode matching of the Gaussian beam waists is obtained in the simplest arrangement by placing a single lens between the probe laser and the waveguide entrance, at a point where the beams (probe beam and virtual beam) have equal spot size [117]. The lens focal length is chosen to match the radius of curvature of the first beam to that of the second. Single lens mode matching is often impracticable because the necessary lens seldom has a readily available, standard focal length. A two lens telecope [118] removes these difficulties by allowing the effective focal length to be varied by adjusting the lens spacing. Further, spatial filtering of the laser beam is possible by placing a pinhole on axis

between the lenses at the minimum beam radius point. The pinhole eliminates the transmission of higher order diffracted radiation. It is generally counter productive to use a pinhole diameter (d) smaller than [119]

$$d_{min} = \frac{2f_1\lambda}{\pi\omega} \tag{7.27}$$

where f_1 is the focal length of the leading element and ω is the beam radius at its principle point.

The telescope system in [118] was analysed in terms of geometrical optics propagation; alternatively, as outlined below, the mode matching conditions can be derived through application of the ABCD law [119], using the familiar Gaussian beam parameters in [45].

If the ABCD matrix for the transfer of paraxial rays through the telescope structure are determined, the complex beam parameter (q_2) of the output beam can be calculated from

$$q_2 = \frac{Aq_1 + B}{Cq_1 + D} \tag{7.28}$$

where q_1 is the input beam parameter. At the beam waist the q parameter is purely imaginary and given by

$$q_0 = \frac{\pi}{\lambda}\omega_0^2 = b_0 \tag{7.29}$$

For the telescopic injection system shown schematically in Figure 7.14, and to satisfy the waveguide mode-matching

condition above, requires that

$$q_1 = b_1 \tag{7.30}$$

$$q_2 = b_2 \tag{7.31}$$

Substituting these equations into equation (7.28) and separating out and equating the real and imaginary components, the mode-matching condition becomes

$$BD + ACb_1^2 = 0 \tag{7.32}$$

$$D^2 + C^2 b_1^2 = \frac{b_1}{b_2} \tag{7.33}$$

and

$$AD - CB = 1 \text{ (Gaussian beam matrix identity)} \tag{7.34}$$

The ray transfer matrix is given by the product of the free-space and twin lens transfer matrices in [45], viz.

$$\begin{vmatrix} A & B \\ C & D \end{vmatrix} = \begin{vmatrix} 1 & d_3 \\ 0 & 1 \end{vmatrix} \begin{vmatrix} 1-d_2/f_1 & d_1+d_2-d_1d_2/f_1 \\ -1/f_1-1/f_2+d^2/f_1f_2 & 1-d_1/f_1-d_2/f_2-d_1/f_2+d_1d_2/f_1f_2 \end{vmatrix} \tag{7.35}$$

$$A = 1 - d_2/f_1 + d_3C \tag{7.36}$$

$$B = d_1+d_2 - d_1d_2/f_1 + d_3D \tag{7.37}$$

$$C = 1/f_1-1/f_2 + d_2/f_1f_2 \tag{7.38}$$

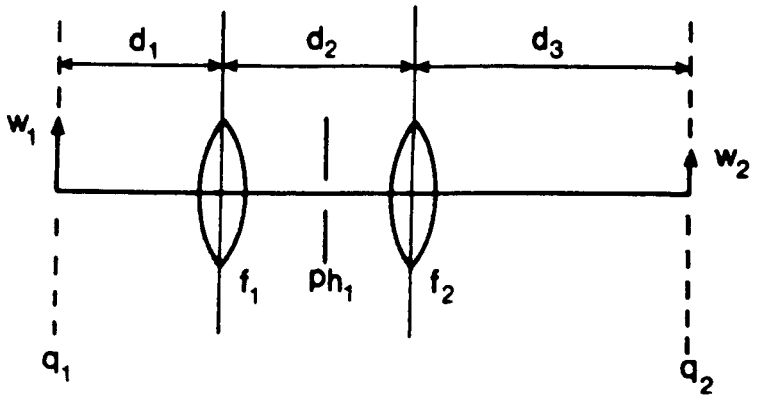

Figure 7.14. General telescope configuration.

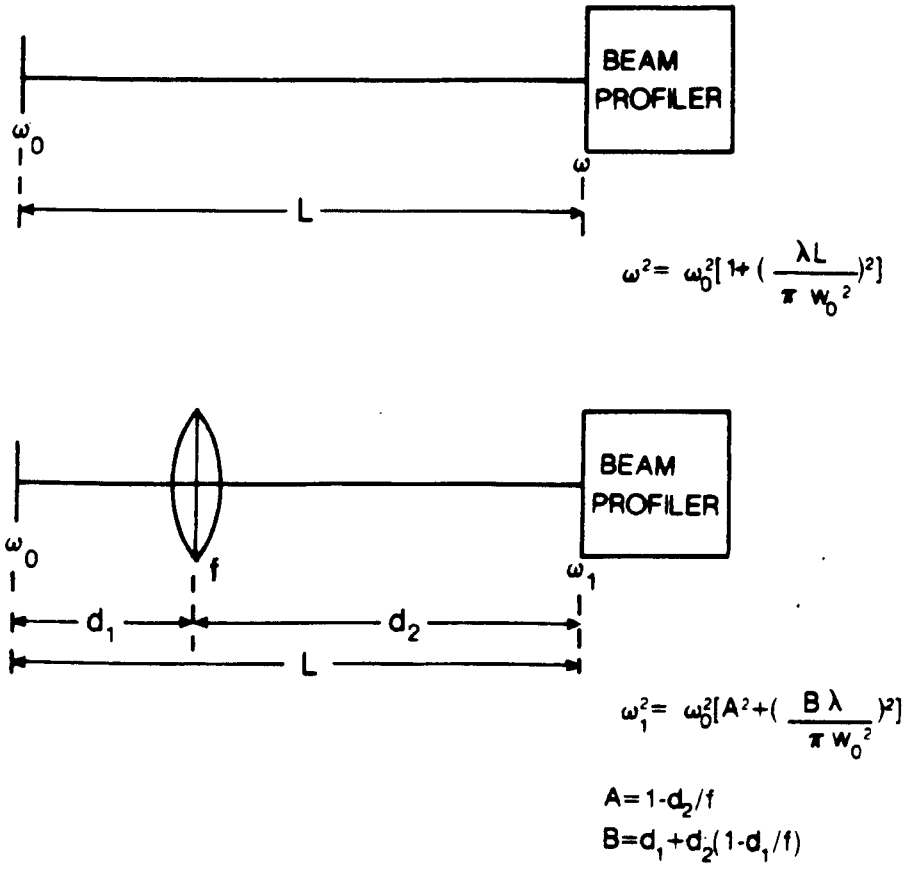

Figure 7.15. Experimental apparatus for probe beam waist determinations.

$$D = 1-d_1/f_1-d_2f_2-d_1/f_2 + d_1d_2/f_1f_2 \qquad (7.39)$$

A general solution of these equations and the mode-matching equations above is too intractable analytically. However, forcing D to be equal to zero, that is, assuming that the quantities f_1, f_2 and b_2 are fixed, gives

$$A = 0 \text{ (from the matrix identity in equation (7.34))} \qquad (7.40)$$

$$B = -b_1b_2 \qquad (7.41)$$

$$C = 1/b_1b_2 \qquad (7.42)$$

The substitution of these greatly simplified conditions into equations (7.36) to (7.29) provides the telescope design parameters, listed below:-

$$d_1 = (b_1b_2 + d_2)\ (d_2/f_1-1)^{-1} \qquad (7.43)$$

$$d_2 = f_1+f_2 + f_1f_2/b_1b_2 \qquad (7.44)$$

$$d_3 = b_1b_2\ (d_2/f_1-1) \qquad (7.45)$$

The derivation of these formula does not take into acount the lengthening of the optical distances by the high refractive index lens material; nor does it include calculations of the sensitivity to misalignment; nor an evaluation of the non-paraxial abberant behaviour. Despite these omissions the telescopic injection and spatial filtering of the probe laser beam into the waveguide ampliifer (described in the next chapter) was readily achieved.

One practical consideration was the determination of the probe laser beam waist to confirm the value calculated from the resonator equation (7.26) above, namely 2.09 mm. A schematic of the experimental configuration chosen is presented in Figure 7.15. Measurements with the tranverse beam profiler (mentioned in Chapter 5) provided a series of one dimensional slices through the probe beam. The slice with the peak intensity was assumed to be the one through the beam diameter. Direct measurement of the waist was not possible because the profiler measurements were uncalibrated. Indirect measurments were obtained by normalising the focussed beam waist measurement to those that excluded the single thin lens between the probe laser and the profiler. The absolute waist determination was derived from the propagation ray matrices for the free-space and focussed paths. The relationship between the absolute (ω_0) and relative waist ($x = \omega_1/\omega$) determinations is easily derived and its final form is given by

$$\omega_0^2 = \left(\frac{\lambda}{\pi}\right)\left[\frac{L^2 - x^2B^2}{x^2A^2 - 1}\right] \qquad (7.46)$$

where L is the separation between the probe laser and the beam profiler, and A and B are the matrix elements of the ABCD ray transfer matrix product for the thin lens.

A composite graph showing the peak intensity slices through the profiled beam for a sample of lens placings, and their corresponding waist determinations, are presented in Figure 7.16.

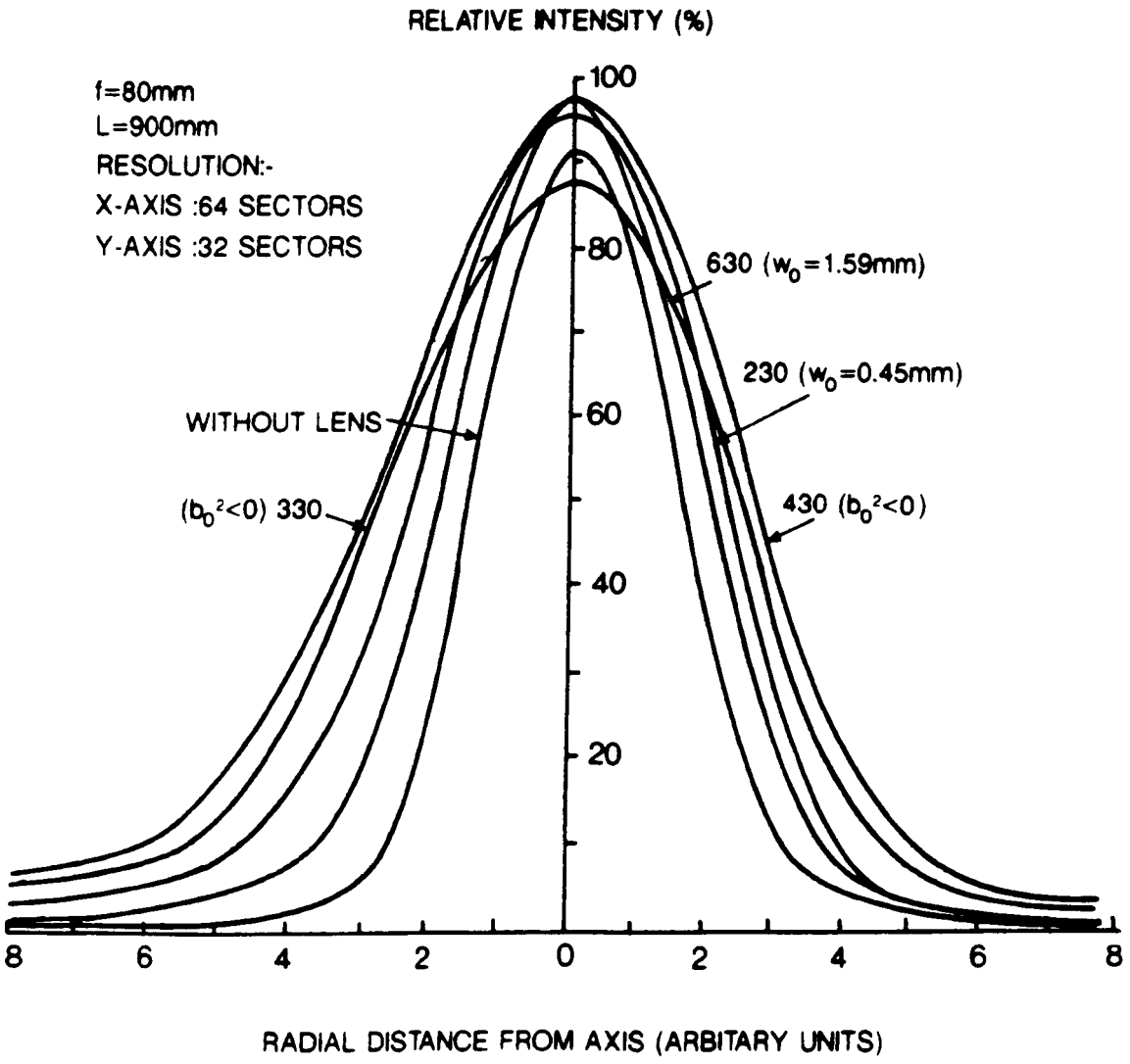

Figure 7.16. A composite graph showing the peak intensity slices through the probe laser beam for various lens placings (see Figure 7.15).

The waist determinations obtained with this experiment varied widely and sometimes gave imaginary values. The reasons for the uncorrelated results may be due to the profiler inherent resolution limit. The format of the profiler data was switch selectable to cater for the various transverse modes encountered in the laser laboratory, so that, for example, a long thin mode might be best taken as a 8 x 256 array, and a round or ovoid mode as a 32 x 64 array (each with a nominal 2 K memory data storage). Consequently, the peak intensity slice through the probe beam did not necessarily describe the beam profile through its diameter; the chance of observing the through-the-diameter slice would inevitably decrease as the probe beam spot size was reduced by the introduction of the focussing lens. Since the verification of the calculated probe beam waist could not be performed with the experimental apparatus at the time, the injection telecope design paramters could not be determined with confidence. Consequently, a telescope assembly with defocussing controls, and a probe laser translation stage were considered an essential part of the waveguide amplifier mode injection apparatus.

The sum of the telescope design parameters, $d_1+d_2+d_3$ (waist-to-waist separation), as a function of probe beam waist are presented in Figure 7.17, for the various fixed focal length lens pairs available at the time. The principal consideration that infuenced the choice of the lens pair was that of space, and whether the injection process

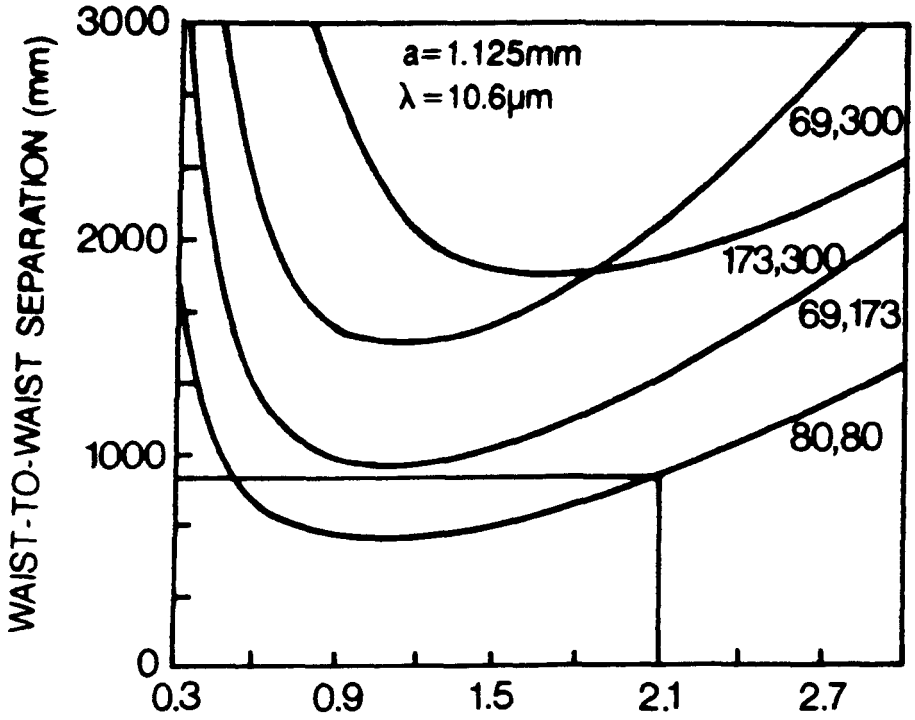

(a)

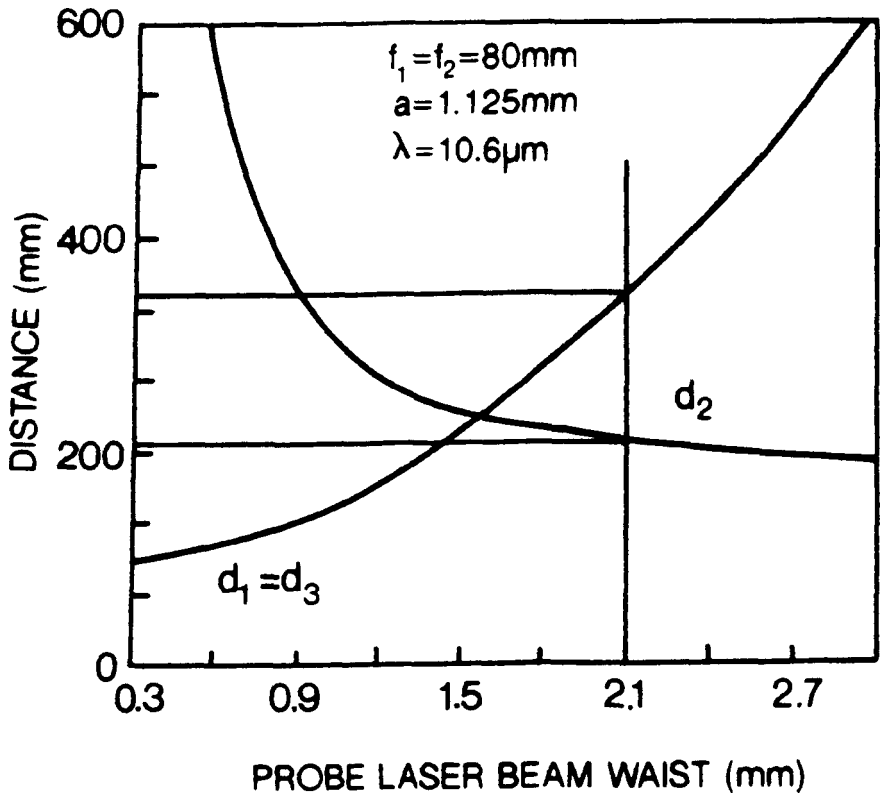

(b)

Figure 7.17. (a) Probe laser resonator waist-to-waveguide entrance spacing as a function of probe laser beam waist for various lens pair foci combinations.

(b) The parameters for the injection telescope used in the experiment.

could be performed without the need for beam concatination with steering optics and possible mode distortion on reflection.

With the chosen focii $f_1 = f_2 = 80$ mm and the calculated waist value $\omega_0 = 2.09$ mm, a waist-to-waist separation of $\sim$ 90 cm was required, with $d_1 = d_3 = \sim$ 35 cm and $d_2 = \sim$ 20 cm. From equation (7.27) the minimum diameter pinhole for effective spatial filtering with this geometry was 0.24 mm; approximately half the 0.5 mm diameter one used in the experiment.

7.4 Amplifier Noise Reduction Structures

If one amplifies coherent light in a travelling-wave CO_2 laser amplifier, then noise is added to the signal as a result of amplified spontaneous emission (ASE) by molecules in the upper laser level. This noise contribution is negligible in power amplifiers, but imposes significant limitations on the sensitivity enhancement achieved with small-signal amplifiers.

The amount of 'noise per mode' added to a signal in an optical amplifier can be significantly reduced by the introduction of a noise reduction structure [104,105]. The simplest kinds of noise reduction structures consist at the most of two aperture stops and a lens, although more complicated structures, like a series of lenses and aperture stops, may be more efficient in improving the signal-to-noise ratio (SNR). All variants take advantage of the

coherence of the signal to be amplified, and the incoherence of the ASE contributions.

The ultimate performance of a class of noise reduction structures was studied in [104], for a uniformly distributed active laser medium between two iris planes, and a signal beam with an approximately Gaussian transverse field distribution. In particular, a system of two aperture stops with an internal lens was considered. A noise reduction set-up of this type, with its output iris in the focal plane (shown schematically in Figure 7.18), $\overset{a}{w_s}$ incorporated into the amplifier experiment described in Chapter 8 (Section 2). To reduce the noise power passing through the hole A_2 to that radiated into a solid angle associated with a single black-body mode, requires a hole with radius

$$a_2 = \frac{f\lambda}{\pi a_1} \tag{7.47}$$

This is also the value that the radius of the signal beam assumes in the focal plane. The noise-in-signal transmitted through the system is proportional to the acceptance factor of the system, defined as

$$a = \frac{A_1 A_2}{d^2 \lambda^2} \tag{7.48}$$

The maximum SNR for any system in this class is achieved with a unity acceptance factor, in this case satisfied when

$$\frac{A_1 A_2}{f^2 \lambda^2} = 1 \tag{7.49}$$

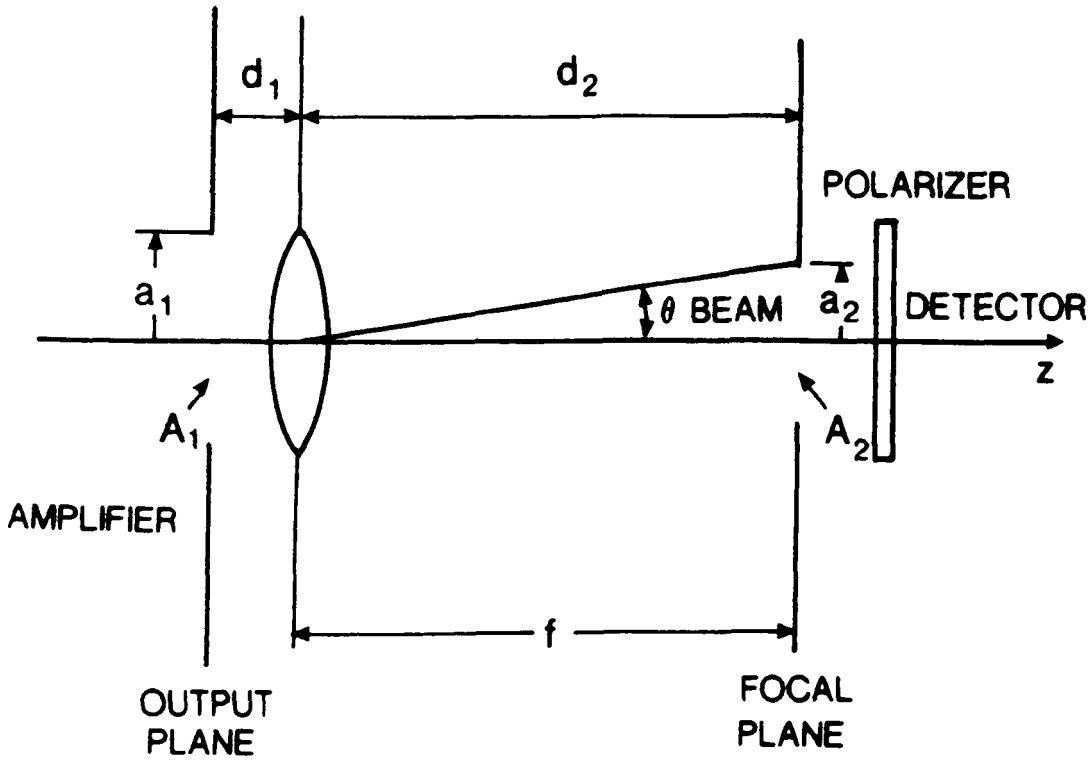

$$d = d_1 + d_2 - \frac{d_1 d_2}{f}$$

Fig. 7.18. Noise reduction structure with iris in focal plane (after Kogelnik and Yariv [104]).

In the experiment the active laser medium was contained within a 4 mm square bore channel and terminated by a 3 mm diameter iris in the amplifier output plane. For f = 100 mm and λ = 10.6 μm, equation (7.47) gives a_2 = 0.225 mm. The signal beam waist was transformed to match the 3 mm iris in the output plane of the amplifier using a single thin lens [117]. The relations above were derived with the assumption that the Gaussian signal beam passed undisturbed through the output iris. Actually an iris with a radius coincident with the spot size of the beam, intercepts 13.5% of the incident beam power. The diffraction effects associated with the resultant truncated Gaussian beam were also neglected.

An additional factor of two in noise reduction may be achieved by placing a polariser after the amplifier output plane. If the polarising element has the correct orientation the linearly polarised signal beam can pass with negligible attenuation. The maximum total noise reduction possible with the arrangement described above is given by

$$\frac{N_0}{N_{tot}} = \frac{2\lambda^2}{\pi A_1} \qquad (7.50)$$

For the parameter values above, the calculated noise reduction is at best 56 dB. The signal reduction for unity acceptance factor systems in this class is at least 2 dB.

The ASE noise contributions are broadband with a structure determined by the amplifier passband. In CO_2 amplifiers the noise spectra has an underlying rotational

line comb structure. Consequently, further noise reduction may be achieved by the introduction of a narrow band transmission filter. A P(20) etalon-stack rotational line filter, exhibiting a bandpass of ∿ 0.02 μm (± 60 GHz) with a transmission of 3% was incorporated in the experiment.

CHAPTER 8

MEASUREMENTS OF LASER AMPLIFICATION

Summary

In the context of achieving a better understanding of CO_2 lasers and single pass amplifiers, and their limitations, it is important to determine the gain parameters of the active medium and their dependences on the selectable parameters. To this end some preliminary experiments have been undertaken to measure the single pass passive and active transmission of the z-fold laser structure, and hence determine the small-signal gain coefficient of the CO_2 discharge and its variation with gas mixture and pressure, and RF power density (8.1). An additional consideration with optical pre-amplification is the signal-to-noise ratio at the amplifier output. In this respect, the performance of a large bore low pressure discharge module is assessed (8.2) using a technique to simultaneously measure the gain and amplified spontaneous emission noise power.

8.1 Folded Waveguide Power Amplification

A CO_2 waveguide amplifier is a suitable candidate for the power amplification of high intensity optical signals, especially those with large bandwidths or frequencies offset from line-centre of the Lorentzian gain profile. This suitability is a consequence of the small discharge tube cross-section and the corresponding increase in gas pressure, resulting in pressure-broadened linewidths as high as 1500 MHz and substantial increases in saturation intensity (see Chapter 1). These benefits are afforded at the cost of the available gain, although the reduction of the discharge gas temperature resulting from favourable collisional de-excitation and improved thermal conduction provided by the waveguide wall proximity, generally means that this is not too severe. Nevertheless, the rather modest small-signal gain coefficients associated with these devices, typically 0.5-1.0% cm, suggests that several meters of gain length is required for appreciable signal amplification, even more so for high intensity or frequency offset input signals that sample diminished gains. It is not practicable to build single segment waveguide amplifiers with the gain lengths required for even modest signal ampification. The same considerations that led to the design of the z-fold laser described in Chapter 4 apply here also.

In this section measurements of the single pass amplification of a frequency stable probe signal telescopically injected into the modified z-fold laser

structure are described. The z-fold laser small-signal gain coefficient and saturation intensity determinations presented in Chapter 5 gave values of 0.66-0.72%/cm and 7.4-8.2 KW/cm^2 respectively, for discharges in a $3He:1N_2:1CO_1$ + 5% Xe gas mixture at pressures between 60 and 80 torr, excited with an RF power of 66.5 W/cm^3 at 125 MHz. The experiment described here was performed at an early stage in the evolution of the z-fold laser with slightly different operating conditions to those above, namely with RF power densities of 10-75 W/cm^3 at 145 MHz, and excluding the Xenon gas additive. Nevertheless, with the typical and expected discharge parameters above it was apparent that for the 1.15 m gain length a small-signal net gain of approximately 3 dB at the most could be expected (assumes a 5% loss per fold), only exhibiting appreciable gain saturation for input signal powers of tens of watts. At the time a probe laser with sufficient output power to enable gain saturation measurements to be performed was not available, consequently the amplifier measurements were restricteed to small-signal inputs.

The experimental apparatus is shown schematically in Figure 8.1. The linearly polarised probe beam was derived from a GTE Sylvania 948 CO_2 laser in which a stable discharge in 8 torr, $3He:1N_2:1CO_2$ was maintained at $\sim$ 12 kV and $\sim$ 5 mA. Analysis of the output spectrum showed that several rotational lines near 10.6 μm would oscillate. The laser could be tuned to oscillate on a single rotational line by varying the cavity length with a piezoelectric transducer

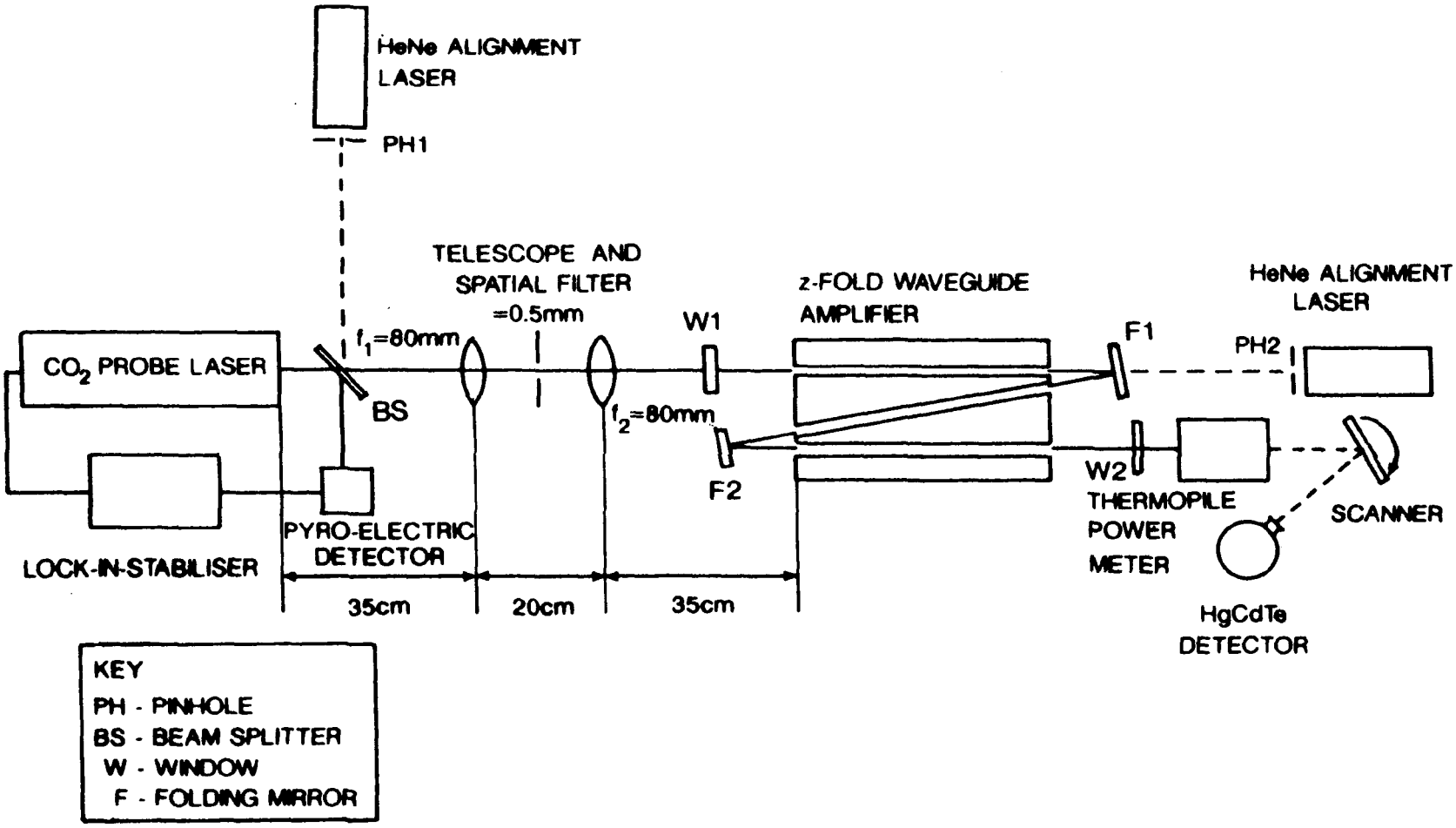

Fig. 8.1. Folded waveguide power amplification: experimental arrangement.

(PZT) while intra-line stability was achieved with a Lansing lock-in stabiliser. This applied a dither bias signal at 512 Hz to the PZT and continuously adjusted the PZT DC bias for maximum laser output power monitored by phase sensitive detection with a pyroelectric detector in a feed-back configuration. Long term stability was aided by using a heat exchanger in a closed circuit water cooling system to maintain the quartz laser cavity tube at 15°C. Measurements of the DC loop gain and the drift in the voltage applied to the PZT to maintain lock-in stabilisation over a 12 hr period suggested a long term stability of 3 MHz or 1:10^7 while a power stability of 1:32 over 30 min was measured with a Coherent power meter. Scanning-rotating mirror beam profile measurements revealed a high TEM_{00} mode content. The unoptimised gas mixture gave an output power of typically 2-4 W cw.

The focal lengths and positions of the telescope components and the spatial filter iris diameter were chosen in accordance with the conditions for optimum mode-matched coupling to the fundamental waveguide mode, and for effective discrimination against higher order probe laser beam output modes (see Chapter 7, Section 3). Alignment of the telescope optics and the first waveguide segment was achieved as follows:- pinholed adhesive tabs were placed centrally over holes burnt in two cards placed at each end of the optical bench and in the path of the probe laser beam. The attitudes of the He-Ne laser beams were then adjusted to pass

through both pinholes to form the common 'visible' optic axis; the alignment of the waveguide axis and then the telescope components was thence easily achieved by observing the He-Ne laser beam transmission patterns on the opposing cards while adjusting the appropriate positioning controls. The alignment process was repeated many times and found to be a reliable technique.

The insertion loss associated with the injection optics was determined by measuring the probe laser powers immediately before and after the telescope stage; and found to be approximately 2.7% (-0.12 dB). Similarly, the ratio of the power entering and exiting the first waveguide segment (with the folding mirror there removed) was measured at best as 97.2 ± 1.9%. Beam profile measurements of the transmitted beam revealed a high quasi-$TEM_{0,0}$ mode content, suggesting that efficient excitation of the $EH_{1,1}$ fundamental waveguide mode had been accomplished. The sensitivity of the transmitted power to the alignment of, and the separation between the probe laser, the telescope components and the waveguide segment was found to be not too great, yet sensitive enough to permit fine in-situ alignment adjustments to be made to maximise the power; a reassuring configuration of a well aligned system. As expected, gross mis-alignments produced undesirable weak multi-mode outputs at the waveguide exit.

The ratio of the power entering the first waveguide segment to that exiting the third, with the folding mirrors

in place and aligned, was 85.7 ± 1.9%. This suggests an average coupling loss per fold of 7.0 ± 2.2% (assuming zero guiding losses and folding mirror reflectivities of 99.6%), which is considerably larger than the 5.34% predicted from the single mode coupling theory (for plane folding mirrors) presented in Chapter 2. The difference between the measured and predicted values was almost certainly due to mis-alignment of the folding mirrors as a result of cumulative errors during the alignment process. Fine adjustments to the alignment of the folding mirrors to maximise the transmitted power was awkward because the mirrors were held in three-pivot point mounts without independent tilt controls about the X or Y axes; and any atempt to iteratively adjust the mirrors invariably resulted in 'walking' the beam with disasterous effects on the mode quality of the output beam. It was at this stage in the evolution of the z-fold laser that steps were taken to improve the alignment control of the folding mirrors by replacing the existing mirror mounts with externally adjustable precision positioners with independent tilt controls.

The amplifier experiments, however were conducted without these interventions but with the best state of alignment that could be achieved at the time with the He-Ne alignment process. The consequences of slight mirror mis-alignment are not serious as far as single pass amplifier measurements are concerned considering that the small-signal

gain coefficient determinations can be derived from measurements of the passive and active transmitted powers [48], that is, from measurements of the transmitted powers with the discharge off and on respectively. The only reservation is that the gain sampled by a probe beam may be dependent on its transverse field distribution due to a non-uniform gain cross-section [120]. In this case, however, the active and transmitted beam profiles showed a predominantly quasi-TEM_{00} mode content with no discernable differences betweeen their shapes. The equation relating the passive (P_p) and active (P_a) powers to the small-signal gain coefficeint (g), mentioned in Chapter 7 and repeated here for convenience, is given by

$$g = \frac{1}{L} \text{Ln} \left(\frac{P_a}{P_p} \right) \qquad (8.1)$$

where L is the gain length.

The gain coefficients derived from measurements with the 2 W probe beam at 10.6 μm (P20) for a range of gas pressures and net RF powers are presented in Figure 8.2. The minimum and maximum RF powers for each gas pressure were restricted by the proviso that the discharge completely filled and was contained within the waveguide channels respectively. Evidently, RF power absorbed by a 'leak' discharge outside the channels would not contribute to signal amplification. and nor would unexcited channel regions (to the contrary, thermally excited gas would absorb the probe radiation), and

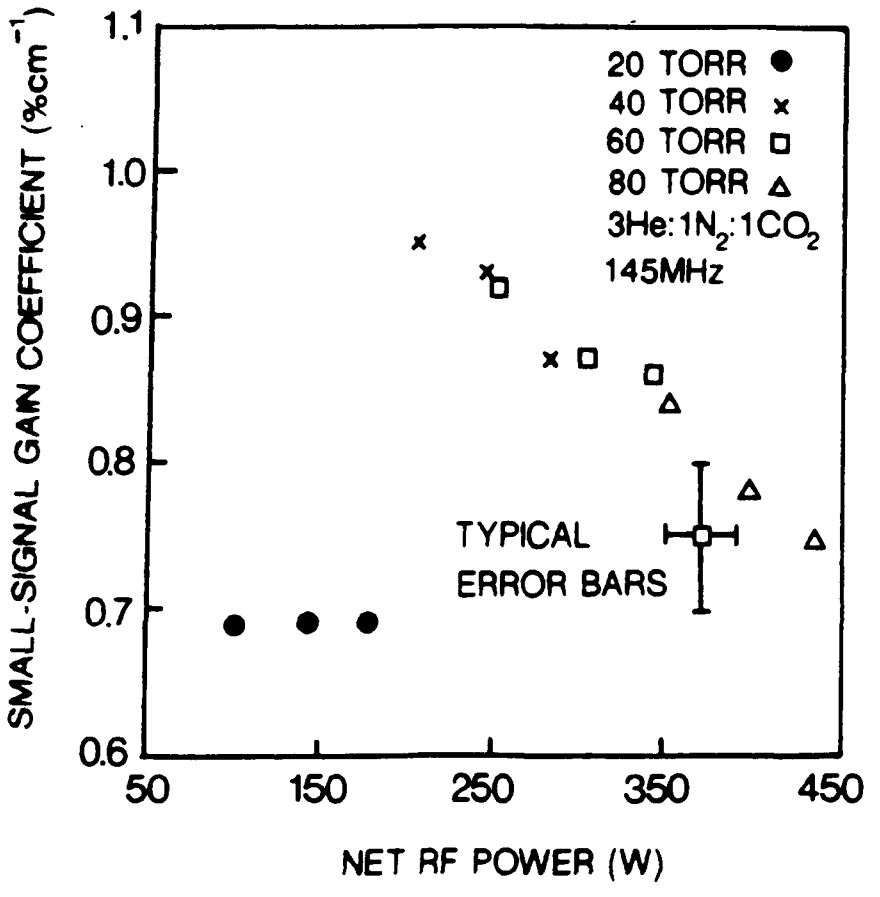

Figure 8.2. z-fold laser amplifier small signal gain coefficient as a function of the net rf power sustaining the discharge for various gas pressures.

the necessary corrections to the RF powers and gain lengths needed to calculate the gain coefficients could not be accurately evaluated. The maximum net power was also limited to the power rating of the RF generator used and the efficiency at which power could be transferred to the discharge region.

The decrease in the small-signal gain coefficients with increasing RF power is generally attributed to gas heating and the subsequent reduction in the population inversion supporting the amplification process by thermal population of the lower laser level. The absence of a maximum in the gain coefficient versus RF power curves in Figure 8.2 suggested that their was insufficient cooling of the discharge region. The cooling network at the time was only to the base of the laser vessel, and was later extended to the top RF electrode via vacuum-tight ceramic insulating pipes. The jump from gain coefficient values of $\sim$ 0.7%/cm at 20 torr to those of between $\sim$ 0.85-0.95%/cm at 40 torr, seems a little abrupt, albeit at RF powers differing by a factor of two (although the RF power per torr remains roughly the same). It is conceivable that at 20 torr and the low RF excitation powers, their may have been significant gain saturation, considering that the probe signal intensity was 100-200 W/cm^2.

The maximum small-signal gain coefficient observed, namely 0.95%/cm, was encouraging, although the corresponding maximum net gain of 1.45 (1.6 dB) was less so. The maximum available net gain possible with this small-signal gain

coefficient and the 1.15 m gain length, occurs with zero insertion loss (i.e. a passive transmission of 100%), and in this case evaluates to 2.98 (4.74 dB). Evidently the potential net gains of folded waveguide amplifiers can only be realised by significantly reducing the folding losses. Nevertheless, waveguide power amplifiers and the few decibels of net gain they can provide at these high operating pressures and hence wide bandwidths, make them attractive for inclusion in LIDAR systems.

8.2 Simultaneous Measurements of Gain and Spontaneous Emission Noise in RF Excited CO_2 Amplifying Media

There is much current interest in the performance of optical amplifiers for CO_2 LIDAR applications, where a weak return signal would benefit from pre-detection amplification with an increase in signal-to-noise ratio. A low noise, high gain, wideband optical pre-amplifier may revive direct detection techniques and enhance optical heterodyne techniques.

One of the fundamental proceses in an amplifying medium is the spontaneous emission of radiation by the molecules in the discharge volume. The higher the gain of the active medium, the higher (other conditions being equal) the spontaneous emission power [103]. Furthermore, the spontaneous emission power increases rapidly with increasing amplifier bandwidth (higher gas pressures), while the available gain decreases [102,103]. Consequently there are

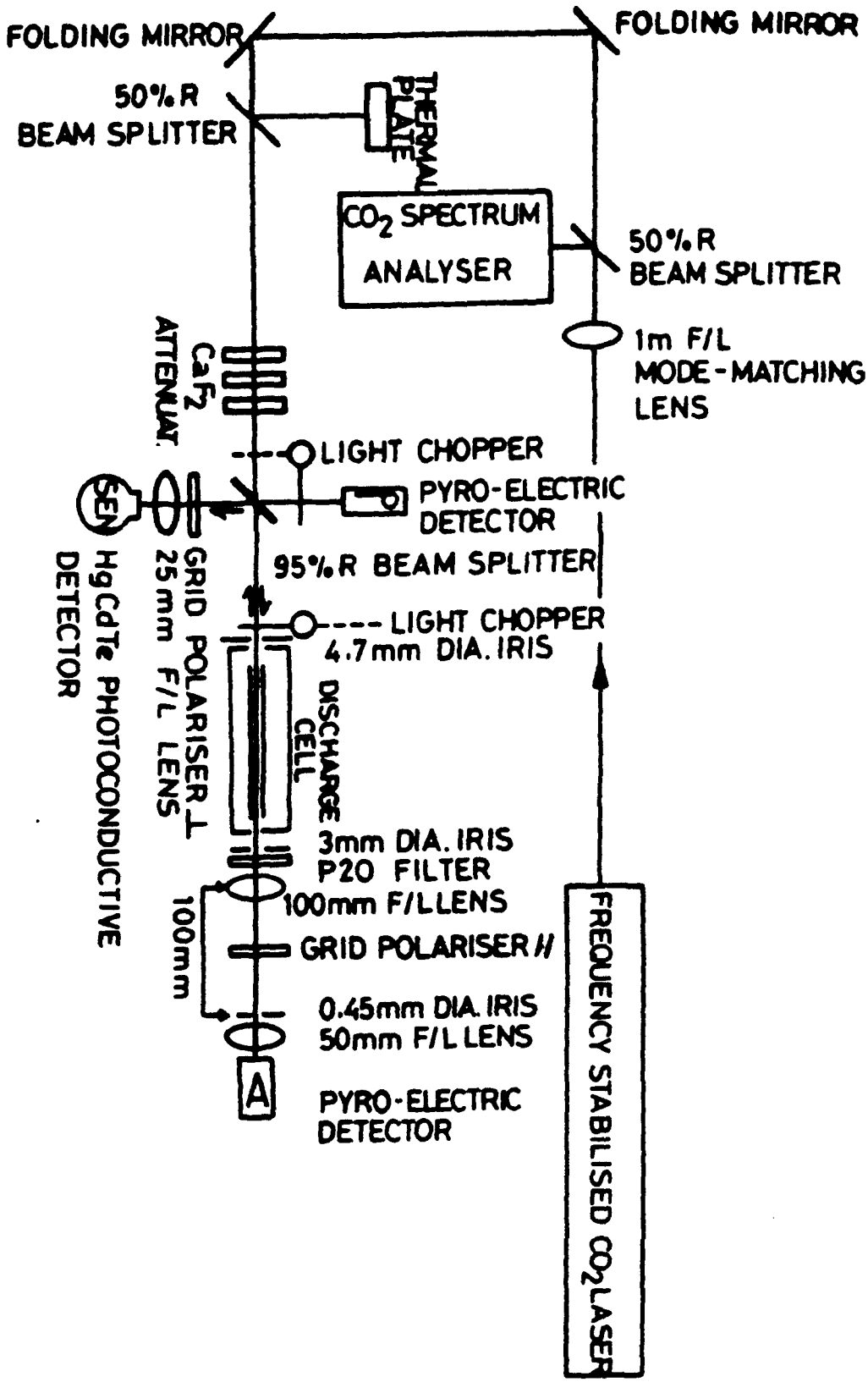

Figure 8.3. Schematic of the optical arrangement.

conflicting requirements in the design of optical amplifiers. There are however optimum operating conditions for particular applications and noise reduction systems (see Chapter 7, Section 4) which optimise the amplifier signal-to-noise ratio by taking advantage of the non-coherence of the spontaneous emission noise, its random polarisation and its broad spectral composition.

In this section an experimental technique is described that was developed to characterise the amplifying behaviour of an RF-excited CO_2 discharge module. In particular the dependence of the small-signal gain coefficient and amplified spontaneous emission (ASE) noise power on gas mixture and pressure, RF excitation frequency and power density were simultaneously measured for various discharge geometries, as part of a continuing activity in optical remote sensing, ranging, velocimetry and optical radar (with the co-operating body - RSRE, Malvern, U.K.)

The frequency stability of the probe laser is of prime importance when measuring the gain characteristics of CO_2 amplifiers because of the strong frequency dependence of gain which is especially prevalent in low pressure discharges. For example, a discharge in a $3He:1CO_2:1N_2$ gas mixture is pressure broadened at a rate of $\sim$ 5 MHz/torr limited to a minimum Doppler broadened value of $\sim$ 50 MHz. Hence a beam from an unstabilised Doppler broadened probe laser amplified in a low pressure discharge may experience a detuned gain diminished by $\sim$ 0.1 dB/MHz fom line centre. The probe laser

power stability is of less importance if appropriate steps are taken to compensate for it, as discussed later.

The amplifying medium was housed in a cell which consisted of an aluminium alloy box vacuum envelope, a side-viewing glass window, a RF vacuum feed-through connector and a vacuum/gas inlet hose port. The discharge was contained between hybrid Al/Al_2O_3 sandwiched electrode pairs up to 370 mm length, as illustrated in Figure 8.4, which could be configured to give a range of discharge cross-sections (both waveguide and non-wavegude). RF power was delivered via a 50 Ohm cable and impedance matching network to the centre of the top electrode. The lower electrode was grounded to the vacuum envelope which provided both an earth and an efficient RF shield. Additional shielding was achieved by placing copper gauze over the side-viewing window. The whole structure was maintained at $\sim$ 15°C by cooling the cell base with a closed circuit water cooling system.

Gas mixtures with varying concentrations of He, CO_2, N_2 and Xe were manufactured in a gas mixing manifold to ensure adequate mixing of the gases. The discharge chamber provided a gas ballast of $\sim$ 6 litres.

The RF and diagnostic systems are shown schematically in Figure 8.5. The RF signal was derived from a RF signal generator used to drive two wideband power amplifiers coupled with a Wilkinson combiner to give an output of up to 250 W at 70 MHz. Forward and reflected powers were monitored with a through-line RF power meter and a bi-directional coupler. A

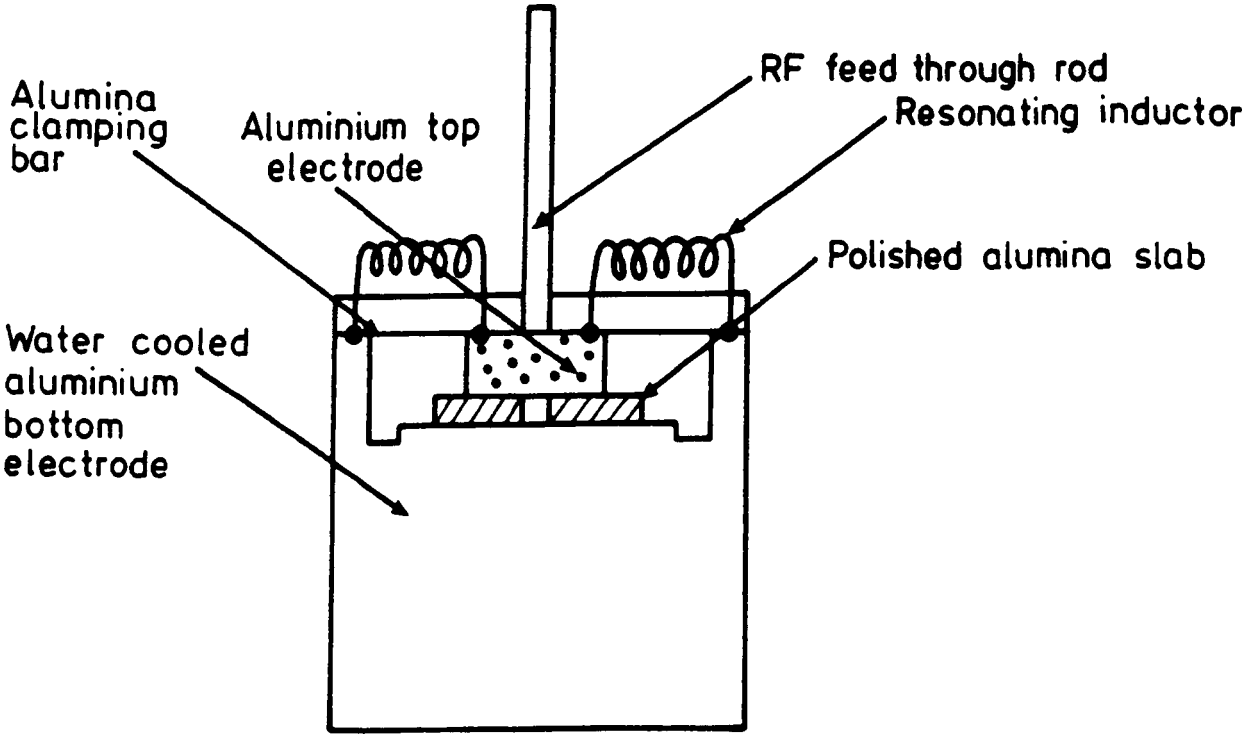

Figure 8.4. Schematic of the electrode structure.

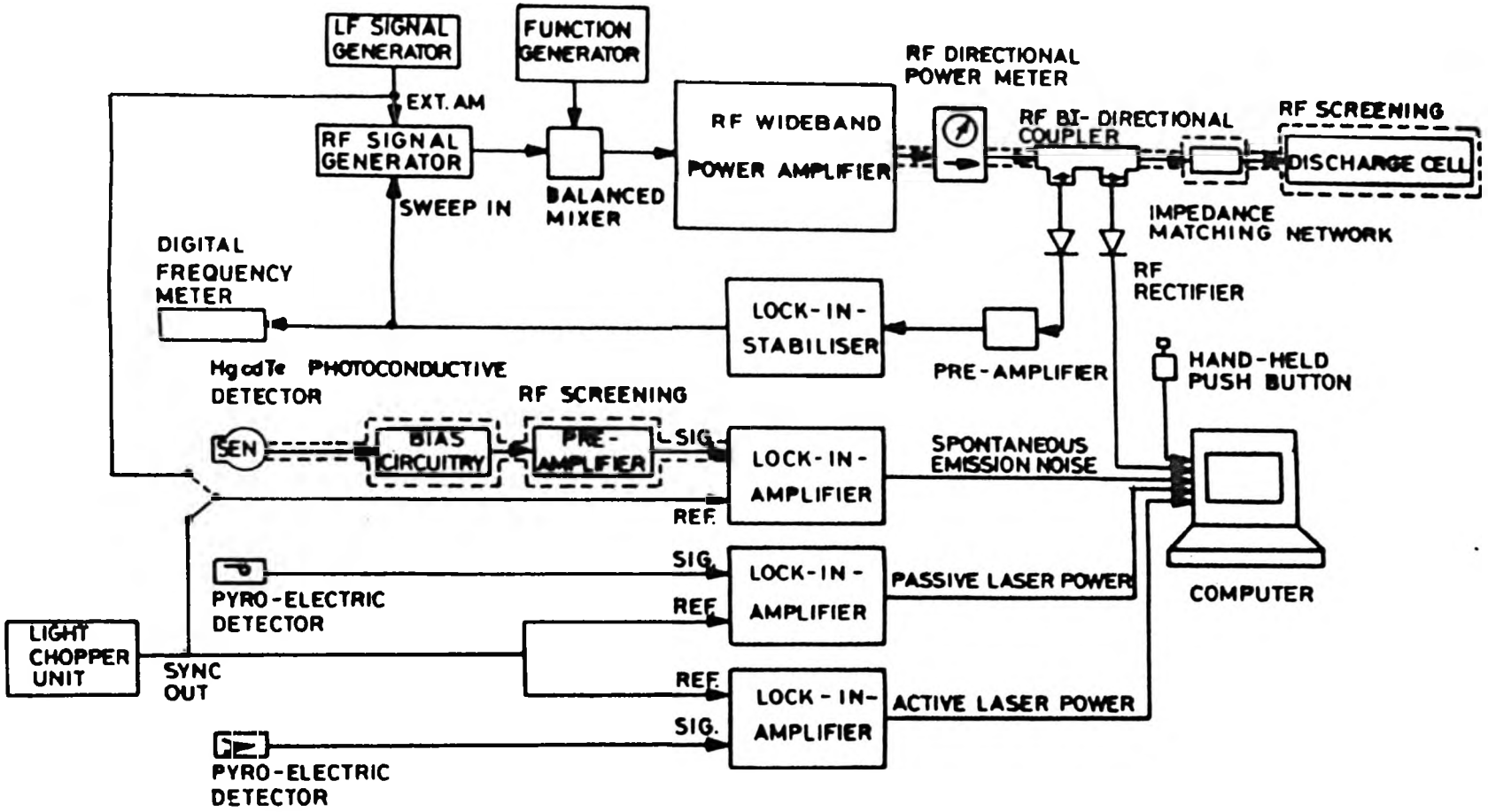

Figure 8.5. Schematic of the rf and diagnostic systems.

pi-impedance network was used to transform the discharge impedance to the 50 Ohm line. An RF sweep generator and bridge were used to adjust the network components for 'perfect' passive matching at the 70 MHz resonant frequency. The resonant frequency was determined by the value of multiple resonating inductors placed at equal intervals across the electrodes in parallel with the channel capacitance. The latter technique is used to reduce the longitudinal voltage variations, and hence gain non-uniformity, that arise because of the transmission line properties of the electrode structure.

A balanced mixer was used to control the RF drive amplitude level in a linear ramp fashion at 0.01-0.1 Hz to allow power dependent measurements of gain and amplified spontaneous emission noise to be made. This method was complicated by the dependence of discharge impedance on RF power density which produces varying degrees of impedance mis-match between the RF source and discharge head. To compensate for this a feed-back loop was introduced to adjust the RF drive frequency continuously for a minimum reflected power. The lock-in signal was produced by frequency modulating the RF drive signal at $\sim$ 100 KHz bandwidth and a dither frequency of 220 Hz. It should be noted that the automatic impedance matching technique developed during the experiments described in this section was later investigated in detail and improved, as described in Chapter 6. Measurements of the forward and reflected RF powers for a typical power ramp are shown in Figure 8.6 illustrating four

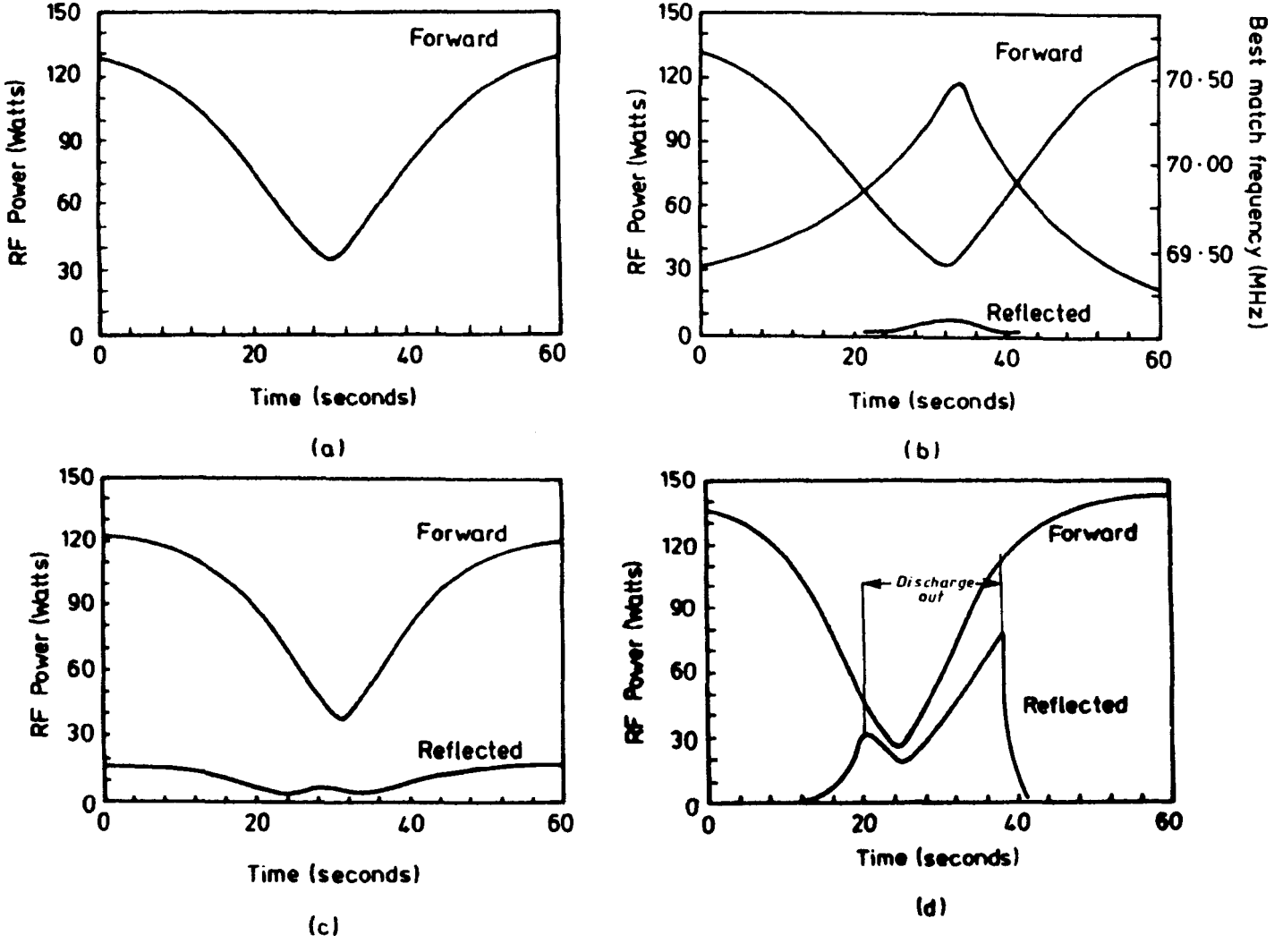

Figure 8.6. RF power ramp a) at 70 MHz into a 50 Ω dummy load, b) with automatic impedance matching while exciting a discharge, c) and d) at 69.5 70.5 MHz respectively, fixed frequency excitation.

operating conditions. Figures 8.6(a and b) show a 'perfect' power ramp into a 50 Ohm dummy load and auto-matching capability to emulate this while exciting a discharge. Significant reflected powers were only observed at low input powers when a rapid change in input impedance occurred as the discharge contracted in length and no longer filled the channel (a region of no practical interest). Figures 8.6(c and d) show the RF power ramp into a discharge at the fixed frequencies corresponding to the low and high power best match frequencies observed with the auto-matched power ramp. The effectiveness of the automatic matching technique is self-evident and reliable enough to permit the measurements of forward power to be taken as the power dissipated in the discharge. Here it was assumed that the reflected power and power losses in the impedance matching network and multiple resonating coils were negligible.

On some occasions it was desirable to apply amplitude modulation to the RF drive signal; this was typically 10% AM @ 500 Hz - 5 KHz square wave provided by an external low frequency signal generator, as discussed later.

A 1 m focal length lens was used to transform the 2.25 mm probe beam waist to a 1.50 mm waist in the input plane of a noise reduction structure placed immediately behind the cells output window. The noise reduction structure (described in Chapter 7) consisted of two aperture stops with a lens and polariser inserted between them. These

optical elements were arranged to form a system with an acceptance factor equal to unity, common to a class of noise reduction structures designed for an optimum signal-to-noise ratio, S_0/N_0; where S_0 is the signal power in the output plane of the amplifier and N_0 is the amount of noise escaping through the first aperture stop and radiating into a solid angle occupied by a single black-body mode. The calculated noise reduction for the particular structure chosen is at best 56 dB while the optimum signal injection loss is at least 2 dB. Additional noise reduction was achieved by the introduction of a narrow-band transmission filter [106] designed for transmission of the P(20) rotational line exhibiting a bandpass of $\sim$ 0.02 μm ($\sim$ ± 60 GHz). In practice it was not possible to detect the filtered noise above detector noise. Unfiltered noise emanating from the cell input window was focussed on to a HgCdTe photoconductive cryogenically-cooled detector element. Back reflections of the probe signal (which might have drowned the noise signal) were blocked by a crossed linear polariser.

The spontaneous emission noise power per mode escaping from an amplifier with a gain-length product G is given by [104]

$$N_0 = Gh\nu \, d\nu \frac{n_2}{n_2 - n_1 \left(\frac{g_1}{g_2}\right)} \qquad (8.2)$$

where n_1 and n_2 are the molecular population densities of the

energy levels coupled by the radiation of g_1 and g_2 are their respective degeneracies. In our case $d\upsilon$ is the amplifier bandwidth of the P(20) transition centred at 10.6 μm. Assuming that the state degeneracies are nearly equal and the density ratio $n_1/n_2 \sim 2$ then the equivalent noise input power to the amplifier is roughly equivalent to two photons per second per unit bandwidth. Hence in the experiment, a gain of ∿ 1%/cm along a 37 cm discharge with a pressure broadened linewidth of ∿ 100 MHz will have an equivalent noise input of ∿ 4 pW per mode and a 'worst-case' total noise over all solid angles and rotational lines of ∿ 1 μW appearing on the HgCdTe detector.

The passive (unamplified) and active (amplified) probe signals were monitored by two matched pyroelectric detectors. The light incident on these detectors was chopped at ∿ 300 Hz to facilitate phase-sensitive detection. The laser beam power was attenuated to provide a small-signal probe of approximately 1 mW which provided ample electrical signals well above the thermal background noise. The magnitude of the probe signal was kept to a minimum to reduce the amount of backscattered signal leaking through the crossed linear polariser placed in front of the HgCdTe detector. The amplified spontaneous emission noise signal, which was typically less than 1 μW, was monitored with phase-sensitive detection. The lock-in signal in this case was provided either by a light chopper placed in front of the cell input window, or by amplitude modulation of the RF power exciting the discharge.

The RF modulation technique mentioned above was used to measure the rate of change of ASE with RF power, or the first derivative of the light chopper measurement dependences (although not at the same time). This method was complicated by a RF interference problem, the seriousness of which becomes apparent when one realises that the interference signals are synchronous with the modulated ASE signal and at the same frequency. There is no way for the lock-in-amplifier to distinguish between the signal of interest and reference signal interference. To overcome this problem it was necessary to apply grounding and shielding techniques, particularly before the input to the HgCdTe detector pre-amplifier which had a power gain of 10^9. The nature of this type of experiment digresses a little from the subject of this section, and is mentioned here only to point out its potential usefulness to investigate the frequency dependences of the depth of modulation of the ASE to determine the effective lifetime of the upper laser level [121].

The HgCdTe photoconductive detector and its associated bias circuitry were calibrated against a standard 500 K black-body source chopped at 300 Hz. Measurements of the output signal as a function of power density incident on the detector element suggested an average responsivity of $\sim$ 1 mV/pW.

The experimental data were sampled by an 8 bit analogue to digital microcomputer interface which facilitated the continuous measurement of up to four voltages. A real

time BASIC program was written to access the analogue to digital conversions, perform a few simple calculations and display graphically the signal-averaged values of gain and spontaneous emission noise. The information was saved on disc for future analysis and/or screen dumped to a printer. The four analogue inputs were proportional to the forward RF power, active laser power, passive laser power, and amplified spontaneous emission noise power respectively. A hand-held push button was used to record the best RF impedance match frequencies observed on the digital frequency meter and their corresponding values of forward RF power at specified frequency increments.

Before any data were sampled it was necessary to allow sufficient time to establish a dynamic equlibrium so that any initial effects caused by the production of dissociation products (principally CO_2 into CO) and gas heating were passed. The RF power ramp period was chosen to minimise any gas heating lead/lag effects caused by the temporal changes in the power dissipated in the discharge region. The static gas pressure associated with a set of measurements was recorded before the discharge commenced because small pressure changes occurred during sample time. These pressure changes were typically of the order of a few percent and were attributed to gas heating and dissociation.

The amplifier gain coefficient is given by

$$g = 1/L \ln \langle V_a/V_p \rangle - \kappa \qquad (8.3)$$

where L is the active length, V_a and V_p are the active and passive laser power analogue input signals, and κ is a constant accounting for the differences in the no-gain powers incident on the pyroelectric detectors and the differing sensitivities of their associated circuitry, given by

$$\kappa = 1/L \ln \langle v_a/v_p \rangle \qquad (8.3)$$

where the lower case indicates that the discharge is off. The "<>" in the above equations indicates that the enclosed parameter has been signal-averaged by numerical integration.

8.2.1 Results and Discussion

A screen dump of data collected in a typical experiment is shown in Figure 8.7, revealing the degree of scatter of the measurement points which were sampled at least 100 times each. Quasi 3-dimensional graphs showing the hand-drawn best fit curves to the experimental data points sampled for a $3He:1N_2:1CO_2$ + 5% Xe gas mixture excited at 70 ± 0.5 MHz in a 4 x 4 x 370 mm^3 discharge channel are shown in Figure 8.8. The span of the RF power ramp was adjusted for each gas pressure to ensure that no data points were recorded outside a window bound by the conditions that the alpha-type discharge [71] completely filled and was contained within the channel region. Of particular interest are the weak dependences of both gain and ASE on RF power density. The gradual roll-off in gain observed at higher power densities and gas pressures is generally attributed to the reduction in the population inversion of the lasing transition by thermal

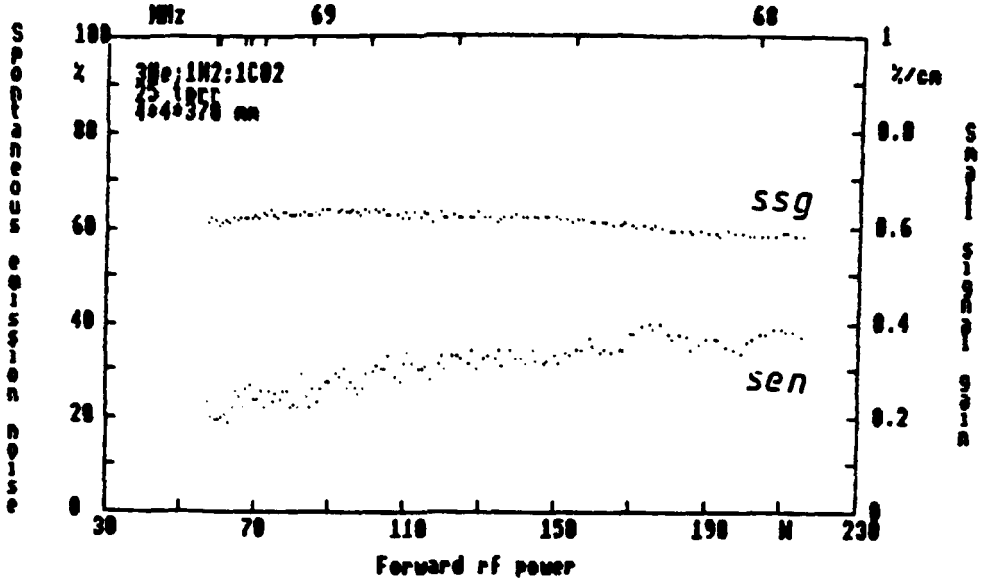

Figure 8.7. Computer screen dump showing the scatter of the signal-averaged data points collected in a typical experiment.

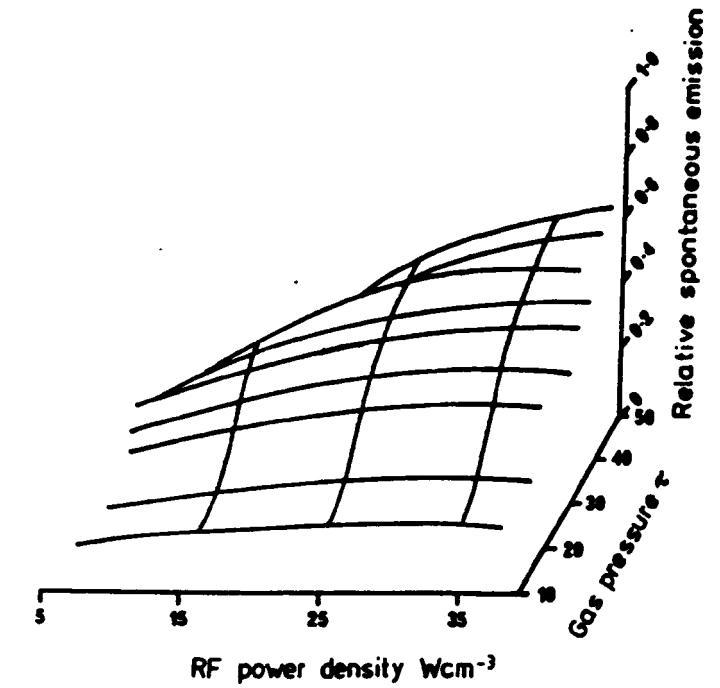

(a)

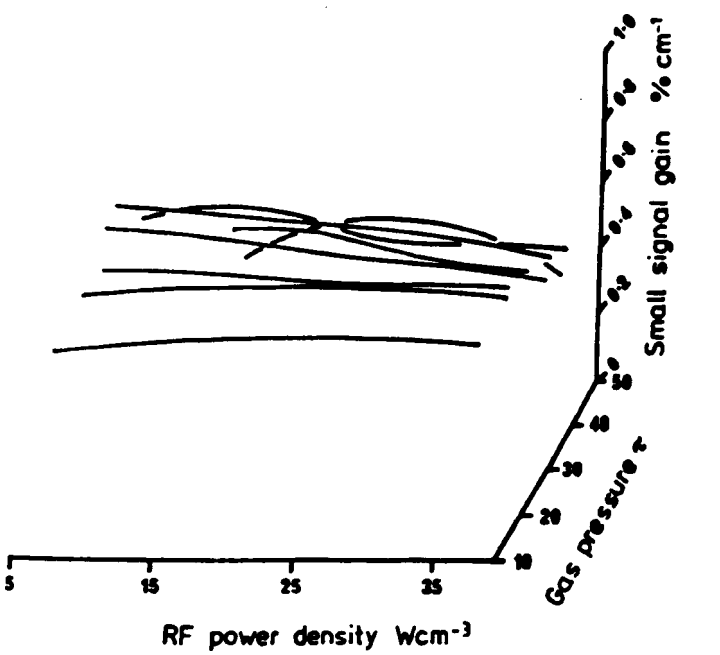

(b)

Figure 8.8. Amplified spontaneous emission (a) (100% = 10 pW), and small-signal gain (b), as functions of rf power density and gas pressure for a 4 x 4 x 370 mm^3 discharge in $3He:1N_2:1CO_2$ + 5% Xe gas mixture at the 70 MHz nominal excitation frequency.

excitation of the lower laser level and collisional de-excitation of the upper laser level respectively. It is not surprising that these trends are partially reflected in the behaviour of the ASE, although it must be appreciated that the rate of spontaneous emission is not linked to the population inversion mechanism, but rather to the density of states that support it. Consequently the ASE characteristics represent the gain-modified behaviour of the spontaneous emission dependences.

The maximum gains observed and the corresponding equivalent noise input powers derived from the simultaneous measurements of the ASE are shown in Figures 8.9(a and b) respectively. Hence the highest gain observed in the experimental parameter space was $\sim$ 0.8%/cm for a 3He:1N_2:1CO_2 + 5% Xe gas mixture with a 'worst-case' equivalent noise input power $\sim$ 1 photon/s/Hz The gain enhancement observed with Xe, seen here to be typically 0.1-0.2%/cm, is well documented in the literature (see for example ref. [36]) and is attributed to a reduction in the mean electron energy which increases the coupling efficiency of energy into the vibrational manifold of the CO_2 electronic ground state.

The measurements of gain in pure CO_2 were performed with a fresh charge of gas for each pressure change to minimise the incremental build up of the CO dissociation product. The dramatic decrease in gain with increasing gas pressure is almost certainly due to the collision de-excitation of the upper laser level and the absence of the nitrogen to replenish it by resonant vibrational energy transfer. The

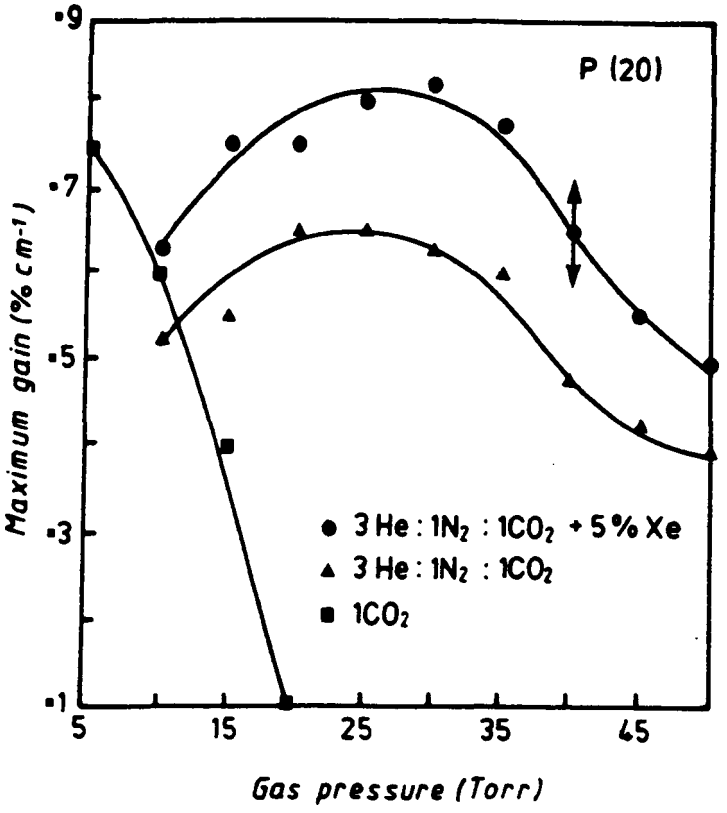

(a)

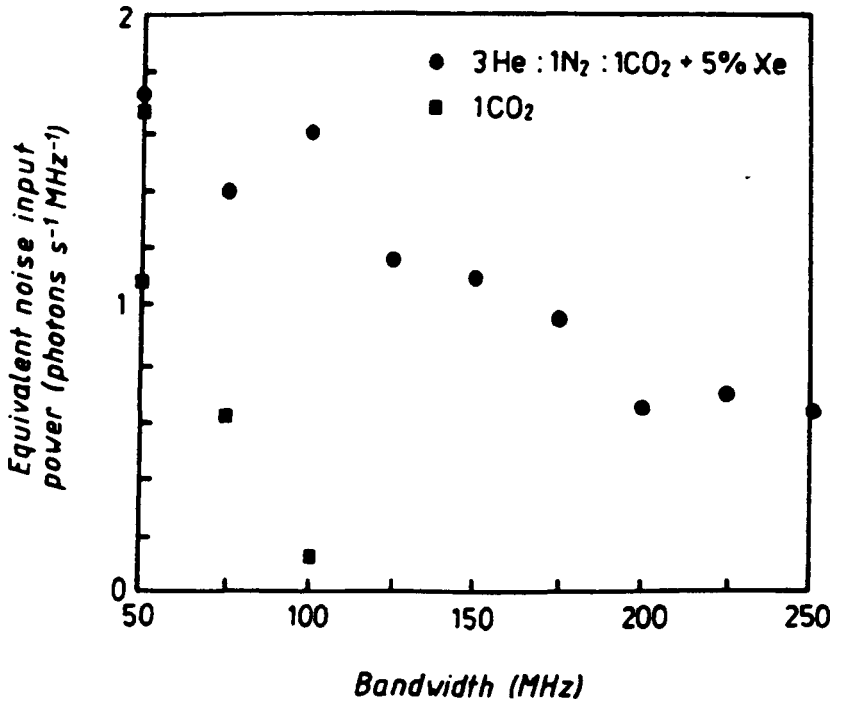

(b)

Figure 8.9. Maximum small-signal gains observed (a) and their associated 'worst-case' equivalent noise input powers (b) as functions of pressure for various gas mixtures.

population inversion is also greatly reduced by the absence of helium to provide the collisional relaxation of the lower laser level.

We have demonstrated an experimental technique used to simultaneously measure the RF input power dependences of small-signal gain and amplified spontaneous emission noise associated with a RF-excited CO_2 amplifier module for a variety of operating conditions. The experiment incorporates a novel automatic impedance matching capability to maintain efficient RF power delivery to the discharge over a wide range of time varying input powers. A computer has been used to sample the experimental data and display graphically their signal-averaged values. The latter techniques allow some degree of automation and hence reduce the data acquisition time. Consequently a systematic study over the large parameter space required to characterise RF-excited CO_2 amplifier modules to explore their potential as pre-detector amplifiers is feasible.

The preliminary results presented in this section are consistent with theoretical predictions and expectations. The rather modest levels of gain observed and their associated noise powers emphasise the limitations of these devices for pre-detection sensitivity enhancement in direct-detection receivers, especially those requiring large bandwidths to incorporate Doppler shifts in the incoming signals.

There are several refinements which can be made to further improve the amplifier performance. The most significant improvements may be achieved by further cooling of the amplifying medium to increase the available gain by suitable refrigeration and/or gas wall confinement proximity. The latter technique is common to waveguiding and its associated higher pressure (and hence larger bandwidth) operation. The considerations that led to the design of the noise reduction structure used in the experiment do not, however, extend to waveguide geometries. Further improvement in gain are possible with pulsed RF excitation where peak gains 5-10 times larger than those observed with continuous excitation are possible over > 100 μs intervals.

CHAPTER 9

9.1 Summary and Proposals for Future Work

In this thesis, theoretical and experimental results have been presented, concerning a compact folded waveguide resonator systems which is capable of producing high power output from a device with dimensions only marginally greater than conventional lower power structures. In the experiments, it has been shown that over 50 W power output was obtained from 115 cm of gain length. The resonator consisted of three waveguide segments coupled by two v-fold reflectors and enclosed by two Case I end reflectors. The detailed theoretical analysis of this z-fold laser resonator has shown that the resonator mode round-trip losses are mostly comprised of coupling losses at the v-folds. These losses strongly favour the fundamental waveguide mode, and for the ideal conditions where the gain medium is uniform and isotropic, this type of optical resonator can produce a quasi-Gaussian output beam.

A direct comparison between the measured z-fold laser output powers for the plane and curved mirror, and partial waveguide folding geometries indicated that the latter provides the lowest loss folding with the largest tolerance to angular misalignment of the reflector. The theoretical models included single and multi-mode coupling and guiding loss evaluations; and numerical, iterative and multi-mode

resonator round-trip loss determinations. Interpretation of the experimental results using a simultaneous Rigrod analysis to derive the resonator round-trip loss and gain parameters provided additional information and confirmation of the theoretical predictions.

The plane mirror v-fold and Case I coupling matrices were readily obtained using existing Hermite-Gaussian and scalar diffraction calculations. These calculations and those describing the waveguide propagation were incorporated into a computer programme that derived the z-fold resonator mode composition and round-trip loss by iteratively propagating an initially intensity normalised multi-mode field round and round the resonator path until a self-consistent resonator mode remained. The computer programme also modelled the z-fold resonator with one tilted fold mirror. The plane mirror folded laser gave a maximum power output of 30 W at the 90 torr discharge pressure in $3He:1N_2:1CO_2$ + 5% Xe, with a high quality quasi fundamental Gaussian mode. The simultaneous Rigrod solutions for the calculated round-trip loss of $\sim$ 20%, gave values of 0.68%/cm and 10.21 kW/cm^3 for the small-signal gain coefficient and saturation intensity respectively.

The curved mirror v-fold coupling matrices could not be calculated using existing coupling treatments due to the asymmetric phase front produced on reflection, and consequently, a new application of the scalar diffraction treatment was developed. The determination of the matrix

elements involved the evaluation of a four-fold integral, which was a time consuming process. The fundamental $EH_{1,1}$ single-mode coupling efficiency dependence on reflector curvature showed that a significant reduction in coupling loss could be achieved with a curved reflector, and since one resonator round-trip involved four v-fold reflections this suggested a reduction in the $EH_{1,1}$-like resonator mode round-trip loss. The iterative multi-mode resonator model determinations, however, indicated an increased round-trip loss for the fold mirror curvature that gave the minimum single mode ($EH_{1,1}$), single pass coupling loss. The accuracy of the latter result was questionable considering that only modes up to $EH_{3,3}$ (restricted by computer time considerations and memory storage limitations) were included in the iteration algorithm, and that the plane mirror v-fold resonator loss determinations were strongly dependent on the modal range (which was not restricted). The curved mirror folded laser gave a maximum power output of 34.5 W, and hence 4.5 W more than the maximum observed with plane mirror folding, without degrading the quality of the output beam. The calculated round-trip loss reduction associated with this power increase was 3.84% (to 15.70%).

The large folding losses associated with the plane and curved mirror v-fold geometries is attributed to their inherent large free-space propagating distances. The partial waveguide v-fold, on the other hand, contains little or no free-space propagation. Instead, the intra-mirror

propagation is by partial waveguiding resulting from the extension of the top, bottom and outer waveguide walls. To date, no attempt has been made to determine the partial waveguide coupling matrices, although their evaluation, which includes an amplitude overlap integral between the launched and entrant fields across the entrant waveguide, is identical to the Case I reflector in the y-direction (with the fold lying in the x-z plane). The x-integral is complicated by the asymmetry resulting from the three wall waveguide sections. The partial waveguide folded laser gave a maximum power output of 53.4 W, and hence 13.4 W more than the maximum observed with the plane mirror folding, with little degradation in the quality of the output beam. The calculated round-trip loss reduction associated with this power increase was 14.39% (to 5.15%) with a 1.10 ± 0.10% single pass loss per fold.

Clearly, the high power extraction of 0.46 W/cm demonstrated with the z-fold laser utilising the apparently hitherto unconsidered partial waveguide folding geometry, represents a significant improvement over the previous v-fold designs. Furthermore, the z-fold laser performance is comparable to that of the 'double' u-fold laser in [12] that produced a maximum of 55 W from 132 cm of gain length (similar bore) at 0.42 W/cm. The folding in the latter case was provided by AR coated total internal reflection triangular prisms with a calculated single pass loss of 3.5 ± 0.5%. The high volumetric efficiency of u-folding is,

however, afforded at the cost of added complexity and expense (the prisms need to be precisely machined, ground and polished). The partial waveguide v-fold, on the other hand, requires only one plane reflecting surface per fold, and replaces the 'waisted' free-space propagation path associated with the previous v-fold designs with an active length; but, because of the inclination between the adjacent waveguide paths, it is (generally) still not as volumetrically efficient as the u-fold. In addition, the tolerance to mis-alignment of the fold reflector is far greater with the partial waveguide folding than with the u-folding reported in [121]; namely, 13 1/3 and 10 mrad, as opposed to 5 and 3 1/3 mrad widths at the half-power points, for tilt about the x and y axes, respectively. The tolerance to mis-alignment must, however, be weighed against the degradation in the quality of the output beam, both in terms of its mode profile and intermediate (beat) frequency spectrum.

It should be noted that not all the z-fold laser operating conditions were optimised. Thus further experiments are needed, and in particular, to obtain the relationship between laser output power and gas composition. An indication that a significant improvement in laser power performance might be possible, is evident [121] where the larger gain length does not alone appear to compensate for the larger round-trip loss to give roughly the same maximum power output as that observed with the z-fold laser. Hence the gain medium in the latter case may have provided a small-signal gain and saturation intensity combination nearer

to the optimum, albeit at a power extraction efficiency (maximum laser power/RF input power) of 8.3% as opposed to the 9.3% reported here.

Clearly, to advance the understanding of the physics of the partial waveguide fold requires further work to evaluate its coupling behaviour as a function of the selectable parameters, particularly the fold-angle. It should be appreciated however that the evaluation of the v-fold coupling matrices and the determination of low loss single pass geometries does not alone provide enough information as regards to predicting the low-loss resonator configurations. Such predictions require multi-mode resonator treatments to include mode interference effects. The possibility that a further reduction in the folding losses might be possible is supported by the recent results in [54], where a z-fold waveguide laser (with a 2.25 mm circular bore and 6.2° v-fold angle) produced a maximum output power of 60 W from 111 cm of gain length at 0.54 W/cm and 10% efficiency. The low-loss v-fold geometry employed in this laser system was not revealed by the authors.

The reduction in the single pass v-fold losses through the introduction of partial waveguide folding is less significant for single pass optical amplification. Here the additional active length needed to compensate for the folding losses is only a small fraction of the total length required for a useful net gain.

From the discussions above it is clear that the partial waveguide v-fold is a suitable geometry for compact and low-loss folding. In the following, two approaches will be proposed for achieving a compact powerful laser system, capable of producing multi-hundreds of watts from a device volume only marginally larger than the conventional lower power structures.

In the first approach, a multilayer folded path utilising both v-folds and u-folds may be used to construct a long linear or ring laser resonator. As the operating power of the folded waveguide lasers is scaled to over the 100 W level, the optical flux incident on the folding mirrors, which is twice that incident on the two resonator folding mirrors, becomes large enough to cause optical damage.

This problem is alleviated in the second approach, where an array of waveguide lasers may be formed by a multiple stack phase locked array. A twin v-fold stack is shown schematically in Figure 9.1. The technique of phase-locking has recently been applied to CO_2 waveguide lasers [122] and particularly those employing RF excitation, where multiple discharge channels can easily be accommodated between transversely excited electrodes. The benefits of phase-locking of laser arrays are three fold; firstly, as mentioned above, high output powers can be achieved from a compact laser while alleviating the mirror damage problem; secondly, the far field output would have the characteristics of a single laser, with the output aperture

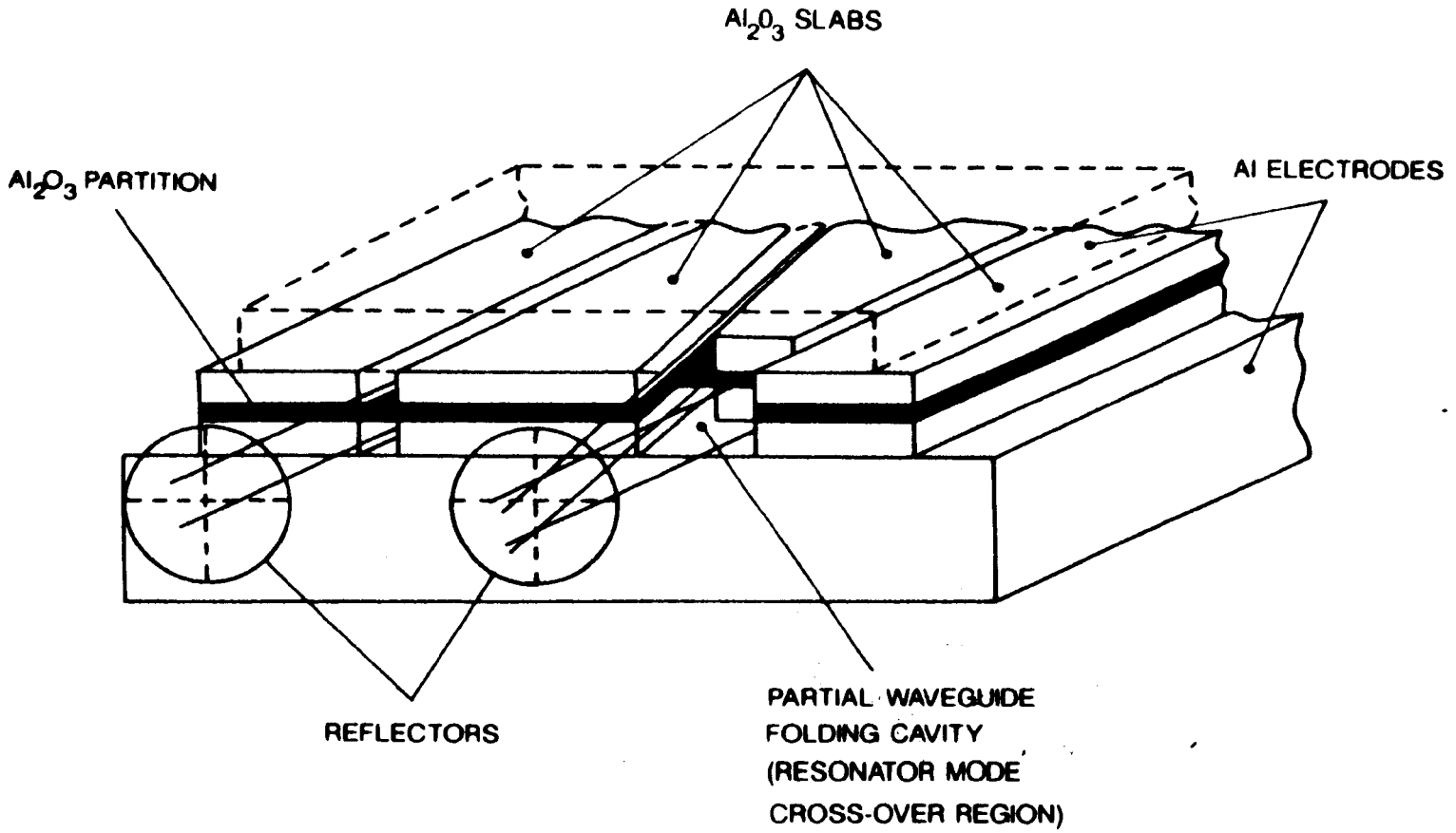

Fig. 9.1. Twin z-fold stack phase array.

corresponding to the area of the array, and an on-axis intensity proportional to the square of the number of individual lasers within the array; and thirdly, the pointing direction of the central intensity lobe could be controlled by programming the individual phase shifts to the individual lasers, producing a scanning beam devoid of any moving parts (in a manner analogous to a microwave phase array radar system).

The phase-locking of waveguides may be achieved with the close proximity of adjacent waveguides by means of radiation coupling via leakage through the guide in a direction transverse to the optic axis, or by exploiting the physics of guide-to-free-space coupling at the end of the waveguide. It is the potential of achieving this latter cross-talk which is inherently provided in a multi-stack v-fold. Here the folded radiation is allowed to leak into the folding cavity by the absence of two of the adjacent walls forming any waveguide path (or perhaps three in the case of a three or more layer stack). The partition between adjacent layers would need to be very thin (perhaps less than 0.5 mm). If a large number of layers were used (forming a linear array) it would be difficult to excite the channels with a single pair of electrodes because of their large separation; instead parallel or series electrode connections to metal partition walls could be used. Although a multiple v- or z-fold stack could only be used to form a linear array at one of the 'loose' ends, it is conceivable that two v-fold stacks placed

side-to-side, perhaps at a slight inclination, forming a w-fold stack could be used to form a two dimensional array of order 2 x N, where N is the number of layers in the stack. The inclination factor would introduce an additional parameter to influence the far field intensity pattern.

APPENDIX A

PROOF OF SYMMETRY IN THE CURVED MIRROR COUPLING COEFFICIENT MATRIX

The work described in this Appendix was undertaken on my behalf by Dr. Choudhury (University of Hull).

We first show that

$$\int_{-1}^{1} dx \int_{-1}^{1} dy f(x,y) = 0 \quad \text{if} \quad f(-x,-y) = -f(x,y)$$

Proof

$$\int_{-1}^{1} dx \int_{-1}^{1} dy f(x,y) = \int_{0}^{1} dx \int_{-1}^{1} dy f(x,y) + \int_{-1}^{0} dy f(x,y)$$

$$= \int_{0}^{1} dx \left[\int_{0}^{1} dy f(x,y) + \int_{-1}^{0} dy f(x,y)\right] + \int_{-1}^{0} dx \left[\int_{0}^{1} dy f(x,y) + \int_{-1}^{0} dy f(x,y)\right]$$

or

$$\int_{-1}^{1} dy f(x,y) = \int_{0}^{1} dx \int_{0}^{1} dy f(x,y) + \int_{0}^{1} dx \int_{-1}^{0} dy f(x,y) + \int_{-1}^{0} dx \int_{0}^{1} dy f(x,y) + \int_{-1}^{0} dx \int_{-1}^{0} dy f(x,y)$$

Make the substitution $x = -x'$, $y = -y'$, $dx = -dx'$, $dy = -dy'$ in the 3rd and 4th integrals in (2):

$$\int_{-1}^{1} dx \int_{-1}^{1} dy f(x,y) = \int_{0}^{1} dx \int_{0}^{1} dy f(x,y) + \int_{0}^{1} dx \int_{-1}^{0} dy f(x,y) + \int_{1}^{0} dx' \int_{0}^{-1} dy' f(-x',-y') + \int_{1}^{0} dx' \int_{1}^{0} dy' f(-x',-y')$$

$$= \int_{0}^{1} dx \int_{0}^{1} dy f(x,y) + \int_{0}^{1} dx \int_{-1}^{0} dy f(x,y) - \int_{0}^{1} dx' \int_{-1}^{0} dy' f(x',y') - \int_{0}^{1} dx' \int_{0}^{1} dy' f(x',y')$$

$$= 0$$

We consider the integrals (general form of equation (2.36))

$$EH^{p'q'}_{pq} = \left(\frac{N\cos^2\theta}{2}\right)^2 \left| \int_{-1}^{1} dX_0 \int_{-1}^{1} dX_2 \int_{-1}^{1} dY_0 \int_{-1}^{1} dY_2 \exp\left[j\pi N \left(X_0^2+X_2^2+Y_0^2+Y_2^2 - \frac{(X_0+X_2)^2\cos^2\theta + (Y_0+Y_2)^2}{2\left(1-\beta\left[\cos\theta - \frac{\sin^2\theta(X_0-X_2)}{2(\cos\theta+F)}\right]\right)}\right)\right]$$

$$\text{upper } \left(\begin{matrix}\text{odd}\\ p's+q's\end{matrix}\right) \quad \cos\left(\frac{pX_0\pi}{2}\right) \quad \cos\left(\frac{p'X_2\pi}{2}\right) \quad \cos\left(\frac{qY_0\pi}{2}\right) \quad \cos\left(\frac{q'Y_2\pi}{2}\right)$$

$$\text{lower } \left(\begin{matrix}\text{even}\\ p's+q's\end{matrix}\right) \quad \sin\left(\frac{pX_0\pi}{2}\right) \quad \sin\left(\frac{p'X_2\pi}{2}\right) \quad \sin\left(\frac{qY_0\pi}{2}\right) \quad \sin\left(\frac{q'Y_2\pi}{2}\right)$$

$$\Bigg| \Bigg/ \left(1 - \beta\left[\cos\theta - \frac{\sin^2\theta\,(X_0-X_2)}{2(\cos\theta + F)}\right]\right)$$

Recall that the sine function is odd whilst the cosine function is even. Examining equation (3), it is clear that if q is odd and q' even or q is even and q' odd, that is, if q + q' is odd, then the integrand of (3) considered as a function of $Y_0 + Y_2$ is an odd function. Hence, using the result (1) we have

$$EH^{p'q'}_{pq} = 0 \text{ if } q + q' \text{ is odd} \qquad (4)$$

Also, the factor

$$\frac{\beta\sin^2\theta(X_0-X_2)}{2(\cos\theta + F)} \ll 1 \text{ and hence can be neglected.}$$

If the argument that led to the result (4) is now applied with the integrand in (3) considered as a function of $X_0 + X_2$ gives immediately

$$EH^{p'q'}_{pq} = 0, \text{ if } p + p' \text{ is odd} \tag{5}$$

to a higher degree of accuracy.

For non vanishing values of (3) we must have either

$$\cos\left(\frac{qY_0\pi}{2}\right)\cos\left(\frac{q'Y_2\pi}{2}\right) \text{ or } \sin\left(\frac{qY_0\pi}{2}\right)\sin\left(\frac{q'Y_0\pi}{2}\right).$$

Under these circumstances the integral (3) remains unchanged under the interchange $q \longleftrightarrow q'$. Hence

$$EH^{p'q'}_{pq} = EH^{p'q}_{pq} \tag{6}$$

Similarly, if we neglect the term

$$\frac{\beta\sin^2\theta(X_0-X_2)}{2(\cos\theta + F)}$$

as pointed out before, the integral in (3) remains unchanged under the interchange $p \longleftrightarrow p'$, yielding the result

$$EH^{p'q'}_{pq} = EH^{pq'}_{p'q} \tag{7}$$

Combining (6) and (7) we get

$$EH_{p'q'}^{pq} = EH^{p'q'}_{pq} \tag{8}$$

APPENDIX B

CO_2 LASER AMPLIFIER SURVEY

A. CW DC-Excited Waveguide Laser Power Amplifier

In 1975 Klein and Abrams [47] reported the results of a theoretical and experimental study of power amplification in a cw DC-excited CO_2 flowing gas waveguide power amplifier. Their theoretical analysis derived expressions relating independent amplifier parameters such as overall length, small-signal gain coefficent, and linewidth to system design requirements such as overall gain output power and output linewidth.

Design specifications

1.65 mm circular bore in BeO

14 discharge sections giving a 77 cm active length

1 m device length

3.3:1.1, 7:1.1:1, 10.5:1.3:1 ($He:N_2:CO_2$) gas mixtures

0-200 torr gas pressure

0-600 gas changes per second

60-180 Wcm^3 DC power density

2.5-17.5 (1.2-3.7%/cm) net P20 unsaturated gain

1-6 KW/cm^2 (5-25 W) saturation intensity

$\sim$ 15% power broadening at 100 torr, 80 W output

This 1 m device consisted of 7 shunted waveguide segments. The 8% insertion losses associated with mode injection and

mis-alignment of the waveguide joints were acceptable when compared to the available net gains of 5600% (flowing gas). Static gas operation with a diminished gain coefficeint of ∿ 1%/cm would require a device length of ∿ 4 m with 32 segments to achieve the same net gain (assumes zero insertion losses). In practice the ∿ 0.7% measured coupling losses at each joint would give a combined total insertion loss of ∿ 21%, reducing the effective net gain by a factor of 2.5 to ∿ 2000%. Hence, including the losses we find that an equivalent static gas device would have a length of ∿ 5.25 m.

The segmented design was a consequence of practical restrictions on the length of available ceramic sections with precision waveguide bores. Although waveguide construction techniques have developed considerably since 1975, there are still problems associated with long straight waveuide fabrication. Alternatively, one might consider folded waveguide paths. The coupling losses between waveguide sections tend to be larger in these devices, although considerable improvements are expected [123]. The obvious advantages of compactness and sealed-off operation are often paramount in field devices.

B. CW DC-Excited CO_2 Multipath Cell Laser Power Amplifier

This device, described by Dezenburg and Merritt [124], comprised a low pressure flowing gas discharge cell within a modified White mirror system, and provided a large gain

length in a compact multipath structure.

Design specifications:

7.7 cm diameter discharge tube

4-30 paths through a 1.5 m active length

$1N_2:0.5CO_2:3.5He$ at 5 torr

$\sim$ 1 gas change per second

$\sim$ 10 W/cm^3 DC power density

1-9 dB ($\sim$ 0.05%/cm) net gain (6 W input)

$\sim$ 65 W/cm^3 50 W) saturation intensity

The disappointing value of the gain coefficient exhibited by this laser amplifier gas mixture was possibly due to insufficient concentrations of CO_2. The amount of helium present in the mixture may have been excessive in view of the marginal gas heating produced by the low power density needed to excite the gas at this pressure.

C. CW DC-Excited Multipath CO_2 Laser Preamplifier

A cw DC-excited CO_2 laser preamplifier utilising a modified White optical reflector was used by Hieslmair et al. in 1980 [125] to amplify low signal 2 μs pulses at 500 Hz PRF.

Design specifications:

4.7 cm diameter discharge tube

16 paths through a 0.6 m active length

$1CO_2:1.4N_2:2.9$ He at torr

17-39 dB (0.4-0.7%/cm) net gain (1-100 mW input pulses)

50 W/cm² saturation intensity

∿ 100 photons/s per Hz NEP

Gain saturation in this device occurred at relatively low input powers of ∿ 100 mW, owing to the periodic re-focussing of the input laser beam at the conjugate foci of the White cell reflectors. Periodic re-focussing is also detrimental to SNR enhancement as ASE noise contributions are guided towards the amplifier output. The gain figures are, however, very encouraging albeit at the Doppler broadened linewidth.

D. CW DC-Excited CO_2 Laser Preamplifier

In 1975 Lotspeich [102] analysed the noise sources involved with optical preamplification and experimented with a two stage DC-excited gas flowing CO_2 preamplifier.

Design specifications:

2 serial optically coupled 19 mm diameter discharge tubes

72 cm active length

5He:1CO_2:0.6N_2 gas mixture at 8 torr

12 gas changes per second

1.5-3.9 dB (0.5-1.3%/cm) net P20 gain

40-90 photons/s per Hz NEP

Lotspeich concluded that the optimum useful gain from an amplifier with a single-line bandwidth of 100 MHz is 6 dB for a background temperature of 300 K, with a corresponding SNR enhancement of 5.9 dB. In addition, the degree of amplifier

enhancement is inversely proportional to amplifier bandwidth. This background noise limited system designed using periscopic and relay optics provided a considerable field of view, but permitted multiple noise modes on the detector.

E. CW RF-Excited CO_2 Laser Preamplifier

Recent research at the author's facility [82] has included the simultaneous measurements of gain and spontaneous emission noise in a static gas RF-excited CO_2 discharge module.

Design specifications:

4 mm square bore Al/Al_2O_3 discharge channel

37 cm active length

$3He:1N_2:1CO_2$ + % Xe

10-50 torr gas pressure

Static gas fill

5-40 W/cm^3 RF power density at 70 MHz

0.8-1.3 dB (0.5-0.8%/cm) net P20 gain

Noise reduction structure with unity acceptance factor

1-2 photons/s per Hz NEP

The marginal net gains associated with this device were a consequence of the short gain length chosen. The data extracted from path studies performed with this module, did, however, provide useful information regarding noise reduction. The recent advances in RF discharge technology make this mode of excitation favourable for devices where wall-proximity cooling is preferable.

F. Pulsed DC-Excited CO_2 Laser Preamplifier

Recent research by McLellan, Fisher (of Pulsed Systems Inc.) and Bufton [110] has produced a commercially available LDP-30 laser detector preamplifier for CO_2 lasers.

Design specifications:

Triode-electrode transverse excitation

± 600 V DC at 0-10 Hz PRF

Uniform rectangular cross-section plasma

7 beam passes through a 30 cm active length

14" x 9.25" . 7.25" device size

6.5:1.5:1.8:0.2, 8.2:0.8:0.8:0.2 ($He:N_2:CO_2:CO$) gas mixtures

5-150 torr gas pressures

0.14 l/min gas flow

28 dB (3%/cm) net gain at 40 torr for 100 μs

7000 photons/s per Hz NEP

G. An RF-Excited Multipath Coaxial CO_2 Discharge Laser Amplifier

In 1985 Biselli and Malota [126] described the cw and pulsed operation of an RF-excited multiple pass reflector coaxial CO_2 discharge laser amplifier. The amplifier was simultaneously used to amplify transmitted and received pulses in both a cw and pulsed heterodyne rangefinder.

Design specifications:

Annular discharge cross-section

5 paths through a 1.2 m active length

(1.8-2.%/cm) saturated gain (<2 W> input at up to 100 Hz PRF)

H. AN RF-Excited Multipath Coaxial CO_2 Discharge Laser Amplifier

The recent development of a compact, multipath, static gas coaxial discharge CO_2 laser utilising a Herriott cell folding system, by Xin and Hall [127] at the author's facility, has potential for laser amplification.

Design specifications:

Annular discharge cross-section

3.4 and 4.6 cm diameter cylindrical electrodes

19 paths through a 26 cm active length

8" x 8" x 24" device size

$3He:1N_2:1CO_2$ + 5% Xe gas mixture

130 W/cm³ RF power density at 42 MHz

10-50 torr gas pressures

CW:

7.5 dB (0.35%/cm) estimated P20 gain

850 W/cm² (∿ 100 W) saturation intensity

18 W input for unsaturated output

Pulsed:

30 dB (1.4%/cm) estimated net P20 gain

REFERENCES

[1] C.K.N. Patel, "Continuous-wave laser action on vibrational-rotational transitions of CO_2", Phys. Rev., Vol. 33, 6A, 1187, 1964.

[2] J-L. Lachambre et al., "A transversely RF-excited CO_2 waveguide laser", Appl. Phys. Lett., 32(10), 652-653, 15 May 1978.

[3] K.D. Laakmann, Paper TUKK3 presented at CLEO, San Diego, February 1980.

[4] G. Allcock and D.R. Hall, "An efficient RF excited, waveguide CO_2 laser, Opt. Commun., 37(1), 49-52, 1 April 1981.

[5] S. Vol'skaya and A.F. Tstelykovskii, "Waveguide CO_2 laser with high frequency excitation", Sov. J. Quantum Electron., 11(5), 666-667, May 1981.

[6] D. He and D.R. Hall, "A 30-W radio frequency excited waveguide CO_2 laser", Appl. Phys. Lett., 43(8), 726-728, 15 October 1983.

[7] G.A. Griffith, "Transverse RF plasma discharge characterisation for CO_2 waveguide lasers', SPIE, 227(6), 6-11, 1980.

[8] E.I. Gordon and A.D. White, "Similarity laws for the effects of pressure and discharge diameter on gain of He-Ne lasers", Appl. Phys. Lett., 3(11), 199-203, 1983.

[9] L. Lundgren, "Pump efficiency and saturation effects in waveguide lasers", Appl. Phys., 48(11), 4484-4485, 11 November 1977.

[10] B.A. Kuzyakov and V.F. Khor-kov, "Saturation parameter of a waveguide CO_2 laser", Sov. Phys. Tech. Phys., 24(10), 1269-1270, October 1979.

[11] R.L. Abrams and W.B. Bridges, "Characteristics of sealed-off waveguide CO_2 lasers", IEEE J. Quantum Electron., 20(5), 509-514, 1984.

[12] D. He and D.R. Hall, "Frequency dependence in RF discharge excited waveguide CO_2 lasers", IEEE J. Quantum Electron., 20(5), 509-514, 1984.

[13] H. Shiahata and T. Fusioka, "Wall depletion effect of population at upper laser level on optical gain in CO_2-He waveguide lasers", Appl. Phys., 47(6), 2452-2453, June 1976.

[14] H. Shields and A.L.S. Smith, "Gas temperature and cooling in waveguide CO_2 lasers", Appl. Phys., 48(11), 4807-4808, November 1977.

[15] D. Marcuse, "Theory of dielectric optical waveguides", Academic Press, 1974.

[16] E.A.J. Marcatili and R.A. Schmeltzer, "Hollow metallic and dielectric waveguides for long distance optical transmission and lasers", Bell Syst. Tech. J., (43), 1783-1809, July 1964.

[17] B. Adam and F. Kneubuhl, "Transversely excited 337 µm HCN waveguide laser", Appl. Phys. D, (8), 281-291, September 1975.

[18] K.D. Laakman and W.H. Steir, "Waveguides: Characteristic modes of hollow rectangular dielectric waveguides", Appl. Opt., 15(5), 1334-1340, May 1976.

[19] H. Krammer, "Field configurations and propagation constants of modes in hollow rectangular dielectric waveguides", IEEE J. Quantum Electron., QE(12), 505-507, August 1976.

[20] H. Nishihara et al., "Low-loss parallel plate waveguide at 10.6 µm", Appl. Phys. Lett., 25(7), 391-393, 1 October 1974.

[21] J.J. Degnan, "The waveguide lasers: A review", Appl. Phys., (11), 1-33, 1976.

[22] R.L. Abrams, "Waveguide gas lasers", in "Laser Handbook", Vol. 3, North Holland, Amsterdam, 1979.

[23] P.W. Smith et al., "Transversely excited waveguide gas lasers", IEEE J. Quantum Electron., QE-17(7), 1166-1181, 1981.

[24] S.A. Gonchukov et al., "Oscillation modes of a gas laser with a waveguide resonator", Sov. J. Quantum Electron., 6(0), 996-997, August 1976.

[25] J.J. Degnan, "Waveguide laser mode patterns in near and far field", Appl. Opt., 12(5), 1026-1030, May 1973.

[26] D.R. Hall et al., "10 µm propagation losses in hollow dielectric waveguides", Appl. Phys,., 48(3), 1212-1216, March 1977.

[27] G.A. Griffith, "Improved discharge uniformity for transverse radio frequency waveguide CO_2 lasers", P. Soc. Photo., 335(69), 1982.

[28] D. He and D.R. Hall, "Longitudinal voltage distribution in transverse RF discharge waveguide lasers", Appl. Phys., 54(8), 4367-4372, August 1983.

[29] P.E. Jackson, "Electrical simulation of RF laser discharges", internal report, University of Hull, 1984 (unpublished).

[30] R.L. Sinclair and J. Tulip, "Parameters affecting the performance of an RF excited CO_2 waveguide laser", Appl. Phys., 56(9), 2497-2501, 1 November 1984

[31] D. He et al., "Discharge striations in RF excited waveguide lasers", Appl. Phys. Lett., 55(1), 4120-4122, 1 June 1984.

[32] F. Moghbeli et al., "Impedance matching in radio-frequency discharge excited waveguide lasers", J. Phys. E: Sci. Instrum., (17), E3297/1-6, 1984.

[33] P. Chenausky et al., in CLEO '82 Technical Digest, Pheonix, April 14-16, 1982, Paper THN2.

[34] D.R. Hall et al., "A compact sealed waveguide CO_2 laser", J. Phys. D, 10(1) 1-6, 1977.

[35] G.M. Carter and S. Marcus, "A high power CO_2 waveguide laser', Appl. Phys. Lett., 35(23), 129-130, 1979.

[36] P. Vidaud and D.R.Hall, "Effect of xenon on the electron temperature of RF discharge CO_2 laser gas mixtures", Appl. Phys., Vol. 57, No. 5, 1757-1758, March 1985.

[37] D. He and D.R. Hall, "The influence of xenon on sealed-off operation of RF ecxited CO_2 lasers", Appl. Phys., (56) 856-857, 1984.

[38] R.L. Abrams, "Coupling losses in hollow waveguide laser resonators", IEEE J. Quantum Electron., (8), 838-843, 1972.

[39] A.N. Chester and R.L. Abrams, "Mode losses in hollow waveguide lasers", Appl. Phys. LEtt., 21(12), 576-5768, 1972.

[40] J-L. Boulnois and G.P. Agrawal, "Mode discrimination and coupling losses in rectangular waveguide resonators with conventional and phase conjugate mirrors", Opt. Soc. Am., 72(7), 853-860, July 1982.

[41] R. Gerlach et al., "Coupling efficiency for waveguide laser resonators formed by flat mirrors: Analysis and experiment", IEEE J. Quantum Electron, 20(8), 948-963, August 1984.

[42] S. Avrillier and J. Verdonck, "Coupling losses in laser resonators containing a hollow rectangular dielectric waveguide", Appl. Phys., 48(21), 1937-1941, December 1977.

[43] J.J. Degnan and D.R. Hall, "Finite-aperture waveguide-laser resonators", IEEE J. Quantum Electron., (9), 901-910, 1973.

[44] R.L. Abrams and A.N. Chester, "Resonator theory for hollow waveguide lasers", Appl. Opt., (13), 2117-2125, 1974.

[45] H. Kogelnik and T. Li, "Laser beams and resonators", Appl. Opt., (5), 1560-1567, 1966.

[46] C.A. Hill and D.R. Hall, "Coupling loss theory of single mode waveguide resonators", Appl. Opt., 24(9), 1283-1290, 1985.

[47] M.B. Klein and R.L. Abrams, "10.6 μm waveguide laser power amplifier", IEEE J. Quantum Electron., 11(8), 609-615, 1975.

[48] R.M. Jenkins and R.W.J. Devereux, "Preliminary studies of a single pass waveguide laser amplifier", RSRE Malvern, PH3 Division, Technical Note, 15 March 1984.

[49] P.A. Forester and K.F. Hulme, "Review - laser rangefinders", Opt. and Quant. Electron., (13), 259-293, 1981.

[50] "LEO RF CO_2 waveguide lasers", Laser Focus, 15(5), 115, 1976.

[51] K.F. Laakmann and P. Laakmann, "The coming of age of waveguide lasers", SPIE, (247), 74-78, 1980.

[52] K.D. Laakmann, "Transverse RF excitation for waveguide lasers", Proc. Int. Conf on Lasers '78, 741-742, V.T. Corcoran, Ed. McLean VA STS Press, 1979.

[53] M.R. Bennet et al., "Lightweight lasers for industry", Phys. Bull., 35, 428-429, 1984.

[54] L.A. Newman and R.A. Hart, "Recent R & D advances in sealed-off CO_2 lasers", Laser Focus/Electro-Optics, 80-96, June 1987.

[55] P.C. Conder, J.R. Redding and R.M. Jenkins, "Novel technology and performance of a high-power CO_2 waveguide laser", Infra. Phys., 25(1/2), 61-67, 1985.

[56] D.R. Hall and C.A. Hill, "RF-discharge-excited CO_2 lasers", in Handbook of Molecular Lasers, ed. P.K. Cheo, Marcel Dekker, 1987.

[57] D.M. Henderson, "Waveguide lasers with intracavity electro-optic modulators: Misalignment loss", Appl.Opt., Vol. 15, 1066-1070, 1976.

[58] C.A. Hill, private communication.

[59] C.A. Hill, "Transverse modes of plane mirror waveguide resonators", submitted to J. Quantum Electron., January 1988.

[60] D.C. Champeney, "Fourier transforms and their physical applications", London Academic Press, 38, 1973.

[61] W.W. Rigrod, "Saturation effects in high-gain lasers", J. Appl. Phys., Vol. 36, No. 8, 1965.

[62] W.W. Rigrod, "Homogeneously broadened cw lasers with uniform distributed loss", IEEE J. Quantum Electron., QE-14, 377-381, 1978.

[63] R.M. Jenkins and R.W.J. Devereux, "Dispersion phenomena in hollow alumina waveguides", IEEE J. Quantum Electron., Vol. QE-21, 1722-1727, 1985.

[65] J.J. Degnan, H.E. Walker, J.H. McElroy and N. McAvoy, "Gain and saturation intensity measurements in a waveguide CO_2 laser", IEEE J Quantum Electron., Vol. QE-9, 489-491, April 1973.

[66] D. He and D.R. Hall, "Influence of xenon on sealed-off operation of RF-excited CO_2 waveguide lasers", J. Appl. Phys., Vol. 56, No. 3, 856-857, August 1984.

[67] B. Carnahan, H.A. Luther and J.O. Wilkes, "Applied numerical methods", John Wiley and Sons Inc., 1969.

[68] Deranox 975, Data Sheet TR207, Andermann and Ryder Ltd., Central Avenue, West Molesey, Surrey, England.

[69] F.E. Terman, "Radio Engineer's Handbook", McGraw-Hill Book Company, 1943.

[70] CRC, "Handbook fo Chemistry and Physics", 64th Edition, CRC Press, 1983-1984.

[71] P. Vidaud, S.M.A. Durrani and D.R. Hall, "Alpha and gamma RF capacitative discharges in N_2 at intermediate pressures", J. Phys. D: Appl. Phys., Vol. 21,. 57-66, January 1988.

[72] P. Vidaud, S.M.A. Durrani and D.R. Hall, "Parameter scaling in diffusion-cooled RF discharge excited CO_2 lasers", submitted IEEE J. Quantum Electron., March 1988.

[73] G. Sowersby, University of Hull, private communication.

[74] "Advice on the protection of workers and members of the public from the possible hazards of electric and magnetic fields with frequencies below 300 Gz: A consultative document, HMSO, ISBN 0859512673, 1986.

[75] C.A. Hill, "Mode control and tunability in RF-excited CO_2 waveguide lasers", Ph.D. Thesis, University of Hull, December 1984.

[76] L. Newman, P.P. Chenausky, Paper, Gaseous Electronics Conference, 1984.

[77] C.A. Hill, P. Monk and D.R. Hall, "Tunable RF-excited CO_2 waveguide laser with variable guide width", IEEE J. Quantum Electron., Vol. QE-23, 1968-1973, 1987.

[78] C.A. Hill, P.E. Jackson and D.R. Hall, "CO_2 waveguide lasers with folds and tilted mirrors", to be published.

[79] CRC Handbook of Lasers, 2nd Edition, CRC Press, 151, 1983.

[80] M.I. Abu-Taha and D.C. Laine, "Frequency stabilisation of a CO_2 gas laser by intra-cavity optoacoustic absortion", Paper 18, presented at Eighth National Quantum Electronics Conference, St. Andrews, September 21-25, 1987.

[81] C.J. Baker, "Gain and saturation studies in RF excited CO_2 lasers", Ph.D. Thesis, University of Hull, 1986.

[82] P.E. Jackson, D.R. Hall, R.M. Jenkins and J.M. Vaughan, "Simultaneous measurements of gain and spontaneous emission noise in RF excited CO_2 amplifying media", Paper 806-15, SPIE Symposium, The Hague, April 1987.

[83] C.A. Hill and P.E. Jackson, "Hooting modes in a CO_2 waveguide laser", submitted to IEEE J. Quantum Electron., January 1988.

[84] D.S. Evans and G.R. Jessop, "VHF/UHF Manual", RSGB Publications, 1986.

[85] A.L.S. Smith and S. Moffat, "Opto-galvanic stabilised CO_2 laser", Opt. Commun., 30(2), August 1979.

[86] K.M. Abramski, J. van Spijke and W.J. Witeman, "On the opto-voltaic measurements in CO and CO_2 lasers", Appl. Phys. B, 36, 149-153, 1985.

[87] C. Stanciulescu, R.C. Bobulescu, A. Surmeian, D. Popescu and I.I. Popescu, "Hertzian and optical impedance spectroscopy", Rev. Roum. Phys., Tome 25, No. 8, p. 915-926, Bucarest, 1980.

[88] A. Von Engel , "Ionised gases", p. 113, Oxford University Press, 1965.

[89] A. Engel, "Ionised gases", Oxford University Press, p. 146-148, 1965.

[90] R.L. Abrams, "Gigahertz tunable waveguide CO_2 laser", Appl. Phys. Lett., vol. 25, p. 304-306, 1975.

[91] P.H. Davies, P.A. Forrester, D.R. Hall, R.M. Jenkins and J.T. Pinson, "Spurious oscillations from 10.6 μm cw CO_2 waveguide lasers", presented at ECOSA '78, Brighton, England, 1978.

[92] C.A. Hill, D.R. Hall and P. Monk, "Tunable rf-excited CO_2 waveguide laser with variable guide width", IEEE J. Quantum Electron., Vol. QE-23, p., 1987.

[93] E. Branagan, University of Hull, internal report, 1987.

[94] G. Schiffner, "Prediction of CO_2 laser signature", IEEE J. Quantum Electron., Vol. QE-8, p. 877-882, 1972.

[95] C.A. Hill and D.R. Hall, "Waveguide laser resonators with a tilted mirror", IEEE J. Quantum Electron., Vol. QE-22, p. 1078-1087, 1986.

[96] K.F. Hulme, "CO_2 laser heterodyne rangefinders, velocimeters and radars", Infrared Physics, vol. 25, no. 1/2, p. 457-466, August 1984.

[97] K.D. Laakmann, "The promise and limitations of 10.6 μm waveguide power amplifiers", Proceedings of the SPIE (San Diego), vol. 69, p. 74-82, August 1985.

[98] G.T. Schappert and M.J. Herbst, "Anomalous dispersion effects on pulse propagation in high pressure CO_2 amplifiers", Appl. Phys. Lett., vol. 26, No. 6, p. 314-315, March 1975.

[99] T. Kurosawa, "Anomalous refractive indices of the amplifying medium in a waveguide CO_2 laser", Appl. Opt., Vol. 25, No. 21, p. 3816-3824, November 1986.

[100] F. Malota, "Theoretical considerations for simultaneous use of an optical amplifier as an end- and preamplifier in a laser heterodyne radar", presented at the 3rd Topical Meeting on Coherent Laser Radar: Technology and Applications (Malvern, U.K.) 1985.

[101] C.J. Oliver, "A comparison of detection methods at 10.6 μm", Infrared Physics, Vol. 18, 303-307, January 1978.

[102] J.F. Lotspeich, "CO_2 laser preamplifier capabilities for low-level 10.6 μm direct-detection receivers", IEEE J. Quantum Electron., Vol. QE-13, No. 6, June 1977.

[103] N.D. Ustinov, "Methods of amplifying and transforming laser signals", J. Sov. Laser Research, Vol. 5, No. 4, 1984.

[104] H. Kogelnik and A.Yariv, "Considerations of noise and schemes for its reduction in laser amplifiers", Proceedings of the IEEE, Vol. 52, 165-172, February 1964.

[105] J. Arnaud, "Enhancement of optical receiver sensitivity by amplification of the carrier", IEEE J. Quantum Electron., Vol. QE-4, 893-899, November 1968.

[106] R.M. Jenkins, U.K. Patent GB 2 075 746 B.

[107] J.E. van de Laan, "Low-pressure gain-cell laser-detector operation with a CO_2 transversely excited atmospheric (TEA) laser", paper WC4-1, presented at Laser and Optical Remote Sensing: Instrumentation and Techniques Topical Meeting (Massachusetts), September 1987.

[108] D.K. Killinger, "Enhanced direct-detection of CO_2 LIDAR returns using a laser preamplifier" paper WC14-1, presented at Laser and Optical Remote Sensing: Instrumentation and Techniques Topical Meeting (Massachusetts), September, 1987.

[109] K. Chan and J.L. Bufton, "CO_2 laser preamplifier for LIDAR application", paper WC3-1, presented at Laser and Optical Remote Sensing: Instrumentation and Techniques Topical Meeting (Massachusetts), September 1987.

[110] E.J. McLellan, R. Fisher and J.L. Bufton, "Design of a CO_2 laser preamplifier for improved LIDAR and rangefinding sensitivity" paper ThI3, CLEO (Anaheim, CA), June 1984.

[111] E.J. McLellan, R. Fisher, D.K. Thomas and J.L. Bufton, "Optical preamplifier performance for CO_2 LIDAR applications, paper FB3, CLEO (San Francisco, CA), June 1986.

[112] A.E. Siegman, "Lasers", Oxford University Press, 1986.

[113] C.P. Christensen, C. Freed and H.A. Haus, "Gain saturation and diffusion in CO_2 lasers", IEEE J. Quantum Electron., 596, 276-283, 1967.

[114] J.R. Klauder et al., "The theory and design of chirp radars", Bell System. Tech. Journal, Vol. 39(4), 745-808, 1960.

[115] D.V. Willets and M.R. Harris, "An investigation into the origins of frequency sweeping in a hybrid TEA CO_2 laser", J. Phys. D, 15(1), 51-67, 1982.

[116] K.D. Laakmann, "Propagation in hollow waveguide amplifiers filled with an inhomogeneous medium", Ph.D. Thesis, University of Southern California, October 1975.

[117] G.E. Francois, "Mode matching with a single thin lens", Appl. Opt., Vol. 10, No. 5, 12157, 1971.

[118] H.J. Baker, "Mode-matching techniques as an aid to laser cavity alignment", Optica Acta, vol. 27, no. 7, 897-903, 1980.

[119] H. Kogelnik, "Imaging of optical mode-resonators with internal lenses", Bell Syst. Tech. J., Vol. 44, 455-494, March 1965.

[12] C.G. Parazzoli and K-R. Chien, "Numerical analysis of a cw RF pumed CO_2 waveguide laser", IEEE J. Quantum Electron., Vol. 22, No. 3, March 1986.

[121] G.M. Miller and C.A. Williams, "Compact high power transmitters for CO_2 laser systems", paper 806-01, SPIE, vol. 806, The Hague, April 1987.

[122] D.G. Youmans, "Phase locking of adjacent channel leaky waveguide CO_2 lasers", Appl. Phys. Lett., Vol. 44, No. 4, 365-167, February 1984.

[123] P.E. Jackson, D.R. Hall and R.M. Jenkins, "Mode coupling losses at a fold in a hollow dielectric waveguide", paper p23, presented at the Eighth National Quantum Electronics Conference (St. Andrews, U.K.), September 1987.

[124] G.J. Dezenberg and J.A. Merritt, "The use of a multipath cell as a CO_2-N_2 gas laser amplifier and oscillator", Appl. Opt., Vol. 6, No. 9, 1541-1543, September 1987.

[125] H. Hieslmair, C.J. Bickart and J.N. Fulton, "Small signal gain of a CO_2 laser amplifier utilising white optical reflector design", IEEE J. Quantum Electron. correspondence, 86-87, January 1970.

[126] E. Biselli and F. Malota, "Heterodyne receiver for range resolved target-velocity measurements", presented at the 3rd Topical Meeting on Coherent Laser Radar: Technology and Applications (Malvern, U.K.), 1985.

[127] J.G. Xin and D.R. Hall, "A compact, multipass, single transverse mode CO_2 laser", Appl. Phys. Lett., Vol. 51, No. 7, 469-71, August 1987.